

Politecnico di Torino

Department of Mechanical and Aerospace Engineering

Master Degree in Aerospace Engineering



Master Degree Thesis

Validation of a XV-15 Tilt Rotor Aerodynamic Database

Supervisors

Giorgio Guglieri

Pierluigi Capone

Federico Barra

Candidate

Flavio Lleshi

2020-2021

To my parents,
for all the sacrifices they made,
for being a source of courage and inspiration.

ABSTRACT

The purpose of this work is the implementation and the description of a real-time flight simulation model of the Bell Aircraft Corporation XV-15 Tilt-Rotor Research Aircraft. The model is developed in the Matlab/Simulink® environment and is integrated with the ReDSim of the ZAV (Centre for Aviation) at ZHAW (Zurich University of Applied Sciences), in Winterthur, Switzerland. The RedSim is a research and development flight simulator employed for educational and industrial applications. The author carried out all the activities as part of an Exchange Program between ZHAW and Politecnico di Torino from September 2020 to November 2020. The first part of the author's work has been focused on the reviewing of the XV-15 aerodynamic model, in terms of both its mathematical formulation, which is described in report CR-166536, *A mathematical model for real-time flight simulation of a generic tilt-rotor aircraft*, S. W. Ferguson, 1988, and its implementation in the Simulink environment. Several modifications have been made to the existing aerodynamic model: the most notable were the wing-pylon subsystem's induced aerodynamics and the rotor wake at the vertical stabilizer. In addition, all the reference systems of the aerodynamic model have been rethought by the author in order to be more simple and suitable. After the reviewing, it has been possible to trim the flight simulation model and to validate the data with both the GTRS model, with the data from NASA Report CR-166537, *Development and validation of a simulation for a generic tilt-rotor aircraft*, by Samuel W. Ferguson, 1989, and the initial model, thus without any modification on the aerodynamic subsystem, in order to assess whether the model was improved. A second validation was made with several flight test data in airplane mode always presented by Report CR-166537. The third part of the activity was implementing some contributes, which were not already present in the model: ground effect, side-by-side effect, jet thrust and landing gear drag. Lastly, a series of pilot-in-the-loop tests took place at the RedSim in order to assess the performance and handling-qualities of the simulated aircraft.

ACKNOWLEDGEMENTS

The path that led me to graduation has been hard and long, but I would be lying if I said I only remember hard work and sacrifices. When I look back, I see great satisfaction, achievements, and the pride I felt every single moment in studying something I loved. The university course has brought me not only knowledge but also a desire to learn more, attention to details and a desire to always improve, as well as great personal growth. The final thesis was the culmination of this journey, still managing to make me grow personally and professionally, but above all, opening my mind to the idea of continuing my studies with a PHD and having another experience abroad. I must say that this would not have been possible on my own. For this, I would like to express my sincere gratitude to:

Prof. Giorgio Guglieri of Politecnico di Torino, for trusting me, giving me the possibility to be a part of this stimulating project and to make this experience abroad, as well as for his commitment to supporting me.

Pierluigi Capone and Federico Barra of Zentrum für Aviatik, Zürcher Hochschule für Angewandte Wissenschaften (Winterthur, Switzerland), for making me feel at home from the very first day, for supporting me with dedication throughout the whole job, encouraging me, as well as sharing their knowledge and expertise.

Pilot Davide Guscelli, for hours spent testing the model on the simulator and for his valuable feedback.

The whole staff of ZAV Zentrum für Aviatik, for making me feel part of the group and, in particular, helping me to practice English.

Zürcher Hochschule für Angewandte Wissenschaften, for the financial support to my experience abroad. In particular, a special thank you to Mrs Prisca Dill for her commitment to helping me from the very first day.

Politecnico di Torino, for educating me during these years. In particular, thanks to all the professors who have left me with a lesson, however small.

Finally, a special thanks to Prof. Ezia Zulfarino, who made me first realize that I would be able to complete my studies.

CONTENTS

1	INTRODUCTION	2
1.1	The Research for a New V/STOL Aircraft	2
1.2	Development of the XV-15	5
1.2.1	The Role of Flight Simulation	7
1.2.2	ReDSim ZHAW	7
1.2.3	Why XV-15	8
1.3	Current Industrial Developments	8
1.3.1	V-22 Osprey	8
1.3.2	AW 609	9
1.3.3	V-280 Valor	11
1.3.4	Electric Tilt-Rotor	12
1.3.5	UAV Tilt-Rotor	13
2	REVIEW AND DEVELOPMENT OF THE MATHEMATICAL AERODYNAMIC MODEL	14
2.1	Overview	14
2.1.1	Rotation Matrix for Forces	16
2.1.2	Rotation Matrix for Moments	18
2.1.3	Rotation Matrix from Body to Wind Axes	18
2.1.4	Geometric Coordinates	19
2.2	Fuselage Model	20
2.3	Horizontal Stabilizer Model	23
2.3.1	Angle of Attack Calculation	23
2.3.2	Sideslip Angle Calculation	26
2.3.3	Dynamic Pressure	26
2.3.4	Loads Calculation	27
2.4	Vertical Stabilizer Model	29
2.4.1	Geometric Distances	30
2.4.2	Rotor Wake	30
2.4.3	Velocities at the Vertical Stabilizer	33
2.4.4	Sideslip Angle	33
2.4.5	Dynamic Pressure	34
2.4.6	Loads Calculation	34
2.5	Wing-Pylon Model	38
2.5.1	Induced Aerodynamics	39
2.5.2	Freestream Aerodynamics	48
2.5.3	Downwash Factor	51
2.5.4	Wing-Pylon Interference Drag	52
2.5.5	Spinner Drag	52
2.5.6	Pylon Drag	54
2.6	Forces and Moments Summation Model	55
3	VALIDATION AND RESULTS	56
3.1	Comparison with GTRS Model	56

3.1.1	Helicopter Mode	58
3.1.2	Conversion Mode	61
3.1.3	Airplane Mode	63
3.1.4	General Considerations	66
3.2	Comparison with Flight Test Data	66
3.3	Other Validation Data	73
3.4	Comparison of Eigenvalues	75
4	NEW IMPLEMENTATIONS IN SIMULINK	77
4.1	Ground Effect	77
4.1.1	The Physical Problem	77
4.1.2	Differences between Helicopter and Tilt-Rotor	80
4.1.3	Implementation	84
4.2	Side-by-Side Effect	86
4.3	Landing Gear Drag	86
4.3.1	Dynamic Pressure	87
4.3.2	Landing Gear Drag in Wind Axes	87
4.4	Jet Thrust	88
4.4.1	Jet Thrust in Wind Axes	88
4.4.2	Jet Thrust in Body Axes	89
5	SIMULATIONS AND RESULTS	91
5.1	General Considerations	91
5.2	Pilot-in-the-Loop Tests	91
5.2.1	Helicopter Mode	93
5.2.2	Conversion Mode	101
6	CONCLUSIONS	116
6.1	Achievements	116
6.2	Future Developments	117
A	AERODYNAMIC MODEL EQUATIONS	119
A.1	Fuselage	119
A.2	Horizontal Stabilizer	120
A.3	Vertical Stabilizer	122
A.4	Wing-Pylon	125
A.4.1	Induced Aerodynamics	125
A.4.2	Freestream Aerodynamics	132
A.4.3	Wing Wake Deflection at the Horizontal Tail	135
A.4.4	Wing-Pylon Interference Drag	135
A.4.5	Spinner Drag	135
A.4.6	Pylon Drag	137
A.5	Landing Gear	137
A.6	Jet Thrust	138
B	AERODYNAMIC TABLES	140
B.1	Fuselage	140
B.2	Horizontal Stabilizer	145
B.3	Vertical Stabilizer	149
B.4	Wing-Pylon	155
C	TRIM RESULTS	162

c.1	GTRS Data	162
c.1.1	Conversion Mode	162
c.1.2	Airplane Mode	164
c.2	Flight Test	167
D	FLIGHT TEST CARDS	169
	List of Figures	177
	List of Tables	182
	Acronyms	183
	List of Abbreviations	183
	Nomenclature	184
	Bibliography	198

1 | INTRODUCTION

1.1 THE RESEARCH FOR A NEW V/STOL AIRCRAFT

Nowadays, airports are usually placed quite distant from city centres, especially in densely populated areas. This reduces the time gained using air transport instead of other means such as rail and road. Moreover, with the ever-increasing demand for the transfer of goods and people worldwide, delays and air traffic congestion have become a serious and urgent problem, partially solved with helicopters, used by people also for small movements alternatively to cars. However, for long movements, the helicopter has limitations of speed and range, bringing the necessity for something new.



Figure 1.1: V-22 Osprey in Helicopter, Conversion and Airplane Mode, from Left to Right, Ref. [1]

The tilt-rotor was the result of the challenge of finding an aircraft type that meets both the hover and cruise-mode performance criteria. It belongs to Vertical and Short Take-Off Landing (V/STOL) aircraft¹, and its peculiarities are:

- in helicopter mode, the prop-rotors operate like conventional helicopter rotors, generating lift and enabling the aircraft to helicopter-like hovering, Vertical Take-Off Landing (VTOL) and low-speed capabilities;

¹ Several configurations belong to this category, but few of these have reached production and are currently deployed as military aircraft.

- in airplane mode, the prop-rotors tilt 90 deg forward, acting like large-diameter propellers and producing thrust, while the wing produces the main part of the lift. Therefore, the aircraft can operate as a conventional propeller-driven airplane and achieve similar cruise speed, range, and efficiency.

Due to these attitudes, it has the pros of a helicopter, therefore the V/STOL ability, which is essential in hostile environments or simply in a town, and the possibility to reach speeds similar to an airplane. Moreover, the mission range is much greater than a helicopter one, allowing longer non-stop missions. Indeed, it is possible to see in Figure 1.2 the range's comparison between Bell 525, blue circle, and Bell-Boeing V-22, black circle.

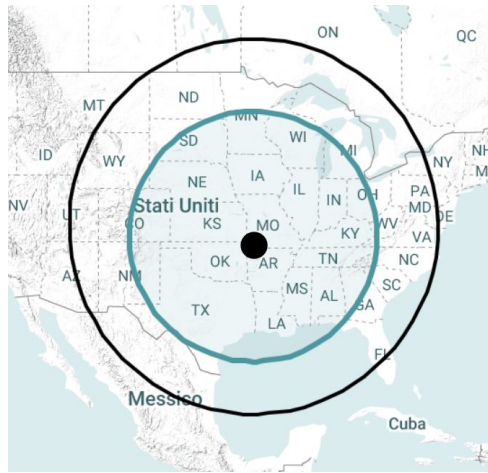


Figure 1.2: Range Comparison between Bell 525 and Bell-Boeing V-22, Ref. [2]

However, it has also cons since it is much less maneuverable than a helicopter², and it has a lower hovering capability due to its greater disk load Figure 1.3. Moreover, it costs currently 3 – 400% more than a helicopter, and several additional operating and maintenance costs shall be considered due to its mechanical complexity and the coexistence of both aircraft and helicopter designs.

The tilt-rotor has been studied since the II World War, but in the '50s, the tilt-rotor and tilt-wing concepts began in earnest. In fact, requirements in terms of hover duration and performance, low-speed maneuvering, agility, and speed and range, after the War, were beyond current helicopter capabilities, resulting in the August 1950 initiation of the joint U.S. Army and U.S. Air Force Convertiplane Program. On this occasion, the tilt-rotor concept made its first appearance with the XV-3 tilt-rotor aircraft (submitted by the Bell Helicopter Company). The XV-3 stood as a chance to demonstrate tilt-rotor potential to overcome several limitations or deficiencies, which the current helicopter design used to involve. Bell Aircraft presented the Bell Model 200 in response to the 1951 Convertible Aircraft Program Request for Proposal (lately designated XV-3 by the Army and Air Force), after extensive research and development activity led by Robert Lichten (previously principal at Transcendental, a company that initiated the

² Since the very beginning, the tilt-rotor also showed some stability problems.

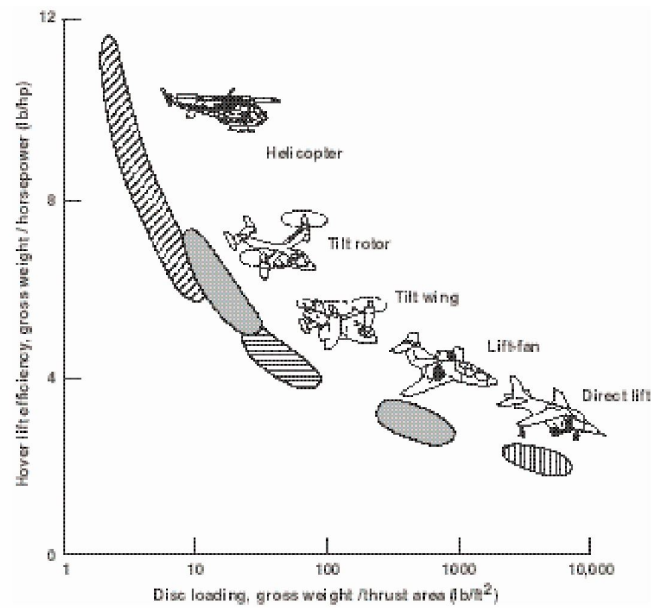


Figure 1.3: Disk Load Comparison between Different Rotor-Aircraft, Ref. [3]

prop-rotor research and development culminated in two prototypes, the Model 1-G and Model 2). Due to the currently limited analysis capabilities offered by the available analytical methods combined with experimental data, dynamicists' ability to understand and resolve the dynamic instability cause was quite primitive. In subsequent flight tests, a full tilt-rotor conversion was achieved, and it was able to reach a speed of 155 kts before incurring into aeroelastic instability. After 13 years of tests, a total of 110 full conversions were performed during 125 flight hours and the XV-3 project demonstrated the ability of the tilt-rotor concept to perform conversions from airplane to helicopter modes safely, even though it still highlighted several problems concerning the handling, in ground effect hovering instability, poor control responses at low-speed, all aspects that also led to several crashes and fatigue failures during wind tunnel tests. In 1966, Bell paid Haviland Platt for all rights to the convertible aircraft patent and continued developing tilt-rotor technology autonomously. The XV-3 final prototype has a two-bladed prop-rotor mounted on a shaft assembly at each wing-tip. Each prop-rotor can be converted over a range of 90 deg, and they are powered by a Pratt and Whitney R-985-AN-1 radial engine mounted in the fuselage. The empennage is a conventional one, plus a ventral fin below the rudder, while the landing gear is a skid type. To increase the stiffness of the wing, fuselage-to-wing tip struts were incorporated. The cockpit contains helicopter-like controls: a collective pitch stick with a twist-grip throttle, a cyclic control stick, and rudder pedals. When the aircraft converts, the collective pitch automatically increases, while the longitudinal cyclic controls are mechanically reduced to meet the required operative range. Neither stability augmentation nor lateral cyclic prop-rotor controls are installed.

1.2 DEVELOPMENT OF THE XV-15

The XV-15 Tilt-Rotor Research Aircraft, originally referred to as Bell Model 301, was developed by Bell Helicopter Textron starting from the early '70s, in the context of a joint program between the U.S. Army and NASA, aimed at providing a new proof-of-concept tilt-rotor technology demonstrator. It represented a significant evolution from its predecessor, the XV-3, with a different empennage³ configuration, an innovative transmission based on gears with *herringbone*⁴ tooth configuration, a more powerful gas turbine power-plants⁵, fuel cells, and a state-of-the-art flight control system.



(a) XV-15 in Airplane Mode



(b) XV-15 in Conversion



(c) XV-15 in Helicopter Mode

Figure 1.4: XV-15 in Different Flight's Configurations, Ref. [4]

The aircraft is a 17.4 m wide, 12.8 m long, and 4.7 m height machine, with two 3.81 m (12.5 ft) radius, three-bladed prop-rotors, and a design gross weight of 5896 kg (13 000 lb). This was the result of two requirements. Firstly, it had

³ XV-3 had a *T* configuration, while XV-15 a *H* one.

⁴ It was possible with the electron beam welding technology, new at the time.

⁵ A variant of the Lycoming T53-L-13B was used instead of Pratt and Whitney PT-6. Cons of this change were the need to redesign the nacelle configuration and the transmission interface and increasing engine weight and fuel consumption.

to be large enough to demonstrate performance, acoustics, handling-qualities, and flight- and structural-dynamics properly of this vehicle class. Secondly, it had to be small enough to be accommodated in the test section of NASA Ames 40 ft \times 80 ft wind tunnel for aerodynamics, loads, and systems performance evaluations.

The wing is non-tapered, with a span of 10 m, a chord of 1.6 m, and a forward sweep angle of 6.5 deg, required to obtain proprotor-to-wing clearance in airplane mode flight.

Moreover, to reduce the hover performance loss caused by the down-force due to the rotor wake on the wing, the flaps can be lowered to three preset deflection positions. At the same time, the ailerons can also be deflected down when the flaps are set, even though the displacement is limited to two-thirds of the flap position. Such surfaces are referred to as *flaperons* and are triggered at high speeds.

The tail is different from XV-3, and it has an *H* configuration, with two vertical fins and one horizontal fin: this change was made to improve the aircraft's stability. Both the tail and the wing are shown in Figure 1.5.

More information about the engines and their development, the free-turbine architecture and its operation in the event of power loss, controls, flight control system, flight characteristics, and conversion, even in case of a total electrical failure, can be found in Ref. [3], in Appendix A.

Figure 1.5 shows a summary of the main components of XV-15.

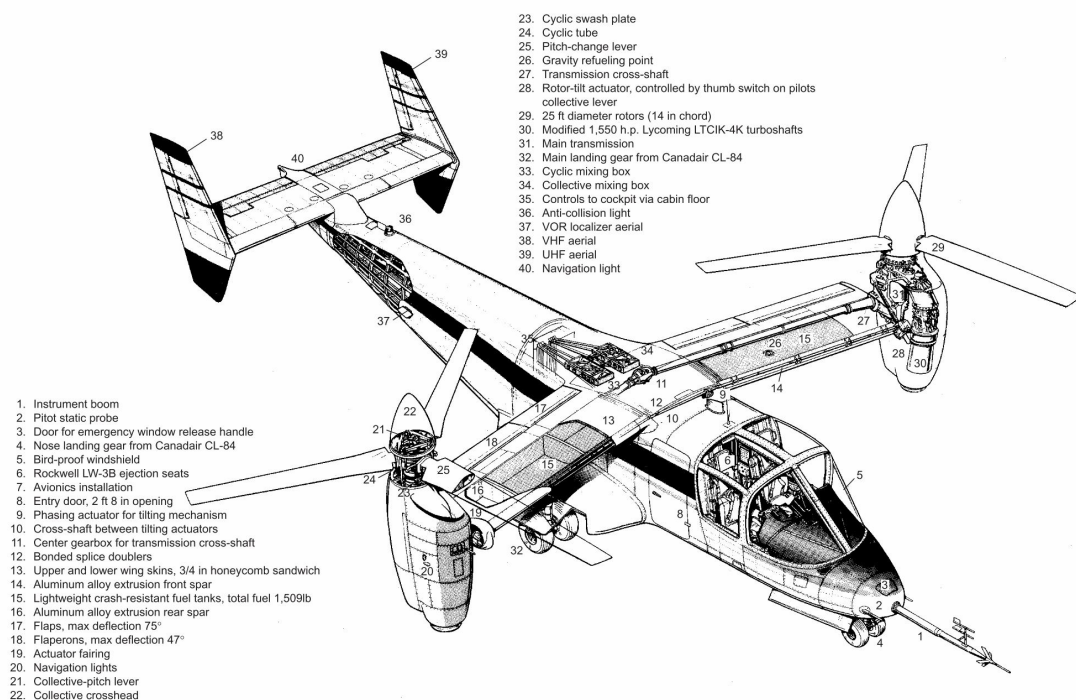


Figure 1.5: General Layout and Major Components of the XV-15 Tilt-Rotor Research Aircraft, Ref. [3]

1.2.1 The Role of Flight Simulation

Flight simulation is a fundamental aspect in the development of a new aircraft as well as for pilot training: given that the very purpose of an aircraft's development is to make it fly and perform its missions as required, being able to simulate how that aircraft behaves appears essential to evaluate every major decision that the design team makes. Indeed, flight simulation brings a consistent improvement in the project in terms of budget savings, time, and safety. On the other hand, flight simulation requires a mathematical model that has to assure the right grade of fidelity and software integration, which have to comply with specific standards that refer to the simulation's specific purpose. Therefore, flight simulation requires considerable efforts in terms of engineering development and involves several areas of expertise, going from basic mechanics to electronics.

1.2.2 ReDSim ZHAW

The ZHAW Research and Didactics Simulator (ReDSim) is a flight simulator developed within the ZAV Centre for Aviation and operative since March 2011. The whole system was designed and integrated by ZAV personnel and ZHAW students.

Thanks to the cockpit-like internal layout, a visual system with a 180-degree field of view, and a control loading system that simulates various feedback feel forces on pilot control, the flight simulator provides an immersive and highly realistic experience. ReDSim is used for research and educational activities, as well as for industrial purposes together with partner companies. It is meant to be a universal platform, providing an interface with a wide range of aircraft models, from conventional fixed-wing airplanes to Unmanned Aerial Vehicles and Rotor-craft, such as conventional helicopters.

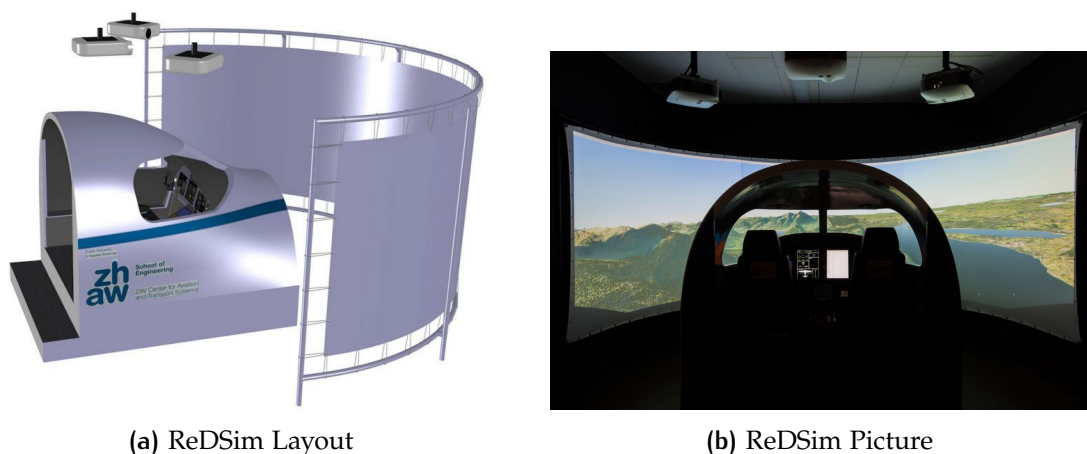


Figure 1.6: ZHAW RedSim, Ref. [5]

A tilt-rotor simulation model is also available in the ReDSim, based on the original Bell/NASA XV-15 model described in Ref. [6]. The development of the model was initiated in 2018 by Federico Barra, who reconstructed the whole

Generic Tilt-Rotor Simulation (GTRS) model from report CR-166536 and adapted it for the Simulink environment of the ReDSim. All the activities carried out by Barra, including the first series of validation activities, are described in his Master's Thesis, Ref. [7]. Then, the rotor model was developed and renewed by two other Master's Thesis students from Politecnico di Torino: Simone Godio and Anna Abà. In particular, the definitive rotor model can be found in her Master's Thesis work, Ref. [8], and the main points were also published in Ref. [9]. The last part still to be developed is the aerodynamic one, which is the present work's aim.

1.2.3 Why XV-15

Reliable flight simulation models are not easy to obtain. They require a considerable effort in terms of mathematical modelling and aerodynamic data processing: both activities involve a great deal of time, expertise, and economic resources. Nevertheless, flight simulation models play a crucial role in handling-qualities prediction as well as flight control law design of highly complex systems, such as convertiplanes. Although many publications have been produced so far about tilt-rotors, especially related to the XV-15 and the V-22 aircraft, sources describing mathematical models for specific real-time flight simulation applications are limited, with the first substantial attempts of developing a GTRS model for real-time flight simulation traced back to the XV-15 Tilt-Rotor Research Aircraft, Ref. [6]. It is believed to have been further modified and extensively improved and currently employed for flight simulation of the V-22 Osprey aircraft of both the U.S. Army and U.S. Navy. Anyway, it has the greatest database of aerodynamic data for a tilt-rotor model, and, as explained in Ref. [6], several tests were accomplished to have data for the rotor wake-aircraft interaction.

1.3 CURRENT INDUSTRIAL DEVELOPMENTS

1.3.1 V-22 Osprey



(a) V-22 Taking-Off from a US Navy Carrier



(b) V-22 in Airplane Mode

Figure 1.7: Bell V-22, Ref. [2]

Bell V-22 Osprey, Figure 1.7, was developed by Boeing Vertol and Bell Helicopter Textron and currently stands as the only operating tilt-rotor. It can be used both for military and civilian purposes. In fact, it can perform across the full range of military operations, refuel⁶ common tanker aircraft, carry shipments on-board⁷, and fast response in case of evacuation and recovery. The last utilising frontier is VIP transport, which Bell considers a lot with special internal design.

In all purposes, the tilt-rotor seems a great compromise, thanks to his abilities as V/STOL aircraft joined to the greater range and velocities that can reach. Figure 1.8 shows a trip comparison between the V-22 and two competitors: the V-22 can complete the mission in a row, while competitors need at least one stop.



Figure 1.8: Comparison between Helicopters and V-22 During a Mission, Ref. [2]

The first V-22 built to production debuted in service in 1999, and eleven units were produced by the end of 2000. Despite registering a few incidents and a major crash (on December 11, 2000), in 2013, the Bell-Boeing V-22 project was awarded five-year U.S. Naval Air System Command (NAVAIR) contract for the supply of 99 more units. Today, more than 200 Ospreys have been produced and are currently in service with the Marine Corps, U.S. Air Force, and Navy, with a total of more than 185000 flight hours. Japan ordered five units for its Self Defence Forces in 2015, becoming the first V-22 export customer. In Ref. [2], it is possible to find the specifications of V-22.

1.3.2 AW 609

The AW 609, Figure 1.9, is a tilt-rotor developed by Augusta Westland. It is smaller than V-22 Osprey even though it is thought for the same purposes. Its specifications can be found in Ref. [10].

⁶ This capability was proven during the trans-Atlantic crossing by US Marine and Air Force crews.

⁷ The shipboard compatibility was an essential requirement for the development.



(a) AW 609 in Airplane Mode



(b) AW 609 in Conversion



(c) AW 609 in Helicopter Mode

Figure 1.9: AW 609, Ref. [10]

Figure 1.10 shows an important skill of the AW 609: the flight altitude is greater than a helicopter one, allowing to fly above the weather, therefore without limitation when it is bad. This is possible because it is the first pressurized rotor-craft seeking certification, a characteristic which comes with several complex implications, as no new helicopter category has been certified since 1946.

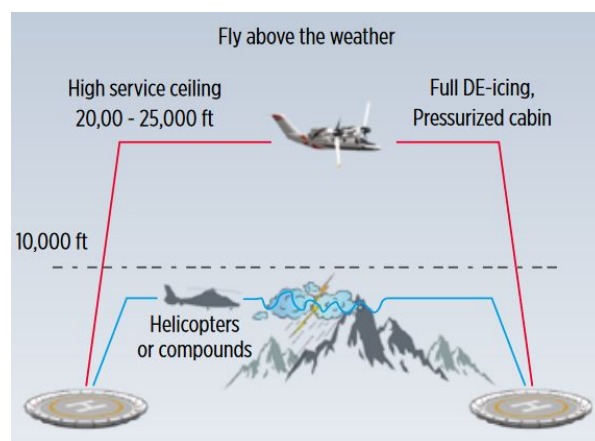


Figure 1.10: Flight Altitude Comparison between AW 609 and a Generic Helicopter, Ref. [10]

The development of this aircraft was highly conditioned by an incident that occurred in 2015 in Italy, during a flight test, where the AW 609 experimented

a dutch roll out of the flight envelopment, which brought the aircraft over its structural limits. On the other hand, this multi-purpose tilt-rotor is a highly innovative machine, exploiting several state-of-the-art technologies such as a triple-redundant, fully fly-by-wire flight control system, and a mostly composite airframe.

1.3.3 V-280 Valor

V-280 Valor, Figure 1.11, is a tilt-rotor developed in cooperation between Bell Helicopter Textron and Lockheed Martin, which is part of the *future vertical lift* (FLV) program that supports the U.S. Army. Indeed, it is mainly thought for military purposes, with an eye on maneuverability.



(a) Bell V-280 in Helicopter Mode

(b) Bell V-280 in Airplane Mode

Figure 1.11: Bell V-280 in Flight, Ref. [2]

It can reach a speed of 280 kts, with a combat range of 500/800 nm. It is interesting to compare this range with the UH-60 Black Hawk one: Figure 1.12 shows that V-280 has a range that is greater than the double.

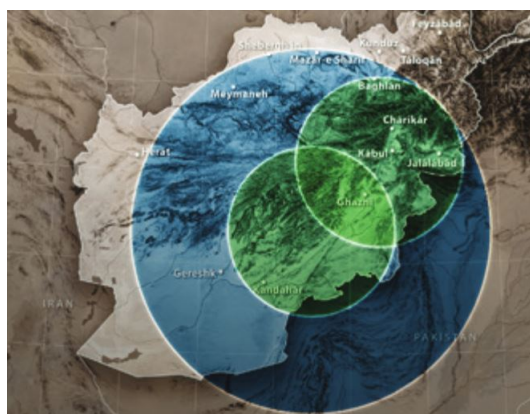


Figure 1.12: Range Comparison between V-280 and UH-60 Black Hawk, Ref. [2]

All aircraft's specifications can be found in Ref. [2]

1.3.4 Electric Tilt-Rotor

Faster transfer of goods, people and information, environmental pollution reduction, and traffic congestion are some of the major challenges for modern society transportation systems. As told, tilt-rotors, with their unique operational flexibility, have the potential to be absolute protagonists in this scenario. Therefore, it came the necessity to develop all-electric propulsion aircraft. An increasing number of aerospace companies invest time and resources to develop new and all-electric tilt-wing and tilt-rotor concepts.

One of the major companies involved in the development of electric aircraft is Airbus, as also demonstrated by the civil transport sector. Regarding tilt-rotor, the most notable is the A^3 Vahana, an all-electric, self-piloted tilt-wing whose goal is increasing the company knowledge base concerning convertible, fully autonomous aircraft, as well as proving the capability of these vehicles to be a cost-comparable replacement for traditional short-range urban transport. Vahana's design started in 2016, while flight tests began in 2018, with the first successful conversion achieved in May 2019. Its major pros are quietness⁸, time-saving⁹, emissions-free, and autonomy¹⁰. More information about this revolutionary aircraft and its first conversion video are available in Ref. [11].



Figure 1.13: Airbus A^3 Vahana During Its First Flight at One of the A^3 Facilities in the Silicon Valley, Ref. [11]

Not only tilt-rotors are developed in electric, but an interesting tilt-wing is being developed by the Swiss company Dufour Aerospace. It aims to revolutionize urban and rural transport by providing a faster and more efficient alternative to conventional means, such as cars. A special attention is dedicated to mountain regions, where transport can be difficult and slow: in Ref. [12], it is shown an interesting comparison for transport between Zermatt and Milan, where more than three hours are necessary by car, while Dufour's tilt-wing needs just 22 minutes to connect them, with consequential save of time, money and emissions.

⁸ Nowadays, acoustic problems are as important as emissions. Indeed, noise pollution is one of the greatest challenges for future mobility.

⁹ Up to four times faster than a car.

¹⁰ It is self-piloted with smart sensors.



Figure 1.14: Rendering of the Electric Tilt-Wing Aircraft Being Currently Developed by Dufour Aerospace, Ref. [12]

1.3.5 UAV Tilt-Rotor

The market of small electric unmanned vehicles (UAV) is in constant growth and represents another context in which convertible concepts can gain a prominent position. Currently, the UAV industry is still strongly conditioned by limited battery duration and long recharging times, and only by increasing vehicle performances, the full potential of these machines can be exploited. Tilt-wing and tilt-rotor designs offer flexibility, performances, and operational capabilities that are desirable for unmanned aircraft. Therefore, convertible technology is being investigated for several missions such as search and rescue, monitoring and surveillance, surveying and mapping, smart farming, entertainment and media, law enforcement, and many more. The application of tilt-rotor technology to military UAVs has also been considered.

An early example is the Eagle Eye Unmanned Aerial Vehicle, developed by Bell Helicopter in the late 1990s. Its prototype crashed in 2006, and Bell could not get enough interest or money to keep the program going.



Figure 1.15: Bell Eagle Eye Tilt-Rotor UAV

2

REVIEW AND DEVELOPMENT OF THE MATHEMATICAL AERODYNAMIC MODEL

The main part of the author's activity at ZHAW School of Engineering was reviewing and developing the Aerodynamic Mathematical Model of the XV-15 Tilt-Rotor, presented in Ref. [6], and called GTRS model.

In this part, the author reviewed the model already implemented in Simulink. Finding references in literature to validate the aerodynamic data was not easy since those present in Ref. [6] were collected in Ames wind tunnel.

Moreover, some issues occur also with units of measure:

- geometric coordinates were provided in *inches*, while geometric lengths in *feet*: a division by 12 is necessary to pass from $[in]$ to $[ft]$. All moments are referred to *feet*;
- aerodynamic coefficients were often dimensional. Therefore, forces and moments have to be calculated in $[lb]$ and $[lb \cdot ft]$ to avoid any conversion error.

Due to the lack of references and the reasons mentioned above, only a previous version of the GTRS model, presented in Ref. [13], could be used for comparison.

Regarding the equations, the majority was similar to the basic aerodynamic ones for lift, drag, side force, and roll, pitch, and yaw moment. Thus, it was possible to compare them with many references to assess whether they were right or not. However, some equations were not referable to a theoretical framework since they were semi-empirical formulation specially derived for the XV-15 (for instance, the induced aerodynamics equations for the wing-pylon presented in Section 2.5.1).

2.1 OVERVIEW

The Aerodynamic Model was developed by Ferguson, Ref. [6], and it is divided into four main parts:

- Fuselage Subsystem;
- Horizontal Stabilizer Subsystem;
- Vertical Stabilizer Subsystem;
- Wing-Pylon Subsystem.

- aircraft body axes, Figure 2.3: they were set for both translation and rotation speeds, Euler's angles, and rotor forces and moments, and hence, not modifiable;

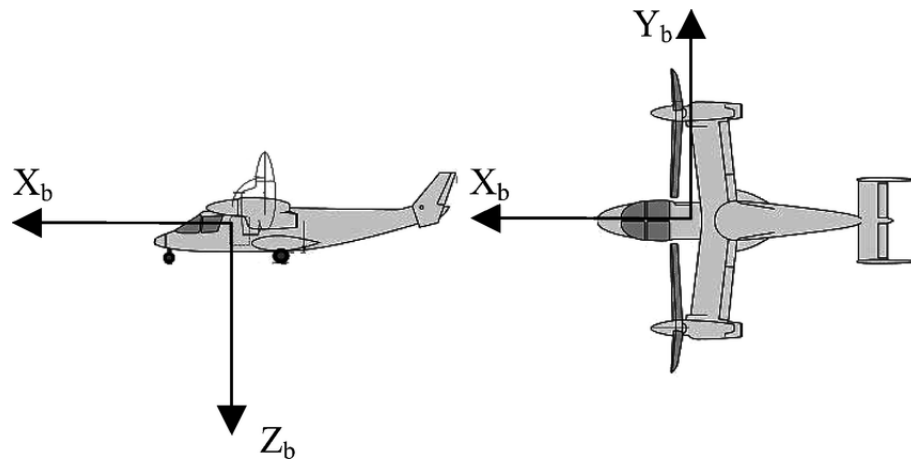


Figure 2.3: Body Axis System, Ref. [15]

- aircraft wind axes: aerodynamic forces and moments were calculated in wind axes. Therefore, they had to be transformed into body axes. There is no general convention for wind axes, as is explained afterwards.

After thinking about different solutions, it was decided to calculate rotational matrices using current systems, not to have problems with aerodynamic tables, to rearrange rotor's wake signs in input for the aerodynamic model, and to calculate the arms in c.g. axes, taking into account the fact that coordinates were on the contrary of body axes.

Changing the rotor model's current reference systems was avoided considering that it was thought and set in previous work with much effort. Moreover, it was optimized for the tilt-rotor and the fact that forces and moments are symmetric in the two rotors. Therefore, it was not reasonable to touch it, but it seemed easier to understand how inputs arrive in the aerodynamic system and to adjust the equations.

Geometric distances were already implemented in the *iniac* routine. Changing them would have been longer. It would have been easier to forget to change some lengths while adjusting the arms' calculation was much easier.

Lastly, a difference occurs in forces wind axes and moments wind axes. Therefore, special attention should be paid to this. As a general rule, forces along X and Z are considered positive in the direction they act (each example, the lift positive upward). In contrast, forces along Y and moments are considered positive in a wind coordinate system concord to aircraft body axes. However, some exceptions may occur, and they will be thorough in the following sections.

2.1.1 Rotation Matrix for Forces

To rotate wind axes into body axes is necessary to calculate a rotation matrix for both angles of attack and sideslip, then it is sufficient to multiply them.

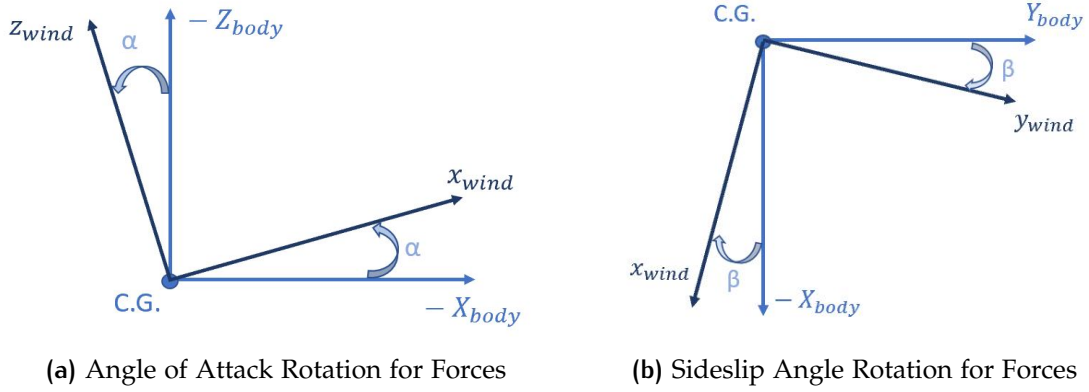


Figure 2.4: Forces Rotation from Wind into Body Axes

First of all, it is possible to calculate the rotation matrix for α , by referring to Figure 2.4a, where α is a generic angle of attack, positive anticlockwise.

$$[R_\alpha] = \begin{bmatrix} \cos \alpha & 0 & -\sin \alpha \\ 0 & 1 & 0 \\ \sin \alpha & 0 & \cos \alpha \end{bmatrix} \quad (2.1)$$

Similarly, the sideslip matrix is calculated by referring to Figure 2.4b, where β is a generic angle of sideslip, positive clockwise.

$$[R_\beta] = \begin{bmatrix} \cos \beta & \sin \beta & 0 \\ -\sin \beta & \cos \beta & 0 \\ 0 & 0 & 1 \end{bmatrix} \quad (2.2)$$

As explained in Ref. [16], it is possible to multiply $[R_\alpha] \cdot [R_\beta]$, obtaining:

$$[R'] = \begin{bmatrix} \cos \alpha \cos \beta & \cos \alpha \sin \beta & -\sin \alpha \\ -\sin \beta & \cos \beta & 0 \\ \sin \alpha \cos \beta & \sin \alpha \sin \beta & \cos \alpha \end{bmatrix} \quad (2.3)$$

Finally, X and Z have to be reported in the body axes coordinates system, as they are on the contrary², by multiplying the following matrix:

$$[R_\pi] = \begin{bmatrix} \cos \pi & 0 & 0 \\ 0 & 1 & 0 \\ 0 & 0 & \cos \pi \end{bmatrix} \quad (2.4)$$

The definitive **rotation matrix for forces** is:

$$[R_F] = [R_\pi] \cdot [R'] = \begin{bmatrix} -\cos \alpha \cos \beta & -\cos \alpha \sin \beta & \sin \alpha \\ -\sin \beta & \cos \beta & 0 \\ -\sin \alpha \cos \beta & -\sin \alpha \sin \beta & -\cos \alpha \end{bmatrix} \quad (2.5)$$

² Note that the body axes convention is shown in Figure 2.3.

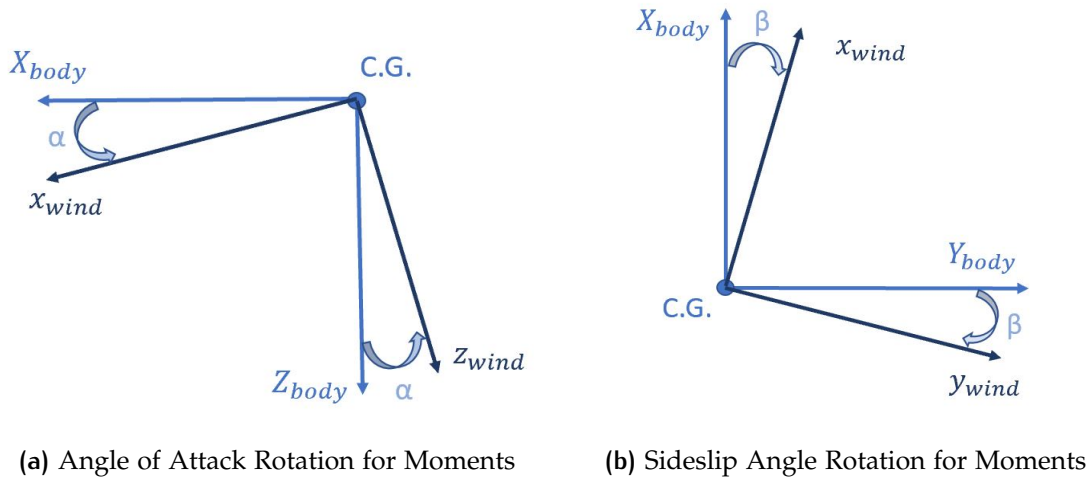


Figure 2.5: Moments Rotation from Wind into Body Axes

2.1.2 Rotation Matrix for Moments

To calculate the rotation matrix for moments, it is possible to refer to Figure 2.5, obtaining:

$$[R_\alpha] = \begin{bmatrix} \cos \alpha & 0 & -\sin \alpha \\ 0 & 1 & 0 \\ \sin \alpha & 0 & \cos \alpha \end{bmatrix} \quad (2.6)$$

and

$$[R_\beta] = \begin{bmatrix} \cos \beta & -\sin \beta & 0 \\ \sin \beta & \cos \beta & 0 \\ 0 & 0 & 1 \end{bmatrix} \quad (2.7)$$

Hence, the **rotation matrix for moments** is:

$$[R_M] = \begin{bmatrix} \cos \alpha \cos \beta & -\cos \alpha \sin \beta & -\sin \alpha \\ \sin \beta & \cos \beta & 0 \\ \sin \alpha \cos \beta & -\sin \alpha \sin \beta & \cos \alpha \end{bmatrix} \quad (2.8)$$

which does not need further modifications, given that wind and body axes are concords in this case.

2.1.3 Rotation Matrix from Body to Wind Axes

This matrix is used only once, but it can be important for further development. The procedure is the same used before, but when the matrices for α and β are known, they have to be multiplied in the opposite order.

By referring to Figure 2.6, it is possible to calculate $[R_\alpha]$ and $[R_\beta]$.

$$[R_\alpha] = \begin{bmatrix} \cos \alpha & 0 & \sin \alpha \\ 0 & 1 & 0 \\ -\sin \alpha & 0 & \cos \alpha \end{bmatrix} \quad (2.9)$$

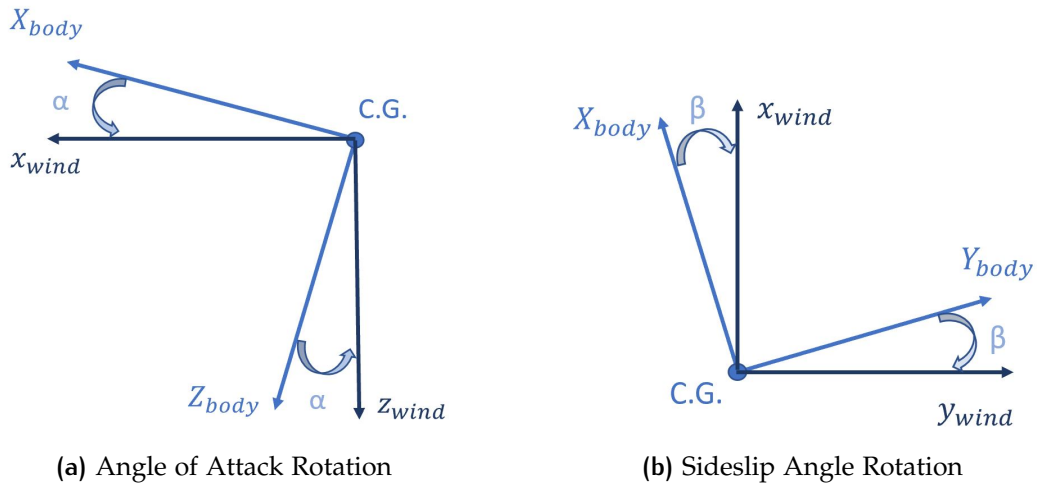


Figure 2.6: Rotations for Transformation from Body into Wind Axes

$$[R_\beta] = \begin{bmatrix} \cos \beta & \sin \beta & 0 \\ -\sin \beta & \cos \beta & 0 \\ 0 & 0 & 1 \end{bmatrix} \quad (2.10)$$

Then, it is possible to obtain the **rotation matrix for transformation from body to wind axes**:

$$[R_W] = [R_\alpha] \cdot [R_\beta] = \begin{bmatrix} \cos \beta \cos \alpha & \sin \beta & \cos \beta \sin \alpha \\ -\sin \beta \cos \alpha & \cos \beta & -\sin \beta \sin \alpha \\ -\sin \alpha & 0 & \cos \alpha \end{bmatrix} \quad (2.11)$$

2.1.4 Geometric Coordinates

Concerning geometric coordinates³, as previously said, the system was not changed for the water line (along Z) and the station line (along X), Figure 2.2. Since they are contrary to X-Body and Z-Body, arms cannot be calculated as the difference between any coordinate and the c.g., but a minus sign is required before using the cross product for the moments. For instance, let's calculate the arm between the fuselage c.p. and the c.g. along X: this is normally $SL_F - SL_{CG}$, but due to the system coordinate, it shall be calculated as $SL_{CG} - SL_F$. A small scheme is shown in Figure 2.7.

Instead, the butt line (along Y) is positive for both Y-Body positive and negative, as shown in Figure 2.2. This would have brought several problems to the vertical stabilizer subsystem. For this reason, the decision was to consider the butt line positive only for Y-Body positive, which was the perfect solution to have as few problems as possible for the vertical stabilizer, and only one coordinate had to be changed. Arms for the butt line can be calculated like usual, hence the difference between any coordinate and the c.g. (for instance, the arm along y for the fuselage can be calculated as $BL_F - BL_{CG}$). This is contrary to the

³ Note that all coordinates are provided in *inches*, while all lengths in *feet*, as explained before.

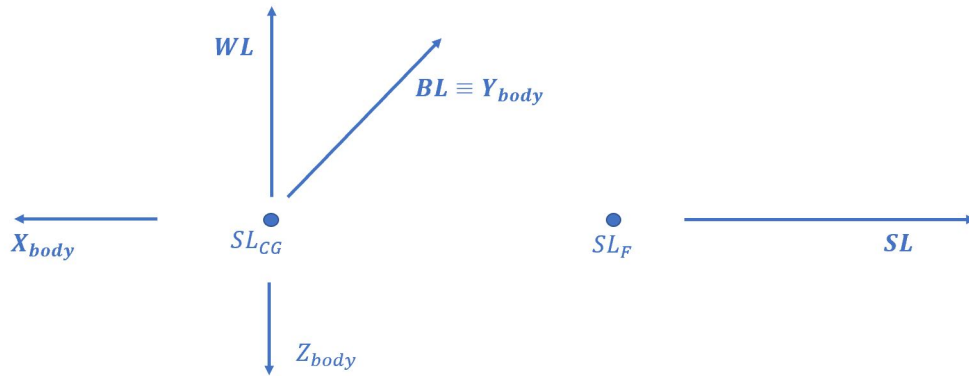


Figure 2.7: Arm Calculation's Example

station and water line convention, but it was the best solution for the different subsystems.

2.2 FUSELAGE MODEL

In Figure 2.8, there is a summary of vectors and angles involved in the fuselage subsystem and their conventions. α_F , the fuselage angle of attack, and V_T , the total velocity are the most important for the fuselage.

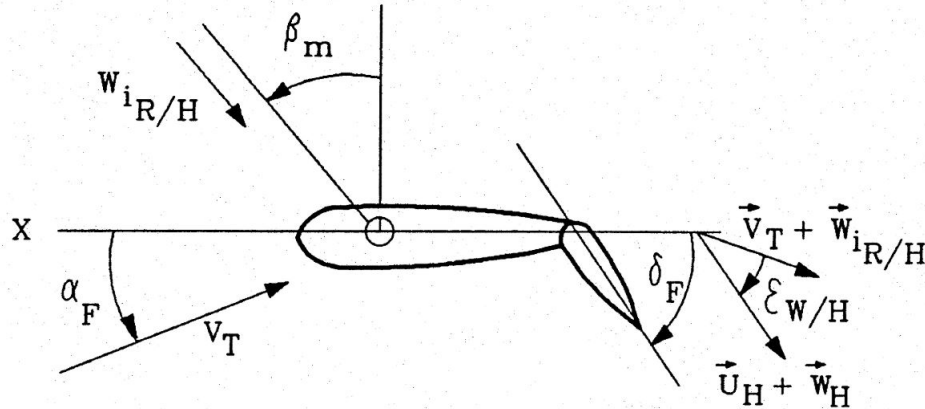


Figure 2.8: Wing and Fuselage Vector Diagram, Ref. [6]

The fuselage subsystem consists mainly of some aerodynamic tables, which provide aerodynamic coefficients for the fuselage and allow the calculation of fuselage forces and moments. These coefficients are dimensional:

- force coefficients are in $[ft^2]$, therefore already multiplied for a reference surface;
- moment coefficients are in $[ft^3]$, therefore already multiplied for a reference surface and a reference length.

This is because data comes from the wind tunnel: the model was in scale [1 : 1], probably the best solution to have those coefficients was a wind tunnel balance, which provides loads⁴, while coefficients can be calculated only with some pressure sensors. However, due to the fuselage's dimension, too many were necessary to obtain reliable coefficients.

Data is provided for both angles of attack and sideslip. Thus, there are nine tables in total: L_α , D_α , M_α , L_β , D_β , Y_β , l_β , M_β , and N_β . When a coefficient depends on α , it is meant for $\beta = 0^\circ$, while when it depends on β , it is meant for $\alpha = 0^\circ$. Only lift, drag, and pitch coefficients depend on α and β , as the lateral-directional ones have a negligible contribution from the angle of attack.

To comprehend the coefficients' calculation (Equation 2.12, 2.13, and 2.14), which contribute to fuselage loads, it is necessary to point out some considerations.

$$CD_{Fuselage} = D_\alpha \cos \beta_F^2 + D_\beta + D_{BF0} + D_{LANG} \quad (2.12)$$

$$CL_{Fuselage} = L_\alpha \cos \beta_F^2 + L_\beta + L_{BF0} + L_{LANG} \quad (2.13)$$

$$CM_{Fuselage} = M_\alpha \cos \beta_F^2 + M_\beta + M_{BF0} \quad (2.14)$$

- Given that aerodynamic data comes from the wind tunnel, coefficients for lift, drag, and pitch contain the constant term and the first-order term of the expansion⁵. This means that the constant term, which is the same⁶ for α and β coefficients, is added twice, and therefore has to be subtracted once. To aim this, three more coefficients are implemented, L_{BF0} , D_{BF0} , and M_{BF0} ⁷, and they are added in force and moment coefficients calculation.
- Coefficients for α are calculated for $\beta = 0^\circ$, therefore with the flow that wet all the fuselage surface, but when there is sideslip, the flow wet only the projected surface and $\cos \beta$ appears in the equation to take this into account (the square is because a surface is projected, so it is bidimensional).
- D_{LANG} and L_{LANG} , respectively, fuselage extra-drag coefficient and fuselage extra-lift coefficient, are added to fit experimental data or take into account some interference effects not specified, as the author thinks.

To get the correct coefficients, α_F and β_F are table inputs in the Simulink model. They are calculated as follows⁸ by referring to Figure 2.9:

$$\alpha_F = \arctan \left(\frac{W}{U} \right) \quad (2.15)$$

$$\beta_F = \arctan \left(\frac{V}{U \sqrt{1 + \frac{W^2}{U^2}}} \right) \quad (2.16)$$

⁴ Divided for the dynamic pressure, they return the aerodynamic coefficients.

⁵ For instance, it is possible to see C_L as $C_L = C_{L0} + C_{L\alpha}\alpha + \dots$

⁶ Indeed, it is possible to calculate the constant term for $\alpha = \beta = 0^\circ$.

⁷ The coefficients are the opposite of the expansion's constant term, and hence, they are added.

⁸ As explained in Section 2.1.1, α is positive anticlockwise, β is positive clockwise. U , V and W are the velocities of aircraft's c.g. in body axes with respect to the air, respectively along x , y and z .

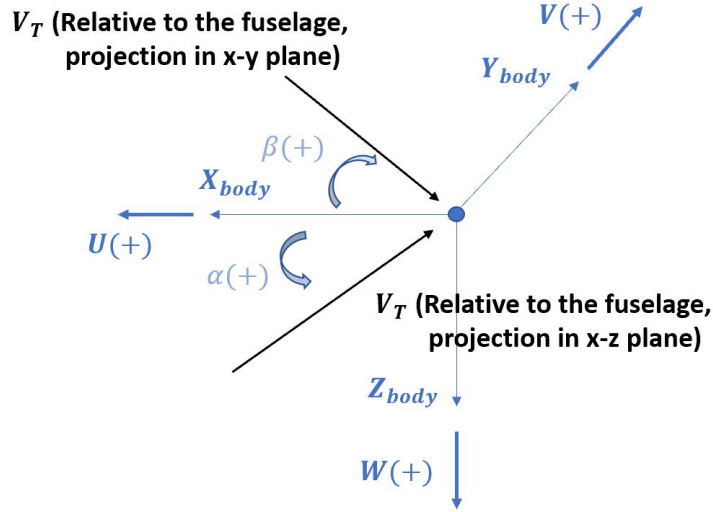


Figure 2.9: Angles of Attack and Sideslip Conventions

Finally, coefficients can be multiplied for the dynamic pressure, $q_F = \frac{1}{2}\rho V_T^2$, to obtain forces and moments in wind axes. Given the rotation matrices previously calculated, Equation 2.5 and 2.8, they are transformed into body axes⁹:

$$\begin{Bmatrix} X_F \\ Y_F \\ Z_F \end{Bmatrix} = \begin{bmatrix} -\cos\alpha\cos\beta & -\cos\alpha\sin\beta & \sin\alpha \\ -\sin\beta & \cos\beta & 0 \\ -\sin\alpha\cos\beta & -\sin\alpha\sin\beta & -\cos\alpha \end{bmatrix} \begin{Bmatrix} D_F \\ Y'_F \\ L_F \end{Bmatrix} \quad (2.17)$$

$$\begin{Bmatrix} l_F \\ M_F \\ N_F \end{Bmatrix} = \begin{bmatrix} \cos\alpha\cos\beta & -\cos\alpha\sin\beta & -\sin\alpha \\ \sin\beta & \cos\beta & 0 \\ \sin\alpha\cos\beta & -\sin\alpha\sin\beta & \cos\alpha \end{bmatrix} \begin{Bmatrix} l'_F \\ M'_F \\ N'_F \end{Bmatrix} \quad (2.18)$$

To consider the moments generated by forces, arms are calculated between fuselage c.p. and aircraft c.g., with the conventions explained in Section 2.1.4¹⁰. Then, they are multiplied to respective forces with a cross product.

$$l_{XF} = SL_{CG} - SL_F \quad (2.19)$$

$$l_{YF} = BL_F - BL_{CG} \quad (2.20)$$

$$l_{ZF} = WL_{CG} - WL_F \quad (2.21)$$

$$\begin{Bmatrix} l_{F_{Forces}} \\ M_{F_{Forces}} \\ N_{F_{Forces}} \end{Bmatrix} = \begin{Bmatrix} l_{XF} \\ l_{YF} \\ l_{ZF} \end{Bmatrix} \times \begin{Bmatrix} D_F \\ Y'_F \\ L_F \end{Bmatrix} \quad (2.22)$$

As the author thinks, this is the best way to get aerodynamic forces and moments without errors. Then, all contributes have to be summed, and they go as output in the subsystem, which calculates total forces and moments.

Complete equations are provided in Appendix A, while tables and graphs are provided in Appendix B. The following subsystems have the same basic idea. Therefore, the same concepts will not be explained again.

⁹ Forces and moments with ' are in wind axes.

¹⁰ In the model, they are divided by 12 to convert from *inches* to *feet*. This happens for all coordinates, and therefore, it will no longer be specified.

2.3 HORIZONTAL STABILIZER MODEL

The horizontal stabilizer subsystem is similar to the fuselage subsystem: the main idea is to calculate the angles of attack and sideslip, allowing for the aerodynamic coefficients and the stabilizer loads estimation.

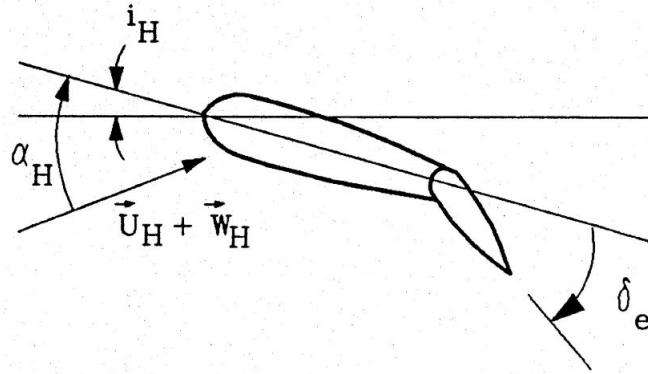


Figure 2.10: Horizontal Stabilizer Vector Diagram, Ref. [6]

Figure 2.10 shows angles and vectors to the horizontal stabilizer, particularly the angle of attack, the incidence and the elevator angle. The angle of attack is positive anticlockwise: **the convention in the figure is wrong.**

2.3.1 Angle of Attack Calculation

Firstly, it is important to define the velocities to the horizontal stabilizer, as it is downstream of the rotors and the wing. Moreover, it has a great arm with the c.g., hence the contribute of angular speeds can not be neglected. In this case, equations were changed from the GTRS model to comprehend the problem better and be sure about signs.

Arms are calculated with conventions explained in Section 2.1.4:

$$l_{XH} = SL_{CG} - SL_H \quad (2.23)$$

$$l_{YH} = BL_H - BL_{CG} \quad (2.24)$$

$$l_{ZH} = WL_{CG} - WL_H \quad (2.25)$$

l_{YH} is calculated for generality since it is null.

To take into account angular velocities, it is sufficient to calculate the cross product between angular speeds and arms ($\vec{\omega} \times \vec{r}$) and add the contributes to the aircraft's linear velocity (from Equation 2.26 to Equation 2.28).

The last contribution is the rotor wake: in *output* from the rotor subsystem, there is the induced speed at the horizontal stabilizer in two components, along

-X body and -Z body¹¹. These are added to the previous contributes, and the complete equations are the following:

$$U_H = U + U_{i_{R|H}} + q \cdot l_{ZH} \quad (2.26)$$

$$V_H = V + r \cdot l_{XH} - p \cdot l_{ZH} \quad (2.27)$$

$$W_H = W + W_{i_{R|H}} - q \cdot l_{XH} \quad (2.28)$$

Given the velocities, it is possible to obtain the aerodynamic angles. Different contributes have to be considered: the stabilizer's incidence, the angle of attack due to the velocities, and the *downwash*. The last one is calculated in the wing-pylon subsystem with a table of data obtained in wind tunnel tests. Instead, the incidence is in *input*, and it is a geometric parameter.

The GTRS model calculates two different angles for drag and lift:

$$\alpha_{HD} = -i_H + \arctan\left(\frac{W_H}{U_H}\right) + \varepsilon_{W/H} + K_e \tau_e \delta_e \quad (2.29)$$

$$\alpha_{HL} = -i_H + \arctan\left(\frac{W_H}{U_H}\right) + \varepsilon_{W/H}, \text{ if } M_N < 0.2 \quad (2.30)$$

$$\alpha_{HL} = -i_H + \arctan\left(\frac{W_H}{U_H}\right) + \varepsilon_{W/H} + K_e \tau_e \delta_e, \text{ if } M_N \geq 0.2 \quad (2.31)$$

The different angles of attack are positive anticlockwise, exactly as the fuselage ones, while the incidence angle is positive clockwise.

The lift angle of attack is different for $M_N < 0.2$ and $M_N \geq 0.2$, and in the second case, the elevator effect is taken into account. Indeed, it has an additional term where the elevator angle, the elevator effectiveness and a mach factor appear. The reason for this difference is not explained, but the hypotheses are two:

- compressibility effects: they are normally negligible for $M_N < 0.3$, but as the flow accelerates around the horizontal stabilizer, this condition is also reached with a freestream M_N smaller than 0.3;
- at low velocities, the elevator's effect is negligible for the lift, while it is not for the drag.

The difference brings a discontinuity in the results between $M_N < 0.2$ and $M_N > 0.2$, which is not physical. An example is shown in Figure 2.11¹², red and black lines.

Unlike the model developed in ZHAW, GTRS model results have not a discontinuity. Therefore, the author searched for another solution to have a continuous

¹¹ Induced velocity vectors arrive directly at the horizontal, while aircraft velocities are meant as relative to the horizontal. That is why they are summed instead of being subtracted. The same considerations are also valid for the vertical stabilizer and the wing-pylon.

¹² The result will be explained in Chapter 3.

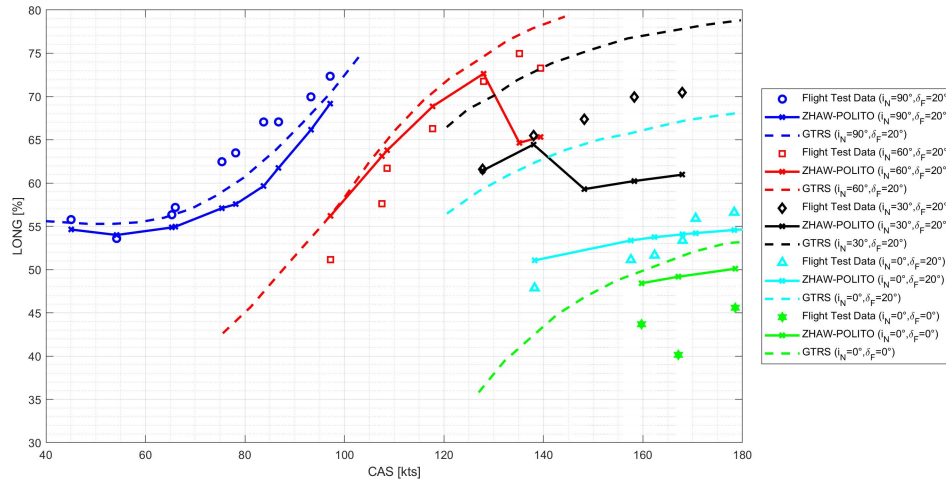


Figure 2.11: Discontinuity Due to the Horizontal Stabilizer's Lift Angle of Attack

function. After several searches, no data was found in literature. Even the previous model, wrote by Bell Helicopter Company in 1973, Ref. [13], was not helpful since the only difference was a sign in the equation, which would not have solved the problem.

In the end, the best solution seemed to change the additional term in order to have a continuous function, and the new equation became:

$$\alpha_{HL} = -i_H + \arctan\left(\frac{W_H}{U_H}\right) + \varepsilon_{W/H} + (1 - K_e)\tau_e\delta_e, \text{ if } M_N \geq 0.2 \quad (2.32)$$

K_e for $M_N = 0.2$ is equal to 1, so the function is continuous. The result is shown in Figure 2.12.

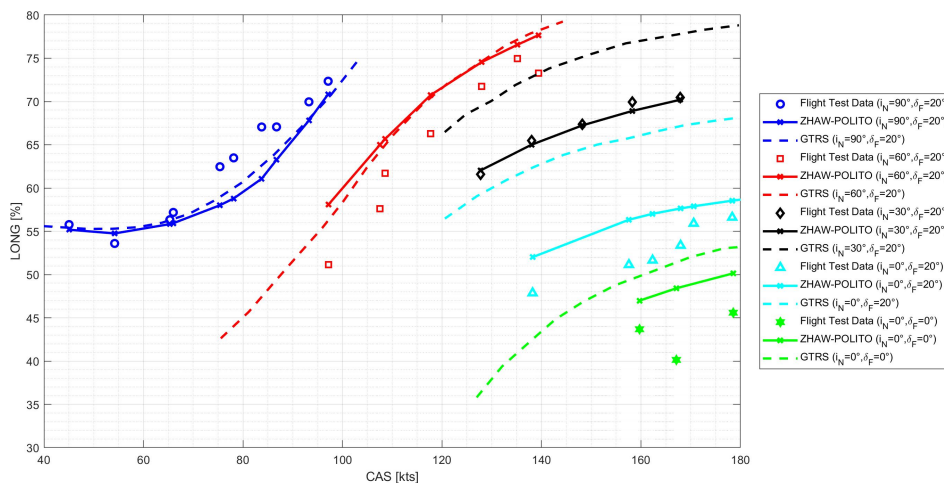


Figure 2.12: Results with the New Horizontal Stabilizer's Lift Angle of Attack

The idea came from some data that shows the elevator effect on the lift for different aircraft: for the ones with a size comparable to the tilt-rotor, the effect

is to increase $C_{L\alpha}$ for $0.3 \leq M_N < 0.8$. The new function for α_{HL} brings the same results, and the tilt-rotor cannot reach the transonic condition.

For consistency, since $\alpha_{HD} = \alpha_{HL}|_{M_N \geq 0.2}$, also α_{HD} was modified:

$$\alpha_{HD} = -i_H + \arctan\left(\frac{W_H}{U_H}\right) + \varepsilon_{W/H} + (1 - K_e)\tau_e\delta_e \quad (2.33)$$

2.3.2 Sideslip Angle Calculation

Given the previous section's velocities, the sideslip angle calculation is already prepared:

$$\beta_H = \arctan\left(\frac{V_H}{\sqrt{U_H^2 + W_H^2}}\right) \quad (2.34)$$

2.3.3 Dynamic Pressure

The angle of attack calculation already considers the wing-pylon wake, through downwash factor, the rotor wake, via induced velocities, and the angular velocities. Further contributing factors have to be considered for the dynamic pressure since interference effects like the wing-body blockage obstruct the flow.

First of all, the total velocity, which contributes to the dynamic pressure at the horizontal stabilizer, has to be defined:

$$V_{THq}^2 = (U\sqrt{\eta_{HS}} + q \cdot l_{ZH})^2 + (W\sqrt{\eta_{HS}} - q \cdot l_{XH})^2 \quad (2.35)$$

η_{HS} is a factor that depends on α_F , β_M and V_T : it considers the wing-body blockage by decreasing the aircraft speed.

The rotor induced velocities do not contribute to the total speed for the dynamic pressure. However, they act by modifying the angle of attack, which will change lift and drag coefficients. The reason may be found in the calculation of lift and drag coefficients in the wind tunnel: probably it was difficult to simulate the rotor wake, and coefficients were calculated only with the freestream contribute and normalized for that.

When the velocity is known, it is possible to calculate the dynamic pressure:

$$q_H = \frac{1}{2}\rho K_{HNU} V_{THq}^2 \quad (2.36)$$

K_{HNU} is the dynamic pressure loss, necessary when detailed wind-tunnel data is not available for mapping horizontal stabilizer dynamic pressure losses due to angle of attack, sideslip and airspeed, as it happens in the GTRS model¹³.

¹³ It is explained in Ref. [6]

2.3.4 Loads Calculation

With the angles of attack, it is possible to obtain lift and drag coefficients from tables provided by the model, which allow calculating lift and drag with the aerodynamic equations ($L = \frac{1}{2}\rho V^2 c_L S$, $D = \frac{1}{2}\rho V^2 c_D S$).

Unlike the fuselage subsystem, coefficients are non-dimensional. Therefore, the stabilizer surface is necessary, and it is an *input* of the model. The coefficients came from the wind tunnel for angles up to stall, while for angles above stall, they are extrapolated from Ref. [17].

C_{LH} , Figure 2.13, is a function of the angle of attack and the elevator angle, which is considered positive clockwise, as shown in Figure 2.10.

points data for block: model_trim/A/C Model/Aerodynamics/Horizontal Stabilizer
(Local Wind Axis)/CLH = f(alphaHL,MN,de)1

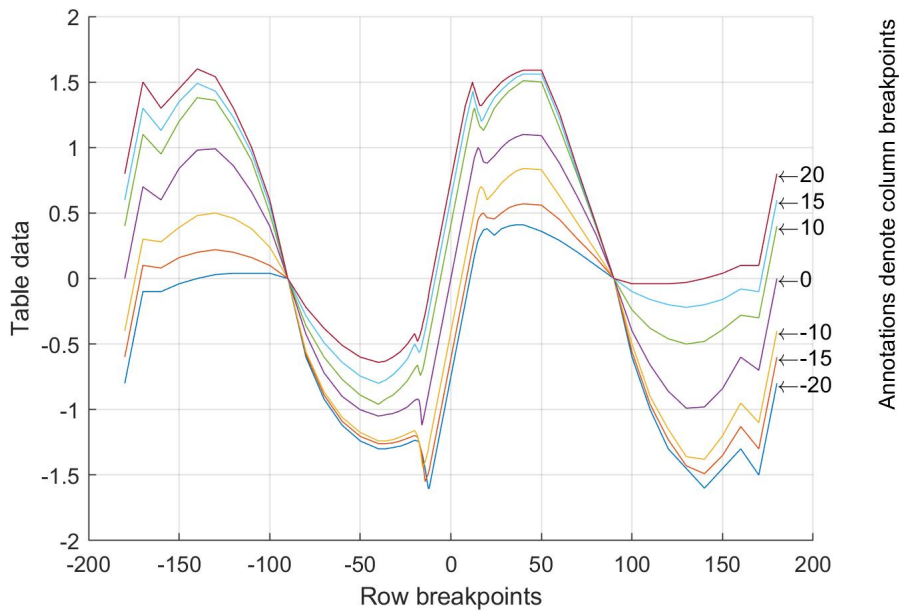


Figure 2.13: C_{LH} Table for $M_N = 0 - 0.2$

The figure shows that C_{LH} is greater when δ_e is greater. This was contrary to the same graph provided in Ref. [13] and a graph reported in the introduction of Ferguson's Model, Ref. [6]. However, it seems correct since the elevator's positive deflection generates an increase of lift, increasing, in turn, the lift on the horizontal stabilizer.

There is a further effect on lift coefficient due to Mach Number: as well as for $M_N = 0 - 0.2$, data is provided for $M_N = 0.4 - 0.5 - 0.6$, but only for $\delta_e = 0^\circ$ and for a smaller range of angle of attack.

The first limitation is easily explainable: at higher velocities, the elevator effect is negligible in lift calculation.

Instead, understanding why data at higher Mach is provided just for a limited range is more laborious: α is defined as the arctangent of the ratio between W and U . For $M_N = 0.2$, airspeed at sea level equals $\simeq 135$ kts. For instance, let's consider a longitudinal speed of $\simeq 100$ kts: to have an angle of attack of $\simeq 20^\circ$,

a vertical speed of $\simeq 45$ kts is necessary¹⁴. At higher Mach, a higher vertical speed is needed to have great α . For these reasons, it is useless to provide data for greater ranges¹⁵ since they are conditions where the tilt-rotor cannot fly.

Besides, data for $-8^\circ < \alpha < 12^\circ$ is not provided: this happens because it is the linear range for the lift coefficients, therefore, in Simulink, it is possible to obtain the desired one at any angle of attack, without further information.

C_{DH} , instead, is a function of the angle of attack and the Mach Number, as shown in Figure 2.14.

points data for block: model_trim/A//C Model/Aerodynamics/Horizontal Stabilizer
(Local Wind Axis)/1-D Lookup
Table

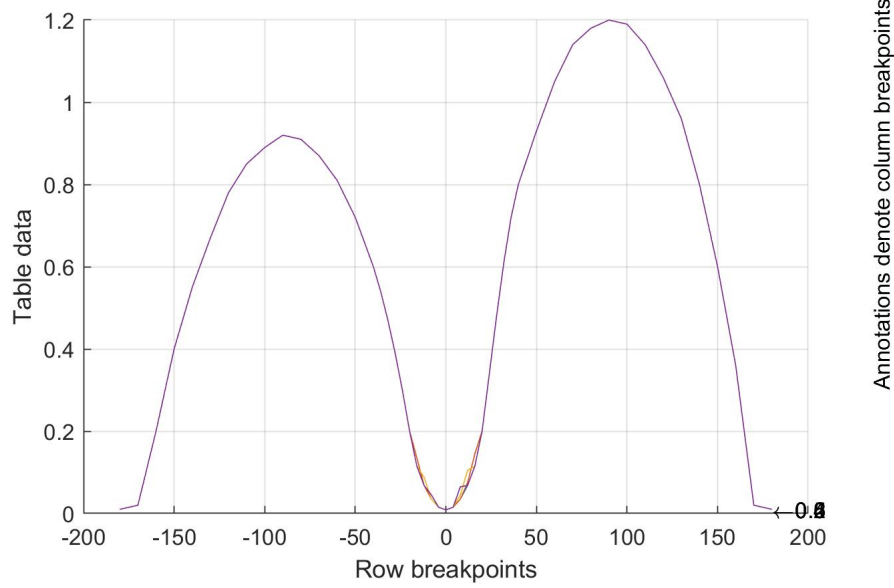


Figure 2.14: C_{DH} Table

As for the lift coefficient for $M_N > 0.2$, data is provided for a small range of angles: the reasons are the same explained before.

Given the coefficients, it is possible to calculate the loads:

$$L_H = q_H S_H [C_{LH} + C_{LH\beta} \cdot \min(15, |\beta_H|) \cos \beta_M] \quad (2.37)$$

$$D_H = q_H S_H C_{DH} \quad (2.38)$$

$$M'_H = q_H S_H c_H (C_{MH0} + C_{MHA} \alpha_{HL}) \quad (2.39)$$

Equation 2.37 considers the lift due to the angle of attack and the loss of lift due to the sideslip angle. In Ferguson's model, there is a further contribute due to the acceleration along z , but it was not possible to implement it in Simulink because it generates an algebraic loop. However, the contribution is negligible.

Finally, it is possible to transform loads from wind axes to body axes with rotation matrix previously calculated, Equation 2.5 and 2.8. Then, they go in *output* at the summation of forces and moments subsystem.

¹⁴ Note that V_T is $\simeq 135$ kts for the example, and therefore, $M_N = 0.2$.

¹⁵ As M_N increases, the data range is smaller; thus, for $M_N = 0.5 - 0.6$, data is even less.

A further *output* is the angle of attack for the horizontal stabilizer:

$$\alpha_H = \arctan \left(\frac{W_H}{U_H} \right) + \varepsilon_{W/H} \quad (2.40)$$

The incidence is not involved in the calculation, and α_H goes as *input* to the vertical stabilizer subsystem¹⁶, where it is needed to transform loads from wind to body axes.

Complete equations are provided in Appendix A, while tables and graphs are provided in Appendix B.

2.4 VERTICAL STABILIZER MODEL

One of the peculiarities of the XV-15 is the vertical stabilizer: common aircraft normally has one fin, while the tilt-rotor two. Thus, the vertical stabilizer model divides the two fins, calculating loads for both. In this way, it is possible to **take into account the different contributes of rotor wakes at the two fins and the asymmetric loads in a maneuver**. Before sending the *outputs* to the summation subsystem, loads for the two fins are summed together as if they were a single subsystem.

Figure 2.15 shows a summary of vectors and angles at the vertical stabilizer, in particular the sideslip angle, positive clockwise, and the rudder angle, positive anticlockwise. Moreover, it shows the position of the fins.

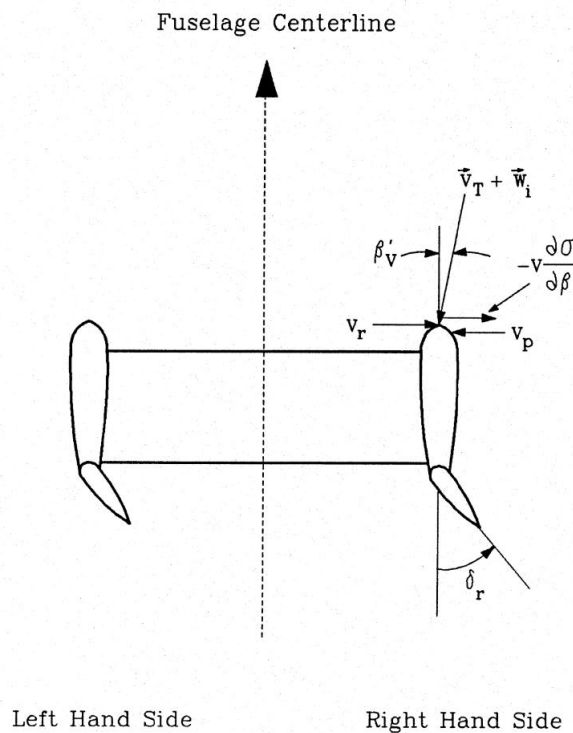


Figure 2.15: Vertical Stabilizer Diagram, Ref. [6]

¹⁶ An angle of attack for the vertical stabilizer is not defined in the model.

2.4.1 Geometric Distances

As explained in Section 2.1.4, some problems occur with the butt line. The easiest way to solve them was to decide a positive direction: the most suitable choice was a butt line positive versus the right rotor, which is concord with the Y-Body axis. This may seem a contradiction, since the station line and water line are opposite to their respective body axes, and the tern between the three lines is left-handed, but two were the advantages:

- just one coordinate had to be changed: the butt line for the left fin;
- the **rotor wake** at the vertical stabilizer was easier to implement and comprehend with this choice.

Given this preamble, it is possible to calculate geometric distances for each¹⁷ fin:

$$l_{XV}(j) = SL_{CG} - SL_V(j), \quad j = 1, 2 \quad (2.41)$$

$$l_{XV}(j) = BL_V(j) - BL_{CG}, \quad j = 1, 2 \quad (2.42)$$

$$l_{ZV}(j) = WL_{CG} - WL_V(j), \quad j = 1, 2 \quad (2.43)$$

In the GTRS Model, the right fin's vertical stabilizer's water line is reported wrong since it is negative, unlike the left one. The water line must be the same for both fins, as shown in Figure 2.2.

2.4.2 Rotor Wake

As the horizontal stabilizer, the vertical stabilizer is downstream of the rotors. Therefore, it is important to implement the wake. To aim this, some considerations are necessary:

- the rotor wake may hit only one fin, so it is necessary to implement different induced velocities for the left and the right ones. The GTRS model does not take this into account, and it considers only one induced velocity for both fins, which turns out to be always null at a careful study;
- the rotor induced velocity is an *output* of rotors subsystem, so it is known;
- the sideslip angle has great importance in the rotor wake and has to be compared with the angles between rotors and fins.

It is not difficult to model rotor wake with these assumptions. However, it is laborious, especially for calculating angles in¹⁸ Figure 2.16.

¹⁷ $j = 1$ for the right fin, $j = 2$ for the left one.

¹⁸ Only angles which connect rotors to the right fin are represented since the ones for the left fin are similar. The picture is taken from Ref. [18], and the author modified it with PowerPoint to show the angles.

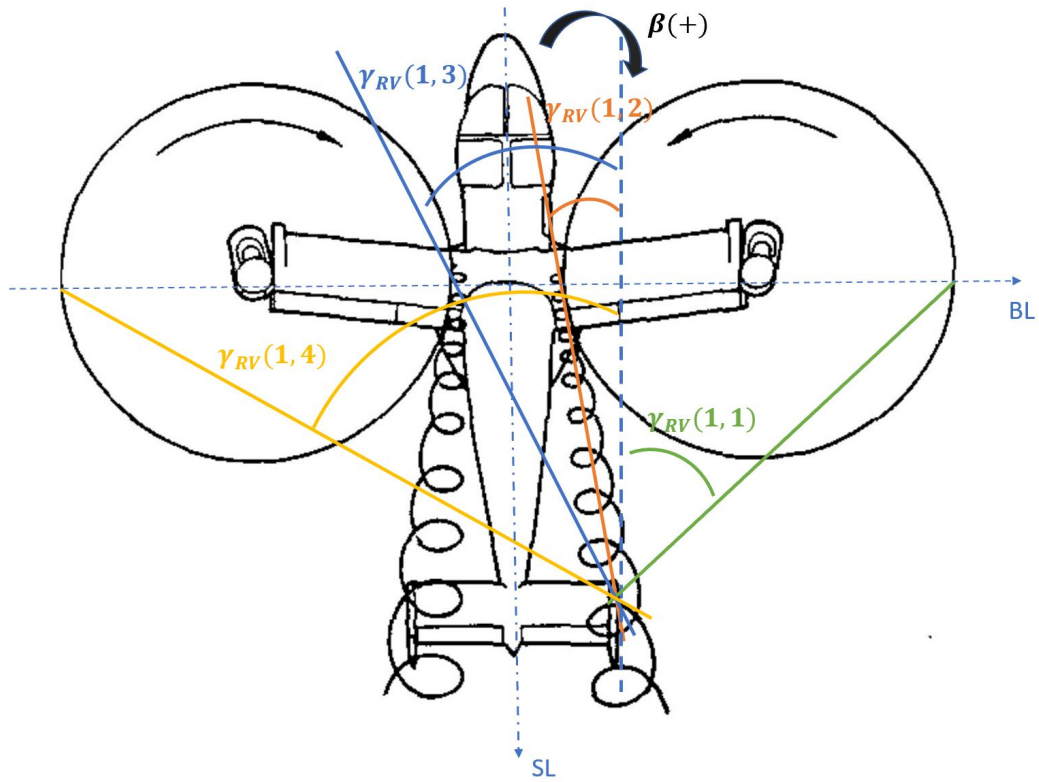


Figure 2.16: Rotor Wake's Angles at the Vertical Stabilizer

Firstly, some distances are necessary¹⁹, along x and y , in order to obtain angles between the lines that connect rotor tips and vertical fins and $X - Body$ axis:

- coordinate of right rotor external tip²⁰ along y :

$$BL_{RTIP_e} = BL_{SP} + R \quad (2.44)$$

- coordinate of right rotor internal tip along y :

$$BL_{RTIP_i} = BL_{SP} - R \quad (2.45)$$

- coordinate of left rotor internal tip along y :

$$BL_{LTIP_i} = -BL_{SP} + R \quad (2.46)$$

- coordinate of left rotor external tip along y :

$$BL_{LTIP_e} = -BL_{SP} - R \quad (2.47)$$

¹⁹ It is not important if they are calculated in $[in]$ or $[ft]$, as they will be part of a ratio, but units must be consistent.

²⁰ BL_{SP} is the butt line of the shaft pivot, hence adding or subtracting the radius, it is possible to obtain the tip coordinates. The shaft pivot and vertical fins are symmetrical to the fuselage line in Figure 2.15.

- distance between a generic fin and the shaft-pivot along x^{21} :

$$l_{X|RV}(j) = SL_V(j) - SL_{SP} + l_m \sin \beta_M, \quad j = 1, 2 \quad (2.48)$$

The best way to proceed is to organize all those coordinates and lengths in matrices and then calculate the needed angles.

Let's define:

- $[T]$ as the matrix with the y -coordinates of the rotor tips:

$$[T] = \begin{bmatrix} BL_{RTIP_e} & BL_{RTIP_i} & BL_{LTIP_i} & BL_{LTIP_e} \\ BL_{RTIP_e} & BL_{RTIP_i} & BL_{LTIP_i} & BL_{LTIP_e} \end{bmatrix} \quad (2.49)$$

- $[B]$ as the matrix with the y -coordinates of the vertical fins:

$$[B] = \begin{bmatrix} BL_{V1} & BL_{V1} & BL_{V1} & BL_{V1} \\ BL_{V2} & BL_{V2} & BL_{V2} & BL_{V2} \end{bmatrix} \quad (2.50)$$

- $[S]$ as the matrix with distances between the fins and the shaft-pivot:

$$[S] = \begin{bmatrix} l_{X|RV1} & l_{X|RV1} & l_{X|RV1} & l_{X|RV1} \\ l_{X|RV2} & l_{X|RV2} & l_{X|RV2} & l_{X|RV2} \end{bmatrix} \quad (2.51)$$

It is possible now to define the matrix with the angles defined previously:

$$[\gamma_{RV}] = \arctan \left(\frac{[T] - [B]}{[S]} \right) \quad (2.52)$$

The arctangent function returns the correct angles only when the butt line is defined as explained previously. Otherwise, it is possible to define different conventions, but distances entering the arctangent must be defined as positive, or angles will be different from expectations. First row's angles of $[\gamma_{RV}]$'s matrix are shown in Figure 2.16.

To get the correct induced velocities at each fin, the transposed matrix of $[\gamma_{RV}]$ is necessary. $[\gamma_{RV}]'$ is a 4×2 matrix: the first column is referred to the right fin, while the second to the left, instead the first and the second row are referred to the right rotor, the third and the fourth row to the left rotor. Therefore, defining a *for* cycle that studies the different cases and separates the two fins is possible.

Let's explain what happens for the right rotor. For the left, the procedure will be the same. In three cases, the rotor wake does not hit the fin:

- the sideslip angle is greater than $\gamma_{RV}(1, 1)$, so the right rotor wake passes in the middle of the two fins; this condition is implemented as $\gamma_{RV}(1, 1) < \beta_F$ and when it is verified the induced velocity at right fin is set to a null value for both components;

21 The last addendum of the equation will be explained in Section 2.5.

- the sideslip is smaller than $\gamma_{RV}(2,1)$ but greater than $\gamma_{RV}(3,1)$. Therefore, the right rotor wake passes external to the right fin while the left rotor wake passes in the middle of the two fins; this condition is implemented as $\gamma_{RV}(3,1) < \beta_F < \gamma_{RV}(2,1)$ and when it is verified the induced velocity is set to zero;
- the sideslip is smaller than $\gamma_{RV}(4,1)$. Thus, the left rotor wake passes external to the right fin; this condition is implemented as $\beta_F < \gamma_{RV}(4,1)$, and when it is verified, the induced velocity is set to zero.

In all the other cases, the induced velocity equals the rotor subsystem's *output*. The cycle is repeated for the left fin with similar considerations.

2.4.3 Velocities at the Vertical Stabilizer

Given the induced velocities, it is possible to calculate the fin's total velocities. The contributes are:

- the rotor induced velocities;
- the linear velocities of the aircraft c.g.;
- the contribute of angular velocities, which is not negligible since the arm between the vertical stabilizer and the c.g. is great. As for the horizontal stabilizer, this contribution is calculated with the cross product between angular velocities and arms, calculated in Section 2.4.1.

It is possible to sum²² them and to obtain the three components of velocities for each fin:

$$U_V(j) = U + U_{B|RV}(j) + q \cdot l_{ZV}(j) - r \cdot l_{YV}(j), \quad j = 1,2 \quad (2.53)$$

$$V_V(j) = V - p \cdot l_{ZV}(j) + r \cdot l_{XV}(j), \quad j = 1,2 \quad (2.54)$$

$$W_V(j) = W + W_{B|RV}(j) + p \cdot l_{YV}(j) - q \cdot l_{XV}(j), \quad j = 1,2 \quad (2.55)$$

2.4.4 Sideslip Angle

While studying the vertical stabilizer, it is important to remember that the role of the "angle of attack" is taken place by the sideslip angle and that the "lift" acts in the y axis as a side force, while no forces act along z ²³. Therefore, the vertical stabilizer has a significant role in *lateral-directional* stability.

The angle of attack at the vertical stabilizer is α_H , which is the same as the horizontal stabilizer, without considering the horizontal incidence in the calculation. It is important to define this to transform loads from wind to body axes.

²² Conventions were described in Section 2.3.1.

²³ Actually, there is a certain force along z , but its contribution is negligible. Moreover, the horizontal stabilizer generates lift for the tail, creating a complete set of loads.

Instead, the angle of sideslip is calculated with the velocities defined in Section 2.4.3:

$$\beta_V(j) = -i_V(j) + \arctan \left(\frac{V_V(j)}{\sqrt{U_V(j)^2 + W_V(j)^2}} \right) + \left(-\frac{1}{2} \frac{b_W}{U_V(j)} \left(\frac{\partial \sigma}{\partial p} p + \frac{\partial \sigma}{\partial r} r \right) - \frac{l_{XV}(j)}{U_V(j)} \frac{\partial \sigma}{\partial \beta_F} \dot{\beta} \right), \quad j = 1, 2 \quad (2.56)$$

The rotor wake effect, the angular velocities, the roll and yaw rate correction and the sidewash factor are considered in the sideslip angle calculation. The last addendum is changed of sign since the arms are calculated differently from the GTRS.

For the drag, another sideslip angle is necessary, where the rudder angle is taken into account since it gives a great contribution to drag (the contribute to side force is negligible):

$$\beta_{VD}(j) = \beta_V(j) + K_r \tau_r \delta_r, \quad j = 1, 2 \quad (2.57)$$

2.4.5 Dynamic Pressure

The dynamic pressure is calculated in the same way for the vertical and horizontal stabilizer. Assumptions are the same as Section 2.3.3. η_{VS} and $k_{\beta VS}$ tables are shared.

$$q_V(j) = \frac{1}{2} \rho K_{VNU} \{ [U \sqrt{\eta_{VS}} + q \cdot l_{ZV}(j) - r \cdot l_{YV}(j)]^2 + [V \sqrt{\eta_{VS}} - p \cdot l_{ZV}(j) + r \cdot l_{XV}(j)]^2 + [W \sqrt{\eta_{VS}} + p \cdot l_{YV}(j) - q \cdot l_{XV}(j)]^2 \}, \quad j = 1, 2 \quad (2.58)$$

2.4.6 Loads Calculation

The procedure is the same used for the horizontal stabilizer. The only difference is that instead of calculating the lift, the side force is obtained.

Coefficients are non-dimensional. Thus, the vertical stabilizer surface is necessary, and it is in *input*. In Ref. [6], the surface in Appendix B is wrong: it is reported as 20.25 ft² instead of 25.25 ft². The right value can be found in Appendix D in the same reference or Ref. [13].

The side force coefficients depend on δ_r , β_V and M_N . As happened for the horizontal stabilizer, coefficients for $M_N > 0.2$ are provided only for a small range of β , and the reasons are the same. Besides, data for $-8^\circ < \beta < 8^\circ$ is not provided since it is the linear range for the side force coefficient. Figure 2.17 shows C_Y for different rudder angles, and it is possible to see that when δ_r grows, C_{YV} grows. Figure 2.15 shows that the rudder rotation is positive anticlockwise.

block: model_trim/A/C Model/Aerodynamics/Vertical Stabilizer/Fin Lift Coefficient
Table2

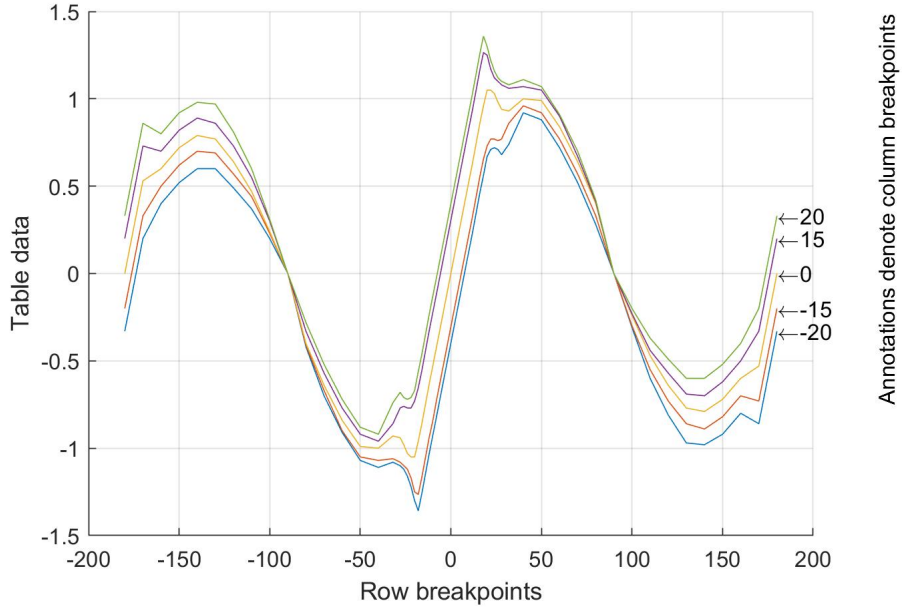


Figure 2.17: C_{YV} Table

This time, the table's *output* is not the searched C_Y , but further algebra is necessary:

$$C_{YV}(j) = C_{YVi|\delta_r=0} \left[K_{\beta r} \left(1 - \frac{\partial \sigma}{\partial \beta_F} \right) \right] + \left[C_{YV(j)|\delta_r} - C_{YV(j)|\delta_r=0} \right], \quad M_N \leq 0.2, \quad j = 1, 2 \quad (2.59)$$

$$C_{YV}(j) = C_{YV(j)|\delta_r=0} \left[K_{\beta r} \left(1 - \frac{\partial \sigma}{\partial \beta_F} \right) \right] + a_V(j) K_r \tau_r \delta_r, \quad M_N > 0.2, \quad j = 1, 2 \quad (2.60)$$

The formula may be different for non-compressible and compressible cases²⁴.

A new factor, $k_{\beta r}$, is introduced to consider the sidewash due to the rotors. This occurs because sideslip angles are usually small, and therefore, this interference can be important in the calculation, while it was negligible for the horizontal stabilizer.

When velocities are higher, the rudder's contribution is important and is taken into account for $M_N > 0.2$, also multiplied for his effectiveness. This time, the difference was made in the coefficient calculation, unlike the horizontal stabilizer subsystem, where it was made for the angle of attack.

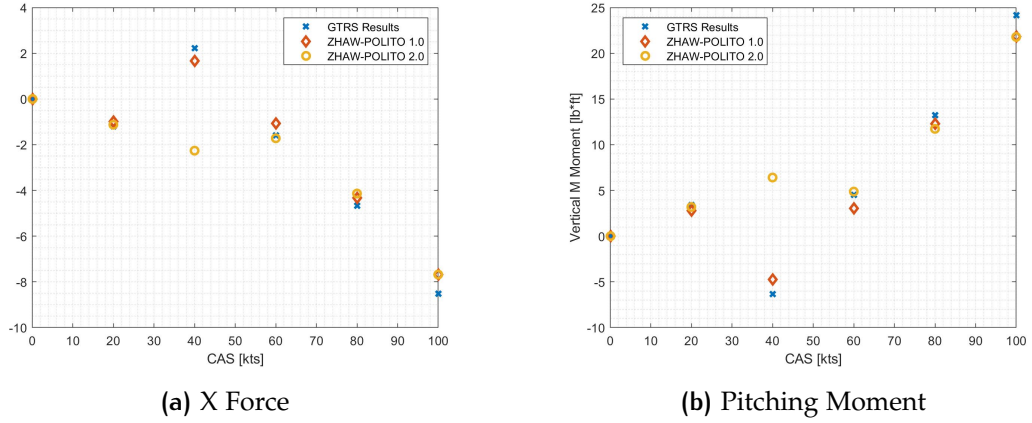
A parenthesis is necessary for the $k_{\beta r}$ table. In Ferguson's model, Ref. [6], there is a value that is not comparable with the others. The one provided from the model is in Table 2.1.

²⁴ The division is set to $M_N = 0.2$ since the stream accelerates around the fins.

Table 2.1: $k_{\beta r}$ Table Provided by GTRS Model

$k_{\beta r}, [-]$	Sideslip Angle, $\beta_F, [deg]$						
Velocity, $V_T, [kts]$	0	± 5	± 10	± 15	± 20	± 25	± 30
0	1	1	1	1	1	1	1
20	1	1	1	1	1	1	1
40	-0.5	0.25	0.8	1.25	1.5	1	1
60	0.2	0.4	0.8	1.1	1.4	1	1
80	0.5	0.6	0.8	1	1.2	1	1
100	0.75	0.8	0.8	1	1	1	1
120	1	1	1	1	1	1	1
350	1	1	1	1	1	1	1

This brings a "V" trend of loads for increasing airspeed, as shown²⁵ in Figure 2.18 for red and blue points.

**Figure 2.18:** Vertical Stabilizer's Loads at Different Airspeed

The logical consequence is to think that the minus was a print error, so the value was changed, and the new one is shown in Table 2.2. Indeed, there is no reason to change the drag coefficient's sign with speed since the force acts in the same²⁶ direction if β remains the same. Besides, the drag is proportional to V^2 .

The loads' trend, yellow points in Figure 2.18, is now growing. Moreover, analyzing eigenvalues, at 40 kts, there was an unstable pole, while with the value in Table 2.2, it disappeared. The eigenvalues could be validated with the Panfield, Ref. [19], and Celi, Ref. [20], and therefore, it is reasonable that the change in Table 2.2 is correct.

The drag coefficient table, shown in Figure 2.19, is a β_V and M_N 's function.

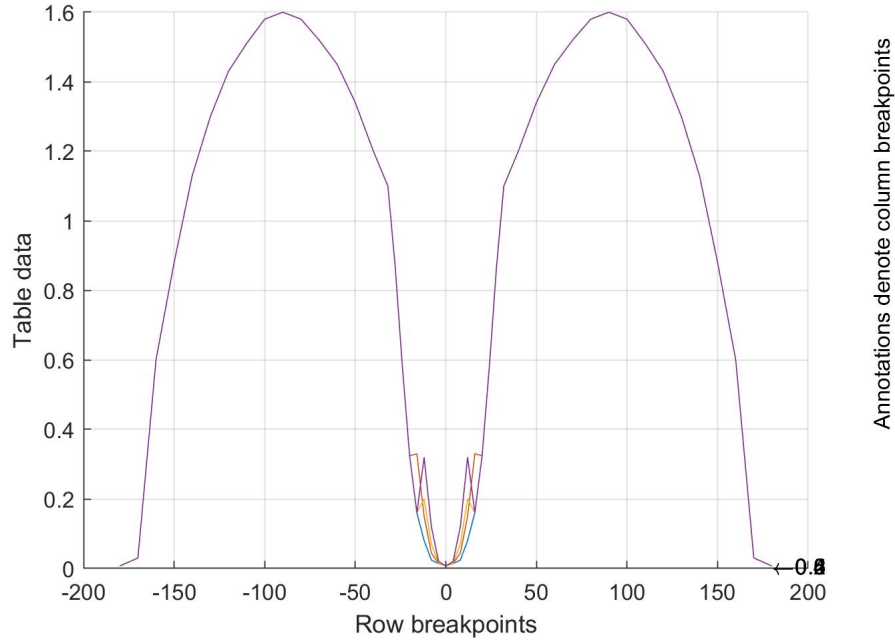
²⁵ The results will be explained in Chapter 3.

²⁶ The sidewash factor is always positive. Therefore, the sign depends on C_{DY} and $K_{\beta r}$.

Table 2.2: Modified $k_{\beta r}$ Table

$k_{\beta r}, [-]$	Sideslip Angle, $\beta_F, [deg]$						
	0	± 5	± 10	± 15	± 20	± 25	± 30
Velocity, $V_T, [kts]$	0	1	1	1	1	1	1
	20	1	1	1	1	1	1
	40	0.5	0.25	0.8	1.25	1.5	1
	60	0.2	0.4	0.8	1.1	1.4	1
	80	0.5	0.6	0.8	1	1.2	1
	100	0.75	0.8	0.8	1	1	1
	120	1	1	1	1	1	1
	350	1	1	1	1	1	1

a for block: model_trim/A/C Model/Aerodynamics/Vertical Stabilizer/Fin Drag Co

Figure 2.19: C_{DV} Table

On the other hand, the drag coefficient, which contributes to the loads, is obtained with some algebra:

$$C_{DV}(j) = C_{DV(j)|\delta_r} \left[K_{\beta r} \left(1 - \frac{\partial \sigma}{\partial \beta_F} \right) \right], \quad j = 1, 2 \quad (2.61)$$

Known the coefficients, it is easy to obtain loads:

$$Y'_V(j) = -C_{YV}(j)q_V(j)S_V(j), \quad j = 1, 2 \quad (2.62)$$

$$D_V(j) = C_{DV}(j)q_V(j)S_V(j), \quad j = 1, 2 \quad (2.63)$$

A minus is necessary for the side force, considering that there is an exception to the general rules about axes explained in Section 2.1. Indeed, the side force

coefficient is positive when β is positive, which means that the side force is calculated positive for a y - wind opposite to Y - Body. Thus, a minus is necessary for the calculation of the side force. Otherwise, it is possible to rearrange the C_Y table, but it is a laborious process due to the dependence on the rudder angle, making it insufficient to change the signs.

There is an error in the drag calculation in Ferguson's model: the minus is not correct, as it is already counted in the rotation matrix.

After calculating loads in wind axes, it is not possible to transform them into body axes, as shown in previous subsystems. However, forces along Z are set to zero, as previously explained. This is necessary to avoid the creation of lift due to the vertical stabilizer at great α_H , which is not physical since it is already counted in the horizontal stabilizer.

Complete equations are provided in Appendix A, while tables and graphs are provided in Appendix B.

2.5 WING-PYLON MODEL

The Wing-Pylon Subsystem is significant in the aerodynamic model. As it happens for all aircraft, the wing is the most important body for aerodynamics: in helicopter mode, when dynamic pressure is low, the wing is important for induced forces, while in airplane mode, it generates the main part of the lift being the dynamic pressure higher.

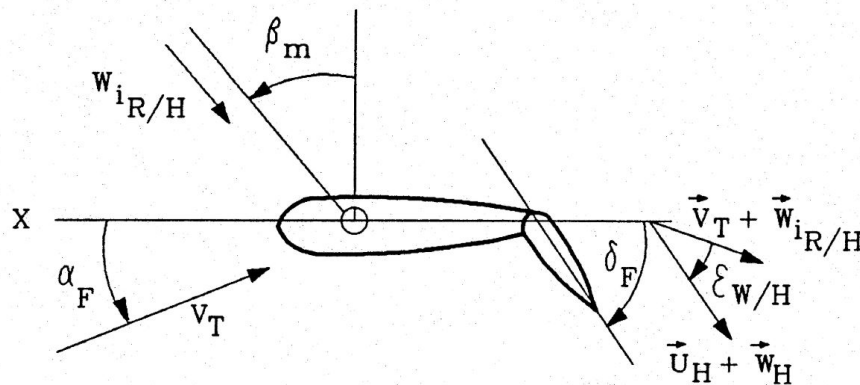


Figure 2.20: Wing Vector Diagram, Ref. [6]

Figure 2.20 shows a representation of angles and vectors at the wing-pylon: the downwash angle, important for the horizontal stabilizer, the induced velocity from the rotor, and the flap angle, which is positive clockwise, as happened for the elevator angle, besides the angle of attack.

To better comprehend the wing-pylon model, defining the considered contributors is important since they can be divided into smaller subsystems.

INDUCED AERODYNAMICS It is the aerodynamic contribute generated by the rotor's induced velocity. These loads are important in helicopter mode and

at low speeds. There are not many theories available in literature²⁷, and therefore, Ferguson's Model provides in Ref. [6] a semi-empirical flow chart developed with experimental data. However, the source is neither specified in Ref. [6] nor in the previous version, Ref. [13].

FREESTREAM AERODYNAMICS It is the aerodynamic contribute generated by the freestream. It affects the wing's part not influenced by the induced aerodynamics, and it is relevant at high airspeed, hence, when the dynamic pressure is high. This part of the wing-pylon model is similar to the horizontal and vertical stabilizer subsystems.

WING-PYLON INTERFERENCE DRAG This drag contribution is caused by the interference between the rotor's pylon and the wing.

SPINNER AND PYLON DRAG They are the drag contribute due to the spinner and the pylon. The induced velocity of the rotors generates them, and they are present both in helicopter and airplane mode, unlike the induced aerodynamics.

Being the different parts clear, it is possible to analyze more in detail each section.

2.5.1 Induced Aerodynamics

The induced aerodynamics is generated by the rotor induced velocity. It is mainly a down-force, but there is also a small contribution to drag.

The resultant down-force is the reason why, during a hover maneuver, the flaps are lowered to the maximum: the flow is over a smaller portion of the wing's surface, decreasing the down-force as a consequence.

Since rotors' wake generates the induced forces, they depend on the aircraft's speed, and the wing's portion affected by the wake decreases as the speed increases, being the wake deflected. Hence, a model that allows the calculation of the affected area and the forces' application point in different flight conditions is necessary.

As explained in the previous section, this model is organized as a flowchart, precisely aiming at the **application point of forces** and the **induced forces' affected surface** calculation for both semi-wings. The flowchart's source is not specified, and not all the variables introduced in it are neither explained nor clear. Despite this, it is understandable that the induced model is comprehensive, considering many situations.

Some of the variables introduced by the model are shown in the top view of Figure 2.21, but no further description is provided. Instead, the front view shows the **theoretical approximation** of the wing loads: the portion under the rotor wake generates a down-force. In contrast, the part affected by the freestream generates lift.

²⁷ Due to its particular rotor-wing configuration.

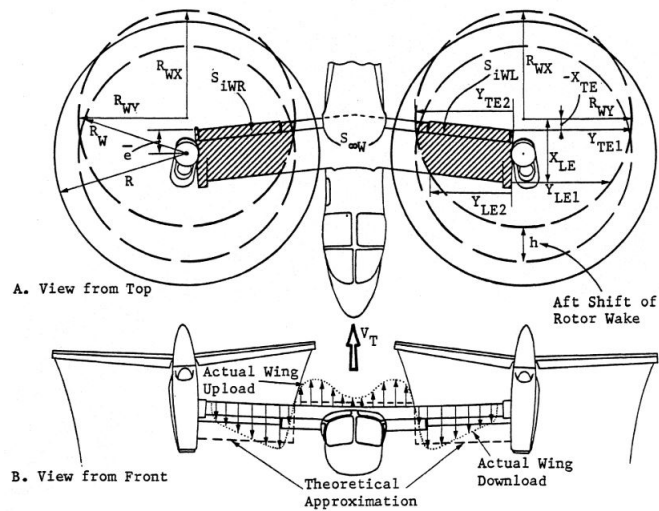


Figure 2.21: Induced Aerodynamics' Scheme, Ref. [6]

However, the model generates a discontinuity in the forces application point's coordinate, and therefore in the induced forces arm, Figure 2.22a and 2.22b, in the affected area, Figure 2.22c, and, as a consequence, in the induced forces and moments, Figure 2.22d, 2.22e and 2.22f. More trim points are calculated near the discontinuity to highlight it.

Finding the error was not easy since some variables were not clear, the source was not specified, and no validation data was provided.

Therefore, several attempts were made. First, the author was concentrated on solving the coordinates' discontinuity: this was possible by changing some equation in the flowchart, where the norm was used to calculate variables where lengths in the same axis were involved, Figure A.1, A.2 and A.3. This was not clear, as the norm is normally used for lengths in different axes, so it was changed with the difference of absolute²⁸ values, and the result was to delete the coordinates' discontinuity, Figure 2.23. Moreover, the mobile coordinates²⁹, Figure 2.23a, was smaller than the wing chord, and it tends to the null value set by the GTRS model when the induced forces are zero, further reasons to think that the correction was right.

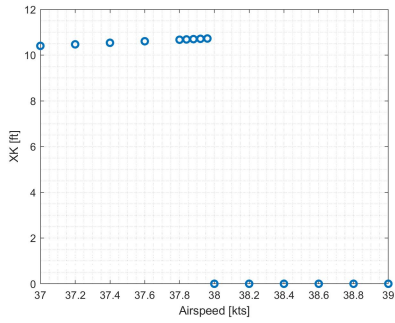
However, these modifications made the tilt-rotor uncontrollable at the simulator; therefore, it was clear that it was not the right way.

After this attempt, the author concluded that the continuity in the application point's coordinate was not necessary. When this runs out of the wing, it is not more of interest since it loses meaning. The important is that forces are continuous and tend to zero at high airspeed since the rotor wake no longer affects the wing. The moments will be continuous as a consequence.

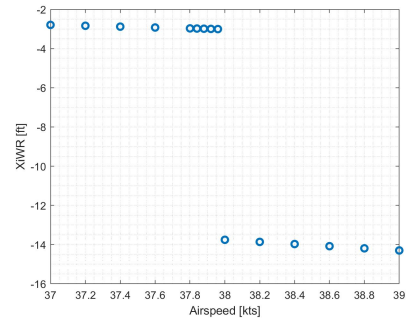
To aim this, the model was compared with the one in Ref. [13], which is less complete but shares some equations with the GTRS. It came out that some

28 As an instance, $\sqrt{R_{WX}^2 - X_{TE}^2}$ became $|R_{WX}| - |X_{TE}|$.

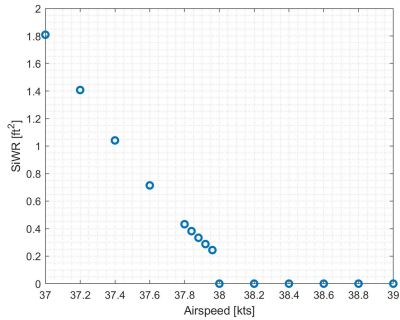
29 The meaning will be explained later when equations will be shown in detail.



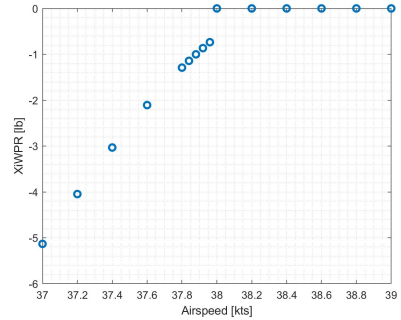
(a) Mobile Coordinate's Discontinuity



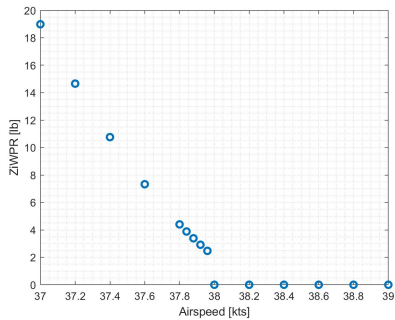
(b) Arm between Forces Application Point and c.g. Discontinuity



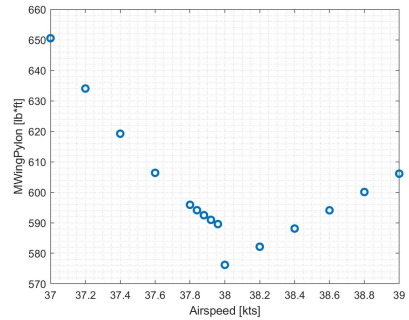
(c) Affected Ares's Discontinuity



(d) Induced Force along X Discontinuity

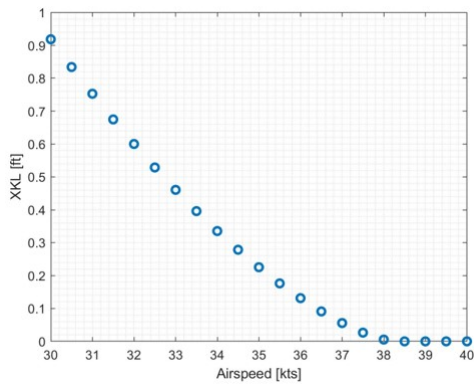


(e) Induced Force along Z Discontinuity

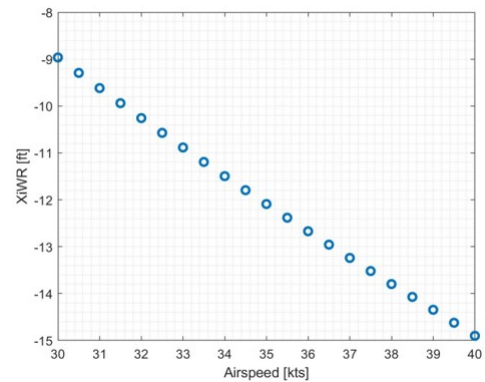


(f) Wing-Pylon's Pitching Moment Discontinuity

Figure 2.22: Induced Forces' Discontinuity



(a) Mobile Coordinate's Continuous



(b) Arm between Forces Application Point and c.g. Continuous

Figure 2.23: Continuity for the Induced Forces' Arm

equations were different, so they were changed in the Simulink model. As a result, forces and moments are now continuous, as shown in Figure 2.24. Trim points were thickened where the wake is near the trailing edge.

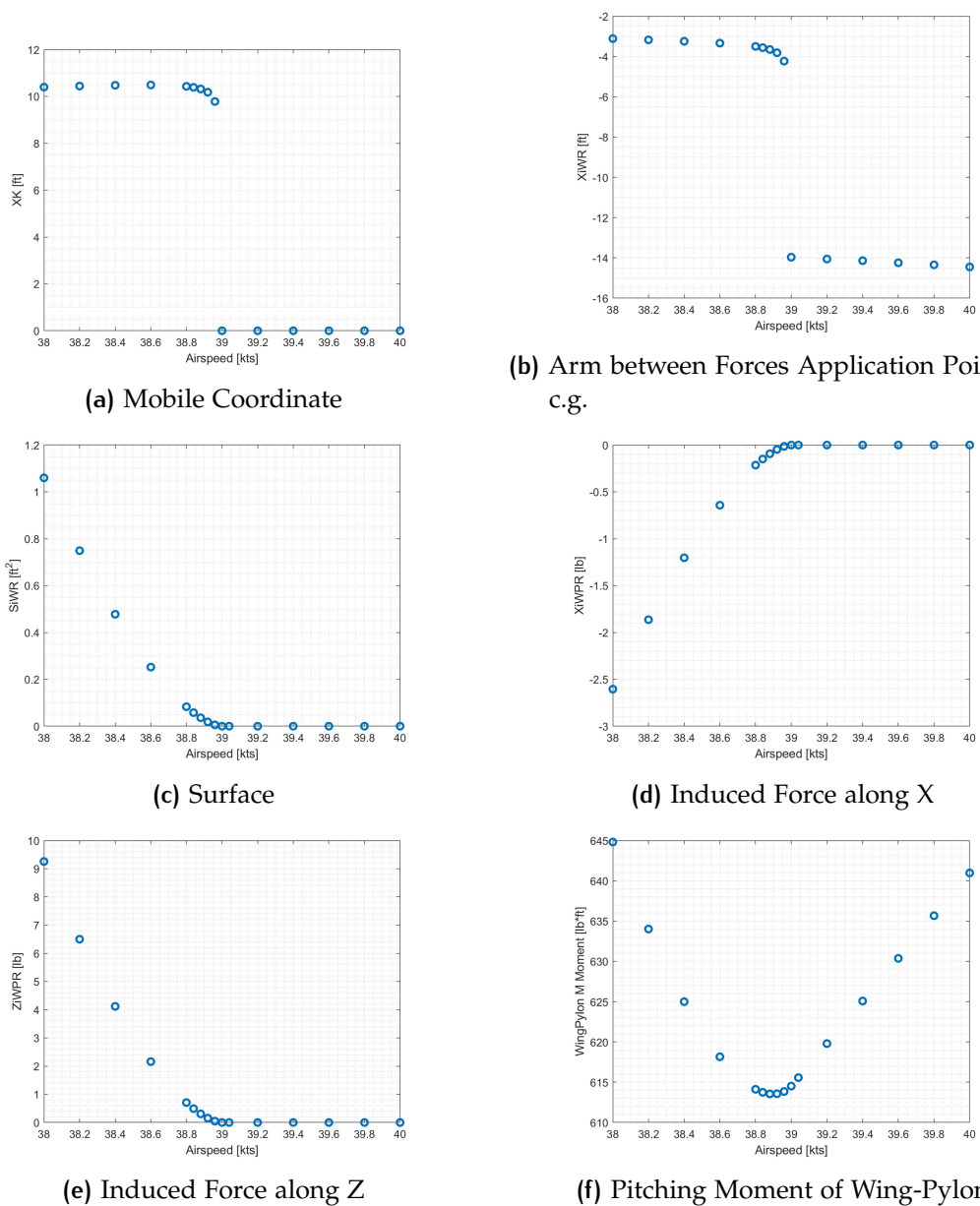


Figure 2.24: Induced Forces' Application Point and Affected Area

Figure 2.24a and 2.24b show that the mobile coordinate and the induced forces' arm have still a discontinuity. As told before, these quantities lose meaning when the wake is out of the wing because induced forces are null, Figure 2.24d and 2.24e. Moreover, the discontinuity is caused by the fact that X_K is set to zero by the model when the induced forces are zero. As a consequence, the arm has a discontinuity.

Even though there are no validation data, it is possible to conclude that the results are realistic. The affected area is a decreasing, continuous function that tends to zero while the wake runs outside the wing, Figure 2.24c. In hover and at

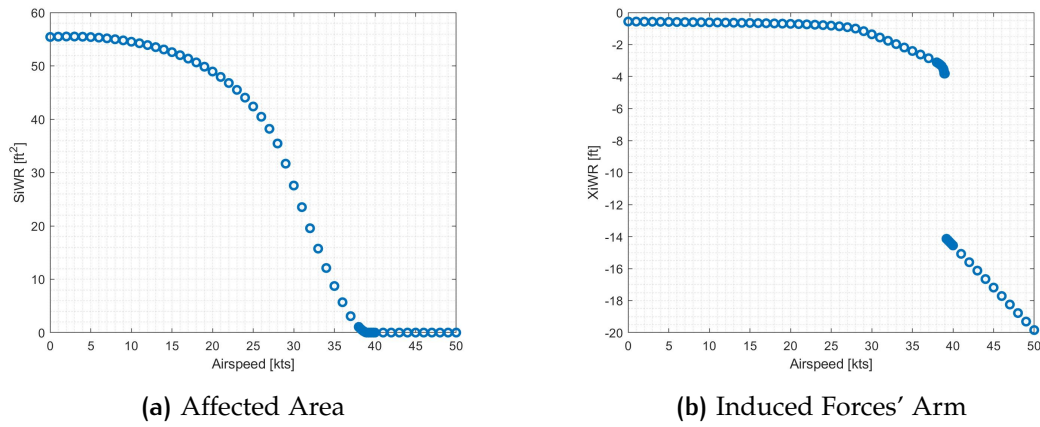


Figure 2.25: Affected Area and Induced Forces' Arm with Airspeed

low speeds, it is comparable to the product³⁰ $R \cdot c_w$, as shown in Figure 2.25a. It remains approximately constant up to $\simeq 20$ kts since the rotor wake is completely above the wing until the wake's front reaches the leading edge (a situation like Figure 2.25b). Then it suddenly decreases to zero, being the wake's front behind the leading edge.

The arm grows for negative values, Figure 2.24b: it is the expected behaviour since the application point moves backwards if the speed grows, as shown in Figure 2.26³¹. Furthermore, the arm has a length, in absolute value, comparable to the wing chord³² when the application point is near the trailing edge. As the affected area, the induced forces' arm is approximately constant until $\simeq 20$ kts. For higher speeds, it grows faster since the wake is running outside the wing, being its front behind the leading edge.

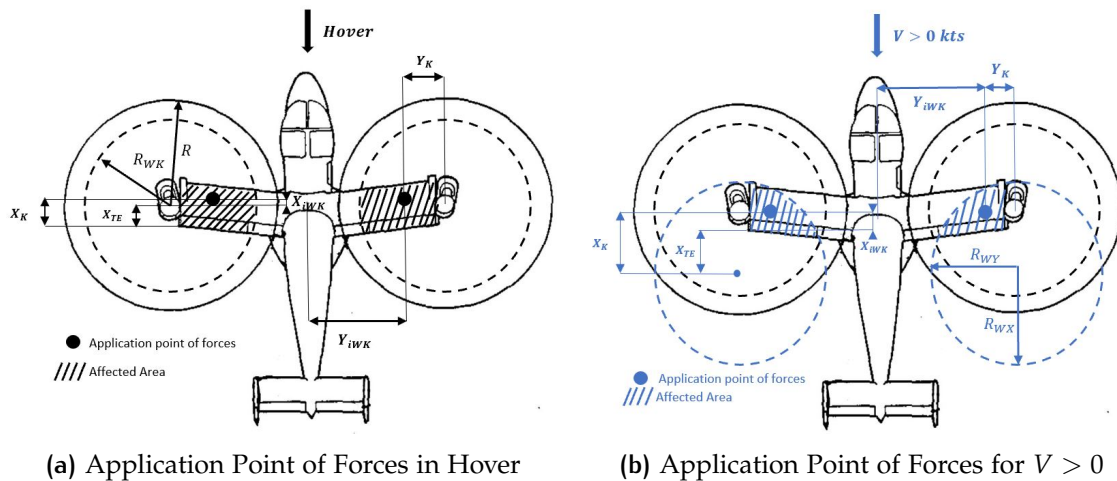


Figure 2.26: Induced Forces' Application Point and Affected Area Layout

Additionally, Figure 2.26 shows the mobile coordinate X_K .

³⁰ R is the rotor radius, c_w the wing chord.

³¹ The figure is taken from Ref. [18], and it was modified by the author using PowerPoint.

³² $c_w = 5.25$ ft

Application point of forces and affected area

The aim is to calculate the application point of forces and the affected area as told previously. Let's see the equations in detail. First of all, some information about the wing has to be implemented³³. Note that the two semi-wings are treated separately since loads can be non-symmetrical in a maneuver or lateral flight:

- Angles for the wake velocities' transformations:

$$G = \arctan \left(\frac{\cos \phi_M \sin \beta_M}{\cos \beta_M} \right), \quad [rad] \quad (2.64)$$

$$SG = \sin G, \quad [ND] \quad (2.65)$$

$$CG = \cos G, \quad [ND] \quad (2.66)$$

$$ZL = l_m \cos \phi_M \cdot CG, \quad [ft] \quad (2.67)$$

- Velocities at the wing (K=R for the right semi-wing, K=L for the left one):

$$U_{WK} = -U - W_{i|RWK} \cdot SG, \quad [ft/s] \quad (2.68)$$

$$W_{WK} = -W + W_{i|RWK} \cos \phi_M \cdot CG, \quad [ft/s] \quad (2.69)$$

$$V_{WR} = V + W_{i|RWK} \sin \phi_M \cdot SG, \quad [ft/s] \quad (2.70)$$

$$V_{WL} = -V + W_{i|RWK} \sin \phi_M \cdot SG, \quad [ft/s] \quad (2.71)$$

Equation 2.68 is reported wrong in the GTRS model since SG is multiplied to the linear velocity U , which does not depend on the nacelle angle.

When the ratio between U_{WK} and W_{WK} , or the ratio between V_{WK} and W_{WK} , is greater than 100, a limitation is made to the ratio. This is implemented because when the ratio is so high, the rotor wake is outside the wing. The complete equations are provided in Appendix A.

- Wing geometry information (K=R for the right semi-wing, K=L for the left one):

$$\bar{e} = SL_{WTE} - SL_{SP}, \quad [ft] \quad (2.72)$$

$$X_{TEK} = -\bar{e} - l_m SG - \frac{U_{WK}}{W_{WK}} ZL K_{RW}, \quad [ft] \quad (2.73)$$

$$X_{LEK} = c_W + X_{TEK}, \quad [ft] \quad (2.74)$$

$$Y_{TIPK} = ZL \left[\tan \phi_M - \frac{V_{WK}}{\sqrt{U_{WK}^2 + W_{WK}^2}} \text{sign}(W_{WK}) \right], \quad [ft] \quad (2.75)$$

$$R_{WXK} = R_{WK} \sqrt{\left(\frac{U_{WK}}{W_{WK}} \sin \phi_M \right)^2 + \left(CG - \frac{U_{WK}}{W_{WK}} SG \cos \phi_M \right)^2}, \quad [ft] \quad (2.76)$$

³³ Special attention is necessary for the units of measure.

$$R_{WYK} = R_{WK} \left\{ \left(\frac{V_{WK}}{W_{WK}} SG \cos \phi_M - SG \sin \phi_M \right)^2 + \left[\cos \phi_M + \frac{V_{WK} \sin \phi_M}{\sqrt{U_{WK}^2 + W_{WK}^2}} \text{sign}(W_{WK}) \right]^2 \right\}^{\frac{1}{2}}, [ft] \quad (2.77)$$

$$\delta_K = \arctan \left(\frac{\frac{U_{WK}}{W_{WK}} \sin \phi_M}{CG - \frac{U_{WK}}{W_{WK}} \cos \phi_M SG} \right) + \arctan \left[\frac{V_{WK} \sin \phi_M}{\text{sign}(W_{WK}) \sqrt{U_{WK}^2 + W_{WK}^2}} \right], [rad] \quad (2.78)$$

$$F_{RWK} = \frac{R_{WYK}}{R_{WXK}}, [ND] \quad (2.79)$$

$$S_{DELK} = \sin \delta_K, [ND] \quad (2.80)$$

$$C_{DELK} = |\cos \delta_K|, [ND] \quad (2.81)$$

It is important to keep the conventions as above since the procedure may calculate a wrong arm if they are changed.

A problem in the units of measure of R_{WXK} and R_{WYK} occurs since Ferguson's model reports R_{WK} as non-dimensional. Actually, it is in $[ft]$, being the right rotor contraction ratio that is a modification of the rotor radius.

Some of those vectors are shown in Figure 2.21, in the top view. After defining these quantities, it is possible to start the procedure to calculate the forces' application point and the affected area. The procedure is described in Ref. [6], while the complete equations are provided in Appendix A, from Figure A.1 to Figure A.6. This section will explain how the model works in order to understand it from a physical point of view and the differences introduced with the model of 1973.

The model takes into account the situations which explanations follow. Affected areas and x and y mobile coordinates (which allow defining the forces' application point, and therefore the arm) are set to zero when:

- $\beta_M > 30^\circ$: the rotors are sufficiently inclined that the wake does not affect the wing;
- $U < 0$: when the aircraft is moving backwards, the rotor wake runs outside the wing. The situation is taken into account by comparing³⁴ X_{1K} and X_{2K} , and when $X_{1K} \geq X_{2K}$ (Figure A.2), the coordinates and the area are set to zero. However, this condition can be verified only if the airplane is going backwards;
- the y -component of the wake is strong enough to slope the wake outside from the wing. This is verified when $Y_{TIPK} > 0$ (Figure A.2);

³⁴ The variables are introduced in the flowchart. Even in the next points, some variables are implemented in the flowchart. Their meaning is not clear, but following the chart is reasonable to understand the significance.

- the aircraft speed is sufficiently great to slope the wake outside the wing. This condition is verified when $X_{TIPK} > X_{1K} \vee X_{TIPK} > X_{2K}$ (Figure A.3). In helicopter mode, this happens for $CAS \simeq 39$ kts, very close to the hypothetical speed of 40 kts provide by Ref. [6].

In all the other cases, the coordinates and the affected area are defined. Moreover, as shown in Figure 2.24c, the surface tends to zero at higher speeds and, consequently, the forces. This is exactly what we expect from the model: by increasing the speed, a decreasing portion of the wing is under the wake, and this tends to a null value when the wake runs outside the wing. The behaviour is shown qualitatively in Figure 2.26.

When it is possible to define the induced forces, the flowchart comes out with one of the five possible procedures depending on the case. As the area interested by the wake is greater, as the procedure's flag is greater and more contributes are summed iteratively.

Lastly, the equations which were changed are presented³⁵:

$$X_{AK} = X_{AK} + \frac{1}{2}X_{A1K} + \frac{1}{3}F_{RWK}S_{DELK} (C_{2K}^3 - C_{1K}^3) - \frac{1}{2}Y_{TIPK} (C_{2K}^2 - C_{1K}^2) \quad (2.82)$$

$$X_{AK} = X_{AK} + \frac{1}{2}X_{A1K} + \frac{1}{3}F_{RWK}S_{DELK} (C_{2K}^3 - C_{1K}^3) - Y_{TIPK} (C_{2K}^2 - C_{1K}^2) \quad (2.83)$$

$$Y_{AK} = Y_{AK} + F_{RWK} \left[\frac{1}{2}X_{A1K}S_{DELK} + \frac{1}{6}F_{RWK} (S_{DELK}^2 - C_{DELK}^2) (C_{2K}^3 - C_{1K}^3) + \frac{1}{2} (R_{WYK}^2 C_{DELK}^2 - Y_{TIPK}^2) (C_{2K} - C_{1K}) \right] \quad (2.84)$$

$$Y_{AK} = Y_{AK} + F_{RWK} \left[\frac{1}{2}X_{A1K}S_{DELK} + \frac{1}{6}F_{RWK} (S_{DELK}^2 - C_{DELK}^2) (C_{2K}^3 - C_{1K}^3) + \frac{1}{2} (R_{WYK}R_{WXK}C_{DELK}^2 - Y_{TIPK}^2) (C_{2K} - C_{1K}) \right] \quad (2.85)$$

Complete equations are shown in Appendix A.

Implementing Equation 2.83 and Equation 2.85, it was possible to remove the discontinuity and to have the desired trend for loads, shown in Figure 2.24.

In *output* from the procedure, there are:

- S_{iWK} in $[ft^2]$, which is the area affected by the rotor wake;
- X_{AK} in $[ft^3]$, divided by the area, returns X_K , a mobile coordinate used to calculate the station line of the application point of forces. It is implemented to consider that the application point changes depending on the flight conditions, and it is shown in Figure 2.26;

³⁵ Equation 2.82 and Equation 2.84 are in Ferguson's model, Equation 2.83 and Equation 2.85 are implemented on Simulink

- Y_{AK} in $[ft^3]$, which divided by the area, returns Y_K , a mobile coordinate used to calculate the butt line of the application point of forces. It is shown in Figure 2.26.

The water line coordinate is not calculated since the wing section is thin, and therefore, distances along z are much smaller than distances along x and y .

Finally, with the mobile coordinates is possible to define the application point³⁶, and therefore to calculate the arms:

$$X_{iWR} = X_R + SL_{CG} - SL_{WTE} - X_{TER} \quad (2.86)$$

$$Y_{iWR} = -Y_R - BL_{CG} + BL_{SP} + Y_{TIP_R} \quad (2.87)$$

$$X_{iWL} = X_L + SL_{CG} - SL_{WTE} - X_{TEL} \quad (2.88)$$

$$Y_{iWL} = Y_L - BL_{CG} - BL_{SP} - Y_{TIP_L} \quad (2.89)$$

These equations, in Ferguson's model, have some errors:

- the length in *output* from the procedure are in ft , while the coordinates are in *in*: a 12 factor is needed in the model in order to have all in quantities in $[ft]$, but this is not considered in Ref. [6];
- in Equation 2.89, the minus before the butt line of the shaft-pivot is correct since it is defined only positive, but the left rotor has a negative butt line. Nevertheless, the butt line of the c.g. has to be subtracted from the shaft-pivot, while in Ref. [6], it is summed. The calculation of the arms and conventions were treated in Section 2.1.4.

Total Velocity, Angle of Attack, Sideslip Angle and Dynamic Pressure Calculation

It is possible to calculate the total velocity, the angle of attack, the sideslip angle, and the dynamic pressure in the same way used for the horizontal and vertical stabilizer. The difference is that the contribution of the angular velocities is negligible. The right and the left semi-wing are treated separately, and as output, there will be loads for both without summing them.

$$V_{TiWK} = \sqrt{\left(U + U_{iB|RWK}\right)^2 + \left(W + W_{iB|RWK}\right)^2} \quad (2.90)$$

$$\alpha_{iWK} = \arctan\left(\frac{W + W_{iB|RWK}}{U + U_{iB|RWK}}\right) \quad (2.91)$$

$$\beta_{iWK} = \arctan\left[\frac{V}{\sqrt{\left(U + U_{iB|RWK}\right)^2 + \left(W + W_{iB|RWK}\right)^2}}\right] \quad (2.92)$$

$$q_{iWK} = \frac{1}{2}\rho V_{TiWK}^2 \quad (2.93)$$

The dynamic pressure introduced in Equation 2.93 is different from zero, even when the aircraft is in hover since there is the rotor wake's contribution.

³⁶ The application point is obtained with different equations for left and right semi-wing.

Lift and Drag Calculation

To obtain the lift and the drag, it is necessary to get the aerodynamic coefficients. They are provided in tables from the model, and they are wind tunnel data for angles below stall, while for angles above stall, they are extrapolated from Ref. [17].

Both C_{LWPK} and C_{DWPK} are a function of α_{iWK} , δ_F , β_M and M_N . As usual, for higher Mach Number, coefficients are provided for a small range of angle of attack, while in the linear range, they are not specified. Moreover, the coefficients are greater for greater flap angles³⁷, as it happened for the horizontal stabilizer.

With the coefficients in *output*, it is possible to calculate the loads:

$$L_{iWPK} = q_{iWK} S_{iWK} C_{LWPK} K_{FW} \quad (2.94)$$

$$D_{iWPK} = q_{iWK} S_{iWK} C_{DWPK} K_{FW} \quad (2.95)$$

K_{FW} is a coefficient that takes into account flap deflection. It is calculated as follows:

$$K_{FW} = K_{FW0} + K_{FWDF} \delta_F \quad (2.96)$$

In the reference model, the equation is wrong since it is reported in this way:

$$K_{FW} = K_{FW0} - K_{FWDF} \delta_F \quad (2.97)$$

In fact, K_{FWDF} is already negative, and when the flaps are lowered, the induced loads have to decrease since the surface wet by the wake decreases. With Equation 2.96, it is possible to obtain the desired result.

Given each semi-wing loads, it is possible to transform them into body axis with the rotation matrix, Equation 2.5. Furthermore, it is possible to calculate the moments due to forces. Complete equations are provided in Appendix A, while tables are provided in Appendix B.

2.5.2 Freestream Aerodynamics

The aerodynamics due to the freestream is the second contribution of the wing-pylon subsystem described. Unlike the induced aerodynamics, this contribution is always present, and its importance grows with the airspeed.

Angles and vectors for the freestream aerodynamics are shown in Figure 2.27. Moreover, the same shows a comparison between the wing outside and under the rotor wake.

Besides the angle of attack due to the freestream, α_F , there is also $\alpha'_{F|W}$, which is due to the composition between the freestream and the rotor induced velocities. The figure shows $-\alpha'_{F|W}$ because its rotation is represented clockwise, but it is positive anticlockwise: that is the minus's reason. In addition, it is possible to see the flap angle and its convention (positive clockwise).

³⁷ The convention of flap angle is shown in Figure 2.20.

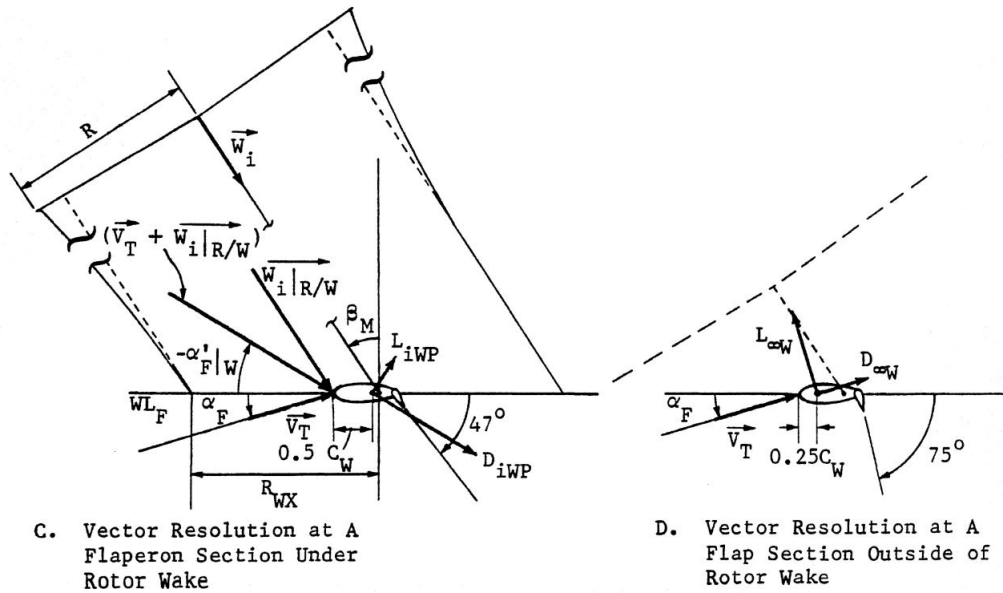


Figure 2.27: Freestream Aerodynamics Vectors, Ref. [6]

Area of the Wing in Freestream Flow

As explained in Section 2.5, the rotor wake contribution affects a portion of the wing. Hence, just the remaining part is affected by the freestream. Certainly, when the wake is outside the wing, all the area is affected by the freestream. This is taken into account by the following equation:

$$S_{WFS} = S_W - (S_{iWL} + S_{iWR}) \quad (2.98)$$

where S_W is the total wing area, which is known, and S_{WFS} is the portion of the area affected by the freestream, while S_{iWL} and S_{iWR} are calculated as explained in the previous section.

Wing Freestream Dynamic Pressure

The dynamic pressure is calculated as usual:

$$q_{WFS} = \frac{1}{2} \rho (U^2 + W^2) \quad (2.99)$$

Unlike the horizontal and vertical stabilizer, the angular velocities' contribution is negligible. Since the wing is not downstream of the rotor, no losses function has to be implemented.

Freestream Angle of Attack

The freestream angle of attack is calculated as follows:

$$\alpha_{WFS} = \alpha_F - K_{XRW} X_{RW} \left\{ \frac{C_{RFR} + C_{RFL}}{\left[\max \left(0.15, \frac{\mu_R + \mu_L}{2} \right) \right]^2} \right\} \quad (2.100)$$

The equation considers a certain interference between the wing and the rotor, which modifies the angle of attack. This is a function of the rotor force coefficient, both left and right, and of the advance ratio, both left and right. $K_{X_{RW}}$ is a coefficient that considers the rotor-wing equation, while X_{RW} is a function with the same aim.

In the way that C_{RF} and μ are defined, they are always positive. Since the wake is directed downward, there is a minus after the fuselage angle of attack. Therefore, when induced velocities are composed with the freestream velocities, the result is a smaller angle of attack. It is possible to understand this in Figure 2.27. The max function at the denominator is used to avoid divisions by zero.

This equation brings an important result: the induced forces may be zero in several cases, but even when this occurs, the rotor wake acts by modifying the angle of attack. Therefore, **there is also an influence due to the rotor**, which is taken into account with the angle of attack.

Freestream Loads in Wind Axis

Now that the angle of attack and the dynamic pressure are already defined, it is possible to obtain the loads due to the freestream.

$$L_{WP} = q_{WFS} S_{WFS} C_{LWP_{FS}} - q_{WFS} S_W C_{L\delta_a} |\delta_a| \quad (2.101)$$

$$D_{WP} = q_{WFS} S_{WFS} C_{DWP_{FS}} \quad (2.102)$$

$$M'_{WP} = q_{WFS} S_W c_W C_{m_{WP}} \quad (2.103)$$

$$Y'_{WP} = q_{WFS} S_W \left[C_{Y\beta} \beta_F + \frac{b_W}{2U} (C_{Yp} p_w + C_{Yr} r_w) \right] \quad (2.104)$$

$$I'_{WP} = q_{WFS} S_W b_W \left[C_{I\beta} \beta_F + \frac{b_W}{2U} (C_{Ip} p_w + C_{Ir} r_w) \right] + \\ + S_W b_W \left[\left(\frac{q_{iWR} + q_{iWL}}{2} \right) (C_{I\delta_a} \delta_a) \right] \quad (2.105)$$

$$N'_{WP} = q_{WFS} S_W b_W \left[C_{n\beta} \beta_F + \frac{b_W}{2U} (C_{np} p_w + C_{nr} r_w) \right] + \\ + S_W b_W \left[\left(\frac{q_{iWR} + q_{iWL}}{2} \right) (C_{n\delta_a} \delta_a) \right] \quad (2.106)$$

Let's analyze the equations:

- the equation for lift, 2.101, considers the lift due to the freestream, subtracting the loss lift due to the aileron's lowering. The lift coefficient is the same used for the induced aerodynamics: **the way the load is generated is different, but the geometry of the wing is the same**, and there is no reason to have different coefficients;
- the drag equation, 2.102, is the classic aerodynamic one. The drag coefficients are the same as the induced aerodynamics, for the identical reason explained above;

- the pitching moment equation, 2.103, uses the total wing surface instead of the freestream one. It is probably an approximation since the pitching moment is not calculated for the induced aerodynamics³⁸. The pitching moment coefficient is provided in a table from the model, and it is a function of the mast angle β_M and the flap angle δ_F . The coefficients are wind tunnel data for angles up to stall, while for angles above stall, they are extrapolated from Ref. [17];
- the side force equation, 2.104, takes into account the side force coefficient and the effect of the angular velocities in wind axis, which transformation from body into wind axis is made by using the rotation matrix, Equation 2.11. The calculation of the coefficient is presented in Appendix A, and they are calculated using equations for stability derivatives from Ref. [21]. Data is provided by wind tunnel whenever possible;
- the yawing and rolling moment equations, Equation 2.106 and 2.105, are similar to the side force equation. Unlike the pitching moment, the reference length is the wing-span b_W . Furthermore, it is also considered the effect of the induced velocities. Equations coefficients calculation is provided in Appendix A. As for the pitching moment, all the lateral loads are multiplied for the total wing area, probably because they are not considered in the induced aerodynamics.

Loads in wind axis have to be transformed in body axis with the rotation matrix, Equation 2.5 and 2.8, then they go as *output* to the summation of forces and moments subsystem.

2.5.3 Downwash Factor

The downwash factor contributes to the angle of attack at the horizontal stabilizer. It considers the flow's deflection due to the wing's presence, which decreases the tail's angle of attack. It is calculated as follows:

$$\varepsilon_{W/H} = \varepsilon_{W/HOGE} \left(\frac{1}{\sqrt{1 - M_N^2}} \right) \quad (2.107)$$

$\varepsilon_{W/HOGE}$ is provided in a table from the model, and it is a function of the freestream angle of attack α_{WFS} , the mast angle and the flap angle. The data comes from the wind tunnel for angles of attack up to stall. It is corrected with the Prandtl-Glauert equation, which takes into account compressibility effects that depend on the mach number.

A certain error may occur in the downwash data due to the blocking effect of the wind tunnel walls, especially when flaps are open, as explained in Ref. [22].

³⁸ However, it is considered the pitching moment caused by lift and drag.

2.5.4 Wing-Pylon Interference Drag

The wing-pylon interference drag is generated because the wing is not "clean", but the rotors' pylon occupies a portion. It is calculated as follows:

$$D_{PYLN} = D_{PYINT} \left(\frac{q_{iWL} + q_{iWR}}{2} \right) \quad (2.108)$$

D_{PYINT} is the drag interference coefficient. It is provided as a table in $[ft^2]$, and therefore, it is already multiplied for a surface since data comes from flight tests, and they were obtained as forces, as explained in Ref. [23].

This equation is a correction or addition to the model in order to account for extra drag due to wing-pylon interference³⁹.

Given the interference drag in wind axis, it has to be transformed in body axis with the rotation matrix in Equation 2.5. Moreover, this load contributes to the moments due to the arm between the wing-pylon and the c.g..

2.5.5 Spinner Drag

The rotor wake generates the spinner drag, but, unlike the induced forces, this contribution is always present since the spinner, being close to the rotor, is always affected by the rotor wake. Firstly, velocities contributing to angles and dynamic pressure have to be defined. Let's start with the calculation of the average⁴⁰ induced velocities in body axis:

$$U_{iSP} = \left(\frac{W_{iL} + W_{iR}}{2} \right) \sin \beta_M \quad (2.109)$$

$$W_{iSP} = - \left(\frac{W_{iL} + W_{iR}}{2} \right) \cos \beta_M \quad (2.110)$$

Then, the total velocity in mast axes (the axes along the pylon and its perpendicular one) and the dynamic pressure:

$$U_{MSP} = U \cos \beta_M + W \sin \beta_M \quad (2.111)$$

$$W_{MSP} = - \left(\frac{W_{iL} + W_{iR}}{2} \right) - U \sin \beta_M + W \cos \beta_M \quad (2.112)$$

$$V_{TSP} = \sqrt{U_{MSP}^2 + V^2 + W_{MSP}^2} \quad (2.113)$$

$$q_{sp} = \frac{1}{2} \rho V_{TSP}^2 \quad (2.114)$$

³⁹ Extract from Ref. [6]

⁴⁰ The two rotors are considered as one, and all quantities are calculated as the average of the two. It is an approximation: it is possible to divide the two for further precision. Besides, Equation 2.110 has a minus since W_{iSP} is positive downward, and hence it generates a negative angle of attack by referring to conventions shown in Figure 2.9. The angle of attack is calculated in Equation 2.117.

The equations can be verified from Figure 2.28.

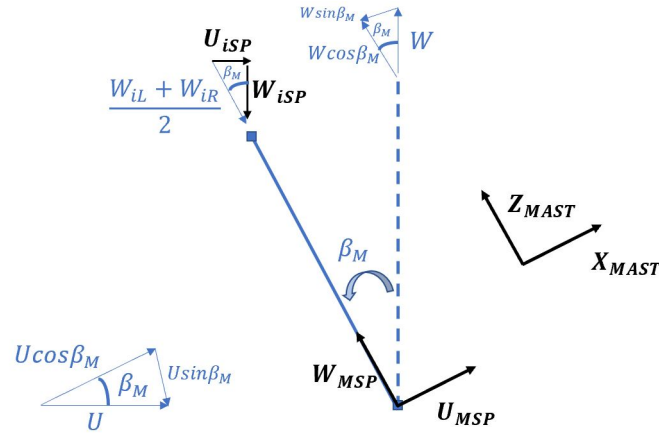


Figure 2.28: Vectors for Average Velocities in Mast Axes

Finally, it is possible to define the spinner angle of attack:

$$\alpha_{SPN} = \arctan \left(\frac{\sqrt{U_{MSP}^2 + V^2}}{|W_{MSP}|} \right), \quad [deg] \quad (2.115)$$

In this case, speeds along x are at the numerator, while the ones along z are at the denominator: this is due to its definition in mast axes and not in body axes. Furthermore, since U_{MSP} is elevated with a square and W_{MSP} is in absolute value, it is not important which direction is considered positive. However, it is important in order to define a convention to choose correct signs for the different contributes.

All quantities are now available for the spinner drag calculation:

$$SD = 2q_{sp} \left[(SD/q)_{\beta_M=90^\circ} + (SD/q) \sin^3 \alpha_{SPN} \right] \quad (2.116)$$

The spinner drag coefficients were determined from wind-tunnel test data of the full-scale XV-15 rotor and pylon, and they are provided in $[ft^2]$. $(SD/q)_{\beta_M=90^\circ}$ represents the drag of the spinner when the conversion angle is 90° . The variable drag portion of the spinner drag equation, which depends on the mast angle, is added to this coefficient. A factor 2 before the dynamic pressure takes into account the presence of two spinners, one for each rotor. It is possible to split the two contributes for further precision, but this is necessary only if the two rotors are in a non-symmetrical position.

Then, it is possible to transform the drag from mast to body axis using the following angles (α_{SP} is positive anticlockwise, β_{SP} clockwise):

$$\alpha_{SP} = \arctan \left(\frac{W + W_{iSP}}{U + U_{iSP}} \right), \quad [rad] \quad (2.117)$$

$$\beta_{SP} = \arctan \left(\frac{V}{\sqrt{(U + U_{iSP})^2 + (W + W_{iSP})^2}} \right), \quad [rad] \quad (2.118)$$

Where $U + U_{iSP} = \min(0.15, U + U_{iSP})$, to avoid division by zero, and the rotation matrix is the one in Equation 2.5.

$$\begin{Bmatrix} X_{SD} \\ Y_{SD} \\ Z_{SD} \end{Bmatrix} = \begin{bmatrix} -\cos \alpha_{SP} \cos \beta_{SP} & -\cos \alpha_{SP} \sin \beta_{SP} & \sin \alpha_{SP} \\ -\sin \beta_{SP} & \cos \beta_{SP} & 0 \\ -\sin \alpha_{SP} \cos \beta_{SP} & -\sin \alpha_{SP} \sin \beta_{SP} & -\cos \alpha_{SP} \end{bmatrix} \begin{Bmatrix} SD \\ 0 \\ 0 \end{Bmatrix} \quad (2.119)$$

Given the spinner drag in body axes, it is possible to calculate the moments due to this:

$$l_{SD} = -Y_{SD} (WL_{CG} - WL_{SP} - l_m \cos \beta_M) \quad (2.120)$$

$$M_{SD} = X_{SD} (WL_{CG} - WL_{SP} - l_m \cos \beta_M) + \\ -Z_{SD} (SL_{CG} - SL_{SP} + l_m \sin \beta_M) \quad (2.121)$$

$$N_{SD} = Y_{SD} (SL_{CG} - SL_{SP} + l_m \sin \beta_M) \quad (2.122)$$

These equations are of great interest due to the arms' calculation since **the position of the forces' application point depends on the nacelle angle**. The arms are calculated by referring to Figure 2.29⁴¹.

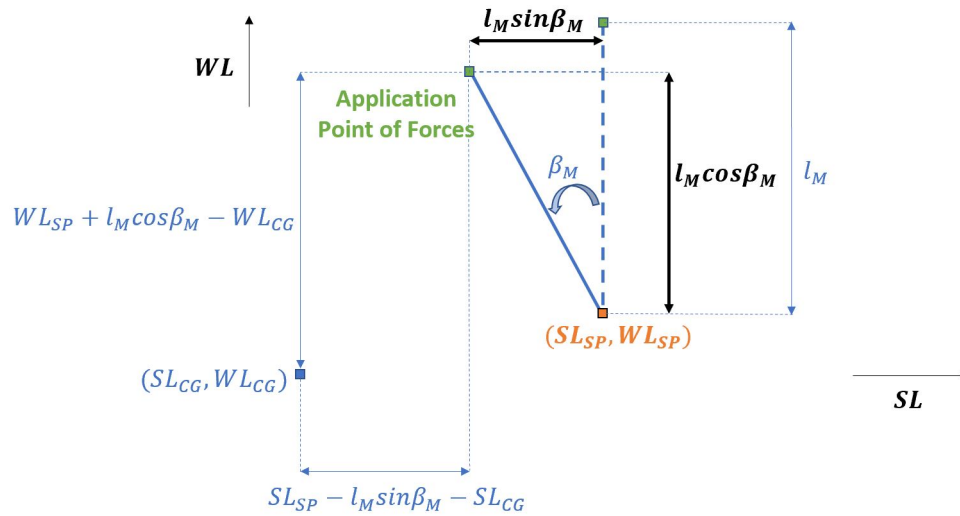


Figure 2.29: Moments' Arms Due to Spinner Drag

2.5.6 Pylon Drag

The pylon drag allows the calculation of additional drag during sideslip. The drag due to forward flight is already taken into account in the wing-pylon drag coefficient, as specified in Ref. [6].

It is calculated as follows⁴²:

⁴¹ Note that in the figure, arms are calculated with station line and water line conventions. All signs have to be changed to transform them into body axes, as explained in Section 2.1.4. The equations are already reported into body axes system.

⁴² PLAT: P=Pylon, LAT=lateral.

$$D_{PLAT} = 2q_{PLAT}S_{PLAT}K_{PLAT} \quad (2.123)$$

Where:

- $$S_{PLAT} = S_{PYL} \left| \frac{V}{\sqrt{U_{MSP}^2 + V^2}} \right| \quad (2.124)$$

is the lateral projection of the pylon surface: it is the portion of the pylon which is wet by the flow due to the sideslip;

- K_{PLAT} is the pylon lateral drag coefficient, and it is non-dimensional. It is a function of α_{PYL} that is equal to α_{SPN} ;
- q_{PLAT} is the dynamic pressure, and it is equal to q_{SP} ;
- a factor 2 is necessary to consider the presence of two pylons. As for the spinner drag, it is possible to separate the two contributes, but it is necessary only if pylons are in a non-symmetrical position.

To convert the drag into body axis, it is possible to use Equation 2.5, while the angles involved are calculated in Equation 2.117 and Equation 2.118.

2.6 FORCES AND MOMENTS SUMMATION MODEL

This subsystem is implemented to join all aerodynamic loads, before summing them with rotor loads, engine loads, landing gear loads, and gravity loads.

All forces and moments calculated in the previous sections are in *input* here, and they are vectorially summed, which mean component for component.

After forces are converted from $[lb]$ to $[N]$, while moments are converted from $[lb \cdot ft]$ to $[N \cdot m]$, hence, the total aerodynamic loads are in output in $[N]$ or $[N \cdot m]$, while the aerodynamic loads of each subsystem are in output in $[lb]$ or $[lb \cdot ft]$.

Indeed, all the model is based on $[lb]$ and $[ft]$ as units of measure because data was supplied in this way. It is not possible to convert every table or equation in $[N]$ and $[m]$ because some coefficients are non-dimensional and may be calculated in a certain measurement system. Hence, it is not possible to use them in a different one or convert them.

To sum up, the best way is to make all the calculations in with the provided system and to convert loads only at the end.

3

VALIDATION AND RESULTS

The second part of the author's activity at ZHAW was the validation of trim points in different flight configurations. Unlike aerodynamic tables, it was possible to find lots of data for this purpose, especially about the performance of a generic tilt-rotor aircraft from the GTRS model. On the other hand, it was possible to find also some flight test data. The greatest part was found on Ref. [23], while the others were in various NASA papers cited afterwards. This part of the work aimed to assess the simulation model's accuracy and reliability and verify and quantify the effects of all the modifications introduced by the author and described in the previous chapter.

First of all, it is necessary to define what a trim point is and how it is obtained. A trim point is a static point of equilibrium in a certain flight condition. It is unknown whether the equilibrium point is stable, unstable, or neutral, since a linear analysis would be required to verify this, Section 3.4.

The trim XV-15 model's trim is operated using a dedicated Matlab routine, called *trimac* and developed by Pierluigi Capone of ZHAW. The routine contained in this function is based on a rotor-craft trim strategy called *periodic shooting*, Ref. [24], in which the initial conditions and controls necessary for a trimmed solution are found by integration through one rotor revolution to obtain errors, followed by an iteration of the Newton-Raphson algorithm.

All parameters necessary for the trim are set in the *TrimLinSim.dat* file, then read by *trimac.m*. It is even possible to give parameters, like airspeed, altitude and nacelle incidence, from the Matlab's Command Window when calling *trimac*. A simulation of one rotor revolution is performed in a dedicated Simulink model, *model_trim.mdl*, at each iteration. All the states, 42 for the ZHAW-Polito model, and the aircraft model's input signals are set directly by the trim function. When convergence of the Newton-Raphson algorithm is achieved, all the parameters which identify the aircraft trim condition are saved in the variable *Par*.

In the *TrimLinSim.dat*, defining the desired accuracy with a tolerance factor and whether to use or not an initial guess is also possible. This was very useful during the trim calculations because it significantly saved time. Nonetheless, it may be important to find a trim condition when convergence cannot be achieved in a row.

3.1 COMPARISON WITH GTRS MODEL

The first validation was against GTRS Model, Ref. [23]. Trim data was provided for different conditions, in helicopter, airplane and conversion mode. Data are

presented in tables, like the one in Figure 3.1. They have to be copied by hand in a Matlab script. Therefore, the work was long, and some errors may have occurred during transcription.

```

***** AIRCRAFT TRIM FLIGHT CONDITIONS *****
*****
*** VT = 0.01 KTS *** NACELLE INCIDENCE = 90.0 DEG *** HELICOPTER ***
*** GW = 13000.0 RPM = 589.00 SLCG = 301.20 WLCG = 81.65 ***
*** MAST ANGLE = 0.00 DEG ***** FLAP SETTING = 40/25 DEG ***
*****

----- EARTH REFERENCE -----
RATE (FPS) 0.1000E-01 0.0000E+00 0.0000E+00
ACCEL (FPS2) -.4319E-02 -.2806E-15 0.5422E-02

----- BODY REFERENCE -----
RATE (FT OR DEG/SEC) UB VB WB P Q R
ACCEL(FT OR DEG/SEC2) 0.9998E-02 0.0000E+00 0.1937E-03 0.0000E+00 0.0000E+00 0.0000E+00
-3.663E-16 -4.366E-01 -1.567E-14

----- ATMOSPHERIC CONDITIONS -----
ALTITUDE (FT) 5000.00
DENSITY ALT. (FT) 0.00
PRESSURE ALT. (FT) 0.00
AMBIENT TEMP (DEG-R) 288.16
OUTSIDE AIR TEMP (DEG-C) 15.00
AIR DENSITY (SLUGS/FT3) 0.2377E-02

----- FLIGHT PATH CONDITIONS -----
CAL. AIRSPEED (KNOTS) 0.00
RATE OF DESCENT (FPS) 0.00
G-LEVEL (G S) 1.00
DYN PRES (SLUGS/FT-SEC2) 0.00
ANGLE OF ATTACK (DEG) 1.110
FLIGHT PATH ANGLE (DEG) 0.000
SIDESLIP ANGLE (DEG) 0.000
ROLL ANGLE (DEG) 0.000
PITCH ANGLE (DEG) 1.110
YAW ANGLE (DEG) 0.000

----- INERTIAS -----
( SLUGS-FT2 )
IXX 0.5280E+05
IXZ 1234.
IYY 0.2136E+05
IZZ 0.6634E+05

----- CENTER OF GRAVITY -----
( IN )
S.L. 301.2
B.L. 0.0000E+00
W.L. 81.65

----- CONTROL DISPLACEMENTS -----
COLL (UP) (IN) (PER)
LONG (FWD) 6.9319 69.32
LAT (RT) 4.8000 50.00
PEDAL (RT) 2.5000 50.00

----- POWER/TORQUE -----
POWER (SHP) TORQUE (FT-LBS) GOV. PITCH (DEG) TIP SPEED (FPS) TIP MACH NO.
LEFT 990.7 8834. 3.801 771.0 0.6906
RIGHT 990.7 8834. 3.801 771.0 0.6906
ENGINE 1075.

----- SWASH PLATE ANGLE (DEG) -----
THETAO LEFT ROTOR RIGHT ROTOR
B1 0.9874 47.0917 0.9874
A1 0.0000 47.0917 0.0000

----- SURFACE POSITIONS -----
ELEVATOR 2.2264 LEFT
AILERON 0.0000 RIGHT
RUDDER 0.0000

----- ROTOR -----
FLAPPING LONG LAT
LEFT 3.0935 -0.9617 -0.2085
RIGHT 3.0935 -0.9617 -0.2085

----- FORCES - MAST AXIS -----
THRUST (LBS) H-FORCE (LBS) Y-FORCE (LBS) JET THRUST (LBS)
7333.92 -125.09 -29.16 99.22
7333.92 -125.09 -29.16 99.22

----- COEFF -----
PROP EFFIC. (ND) ADVANCE RATIO (ND) INDUCED VELOCITY (FPS) INFLOW RATIO (ND) COEFF POWER (ND) COEFF THRUST (ND) COEFF DRAG (ND)
0.0000 0.0000 52.6213 0.0682 0.001019 0.010574 0.026391
0.0000 0.0000 52.6213 0.0682 0.001019 0.010574 0.026391

----- CD -----
CDRISE (ND) CTCL (ND) CDALPHA (ND) CDLIM (ND) CDMACH (ND) CDFACT (ND)
-0.03020 0.01602 0.01000 0.85000 0.35000 0.20000
-0.03020 0.01602

```

Figure 3.1: Trim Data Example from Ref. [23]

The different trim conditions for which data is supplied are shown in Table 3.1.

Table 3.1: Trim Conditions for GTRS Model, Ref. [23]

Test Page	Nacelle Incidence [deg]	Rotor RPM [rpm]	Flap/Flapp. Position [deg]	Altitude [ft]	True Airspeed [kts]
A003	90	589	40/25	Sea Level Standard	0:20:100
A024	75	589	40/25	Sea Level Standard	40:20:120
A042	60	589	20/12.5	Sea Level Standard	80:20:140
A057	30	589	20/12.5	Sea Level Standard	100:20:160
A072	0	589	20/12.5	Sea Level Standard	120:20:180
A087	0	589	0/0	Sea Level Standard	140:20:220
A105	0	517	0/0	Sea Level Standard	140:20:220
A132	0	517	0/0	12000 Standard	140:20:220

The station line of the c.g., provided without the effect¹ of the nacelle angle, is 301.2 in for all conditions, while the gross weight is 13 000 lb.

¹ While tilting the nacelles, the c.g. changes since the rotors c.g. is moving.

Three cases are shown in this section, one in helicopter mode (A003), one in airplane mode (A105), and one in conversion (A042). Complete plots are provided in Appendix C.

The following quantities will be analyzed during the presentation:

ANGLE OF ATTACK It is the angle of attack of the aircraft (α_F), and in a static condition, like the trim, it equals the pitch attitude since the flight path angle is null.

LONGITUDINAL STICK It controls both the longitudinal flapping of rotors and the elevons deflection.

ROTOR FORCES AND MOMENTS IN THE LONGITUDINAL PLANE They are the forces along $X - Body$ and $Z - Body$, and the pitching moment, of the rotor. The lateral-directional ones are not reported since they shall be null for a trim point.

AERODYNAMIC FORCES AND MOMENTS IN THE LONGITUDINAL PLANE They are the total loads of the aerodynamic subsystem. Therefore, they comprehend the fuselage, horizontal and vertical stabilizer and the wing-pylon. The lateral-directional shall be null, as explained above.

FLAPPING ANGLES Or rotor multi-blade coordinates (β_0 , β_{1S} and β_{1C}). They result to be the same for left and right rotor since, for a trim condition, loads are symmetrical in the longitudinal plane. β_{1C} and β_{1S} are changed of sign respect the GTRS model due to different conventions.

ROOT COLLECTIVE PITCH θ_0 It acts on the blades' pitch, resulting in a power change. It shall be varied using the collective lever in helicopter mode and the collective governor in airplane mode, at a selected RPM which shall be maintained.

OTHER CONTRIBUTES When necessary, other quantities will be presented to explain some results.

3.1.1 Helicopter Mode

Results in helicopter mode are shown from Figure 3.2 to 3.5. The blue crosses show GTRS data, while red diamonds show the initial model² results, without the work presented in Chapter 2. Finally, yellow circles show the results after the aerodynamic review. This division will be valid for all conditions and plots shown in this part.

Figure 3.2 shows that the angle of attack has a difference of $\simeq 1$ deg between the GTRS and ZHAW-Polito Model, and the trend is improved after the updates. Similarly, the longitudinal stick shows a better matching after the modifications, reducing a previous offset.

² The model developed in ZHAW will be called ZHAW-Polito.

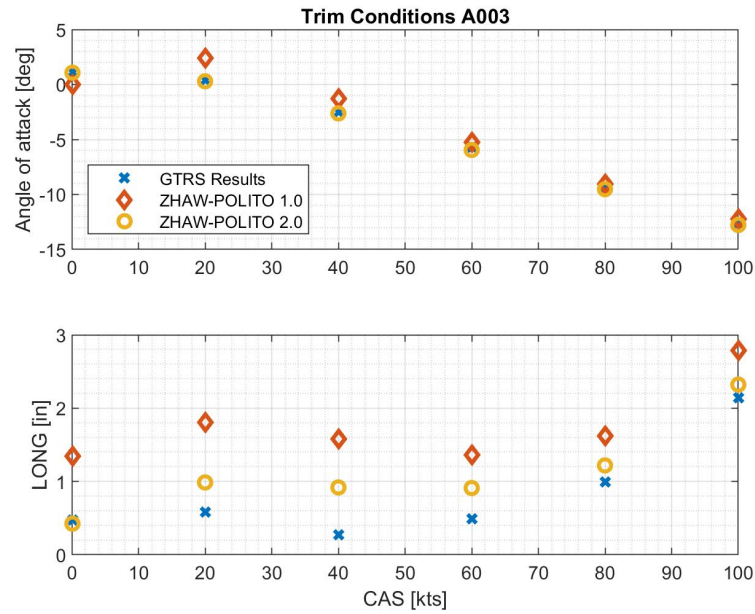


Figure 3.2: Angle of Attack and Longitudinal Stick, Test A003

Figure 3.3 shows a comparison for both $X - Force$ of aerodynamics and rotors. The summation of all forces for a trim condition has to be null, and the difference between the rotor forces and the aerodynamic forces is the gross weight. The correlation between aerodynamic drag³ is fine, with a small error. At the same time, the rotor's thrust has an offset due to a small error in the angle of attack, which brings an error in the transformation of the gross weight.

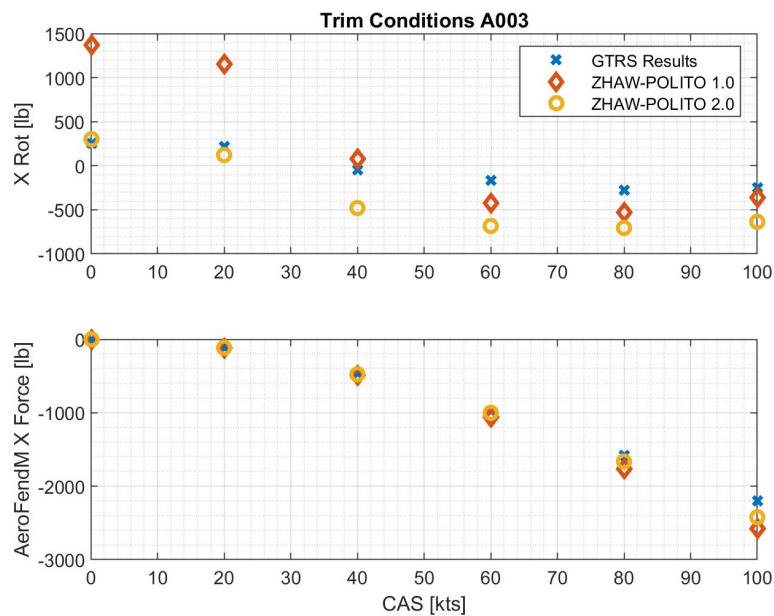


Figure 3.3: Rotor and Aerodynamic X Force, Test A003

³ It is on body axis. Therefore, when there is drag, it is negative. The same happens for the lift.

Along $Z - Body$, Figure 3.4, it is possible to see that both aerodynamics and rotors still have an offset. The reason can be a small error in the angle of attack. It is interesting to study the aerodynamic force along Z :

- at low velocities, it is directed downward, due to the induced aerodynamics;
- as the speed increases, the induced aerodynamics becomes lower, while the dynamic pressure grows: both cooperate in generating lift;
- at very high speed, the induced aerodynamics is null, while $Z - Force$ decreases, returning downward at $\simeq 100$ kts because the angle of attack drops and the aircraft keeps pitching down. This is a significant consideration, as it is even a pilot's feeling during simulations⁴.

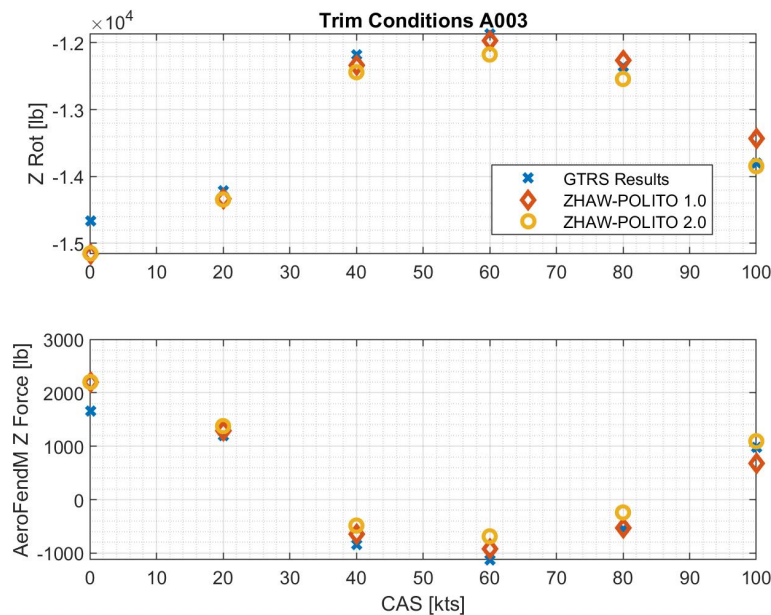


Figure 3.4: Rotor and Aerodynamic Z Force, Test A003

In Figure 3.5, it is shown that the root collective pitch has an offset compared to the GTRS results.

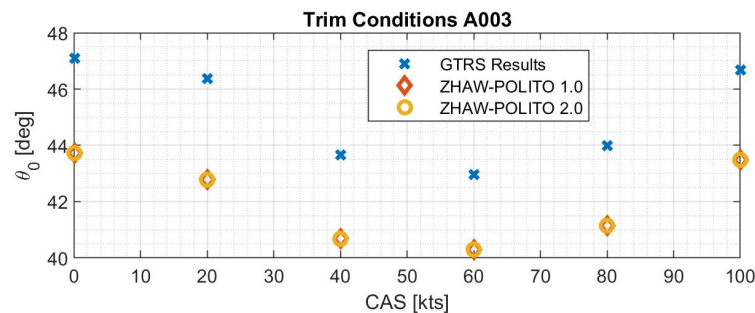


Figure 3.5: Root Collective Pitch, Test A003

⁴ Results of simulations will be presented in Chapter 5.

Figure 3.6 shows flap angles: β_{1S} is almost the same after the aerodynamic review. Instead, comparing β_{1C} , there is an offset between red and yellow points, but both do not match the GTRS.

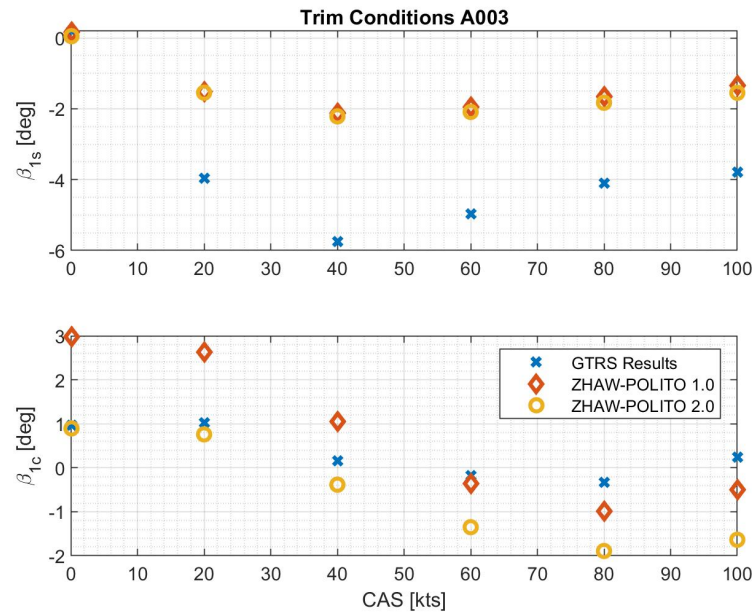


Figure 3.6: Rotor Disk Flapping Angles, Test A003

3.1.2 Conversion Mode

Conversion mode results are shown from Figure 3.7 to 3.10 for a nacelle incidence of 60 deg. The presented quantities have still an offset compared to the GTRS results, but trends are more similar.

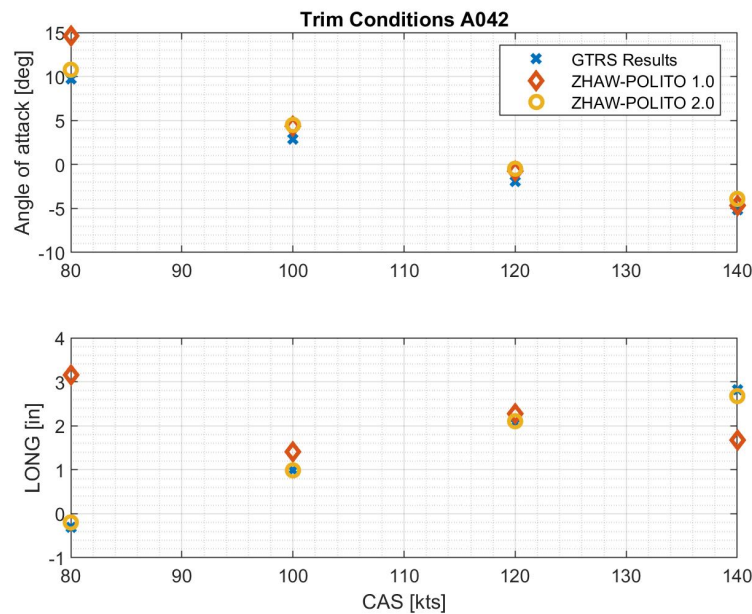


Figure 3.7: Angle of Attack and Longitudinal Stick, Test A042

The errors are probably generated by an offset of the angle of attack: looking at the aerodynamic table, it is possible to see that a difference of $\simeq 1^\circ$ can even generate a difference of $\simeq 10\%$ in aerodynamic loads.

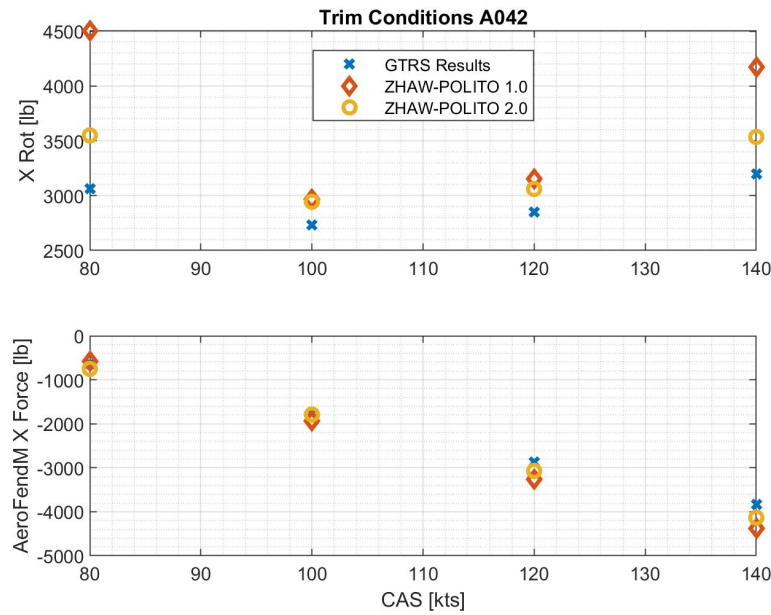


Figure 3.8: Rotor and Aerodynamic X Force, Test A042

A final consideration can be made regarding forces along Z: while in helicopter mode, especially at low speeds, almost all the lift is generated by the rotors, in conversion mode, it is split between rotors and aerodynamic surfaces. This is one important characteristic of the tilt-rotor. During the conversion from helicopter to airplane mode, the lift is "transferred" from the rotor to the wing (during conversion from airplane to helicopter mode, it happens the contrary).

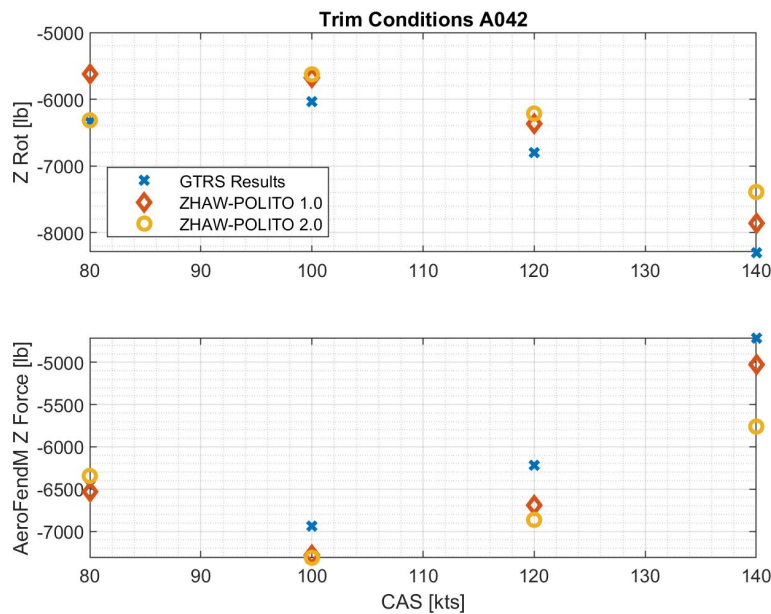


Figure 3.9: Rotor and Aerodynamic Z Force, Test A042

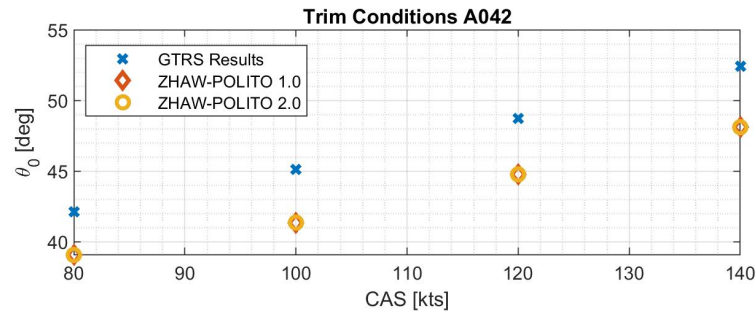


Figure 3.10: Root Collective Pitch, Test A042

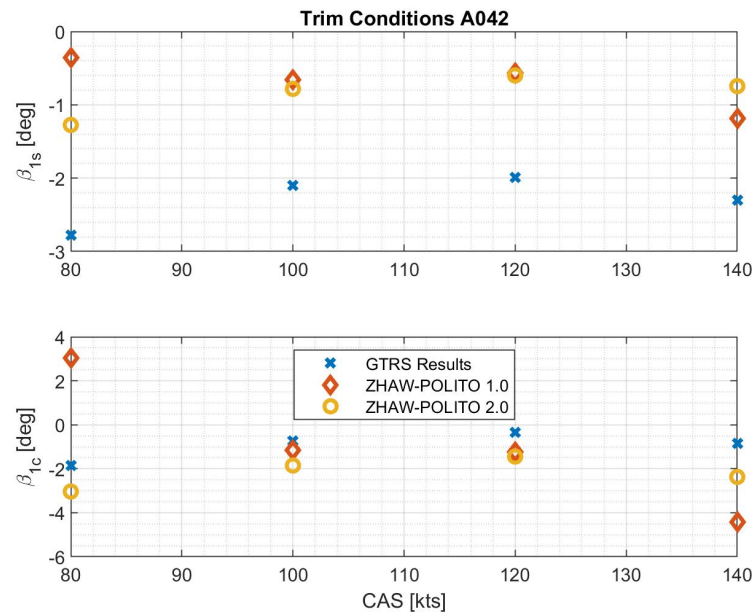


Figure 3.11: Rotor Disk Flapping Angles, Test A042

3.1.3 Airplane Mode

Results in airplane mode at sea level are shown from Figure 3.12 to 3.16.

Figure 3.12 shows that the angle of attack has an error of $\simeq 1^\circ$, decreasing as the speed increases. Instead, the longitudinal stick has an offset. The stick can move in the range $(-4.8;4.8)$; therefore, the percentage error is less than 5%.

Figure 3.13 and 3.14 show that aerodynamic and rotor loads have still an offset.

In airplane mode, the lift is mostly generated by the wing. In the ZHAW-Polito model, the wing generates more lift than the gross weight. Therefore, the rotor generates a down-force.

Flap angles and collective pitch, Figure 3.15 and 3.16, have still an offset compared to GTRS results. Due to the differences in the rotor model between ZHAW-Polito Model and GTRS, the β_{1c} and β_{1s} signs has been changed compared to this in Ref. [23]. The root collective pitch is underestimated, like in airplane and conversion mode.

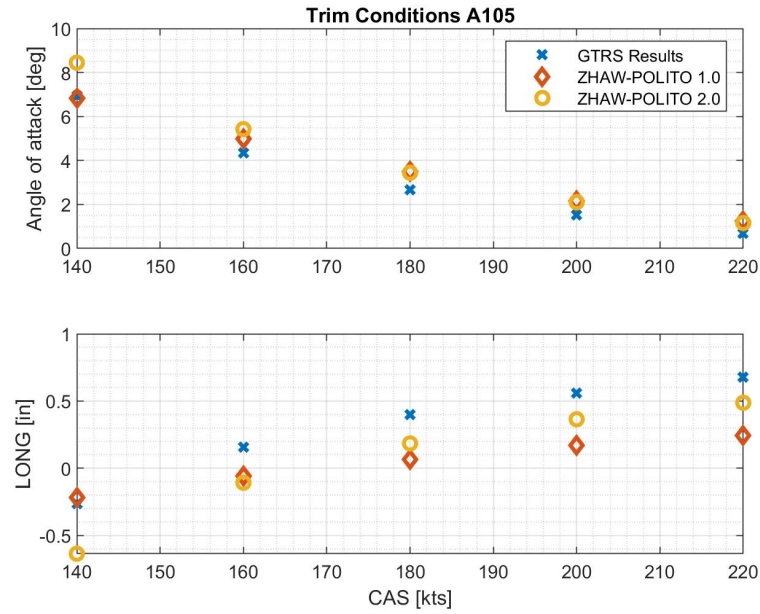


Figure 3.12: Angle of Attack and Longitudinal Stick, Test A105

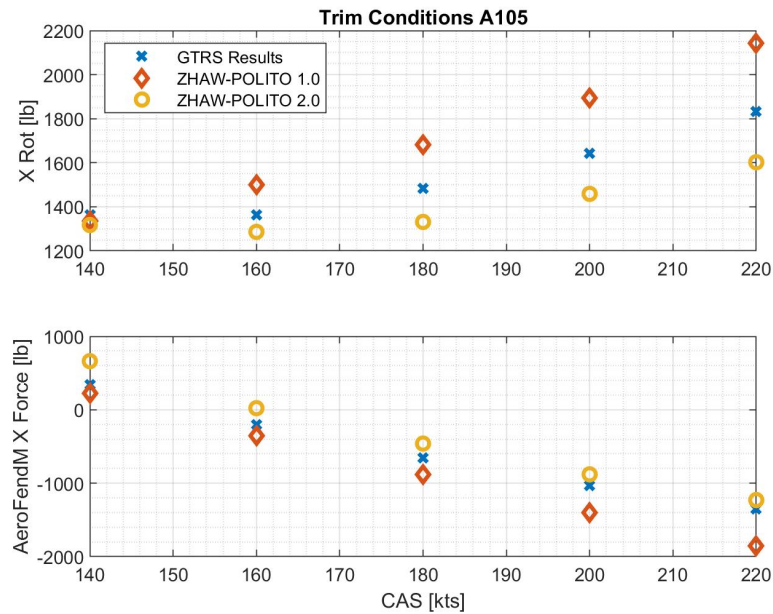


Figure 3.13: Rotor and Aerodynamic X Force, Test A105

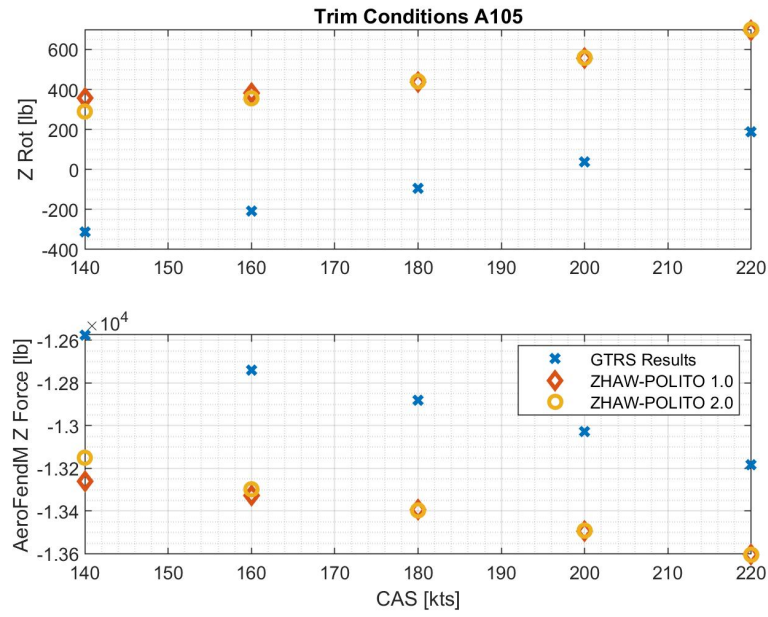


Figure 3.14: Rotor and Aerodynamic Z Force, Test A105

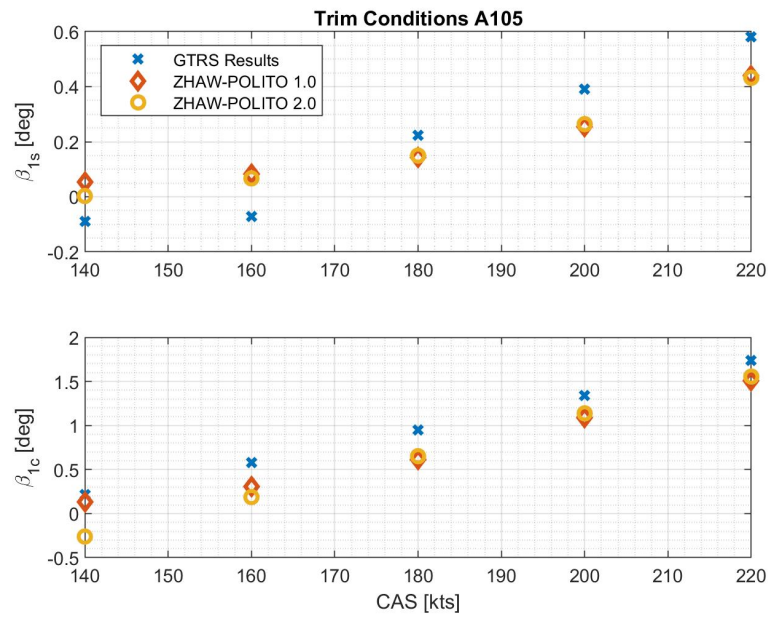


Figure 3.15: Rotor Disk Flapping Angles, Test A105

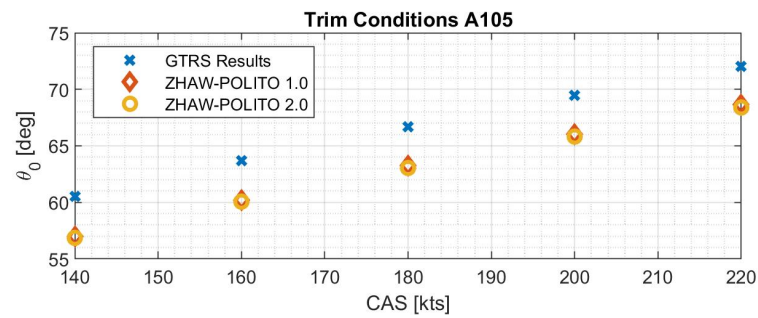


Figure 3.16: Root Collective Pitch, Test A105

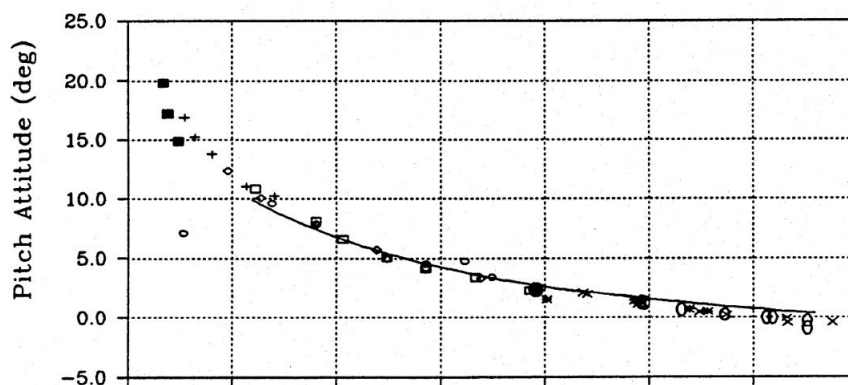
3.1.4 General Considerations

A great effort during the activity was made to solve the problems in aeroplane mode results, especially the fact that the wing generates more lift than the gross weight. Although the changes in the angle of attack calculation at the horizontal stabilizer, explained in Section 2.3.1, nothing was solved. Indeed, **changing the angle of attack at the horizontal stabilizer results in a change in the longitudinal stick but not in the loads.**

Explaining a reason for this phenomena is not simple: the trim procedure is iterative, and therefore, it is not possible to say, each example, whether the angle of attack brings an overestimation of loads or vice-versa⁵. Apart from an error in the transcription of results in Ref. [23] for this configuration, another possibility is that there are more trim points, and the ZHAW-Polito model misses some constraints. The last option, which comes from results in Figure 3.3, is that the ZHAW-Polito model has greater precision in transforming body axes' gross weight.

3.2 COMPARISON WITH FLIGHT TEST DATA

The second part of the validation involved some flight test data in airplane mode, always provided by Ref. [23].



Airplane mode

The trim conditions for the aeroplane mode's flight test are summed up in Table 3.2. Airspeed is not reported, but it is possible to see them in the figures' x-axis, like Figure 3.17. This time, speeds are calibrated, so there is no correction due to compressibility or altitude, unlike the TAS.

Table 3.2: Trim Conditions for Flight Test Data in Airplane Mode

Flight Test	Gross Weight [lb]	c.g. for $i_N = 90^\circ$ [in]	Altitude [ft]
129B	13219	299.3	8402
132A	13219	299.3	12033
132B	13219	299.3	17070
157A	13934	299.6	9879
157B	13934	299.6	20149
158A	13934	299.6	14879
196C1	13997	300.0	9533
196C2	13997	300.0	13810
197A	13997	300.0	18786

Test 129A, 132A and 132B are part of a test group made with the XV-15 Ship Number (S/N) 703 in Ref. [23], and they were located in NASA Arc.. The others are part of another group made with the XV-15 S/N 702, and they were located in BHT. It is important to remark this because the model developed at ZHAW fits the first group, while it has a small offset with the second. One test for the first group and two for the second group, in order to cover a wide range of speeds, are reported in this section, while all the graphs are reported in Appendix C.

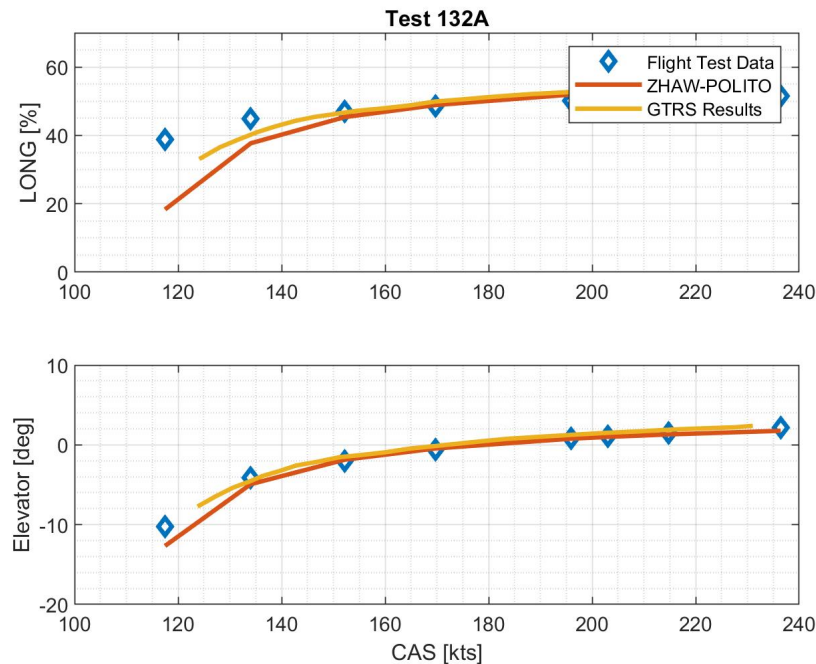


Figure 3.18: Longitudinal Stick and Elevator Angle, Test 132A

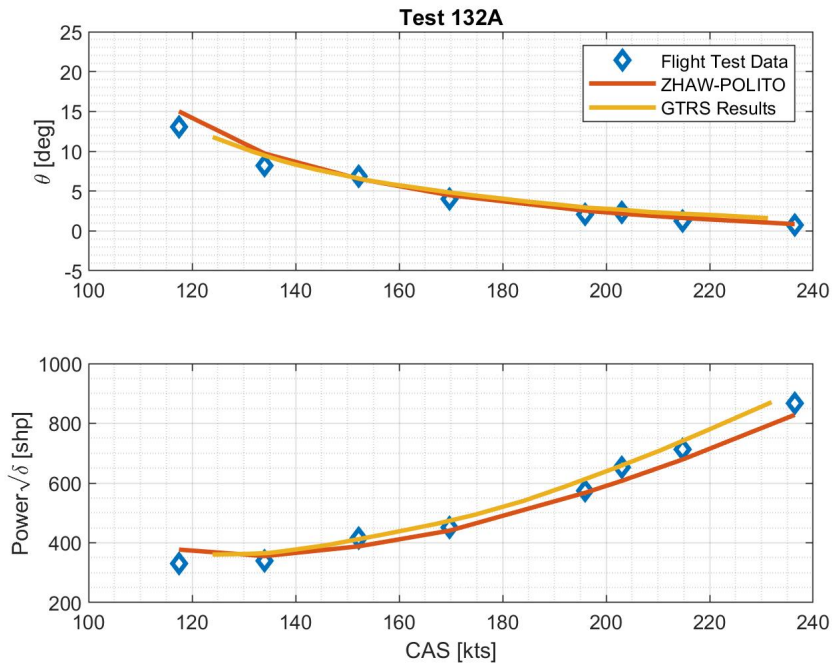


Figure 3.19: Pitch Angle and Corrected Power, Test 132A

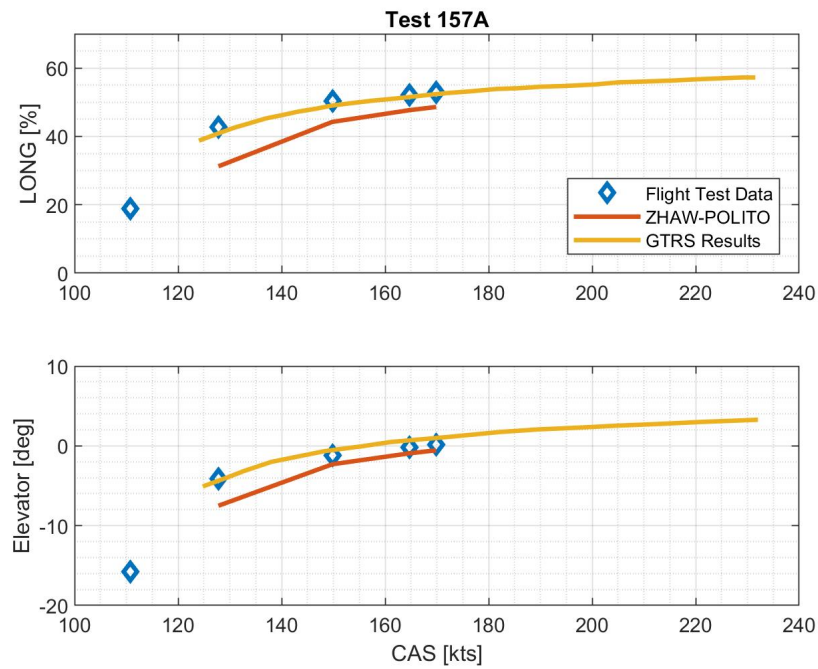


Figure 3.20: Longitudinal Stick and Elevator Angle, Test 157A

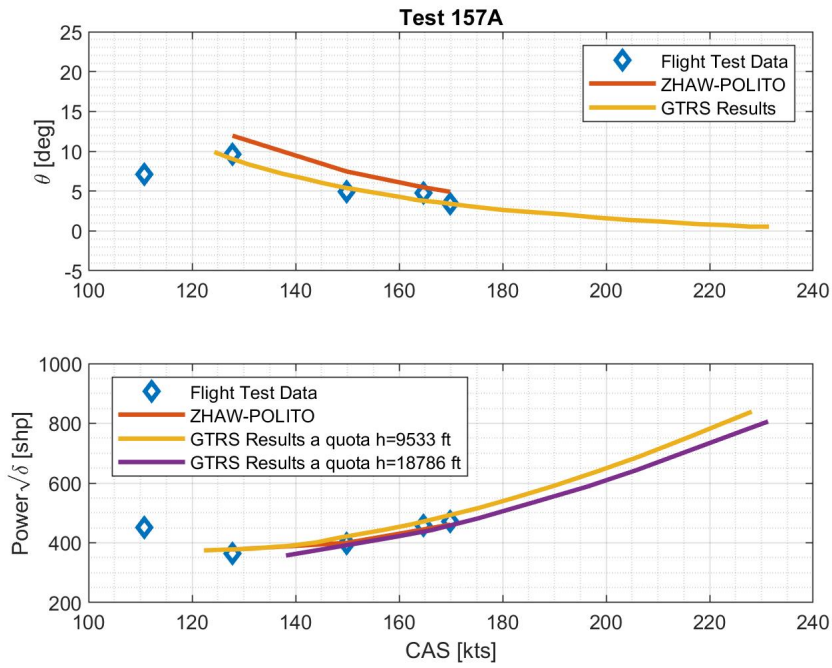


Figure 3.21: Pitch Angle and Corrected Power, Test 157A

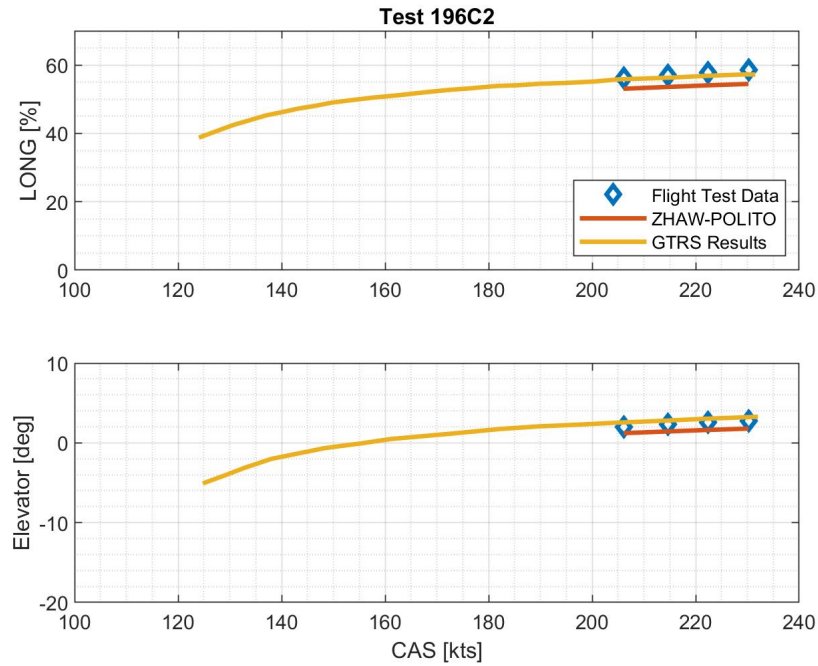


Figure 3.22: Longitudinal Stick and Elevator Angle, Test 196C2

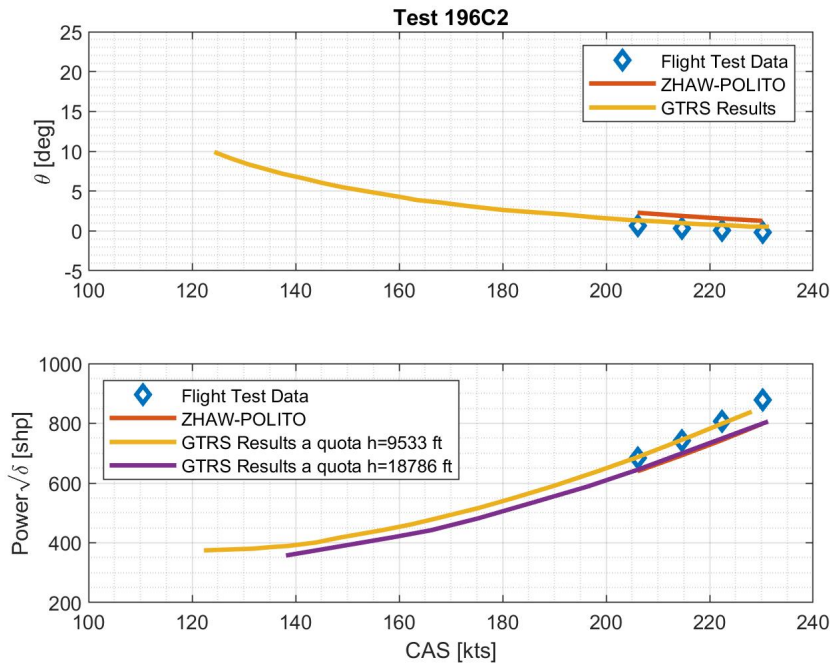


Figure 3.23: Pitch Angle and Corrected Power, Test 196C2

As told before, it is possible to see that data from Test 132A, the first set, are fitted by the ZHAW-Polito model better than GTRS. Indeed, as admitted in Ref. [23], the GTRS model fits better test from S/N 702, while it does not fit as well test from S/N 703.

The ZHAW-Polito model has an offset for test 157A and 196C2, and the reasons may be several⁶:

- some small differences in the aircraft configuration between the two sets of data;
- a problem in the lecture of data with plot digitizer;
- differences in flap position, which is not specified;
- a problem with the graphs' scale, which brings a wrong lecture.

The last point, in particular, seems reasonable. In fact, comparing, for instance, the top plot with the bottom plot in Figure 3.18, something does not add up since, between the longitudinal stick and the elevator, there is just a transmission ratio. However, the trend is different and, while the elevator angle is matched, the longitudinal stick is not. The same appears in Figure 3.20. Therefore, it is possible to think that several problems may have occurred in the extrapolation and transcription of the data, as admitted for the longitudinal stick of S/N 703 and for which is also provided with a correction⁷.

⁶ Excluding left errors in the ZHAW-Polito model.

⁷ The result is shown in Figure 3.24

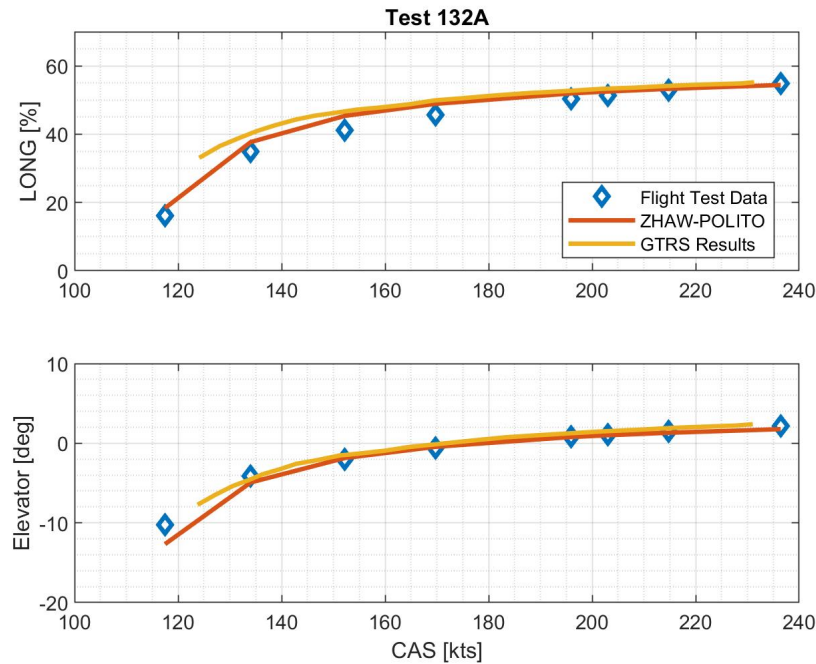


Figure 3.24: Longitudinal Stick of Test 132A with the Correction Provided by Ref. [23]

Certainly, noticeable is that the ZHAW-Polito model gives results close to the flight test for different altitude, airspeed, gross weight and c.g. positions. Furthermore, results compared to the flight test are better than those compared with the GTRS model⁸ in the previous section.

On the other hand, it is difficult to say why the ZHAW-Polito model fits better one group of data, while the GTRS the other⁹. Some possible reasons are:

- different rotor model, which can have a great impact on the results as explained in Ref. [23];
- differences between the ZHAW-Polito and GTRS model;
- a different configuration between XV-15 S/N 702 and S/N 703, which is assumed to be the same in Ref. [23], but without being sure;
- an error in the reading of data;
- instrumentation errors, which are admitted for the longitudinal stick of XV-15 S/N 703 tests;
- the sensibility to longitudinal stick position to the downwash factor: a difference of 0.5 deg of downwash can bring a difference of $\pm 2\%$ in the stick position.

To sum up, it is possible to evaluate the model implemented at ZHAW. However, it is not possible to quantify the exact error due to the many unknown variables present and "some confusion¹⁰ in flight test data".

⁸ Especially the Power, which was strongly underestimated.

⁹ It is interesting to report that.

¹⁰ Ref. [23] report these exact words.

Helicopter Mode

Flight test data is also provided for one helicopter condition, Table 3.3.

Table 3.3: Trim Conditions from Flight Test Data in Helicopter Mode

Flight Test Number	Gross Weight [lb]	SL_{CG} [in]	i_N [deg]	Altitude [ft]
159C	13400	299.7	85	-

Data for flaps and altitude are not specified, so there is uncertainty in the results. This is a possible explanation of the difference with the flight tests since, especially the altitude, may change the power results.

As it happens for the airplane mode, Ref. [23] provides some useful information about flight test in helicopter mode:

- since the XV-15 is a proof of concept tilt-rotor and not a helicopter, there is a shortage of data in this mode, while lots are available in airplane mode because it is the biggest fraction of the flight time;
- the helicopter mode is where the conversion begins or ends and, due to this, it is a critical evaluation task;
- except for the previous results for $i_N = 85^\circ$, data in helicopter mode are confusing.

For these reasons, these evaluation data should be taken **with caution**¹¹.

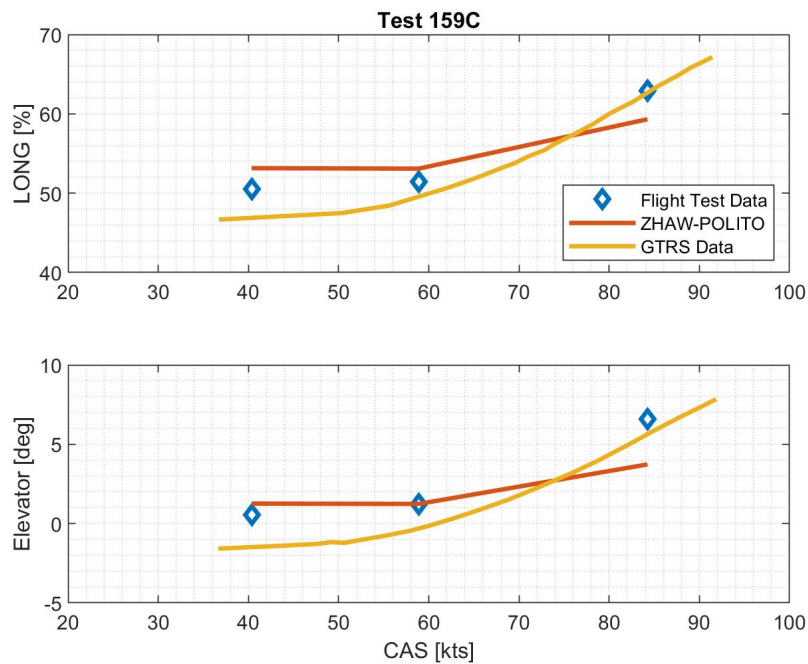


Figure 3.25: Longitudinal Stick and Elevator Angle, Test 159C

¹¹ Extract from Ref. [23].

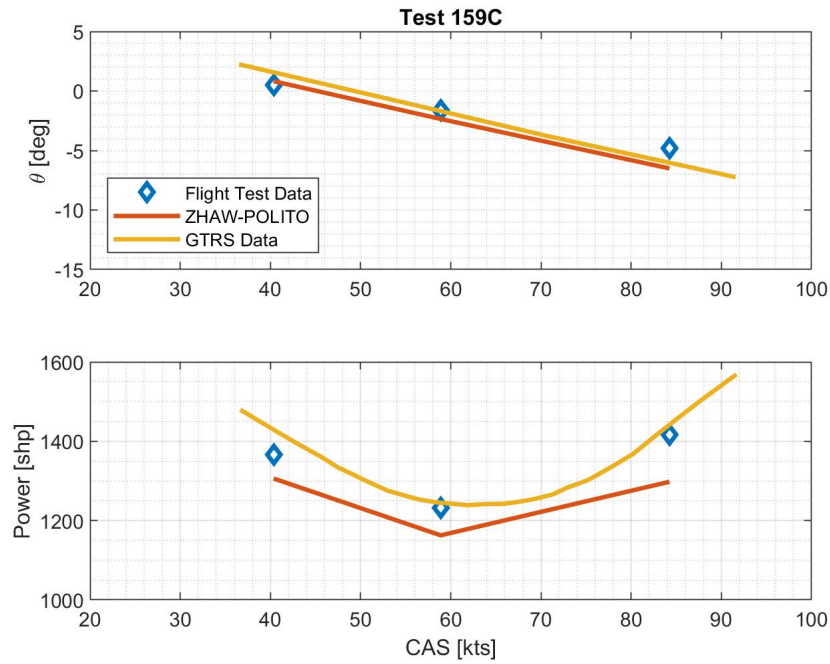


Figure 3.26: Pitch Angle and Corrected Power, Test 159C

3.3 OTHER VALIDATION DATA

Some longitudinal pitch data are provided from Ref. [22] for different nacelle incidences and both the GTRS model and Flight Tests. Conditions are shown in the legend of the figure, but no information was supplied for the c.g., the altitude and the gross weight, hence they were set in this way:

Table 3.4: Trim Conditions Set for the Map

SL_{CG}	Gross Weight	Altitude
300 in	13 000 lb	0 ft

Analyzing Figure 3.27, ZHAW-Polito Model shows more accurate than the GTRS model, compared to flight tests, in all conditions except helicopter mode. Reasons may be several: some correction in the aerodynamic part explained in the previous chapter and a more detailed rotor model.

In helicopter mode, data seems to fit worse: actually, for the same conditions, flight tests report more than one trim point. It is reasonable that some difficulties¹² occurred while obtaining data, and hence, it is not easy to assess the models' accuracy.

Lastly, comparing Figure 3.27 with Figure 2.11 shows that the change in the horizontal stabilizer's lift angle of attack allows a better matching in the data.

This map is significant since it covers a wide range of conditions, showing the ZHAW-Polito model's goodness and reliability.

¹² The same was explained in the previous section.

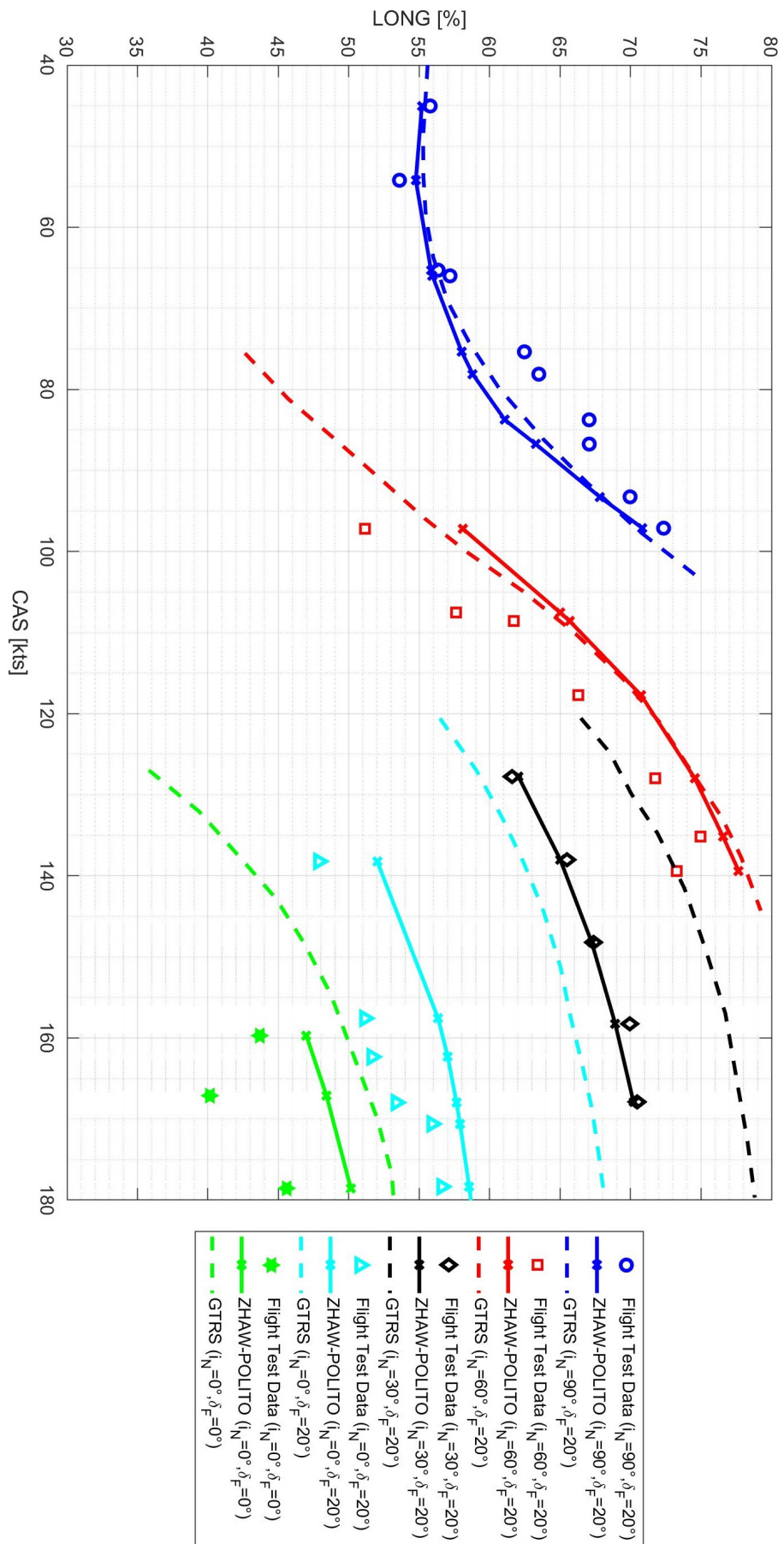


Figure 3.27: Longitudinal Stick Map

3.4 COMPARISON OF EIGENVALUES

The last part of the validation consisted of the comparison of eigenvalues. In Ref. [19], there are some results in helicopter mode, while in Ref. [20], there are both values for the model developed by Celi and from flight test data.

As explained in the previous section, with the *trimac.m* routine is possible to find an equilibrium point without knowing whether it is stable, unstable or neutral.

Another routine is necessary to aim at the last point, and it is called *linac.m*. It operates by giving some commands to the aircraft exiting the equilibrium condition found with the trim and linearising its answer. In *output*, there are the poles, which eigenvalues describe the trim point's dynamic stability.

There is an eigenvalue for every state of the *trimac.m* routine, but just the nine of the flight mechanics will be compared. To obtain these, it is necessary to **condense** all the states, except Euler's angles¹³, longitudinal and angular velocities¹⁴ and the aircraft position¹⁵, with the already implemented function *scond*. Given these, it is necessary to **delete** ψ , x and y to obtain nine states, with the already implemented function *sdel*.

The conditions for the comparison are shown in Table 3.5.

Table 3.5: Conditions for Eigenvalues Comparison

Nacelle Incidence [deg]	Airspeed [kts]
90	Hover

No data about c.g., gross weight and flap angles were provided in the references, and therefore, they are set arbitrary: $SL_{CG} = 300$ in, $GW = 13\,000$ lb, while flaps are set to 75 deg.

Results in hover are summarized in Table 3.6.

Table 3.6: Eigenvalues Comparison in Hover

ZHAW-POLITO	Padfield	Celi	Flight Test
$0.17689 \pm 0.43916i$	$0.1471 \pm 0.4208i$	$0.1483 \pm 0.4616i$	$0.2681 \pm 0.5132i$
$0.11224 \pm 0.31085i$	$0.1356 \pm 0i$	$0.0579 \pm 0.2321i$	$0.1868 \pm 0.4061i$
$-0.006085 + 0i$	$0.0064 \pm 0.3120i$	$-0.0033 + 0i$	$0 + 0i$
$-0.14976 + 0i$		$0 + 0i$	$0 + 0i$
$-0.18447 + 0i$	$-0.681 + 0i$	$-0.1312 + 0i$	$-0.102 + 0i$
$-0.53662 + 0i$	$-0.7904 + 0i$	$-0.7892 + 0i$	$-1.23 + 0i$
$-0.61257 + 0i$	$-1.1426 + 0i$	$-1.1861 + 0i$	$-1.32 + 0i$

¹³ ϕ , θ and ψ

¹⁴ U , V , W , p , q and r

¹⁵ h , x and y

The table shows that there are two complex conjugate couples of unstable poles. For the first complex couple, the imaginary part matches for mathematical models, while a difference of $\simeq 10\%$ is present in the real part. Instead, the Padfield model provides a real eigenvalue for the second couple, while Celi has real and imaginary parts smaller than ZHAW-Polito ones.

In this case, it is essential to know flaps, c.g. and gross weight. For instance, with a gross weight of 13 400 lb and $SL_{CG} = 299.7$ in, eigenvalues are more similar to Celi's model. Moreover, also being in ground effect has a great impact.

For these reasons, the comparison should be taken with caution.

4 | NEW IMPLEMENTATIONS IN SIMULINK

The last part of the activity carried out in ZHAW by the author was implementing some contributes, which were not yet in the model.

4.1 GROUND EFFECT

The first contribution developed by the author was the ground effect.

In Ref. [6], the ground effect's contribution is calculated in a flow chart together with the inflow model. However, this was not usable since the rotor's inflow model was changed from the one presented in the reference and the ground effect model was not adaptable.

In fact, the rotor dynamic inflow was modelled according to the formulation introduced by Pitt and Peters¹, and it is presented in a previous work carried out in ZHAW, Ref. [9].

For this reason, it was necessary to search for a new way to implement the ground effect, despite the shortage of data available in literature. Many papers deal with the ground effect, but the majority presents Bennet's theory, which was thought for helicopters, while nothing was found for the tilt-rotor. Moreover, no modifications of Pitt and Peters inflow model In Ground Effect (IGE) are available in literature.

Therefore, to implement the ground effect, Bennet's theory was used, but some considerations and modifications were necessary to suit the tilt-rotor.

4.1.1 The Physical Problem

The ground effect problem was explained by Leishman in Ref. [27].

It is present when there is the ground or a boundary that constrains the rotor wake development. The hover case has to be divided from the forward flight near the ground since its physic is different.

Hovering Near the Ground

Consider a rotor hovering near the ground: the ground must be a streamline to the flow, and therefore, the rotor slipstream tends rapidly to expand as it approaches the surface. This phenomenon is shown in Figure 4.1, and it alters the

¹ Ref. [25], and [26].

slipstream velocity, the induced velocity in the plane of the rotor and, therefore, rotor power and rotor thrust.

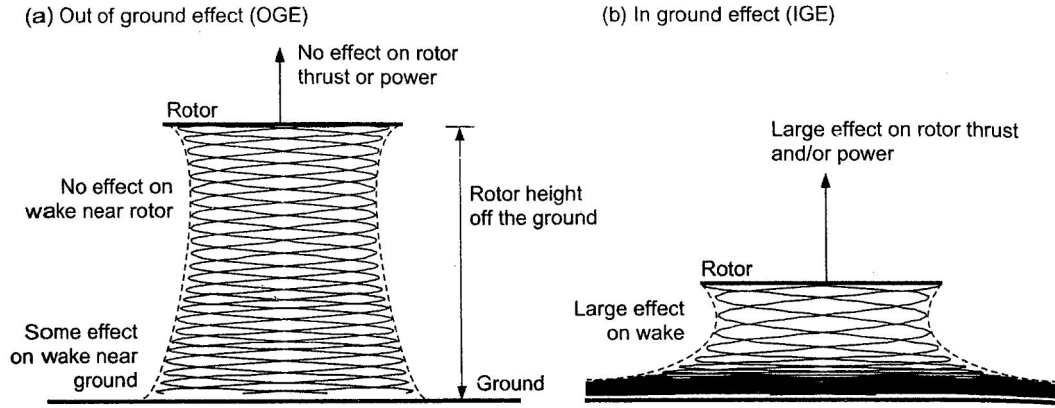


Figure 4.1: Behaviour of a Hovering Rotor's Wake, Ref. [27]

Even though the problem has long been recognized, it is still not fully understood, and the only theory which seems to respect flight test data is the one developed by Bennet with the method of images. The theory relates the thrust IGE and Out of Ground Effect (OGE) with a function which depends on the rotor radius R , the distance between the rotor and the ground z , the advance ratio μ and the inflow λ :

$$\left[\frac{T_{IGE}}{T_{OGE}} \right]_{P=CONST} = \frac{1}{1 - \frac{\left(\frac{R}{4z}\right)^2}{1 + \left(\frac{\mu}{\lambda_i}\right)^2}} \quad (4.1)$$

In hover, the expression is simply a function of the ratio between R and z , since $\mu = 0$:

$$\left[\frac{T_{IGE}}{T_{OGE}} \right]_{P=CONST} = \frac{1}{1 - \left(\frac{R}{4z}\right)^2} \quad (4.2)$$

Figure 4.2 shows that Bennet's equation fits really good the flight test data for a ratio $z/R > 0.5$.

Furthermore, the ground effect can be seen as an increase of thrust for constant power. For a ratio $z/R > 2$, its contribution is negligible.

Since for a constant power $\lambda_{IGE} C_{T_{IGE}} = \lambda_{OGE} C_{T_{OGE}}$, Equation 4.1 also relates the inflow IGE and OGE. This consideration is important for implementing the ground effect in Simulink.

Forward Flight Near the Ground

The effects of ground effect during a forward flight are also important, even though weaker than in hover. Moreover, the physics of the flow is much more complicated. Figure 4.3 shows the rotor wake configurations in a forward flight, depending on the speed.

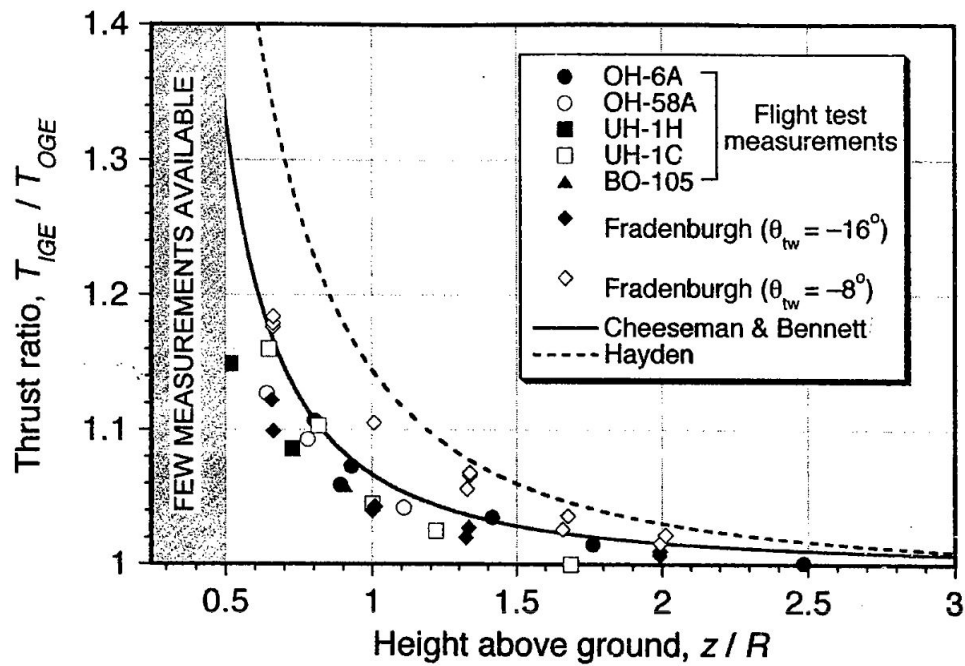


Figure 4.2: Comparison between Flight Test Data and Bennet's Equation, Ref. [27]

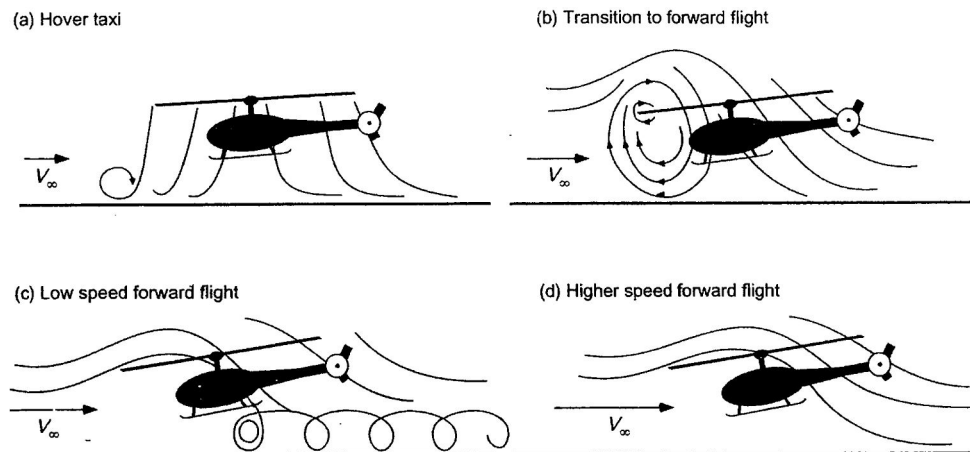


Figure 4.3: Flow's Behaviour for a Rotor in Forward Flight Near the Ground, Ref. [27]

A flow recirculation region is formed upstream of the rotor near the ground, at low forward speeds, Figure 4.3 subfigure *b*. This phenomenon has negligible effects on performance, but it can be dangerous if small objects in the ground can hit the rotor. For higher forward speeds, the recirculation develops into a small vortical flow region between the ground and the helicopter and around the leading edge of the rotor, Figure 4.3 subfigure *c*. These results are confirmed in both wind-tunnel tests and flight operations. When speed is sufficiently high, the phenomenon disappears, Figure 4.3 subfigure *d*, since the wake goes downstream of the rotor. Ground effect is usually considered negligible for an advance ratio greater than 0.1 or $V_\infty > 2V_H$. Equation 4.1 already takes into account the forward-moving by considering the rotor wake angle with the ratio between μ and λ .

Similar information for the forward-moving near the ground can be found in a paper published by NASA and wrote in Ames Research Center, Ref. [28]. The problem is not studied in detail as in Figure 4.3, but it is clearly explained that as the forward speed increases, the rotor's wake is rapidly swept rearward and, as a result, the effect of the ground is rapidly reduced.

Equation 4.1 was also used to modify Patt and Peters inflow model in joint work between Delft and National Aerospace Laboratory of Netherlands, Ref. [29].

Considering the tilt-rotor, Ref. [6] explains that the ground effect is negligible in helicopter mode if the forward speed is greater than 40 ft s^{-1} .

4.1.2 Differences between Helicopter and Tilt-Rotor

When the ground effect's problem was clear, some considerations were necessary before implementing it since Bennet's equation was thought for a helicopter and not for a tilt-rotor. Therefore, differences between the two aircraft had to be clarified in order to understand whether Equation 4.1 was suitable or not for the XV-15 tilt-rotor:

- the helicopter has one main rotor, while the tilt-rotor two: this was not a big issue since it was possible to implement the equation for both the rotors. Apart from the distance between the rotor and the ground, no other lengths nor information for the position of the rotor are considered in Equation 4.1, and therefore, it was assumed that the butt line and station line position are negligible;
- the helicopter is a rotor aircraft, while the tilt-rotor is a rotor-wing aircraft. Therefore, the influence of the wing has to be considered;
- the helicopter and the tilt-rotor have a difference in the disk load² at equal thrust: helicopter's rotor radius is greater, and therefore, the disk load is smaller;
- the helicopter's rotor cannot tilt, while the tilt-rotor nacelles can. Therefore, the contribution of the nacelle incidence has to be added.

Furthermore, Bennet's equation considers the power constant, and hence, there is another approximation.

It was complicated to find articles that write about these problems in literature, and therefore, the author had to make do with the limited, available data.

Bennet and Cheeseman provide some important information about their equation in Ref. [30], which was not proper for the tilt-rotor, but it helped in the work.

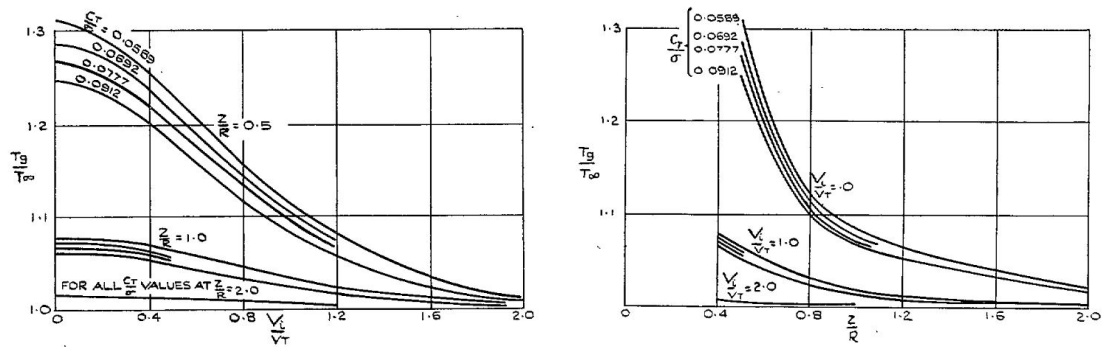
Disk Load

They estimated the effect of blade loading³ coefficient on the ground effect at a given forward speed or altitude, at constant power. They show that for a wide

² It is the ratio between the rotor load and the rotor area.

³ It is proportional to the disk load.

range of blade loading coefficient, the ground effect does not change considerably for different altitudes, Figure 4.4a, and advance ratios, Figure 4.4b.



(a) Ground Effect with Blade Loading at a Given Height (b) Ground Effect with Blade Loading at a Given Speed

Figure 4.4: Ground Effect with Blade Loading in Different Flight Conditions, Ref. [30]

The same results were also obtained for a quad-rotor in Ref. [31], Figure 4.5.

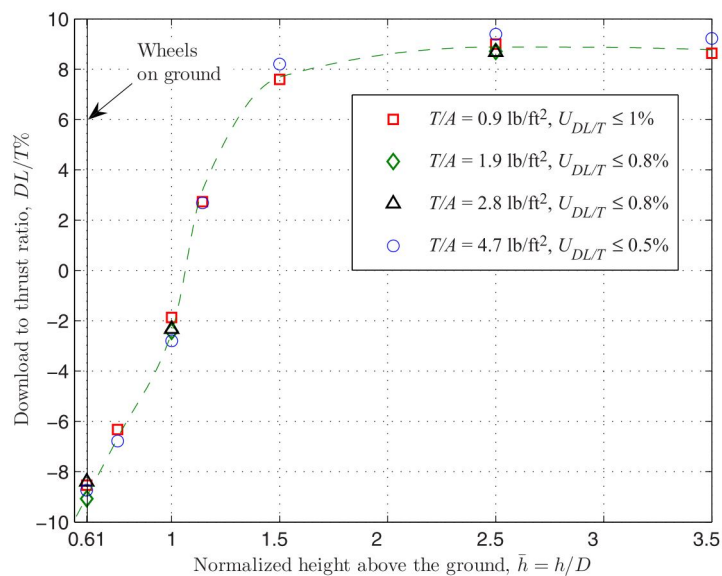


Figure 4.5: Ground Effect at Different Disk Load for a Quad tilt-rotor, Ref. [31]

Therefore, it is reasonable to think that Equation 4.1 can be used for the tilt-rotor without further correction due to disk load.

Wing-Rotor Combination

The wing area affects the ground effect in two ways:

- the wing is a constraint similar to the ground, and therefore, it creates itself a contribution to ground effect, with the difference that is closer to the rotor than the ground, Figure 4.6;

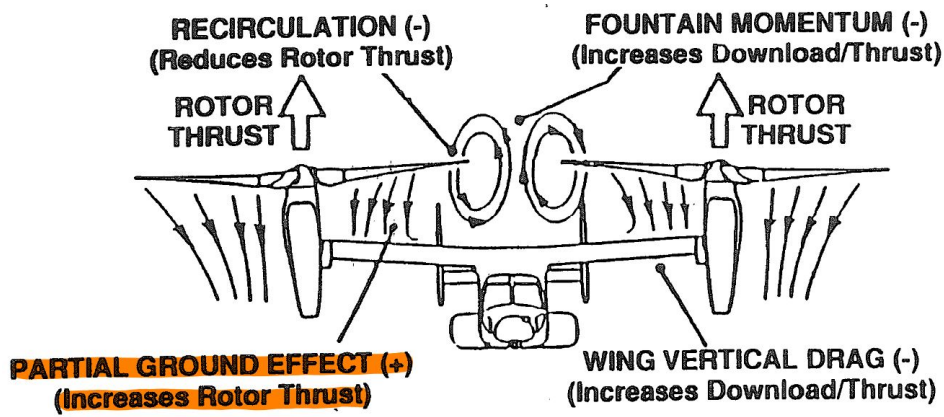


Figure 4.6: Partial Ground Effect Due to the Wing, Ref. [32]

- if there is some recirculation of the inflow under the wing, it can create a certain upward force.

In Ref. [30], Bennet and Cheeseman present some **experimental results** for wing's interference. They are shown in Figure 4.7.

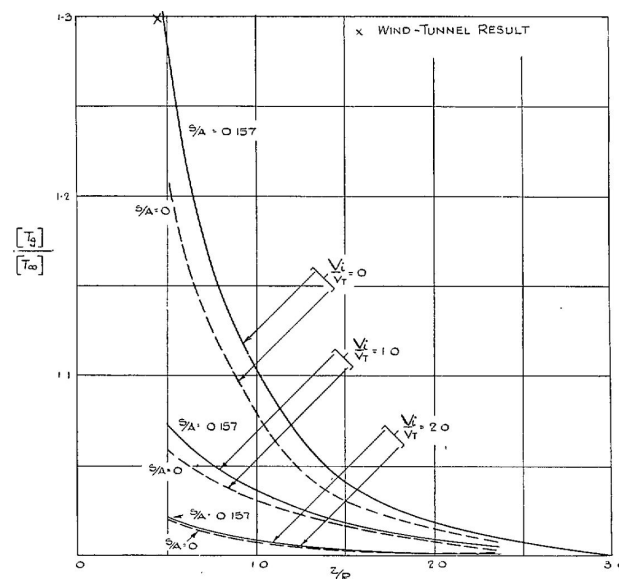


Figure 4.7: Ground Effect for a Wing-Rotor Combination, Ref. [30]

It is shown that until the ratio between the wing area and the rotor area is smaller than 0.157, the wing's interference is negligible. For greater ratios, further correction is necessary. Studying the XV-15 tilt-rotor, it is possible to calculate the requested ratio. Indeed, the rotor radius is known, and the area can be calculated with the circle's area formula:

$$R = 12.5 \text{ ft} \quad (4.3)$$

$$A = \pi R^2 = 490.63 \text{ ft}^2 \quad (4.4)$$

The wing area which interests the rotor can be overestimated by considering a rectangle with dimensions the wing chord and the rotor radius:

$$c_W = 5.225 \text{ ft} \quad (4.5)$$

$$S = c_W \cdot R = 65.31 \text{ ft}^2 \quad (4.6)$$

Therefore, the ratio is:

$$\frac{S}{A} = 0.133 < 0.157 \quad (4.7)$$

In conclusion, since the ratio is also overestimated, Equation 4.1 does not need further corrections for the wing's interference.

Nacelle Angle Effect

The last difference is the possibility of tilting nacelles. No papers were found in literature about this contribution. However, it was not difficult to arrange Equation 4.1 since the ratio between μ and λ takes into account the rotor wake's angle. Therefore, to consider nacelle incidence, it is possible to divide the inflow's contribution into two components dependent on β_M , as shown in Figure 4.8. The inflow's component, which is on the same axis of the advance ratio, can be summed to it.

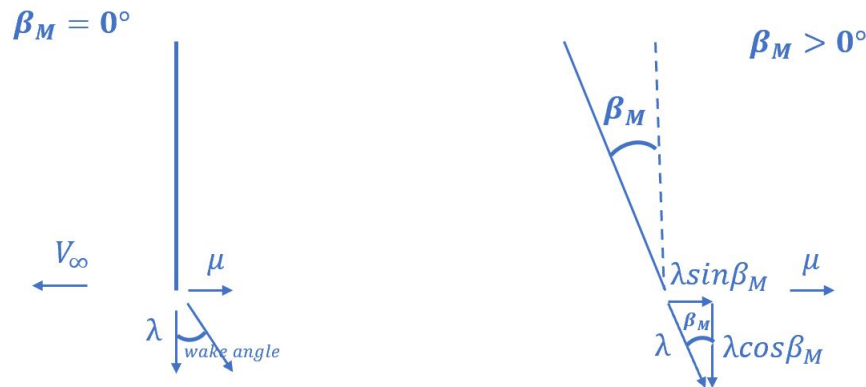


Figure 4.8: Ground Effect with Nacelle Angle

Given this, the ground effect equation that considers the effect of the nacelle angle is the following:

$$\left[\frac{T_{IGE}}{T_{OGE}} \right]_{P=COST} = \frac{1}{1 - \frac{\left(\frac{R}{4z}\right)^2}{1 + \left(\frac{\mu + \lambda_i \sin \beta_M}{\lambda_i \cos \beta_M}\right)^2}} \quad (4.8)$$

Considering the inflow, the same equation becomes:

$$\left[\frac{\lambda_{OGE}}{\lambda_{IGE}} \right]_{P=COST} = \frac{1}{1 - \frac{\left(\frac{R}{4z}\right)^2}{1 + \left(\frac{\mu + \lambda_i \sin \beta_M}{\lambda_i \cos \beta_M}\right)^2}} \quad (4.9)$$

4.1.3 Implementation

Finally, it was possible to implement Equation 4.9 in the Simulink model. The last point was to decide where to calculate the ground effect. The author made several attempts to aim this, and it turned out that the best solution was to put it downstream the inflow calculation.

The model calculates a coefficient called K_{GE} , which is the ratio between the inflow in Equation 4.9, where $z = WL_{SP} - WL_{CG} + h_m - h_{m_{GND}}$ is the distance between the rotors and the ground. It is calculated as the difference between the water line of shaft-pivot and the water line of c.g.. To this contribute, it is summed the difference between the aircraft's⁴ altitude h_m and ground's altitude $h_{m_{GND}}$. Then, the ground effect coefficient multiplies the three states⁵ of the inflow.

The same ground effect model is implemented in Simulink for both left and right rotor as told in the previous section. It is shown in Figure 4.9.

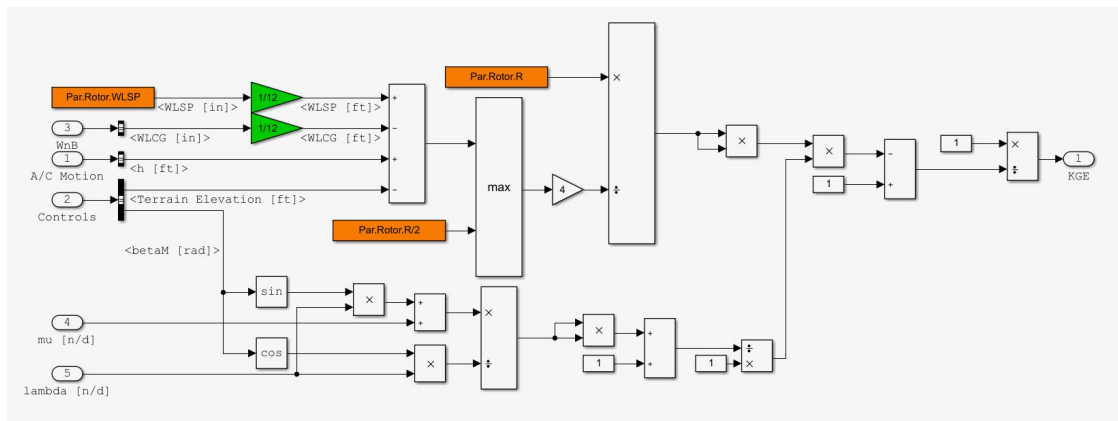


Figure 4.9: Ground Effect Model in Simulink

Ground Effect Results

By calculating the trim point in different flight conditions, it is possible to notice that the behaviour is the one expected:

- $K_{GE} \downarrow$ when the TAS \uparrow , and at 40 kts $K_{GE} \simeq 1$, as expected in Ref. [6];
- $K_{GE} \downarrow$ when $h_M \uparrow$;
- $K_{GE} \downarrow$ when $\beta_M \uparrow$.

In Figure 4.10, it is possible to compare trim points IGE and OGE with flight conditions of test A003, specified in Table 3.1.

⁴ It is measured from the aircraft c.g..

⁵ ZHAW-Polito model has the inflow model proposed by Pitt and Peters, which has three states.

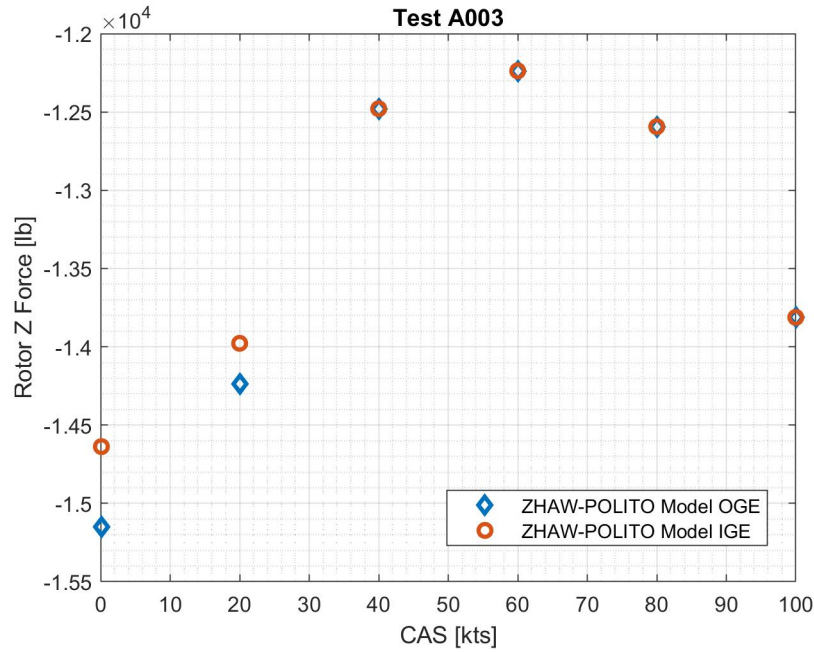


Figure 4.10: Rotor Thrust IGE and OGE

The plot shows that the ground effect is negligible for an airspeed greater than 40 kts. Comparing the rotor thrust reduction in hover and at sea level of the tilt-rotor with the maximum expected for a helicopter in Figure 4.2, it is possible to notice that it is smaller: the reason is simple since the rotor radius of a tilt-rotor is smaller than a helicopter's one, therefore, for a tilt-rotor the ratio z/R is higher, resulting in a reduction of ground effect coefficient.

Lastly, the ground effect also impacts the analysis of the eigenvalues. For instance, let's consider a hover condition: a summary of eigenvalues is shown in Table 4.1.

Table 4.1: Eigenvalues Comparison in Hover and IGE

ZHAW-POLITO IGE	Padfield	Celi	Flight Test
$0.17571 \pm 0.43174i$	$0.1471 \pm 0.4208i$	$0.1483 \pm 0.4616i$	$0.2681 \pm 0.5132i$
$0.08483 \pm 0.28437i$	$0.1356 \pm 0i$	$0.0579 \pm 0.2321i$	$0.1868 \pm 0.4061i$
$-0.097783 \pm 0.67609i$	$0.0064 \pm 0.3120i$	$-0.0033 + 0i$	$0 + 0i$
		$0 + 0i$	$0 + 0i$
$-0.13659 + 0i$	$-0.681 + 0i$	$-0.1312 + 0i$	$-0.102 + 0i$
$-0.5611 + 0i$	$-0.7904 + 0i$	$-0.7892 + 0i$	$-1.23 + 0i$
$-0.60038 + 0i$	$-1.1426 + 0i$	$-1.1861 + 0i$	$-1.32 + 0i$

This confirms the consideration made in Section 3.4: to compare the eigenvalues is important to know if they are calculated IGE or OGE.

4.2 SIDE-BY-SIDE EFFECT

Another effect that was not considered in the model is the side-by-side: it is the mutual interference between the two rotors, which results in an additional term to the inflow.

This time GTRS model was helpful since it provides an expression for the additional induced velocity due to side-by-side in Ref. [6] that was suitable also for Pitt and Peters inflow model:

$$\Delta V_{iss} = X_{SS} \frac{\Omega R C_T}{2B^2\mu} \quad (4.10)$$

ΔV_{iss} is the extra-induced velocity term added to the induced velocity. It depends on rotor radius R , the rotational speed of the rotors Ω , the thrust coefficient C_T , the advance ratio μ , and the blade tip loss factor B . All the expression is multiplied for the mutual induction coefficient X_{SS} , which depends on the advance ratio, and it is provided in a table from Ref. [6].

Implementing this expression in Simulink, it turned out that the model went into an algebraic loop due to the thrust coefficient's presence. To solve this, it is possible to add both rotors' thrust coefficient to the states' matrix, but this was not changed for lack of time.

Another possibility is supplied from a NASA paper in Ref. [33], which use a constant coefficient of $\simeq 0.98$ that divides the induced velocity. The model seemed too simple since the coefficient is constant for all flight conditions and depends only on the ratio⁶ $b/(2R)$. Moreover, comparing hover cases between this solution and the GTRS model, it turned out that they give different results. Therefore, it was decided not to implement it.

It was not possible to found other data in literature. Even Ref. [33] confirms this lack since the mutual effect of the rotors is a problem that is not studied enough, being typical only for the tilt-rotor.

4.3 LANDING GEAR DRAG

The landing gear model was already implemented in the ZHAW-Polito simulator. It is a homemade model, and therefore, it is different from the one provided in Ref. [6]. This model allows the calculation of both main and nose gear's compression due to the touch with the ground, but the drag was not implemented yet.

To aim this, one from the landing gear drag models provided in Ref. [6] was used by the author. Indeed, it suggests two ways to calculate the drag:

- VAX Version: it considers the drag coefficient as a function of the landing gear's extension (0% if it is retracted, 100% if extended). The percentage main and nose gear extension is a function of the present computer frame

⁶ b is the wing-span, while $2R$ is the rotor diameter.

time t , computer cycle time Δt and total time for the landing gear to extend T_{DN} or retract T_{UP} ;

- Sigma 8 Version: it considers the drag coefficient as a function of the cycle time of extension and retraction, but it provides different drag coefficients for the two cases.

Considering that the position of the gear has to be decided a priori since trim points are static, and that with the simulator is possible to command the extension of the gear in realtime and that it can manage by itself time, the decision was to use the VAX version, which does not need distinction whether the landing gear is in extension or retraction.

4.3.1 Dynamic Pressure

The first quantity that is calculated is the dynamic pressure, which is the same as the fuselage model:

$$q_F = q_{LG} = \frac{1}{2} \rho V_T^2 \quad (4.11)$$

4.3.2 Landing Gear Drag in Wind Axes

When the dynamic pressure is known, it is possible to calculate the drag for both main and nose:

$$D_{MG} = q_{LG} (D_{0MG} + D_{POD}) \quad (4.12)$$

$$D_{NG} = q_{LG} D_{0NG} \quad (4.13)$$

Where D_{0MG} is the main gear's drag coefficient, and D_{0NG} is the nose's drag coefficient. They both depend on gear extension, as shown in Table 4.2.

Table 4.2: Landing Gear Drag Coefficient

Gear Extension [%]	Nose Gear Drag [ft ²]	Main Gear Drag [ft ²]
0	0	0
10	0.28	1.04
20	0.48	1.38
30	0.5	1.5
40	0.62	1.9
50	0.74	2.26
60	0.82	2.54
70	0.9	2.76
80	0.96	2.92
90	1.0	2.98
100	1.0	3.0

D_{P0D} is the drag coefficient due to the main gear pod, which is different from zero even if the gear is retracted. All coefficients are dimensional, and they are provided in $[ft^2]$ since they come from the wind-tunnel.

Given the drag in wind axes, it is possible to transform it in body axes with the rotation matrix for forces in Equation 2.5, where $\alpha_{LG} = \alpha_F$ and $\beta_{LG} = \beta_F$. Then, it is possible to calculate the moments generated by the forces: the arms are calculated following conventions in Section 2.1.4. Complete equations are provided in Appendix A.

4.4 JET THRUST

The author's last addition was the jet thrust, so the additional thrust due to the engines' jet. A model is supplied in Ref. [6]. However, the rotor model is different, and Ferguson's model was not compatible. Therefore, it was necessary to rearrange it.

4.4.1 Jet Thrust in Wind Axes

The jet thrust, from Ref. [6], can be calculated as:

$$JT_K = K_{JT1} + K_{JT2}HP_{ENG}X_{EK} \quad (4.14)$$

Where $K = L, R$ whether it is the left or right engine.

K_{JT1} is a jet thrust coefficient, function of the total velocity, supplied from the model as a table⁷. K_{JT2} is another jet thrust coefficient with similar characteristics compared to the first. The main difference is in the dimensions: the first one is on $[lb]$, while the second on $[lb/SHP]$. Lastly, X_{EK} is a flag that considers whether the engine is working or not: when $X_{EK} = 1$, the engine is on, while when $X_{EK} = 0$, it is off.

Table 4.3: Jet Thrust Coefficients

V_T [kts]	K_{JT1} [lb]	K_{JT2} [lb/SHP]
0	16	0.084
100	-17	0.063
200	-57	0.045
300	-100	0.030

The two engines are treated separately for generality.

The difference with Ferguson's model was the calculation of HP_{ENG} . It uses a flow-chart to obtain it, but it was necessary to change the calculations since the models were different. Hence, as power was used a table, that provides the

⁷ Both coefficients are shown in Table 4.3.

power in output as a function of the throttle (collective cycle θ_0). The table has data both for XV-15 S/N 703 and S/N 702, but the first set was implemented in the model since they are more conservative. Data is shown in Table 4.4.

Table 4.4: Jet Thrust Horse Power

X_{THK} [deg]	R_{SHP} S/N 703 [SHP]	R_{SHP} S/N 702 [SHP]
42	105	127
45	120	140
50	160	183
55	235	263
60	320	355
65	430	473
70	560	613
75	718	783
80	890	968
85	1070	1160
90	1250	1355
95	1390	1505
100	1520	1645
105	1622	1755

4.4.2 Jet Thrust in Body Axes

The jet thrust previously calculated is in wind axes. Therefore, it has to be transformed into body axes. To aim this, it is necessary to use the mast angle β_M and the lateral mast tilt ϕ_M . This last contribute is not considered by Ferguson. However, it was added in the ZHAW-Polito model for further precision, which can be important, especially if one engine is off or in a maneuver or lateral flight.

The transformations for right and left engines are different for the force along Y and they are presented in the following equations:

$$X_{JTR} = JT_R \sin \beta_M \quad (4.15)$$

$$Y_{JTR} = JT_R \sin \phi_M \quad (4.16)$$

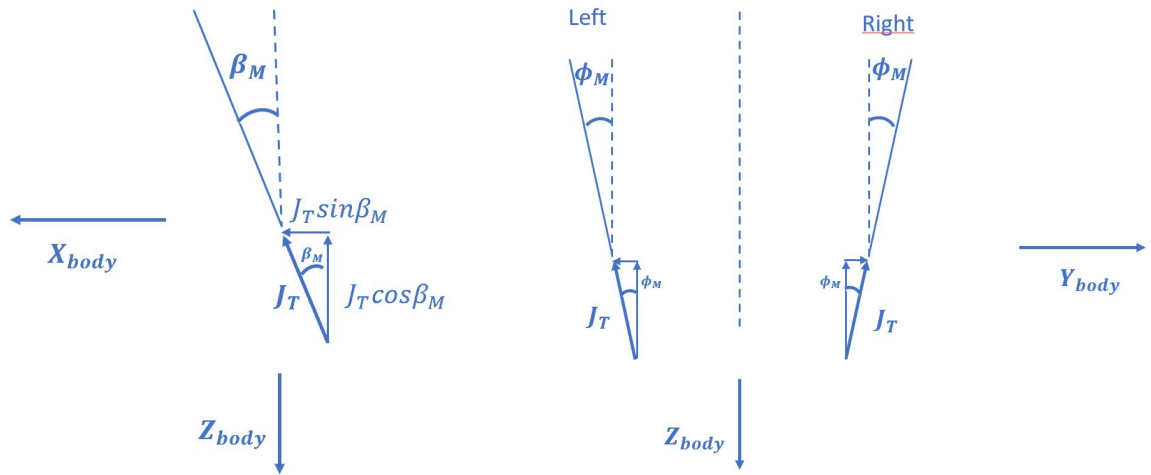
$$Z_{JTR} = -JT_R \cos \beta_M \cos \phi_M \quad (4.17)$$

$$X_{JTL} = JT_L \sin \beta_M \quad (4.18)$$

$$Y_{JTL} = -JT_L \sin \phi_M \quad (4.19)$$

$$Z_{JTL} = -JT_L \cos \beta_M \cos \phi_M \quad (4.20)$$

In order to find the rotation matrix used in these equations, it is possible to refer to Figure 4.11.



(a) Jet Thrust in the Longitudinal Plane (b) Jet Thrust in the Lateral-Directional Plane

Figure 4.11: Jet Thrust Transformation from Wind into Body Axes

Rotations due to β_M generate the following matrix⁸:

$$[R_{\beta_M}] = \begin{bmatrix} \sin \beta_M & 0 & 0 \\ 0 & 1 & 0 \\ 0 & 0 & -\cos \beta_M \end{bmatrix} \quad (4.21)$$

Rotations due to ϕ_M generate the following matrix for the right⁹ engine:

$$[R_{\phi_M}] = \begin{bmatrix} 1 & 0 & 0 \\ 0 & \sin \phi_M & 0 \\ 0 & 0 & \cos \phi_M \end{bmatrix} \quad (4.22)$$

By multiplying these matrices, it comes out the complete rotation matrix for the right engine¹⁰:

$$[R_{JTR}] = [R_{\beta_M}] \cdot [R_{\phi_M}] = \begin{bmatrix} \sin \beta_M & 0 & 0 \\ 0 & \sin \phi_M & 0 \\ 0 & 0 & -\cos \beta_M \cos \phi_M \end{bmatrix} \quad (4.23)$$

Given the forces in body axes, it is possible to calculate the moments due to jet thrust. Complete equations are provided in Appendix A.

⁸ The minus in $\cos \beta_M$ is necessary since $Z - Body$ is positive downward.

⁹ For the left rotor, the second row, which describes the rotation along Y , is changed of sign since the tilt is in the opposite direction.

¹⁰ Like for $[R_{\phi_M}]$, the second row is changed of sign for the left engine

5 | SIMULATIONS AND RESULTS

At the end of the validation process, it was important to assess whether the modifications, previously explained, also improved the flight simulation of the XV-15. To aim this, some proves were conducted at the ReDSim simulator of the ZAV Centre for Aviation of ZHAW with the pilot Davide Guscetti. This activity took place on 17th November 2020.

5.1 GENERAL CONSIDERATIONS

Before starting with the tests, it is important to point some critical issues:

- the pilot involved in the activity is not a test pilot. He has ever had any real experience piloting tilt-rotor aircraft. However, he has already tried the XV-15 at the ReDSim in some previous Master Thesis works at ZHAW and he had some time to try the tilt-rotor before starting with the tests;
- the ReDSim cockpit is not thought for a tilt-rotor. Therefore, the visual and reference points are not optimized for this aircraft. As it will be explained later, this brought some issues during the tests;
- the number of tests was heavily conditioned by the limited availability of the pilots and the ReDSim due to the current sanitary emergency.

There was a co-operation between the pilot and the author during the tests. The first was asked to give feedback during the tests to acquire them and point out the updated simulation model's weaknesses and strengths. This information is collected in flight test cards, which are provided in Appendix D. At the end of any test, the pilot had to assess the level of handling-qualities of the simulated aircraft with the Cooper-Harper rating scale, designed by NASA in Ref. [34] and shown in Figure 5.1.

Besides, during the simulation, it is possible to obtain the data for various quantities (commands, rotors, aerodynamics), which are useful for assessing whether the feedback and the pilot's feeling were correct or not and to analyze the issues that may occur during the tests.

5.2 PILOT-IN-THE-LOOP TESTS

The tests were made both in helicopter mode and in conversion mode. Tests in helicopter mode were taken from Ref. [35], and the choice fell on:

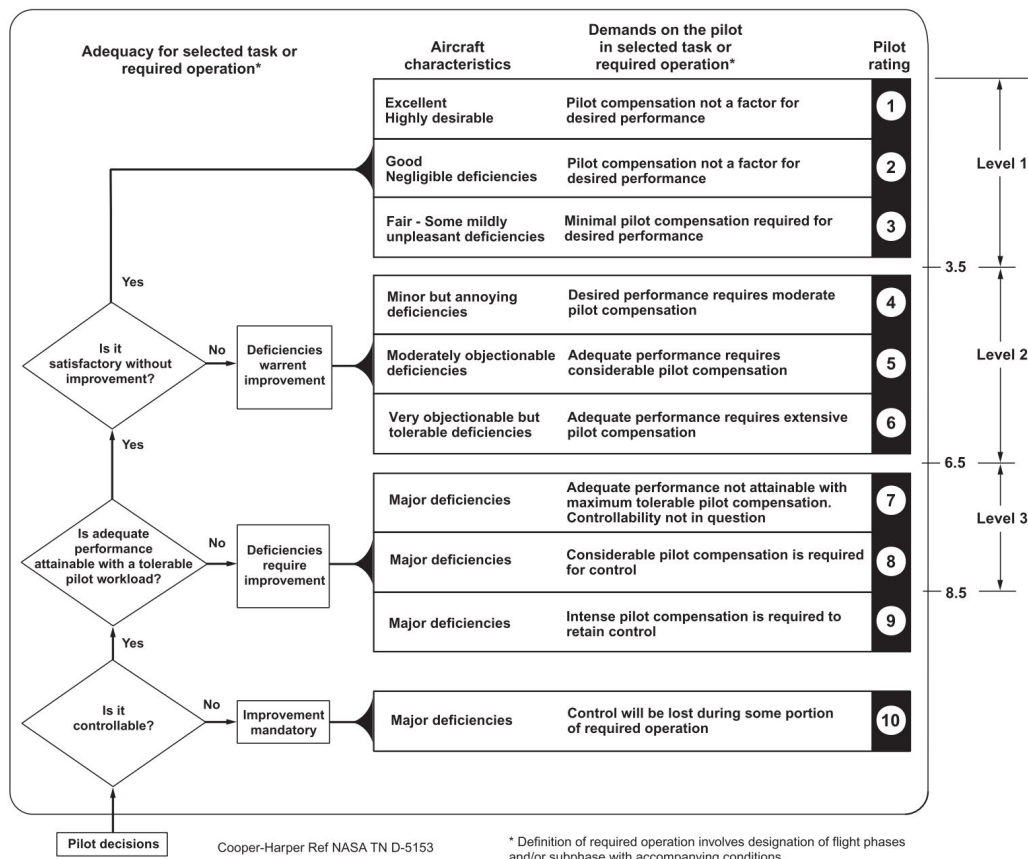


Figure 5.1: Cooper-Harper Rating Scale, Ref. [35]

- Pirouette
- Vertical Maneuver
- Depart/Abort

These tests were chosen because they were usually used to assess the improvement of the XV-15 tilt-rotor simulator in the previous master thesis works. Therefore, it could be possible for the pilot to compare these tests with the previous ones to have a more accurate overview.

Ref. [35] does not supply tests for the conversion and no information about the right way to do it was found in literature. Hence, the pilot made the conversion trying to stay inside of the conversion corridor of the XV-15 tilt-rotor, which is shown in Figure 5.2.

Before starting with the tests, the pilot had some time to familiarize himself with the aircraft: during this time, he gave some feedback, and at first, it seemed that the tilt-rotor was much more stable in yaw and hover. The fact that yaw stability was better gave some important information about the vertical stabilizer's modifications, suggesting their correctness. Moreover, the pilot said that a few months before, the aircraft was stable like that just with SCAS-ON.

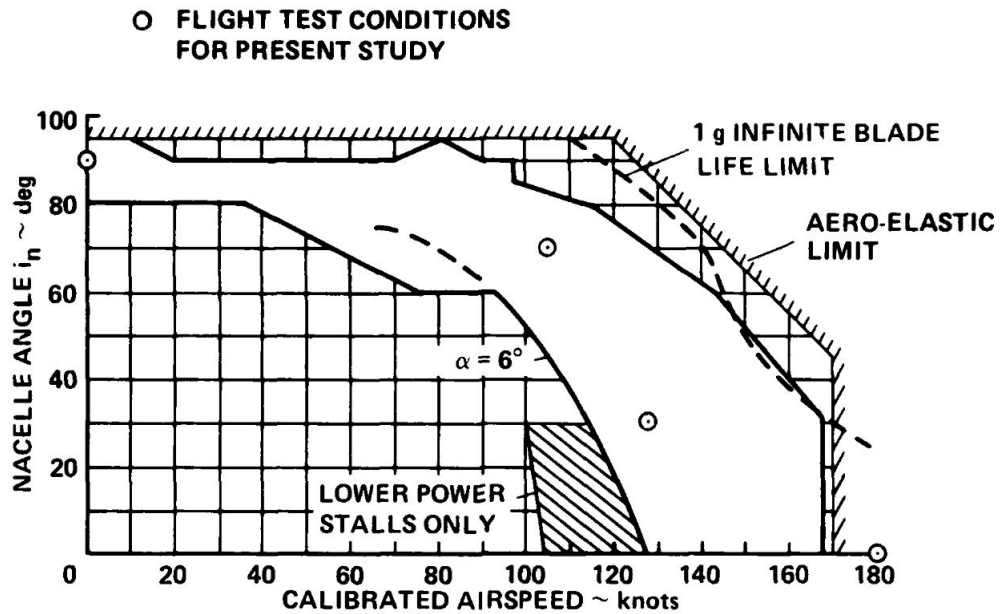


Figure 5.2: Conversion Corridor for XV-15 Tilt-Rotor, Ref. [36]

5.2.1 Helicopter Mode

As told in the previous section, the first part of the tests was made in helicopter mode and tasks were taken from Ref. [35].

For each test, the reference provides some standards, which aim is to suggest whether the aircraft succeeded or not in a particular attempt. Standards are divided into Good Visual Condition (GVE) and Degraded Visual Condition (DVE). Generally, GVE means clear daylight with good cueing and unaided vision. In contrast, DVE means a night with some illumination level (moon and overcast) while using the actual mission equipment vision aid. Since the cockpit is not optimized for the tilt-rotor, the DVE data will be used to evaluate the performance. Both GVE and DVE standards are then divided into desired and adequate performance. Therefore, the aim is to respect DVE **standards** for the **desired performance**.

Every test was tried more than once for several reasons:

- the pilot did need some trial to learn the maneuver involved and to learn reference points;
- it is possible than one attempt is not good for a human mistake;
- to have as many feedback as possible.

PIROUETTE

The first test was the Pirouette, which preparation is shown in Figure 5.3.

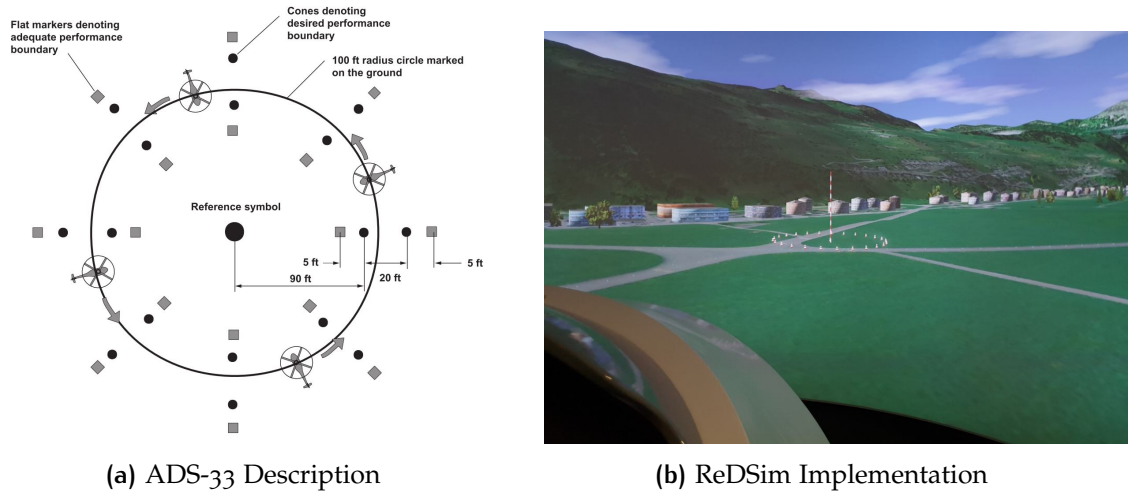


Figure 5.3: Pirouette Task Preparation

Task Description

The maneuver has to start from a stabilized hover over a point on the circumference of a 100 ft radius circle and at a hovering altitude of approximately 10 ft. The pilot shall accomplish a lateral translation around the circle, keeping the rotor-craft's nose pointed at the centre of the circle and the circle's circumference under a selected reference point on the rotor-craft. The lateral ground-speed has to be maintained essentially constant during the lateral translation. The maneuver shall finish with a stabilized hover over the starting point.

Task Standards

They are shown in Table 5.1.

Table 5.1: DVE Performance Standards for the Pirouette, Ref. [35]

Performance Request	Desired	Adequate
Maintain a selected reference point on the rotor-craft within $\pm X$ ft of the circumference of the circle	10	15
Maintain altitude within $\pm X$ ft	4	10
Maintain heading so that the nose of the rotor-craft points at the center of the circle within $\pm X$ deg	10	15
Complete the circle and arrive back over the starting point within [sec]	60	75
Achieve a stabilized hover (within desired hover reference point) within X seconds after returning to the starting point	10	20
Maintain the stabilized hover for X [sec]	5	5

Task Results

The best attempt results are shown in figures from Figure 5.4 to Figure 5.6.

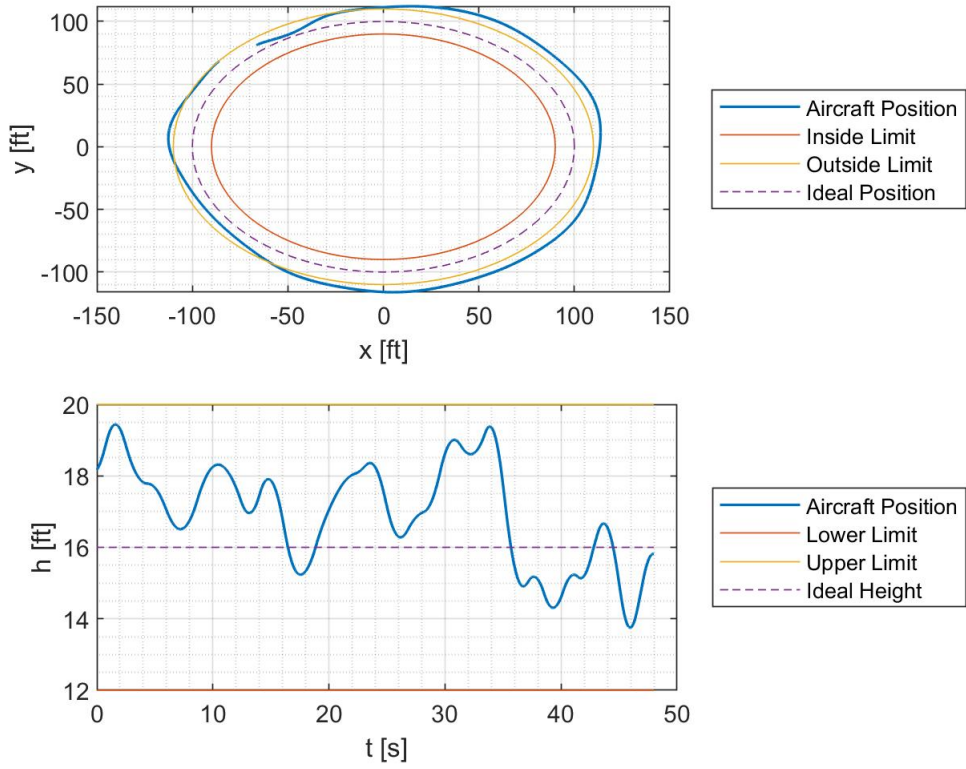


Figure 5.4: Height and Position During Pirouette

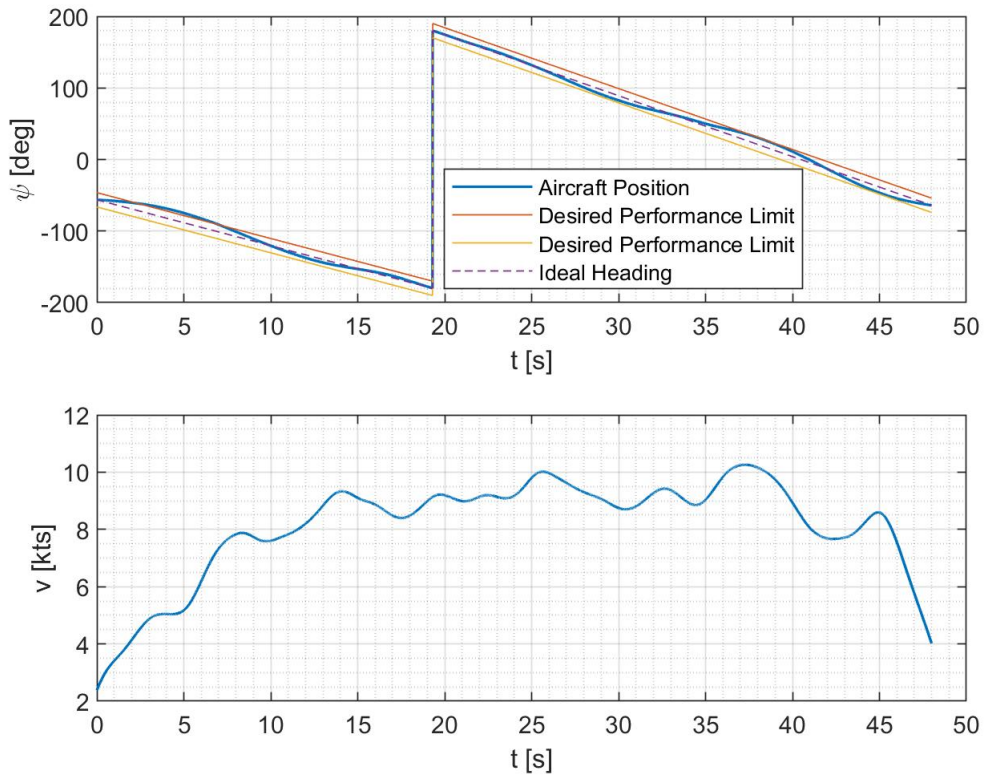


Figure 5.5: Heading and Lateral Velocity During Pirouette

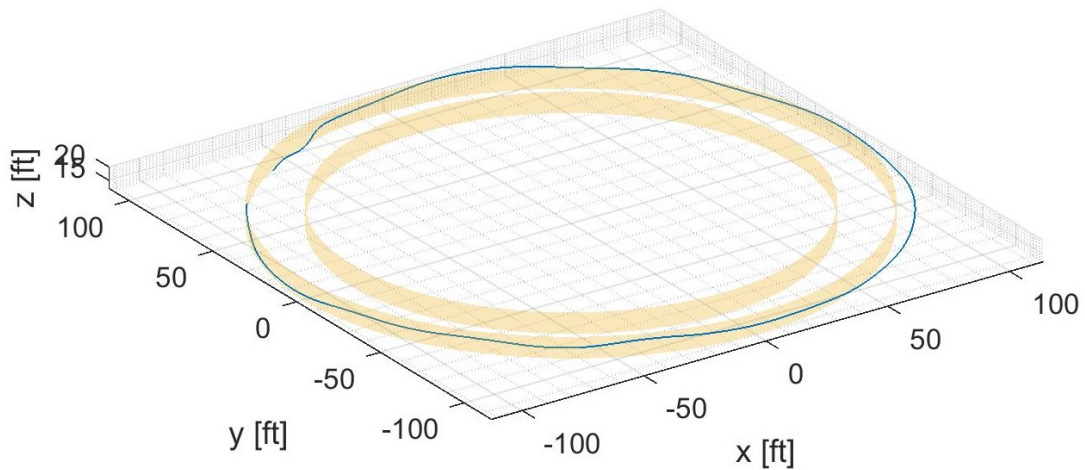


Figure 5.6: 3D Position During Pirouette

Figure 5.6 shows the 3D position of the aircraft during the pirouette. In Figure 5.4, there is the detail of the position in the xy -plane and the height. The pilot followed almost perfectly the external circumference and respected the height limitations. Due to very bad reference points from the cockpit, the pilot could not use a height of 10 ft as suggested from ADS-33 since cones were hidden. Therefore, he needed to stay higher to have a better reference. The same reason also explains the difficulty of following a circumference of 100 ft since the pilot should have stayed above the cones, following them on the side. However, due to the bad reference, he could not see them, and he had to stay back to have a better one.

In Figure 5.5, it is possible to see that the pilot could respect the heading limitations. In fact, he noticed that yaw was really better. Moreover, the pilot could keep an almost constant lateral speed during the maneuver¹, and he respected the limit time of 60 s, being able to complete the task in 48 s. Lastly, he stabilized the aircraft in hover almost immediately when the maneuver was finished.

Other Attempts and Pilot Considerations

During the simulation, the pilot tried the maneuver several times, both in the clockwise and anticlockwise direction. Not all the attempts were good: at the beginning, he had to gain confidence with the maneuver and with reference points, but he noticed that the aircraft was more controllable, and for this reason, he could move slower during the maneuver. He had much more difficulties during clockwise attempts since he had to move on the opposite side from his location, and he could not follow the cones. Given that the maneuver was successful anticlockwise, there is no other reason for the clockwise maneuver's failure, apart from the bad references. Following the Cooper-Harper Rating Scale, the final evaluation was 3, which corresponds to the **handling-qualities first-level**. All the flight test cards are provided in Appendix D.

¹ Except for the begin and the end of the maneuver.

VERTICAL MANEUVER

The second task tried during the simulations was the vertical maneuver. The preparation suggested by Ref. [35] is shown in Figure 5.7.

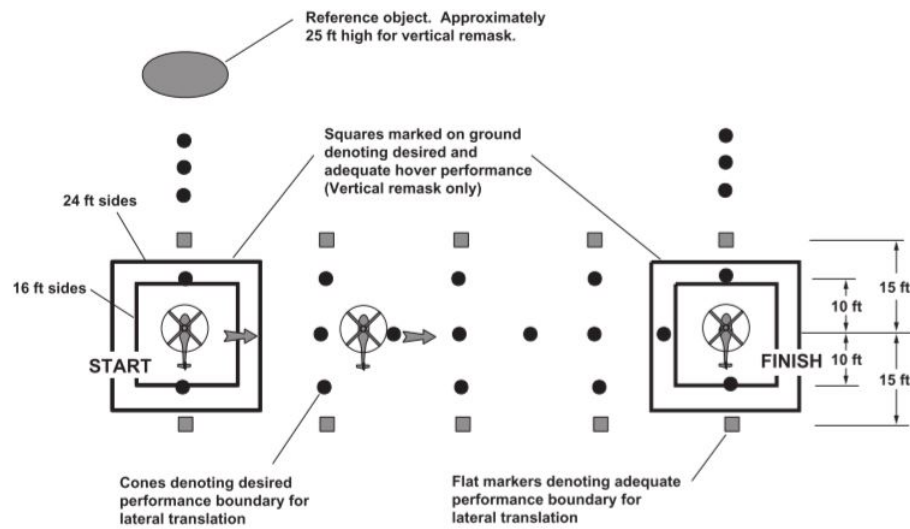


Figure 5.7: Vertical Maneuver Task Preparation

Task Description

The pilot shall initiate a vertical ascent of 25 ft from a stabilized hover at an altitude of 15 ft. When the ascent is complete, the pilot should stabilize the aircraft for 2 seconds. Then he should descend back to the initial hover position.

Task Standards

They are shown in Table 5.2. Unlike the pirouette, there is also a further difference in the standards, which depends on the aircraft category. The table refers to a scout/attack aircraft.

Table 5.2: DVE Performance Standards for the Vertical Maneuver, Ref. [35]

Performance Request	Desired	Adequate
Maintain the longitudinal and lateral position within $\pm X$ ft of a point on the ground	10	20
Maintain start/finish altitude within $\pm X$ ft	3	6
Maintain heading within $\pm X$ deg	3	6
Complete the maneuver within [sec]	13	18

Task Results

Results of the best attempt are shown in Figure 5.8 and 5.9.

Figure 5.8 shows that the pilot was able to respect limitations in the longitudinal and lateral position, while Figure 5.9 also shows that the heading was within

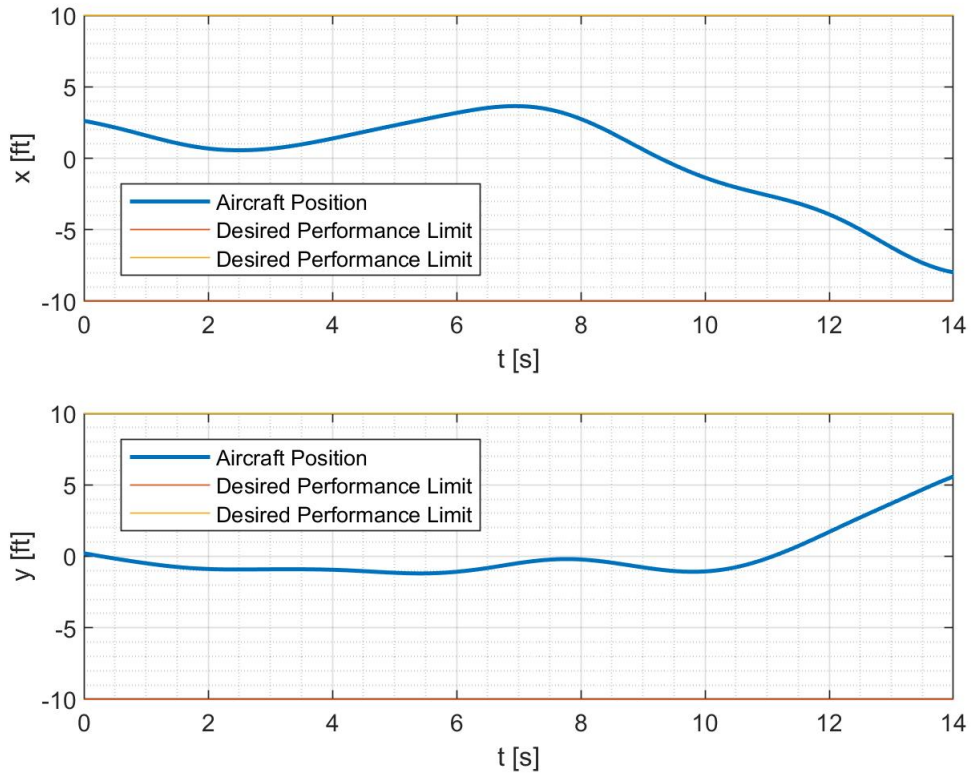


Figure 5.8: Aircraft Position During Vertical Maneuver

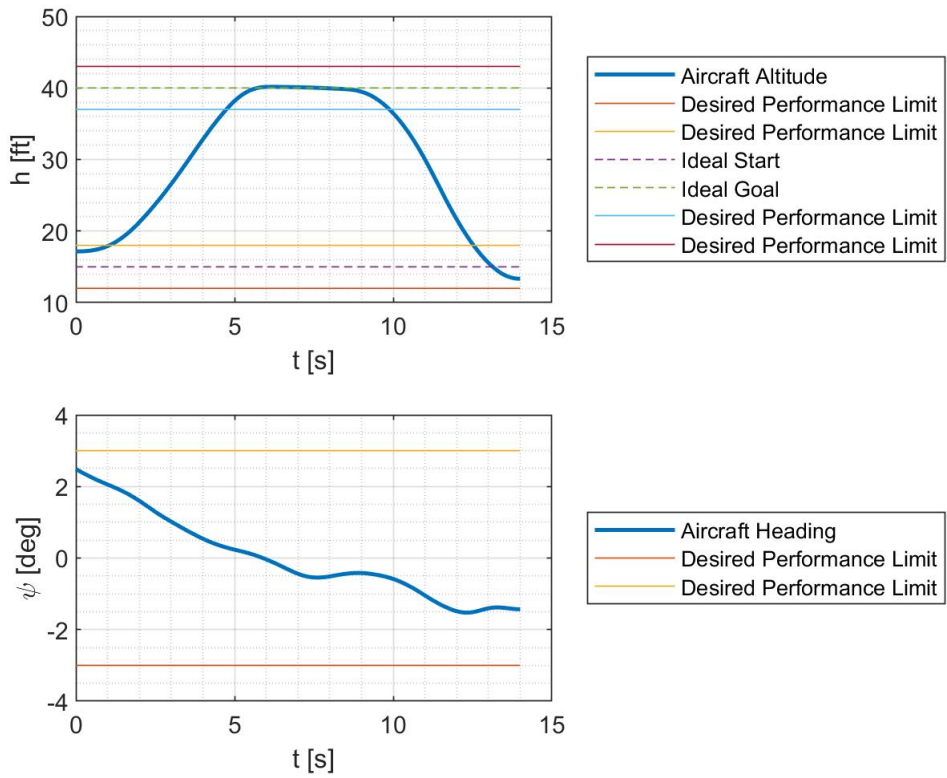


Figure 5.9: Aircraft Height and Heading During Vertical Maneuver

the limits. The height was respected both during the hover and at the maximum altitude. The peak's hover lasted slightly longer than 2 s, but it was perfectly at 40 ft since the pilot had a good reference point. The maneuver lasted $\simeq 14$ s, but actually, it was shorter since both at the beginning and the end, it is at a constant altitude. The pilot was able to stabilize in a hover at the end of the task. In conclusion, the pilot succeeded in this task.

Other Attempts and Pilot Considerations

The pilot tried the maneuver four times since it was easy and the aircraft was well controllable, especially in yaw. Furthermore, the pilot was able to identify the best attempt. He evaluated 2 in the Cooper-Harper rating scale, which corresponds to the **handling-qualities first level**. Complete flight test cards are provided in Appendix D.

DEPART/ABORT

The last maneuver tried in helicopter mode was the depart/abort. The preparation suggested from Ref. [35] is shown in Figure 5.10.

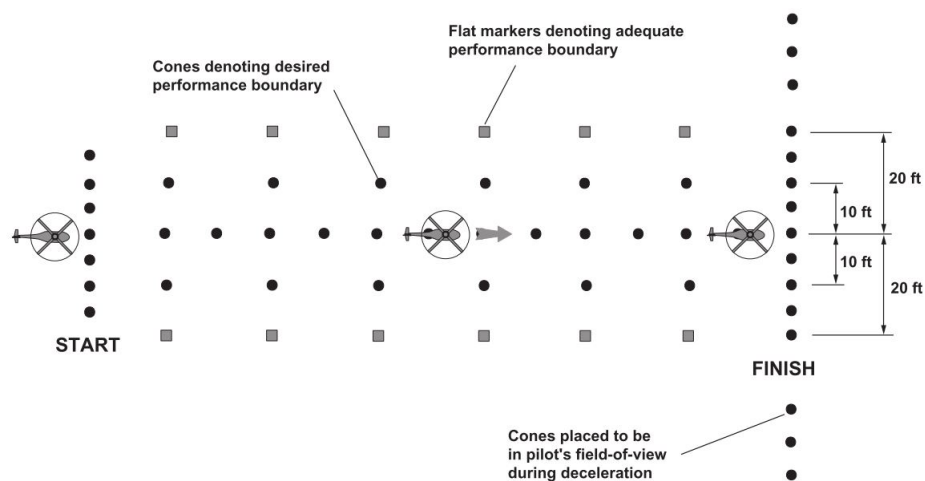


Figure 5.10: Depart/Abort Task Preparation

Task Description

The maneuver should start from a stabilized hover at 35 ft wheel height and 800 ft from the intended endpoint. The pilot shall initiate a longitudinal acceleration to perform a normal departure and shall abort the departure and decelerate to a hover after reaching a ground-speed of 40/50 kts. At the manoeuvre's termination, the cockpit shall be within 20 ft of the intended endpoint. It is not allowed to overshoot the intended endpoint and move back. The maneuver is not complete until it is within 20 ft of the intended endpoint, even if the aircraft stops shorter. The acceleration and deceleration phases shall be accomplished in a single smooth maneuver, and the maneuver is complete when the pilot is able to maintain a stable hover.

Task Standards

They are shown in Table 5.3.

Table 5.3: DVE Performance Standards for the Depart/Abort, Ref. [35]

Performance Request	Desired	Adequate
Maintain lateral track within $\pm X$ ft of a point on the ground	10	20
Maintain radar altitude below [ft]	50	75
Maintain heading within $\pm X$ deg	10	15
Time to complete maneuver [sec]	25	30

Task Results

Results of the best attempt are shown in Figure 5.11 and 5.12.

Figure 5.12 shows that both height and heading limitations were respected during the maneuver, unlike the lateral track shown in Figure 5.11. In fact, the pilot complained about the lack of reference points during the maneuver. Therefore, he had many difficulties in respecting the lateral track. The results show that his sensation was right. The maneuver was completed within 25 s, and Figure 5.11 shows that the deceleration started when the speed was about 50 kts. The maneuver was longer than 800 ft due to bad reference points.

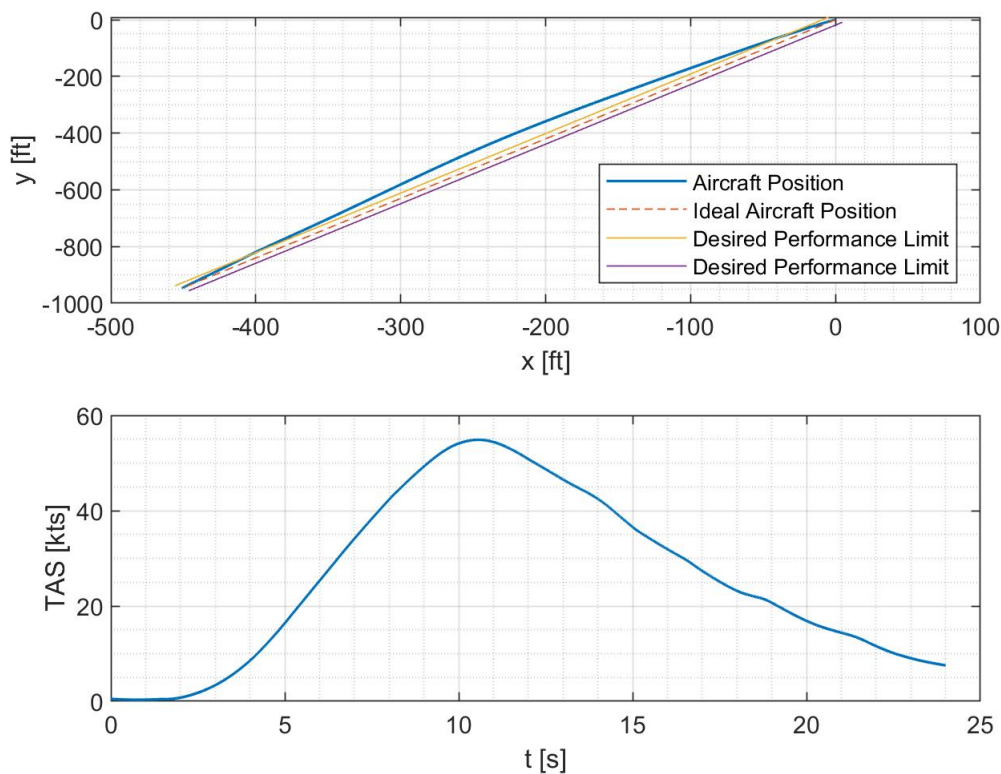


Figure 5.11: Aircraft Position During Depart/Abort

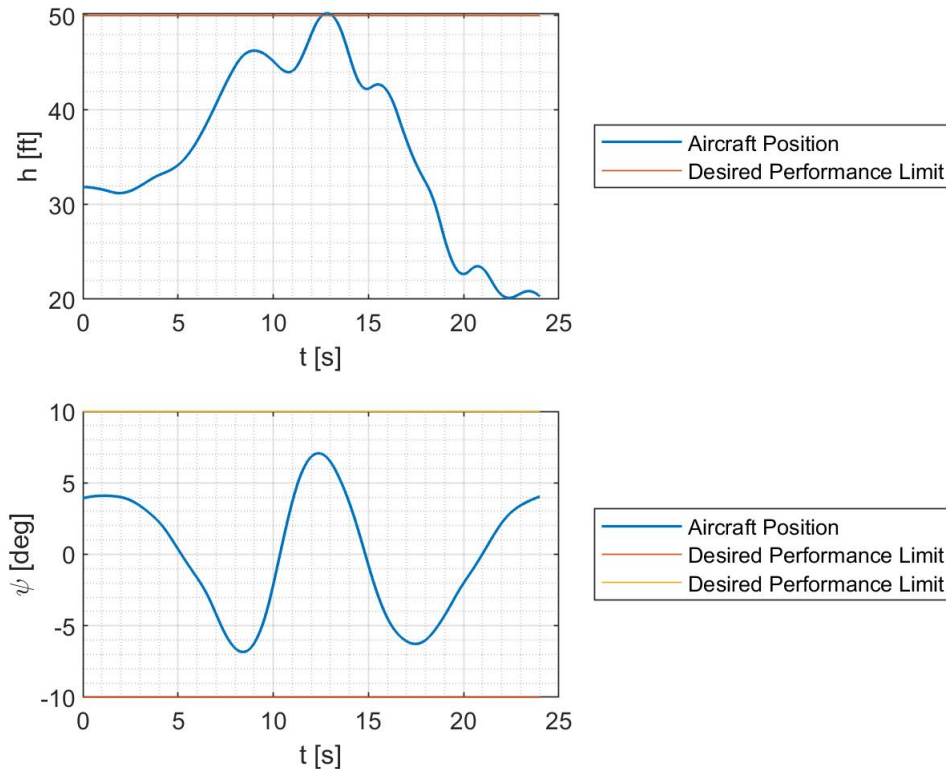


Figure 5.12: Aircraft Heading and Height During Depart/Abort

Other Attempts and Pilot Considerations

The pilot tried the maneuver several times, complaining about very bad reference points, which did not allow good attempts. Moreover, he also had to control the height using the radar, which distracted him from following the track. However, he noticed a great improvement in the aircraft's stability and controllability during the maneuver since the last time: his final comments were "**it flights very well**" and "**this maneuver can be done really well**". The final evaluation following the Cooper-Harper rating scale was **2**, which is another time in the *handling-qualities first-level*. Complete flight test cards are provided in Appendix D.

5.2.2 Conversion Mode

After accomplishing the helicopter mode task, the following step was the conversion attempt.

As told in the previous section, there were no reports in literature about the correct procedure for the conversion. Therefore, the pilot tried it with the conversion corridor as the only constraint.

During the helicopter mode flight, the pilot noticed that the ascent/descent ratio was better, and the manoeuvrability at higher speeds was improved.

Furthermore, he noticed some oscillation in pitch when an airspeed of $\simeq 70$ kts is reached, as shown in Figure 5.13, but the aircraft was still maneuverable.

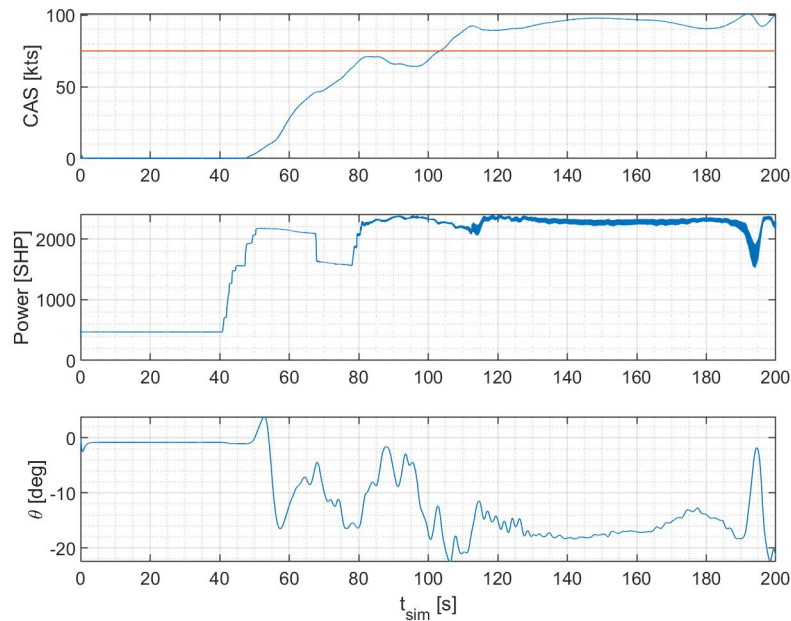


Figure 5.13: Pitch and Power with CAS

This seems to be caused by the problem reported in Ref. [23]: *"In several of these cases, results generally compare quite well at 90 deg nacelle incidence up to a calibrated airspeed of approximately 75 kts. At this airspeed, a strange thing happens in that the mathematical model predicts a strong nose-up pitching moment as the power required also increases dramatically. The XV-15 does not seem to exhibit this trend. At present, this effect is not totally understood, and further investigation will be conducted in an attempt to explain this discrepancy. Indeed, it is possible to see in Figure 5.13 that the increase in power is also shown from the ZHAW-Polito model 500 SHP, which corresponds to $\simeq 30\%$ of the initial value.*

In addition, it is important to highlight a pilot's comment that relates power and pitch. Indeed, he told that the change of power negatively affects the pitch. This feeling seems to be confirmed² in Figure 5.13.

From Helicopter to Airplane Mode

The conversion from helicopter to airplane mode was usually³ successful. An important role was played by flaps, which needed to be lifted to decrease the drag.

During the conversion, the pilot noticed that lowering the nacelles generated a pitching down of the aircraft. Therefore, he needed to correct this behaviour. Moreover, he explained that the *auto-trim* was a disturbance during the conversion since flight conditions change rapidly.

Plots for conversion from helicopter to airplane mode are shown from Figure 5.14 to Figure 5.22. There are shown the following quantities as a function of the simulation time:

² Simulation time from 40 s to 80 s and 180 s to 200 s.

³ When it was not, there were some problems by switching on and off the *auto-trim*.

- **Nacelles Mast Angle:** during the conversion from helicopter to airplane mode, nacelles are lowered, and the mast angle goes from 0° to 90° .

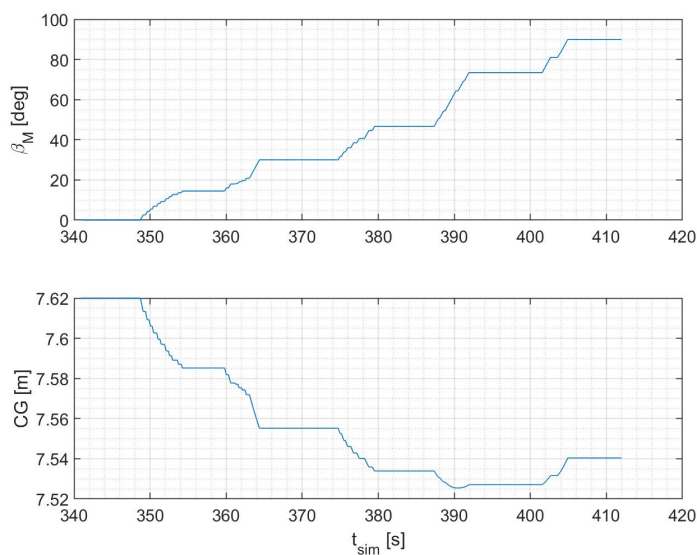


Figure 5.14: Mast Angle and Centre of Gravity in H→A Conversion

- **Centre of Gravity:** the station line of the c.g. is a function of the nacelle angle, indeed lowering or lifting them, their c.g. changes of place and so does the aircraft centre. It is logical to think that the c.g. advances with them, but as shown in Figure 5.14, the aircraft c.g. steps back a little just before ending the conversion. This is not an error, but it is a consequence of the formulas provided in Ref. [6].
- **Conversion Corridor:** as already told, the only constraint was to remain inside the *conversion corridor* during the maneuver. Figure 5.15 shows that the conversion was successful from this point of view.

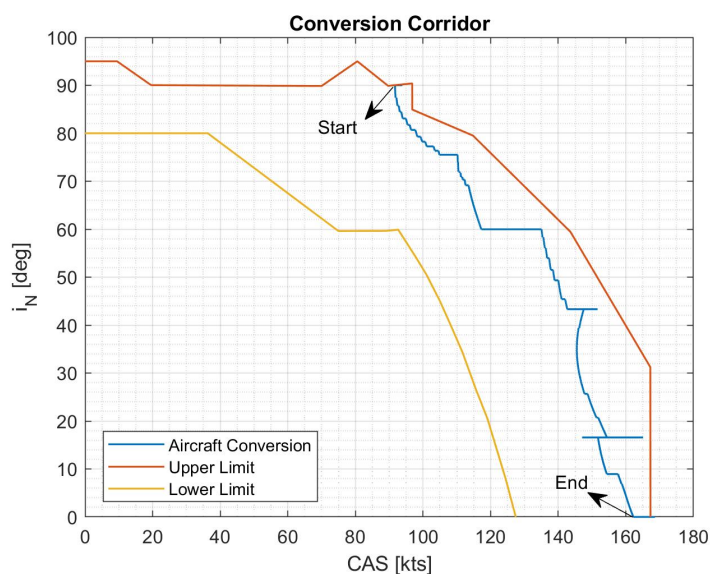


Figure 5.15: Conversion Corridor from Helicopter to Airplane

- Aircraft Commands** During the conversion, the longitudinal stick follows the mast angle trend to balance the pitching down caused by the nacelles lowering. The collective is lowered to avoid the raise of power caused by the increasing speed. Pedal and lateral are almost constant.
- Euler's Angles** In Figure 5.17, it is possible to see that the pitch angle grows: the pilot noticed that during the conversion, the aircraft tend to pitch down, and therefore, he corrected this effect. The yaw angle always tends to grow at the end of the conversion: it is probably due to a coupling with the collective lowering. The roll angle has a strong oscillation at the end: this is caused by a suddenly grow in the sideslip angle (indeed also forces suddenly grow, and the lateral command shows an impulse).

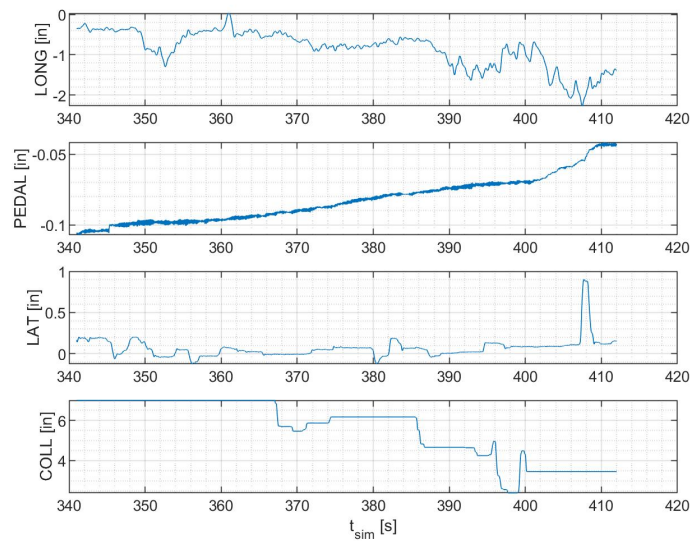


Figure 5.16: Commands in H \rightarrow A Conversion

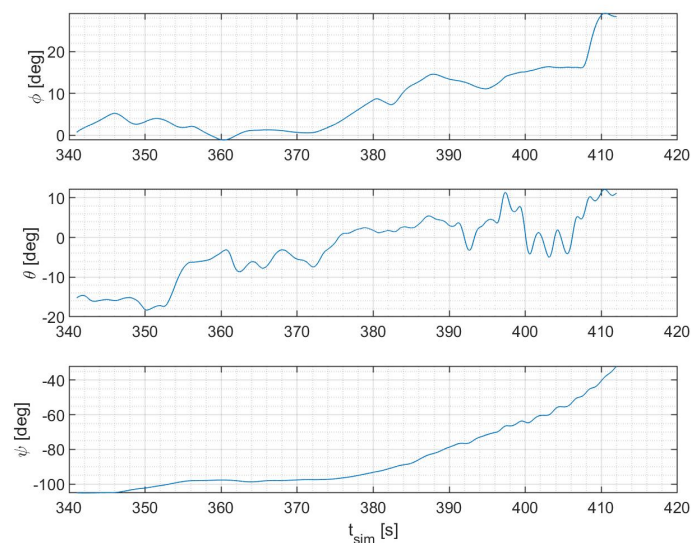


Figure 5.17: Euler's Angles in H \rightarrow A Conversion

- Right Rotor Forces and Moments** The force along X increases because the speed increases, generating more drag, which need to be balanced. Instead, the up-force along Z decreases⁴, since while speed increases, the wing's contribution became predominant: the lift is transferred from the rotor to the wing. This is shown in Figure 5.18 for the right rotor, while the left rotor's behaviour is identical since the flight condition is symmetrical.

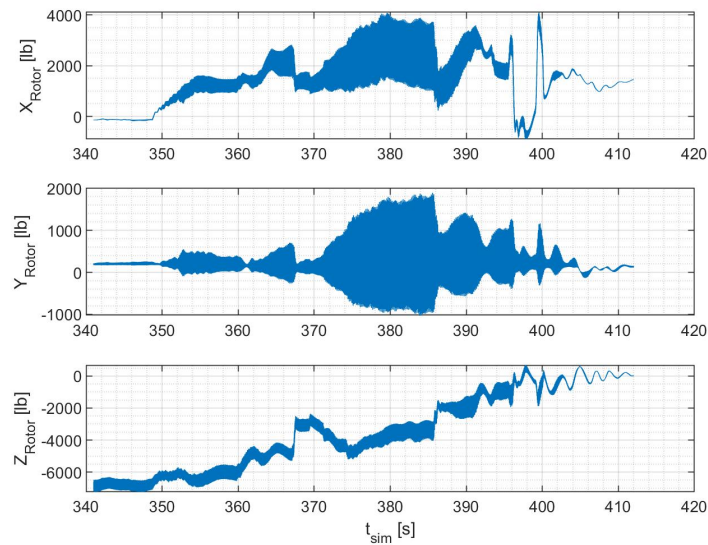


Figure 5.18: Right Rotor Forces in H→A Conversion

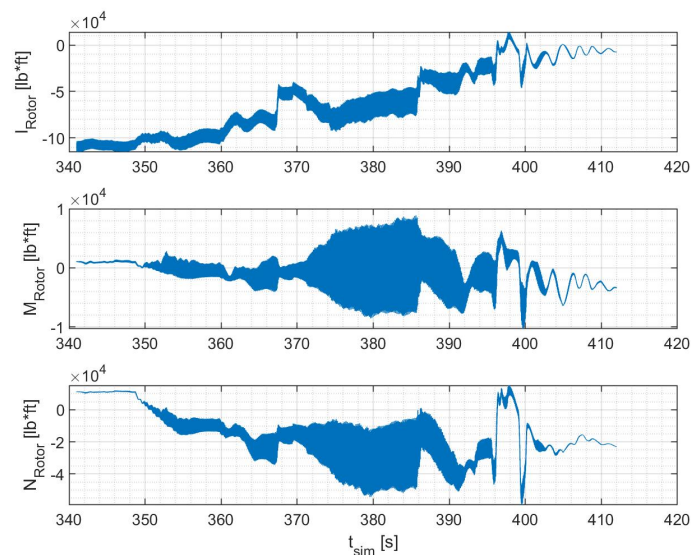


Figure 5.19: Right Rotor Moments in H→A Conversion

- Power** The requested power, Figure 5.20, is almost constant during the conversion since the collective was lowered to aim this. During another

⁴ Note that Z-Body is positive downward, and therefore, the lift generated by the rotor decreases.

conversion, the pilot did not touch the collective. Therefore, the power quickly grew with airspeed⁵.

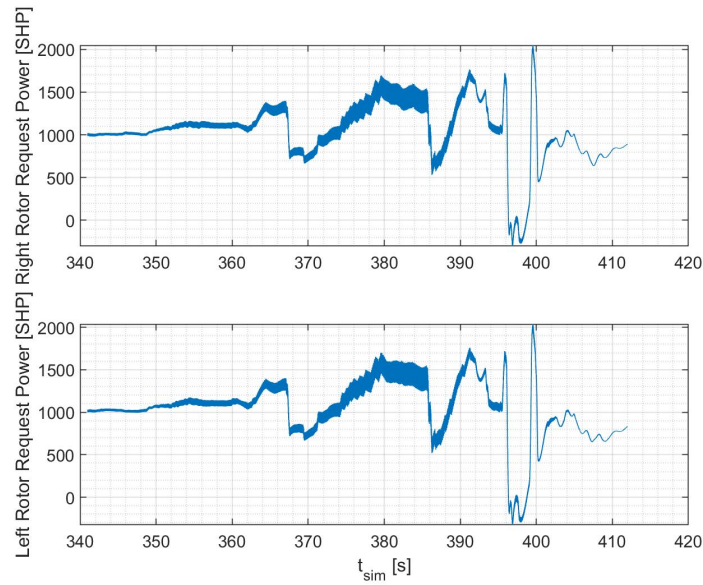


Figure 5.20: Power in H \rightarrow A Conversion

- Aerodynamic Forces and Moments** The force along X is almost constant, while along Z, there is a decrease. The consideration made before for the rotor is still valid, and the lift is transferred from the rotor to the wing while the speed increases, yet there is also an effect of the pitch that grows.

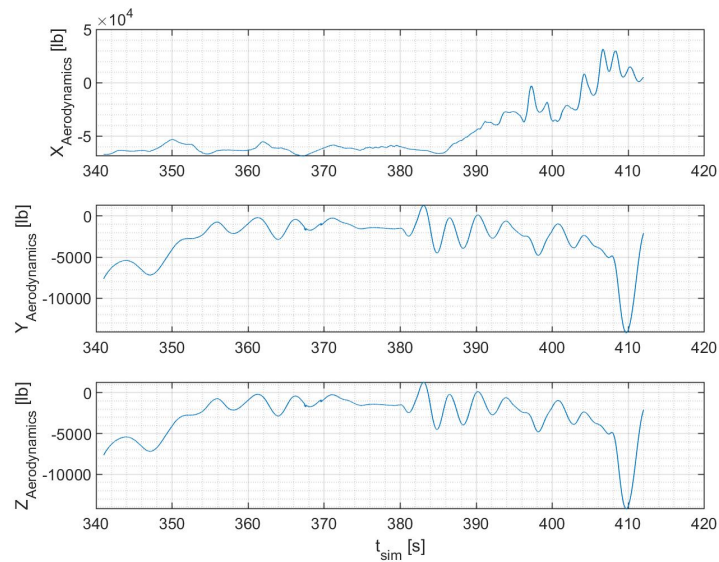


Figure 5.21: Aerodynamic Forces in H \rightarrow A Conversion

⁵ The power is proportional to V^3 .

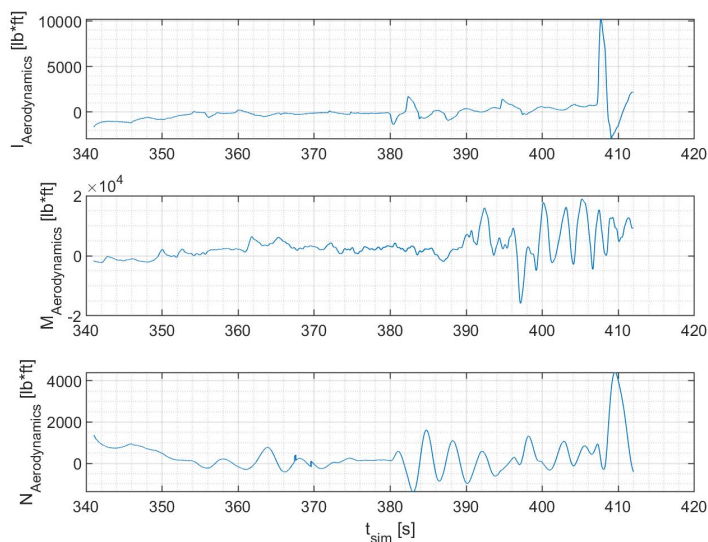


Figure 5.22: Aerodynamic Moments in **H** \rightarrow **A** Conversion

- **Flap Angle** The flaps are lowered in order to decrease the drag. Actually, the effect is an increase in Mach Number instead of a decrease in drag, as shown in Figure 5.23.

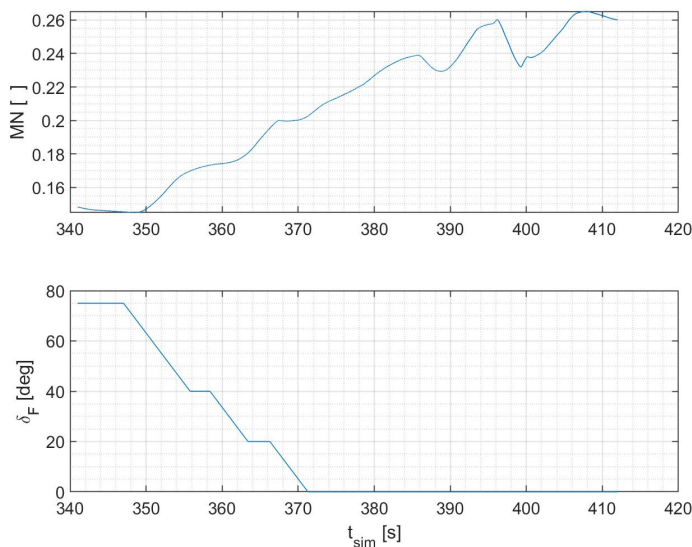


Figure 5.23: Flaps and Mach in **H** \rightarrow **A** Conversion

The evaluation given by the pilot for this conversion was **4/5** following the Cooper-Harper rating scale. The judgment is affected by the fact that the correct conversion procedure is unknown. The critical points highlighted by the pilot were the pitch oscillations and the fact that the aircraft is pitched down in helicopter mode due to auto-trim, while he would prefer to have a pitch up before starting the conversion.

From Airplane to Helicopter Mode

The conversion from airplane to helicopter was a critical task. The pilot tried several times before succeeding, but he converted it twice in a row when he learned the procedure. Some reasons which may have caused the conversion to fail are:

- flaps kept at 0 deg, while they need to be lowered in order to increase the drag and decelerate the aircraft;
- the aircraft went out of the conversion corridor;
- ascent ratio which did not decrease. A possible explanation was the errors left⁶ in the aerodynamic model, which were corrected successively or are still in the model;
- the power did not decrease, despite the raising altitude and the fact that the pilot lowered the collective to the minimum.

Results for a successful conversion are shown from Figure 5.24 to Figure 5.32. The following quantities are shown:

- **Mast Angle** It passes from 90 deg to 0 deg: due to this conversion, the station line of the c.g. grows. This is shown in Figure 5.24.

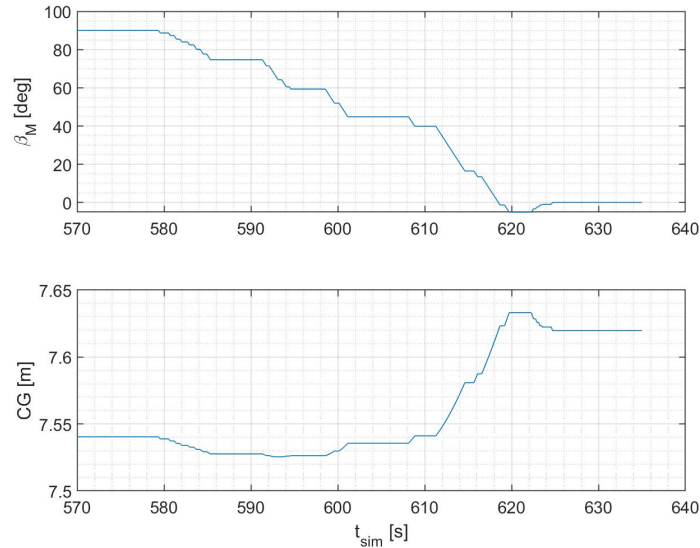


Figure 5.24: Mast Angle and Centre of Gravity in A→H Conversion

- **Conversion Corridor** During the conversion, the pilot tried to follow the conversion corridor. Since it was not displayed, it was not easy to keep the aircraft in that range, indeed Figure 5.25 shows that sometimes the aircraft

⁶ For example, the angle of attack for the wing-pylon was still wrong the day of the simulations, Equation 2.100.

was outside. This may be one reason for failing the conversion on some occasions.

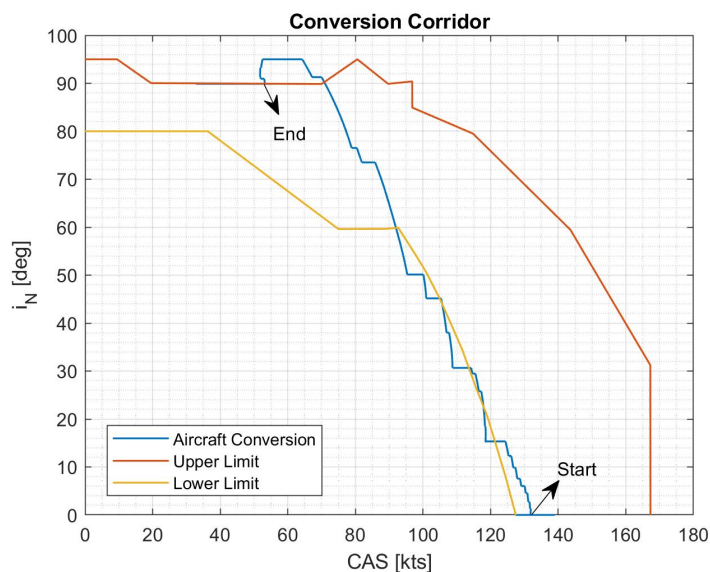


Figure 5.25: Conversion Corridor from Airplane to Helicopter

- **Commands** The collective is always at the minimum because the power needs to decrease during the conversion, Figure 5.26. At the end of the conversion, it was lifted from the pilot. He needed to use the pedal and lateral to control the aircraft due to the coupling.

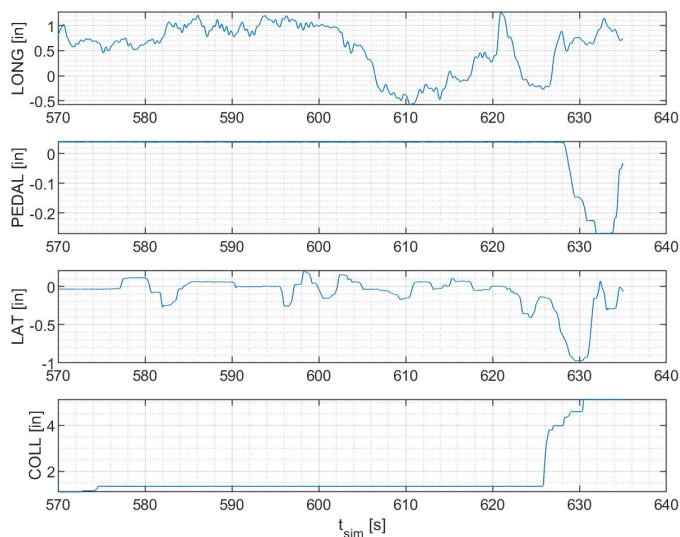


Figure 5.26: Commands in A → H Conversion

- **Euler's Angles** At the end of the conversion, the yaw angle increases due to a coupling with the collective, Figure 5.27. The pilot triggered the pedal to control the aircraft.

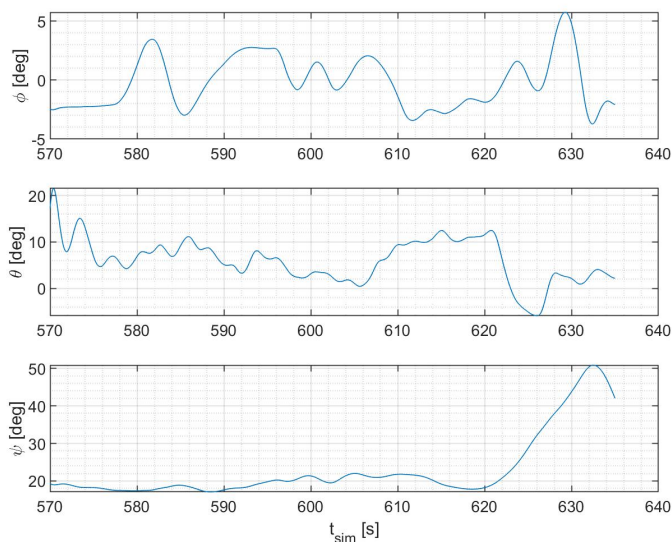


Figure 5.27: Euler's Angles in **A**→**H** Conversion

- Rotor Forces and Moments** Forces along X and Z have an opposite trend than the conversion from helicopter to airplane mode. Since the drag decreases with the airspeed, the rotor generates less force along X , while it generates more force along Z as the lift decreases.

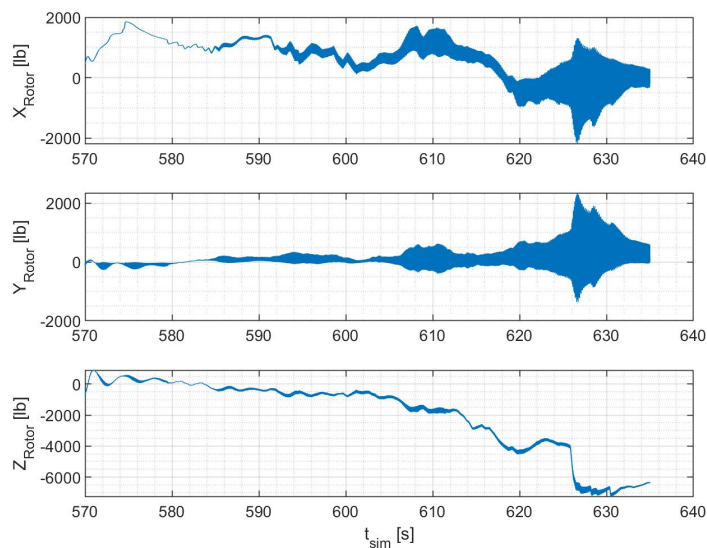


Figure 5.28: Right Rotor Forces in **A**→**H** Conversion

- Power** The power, after an initial increase, decreases with the altitude, Figure 5.30. This was one of the critical issues: even though the collective was at a minimum and the aircraft was climbing, the power sometimes did not decrease as expected, and this may have failed some conversions. At the end of the conversion, the power increases because the pilot raised the collective.

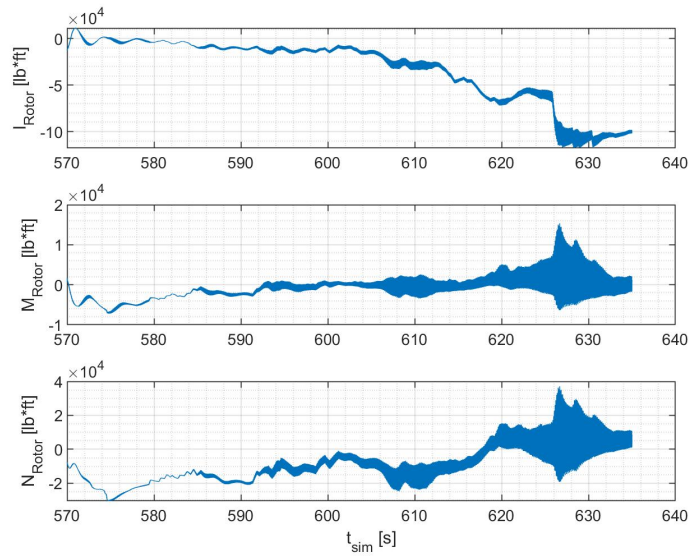


Figure 5.29: Right Rotor Moments in A \rightarrow H Conversion

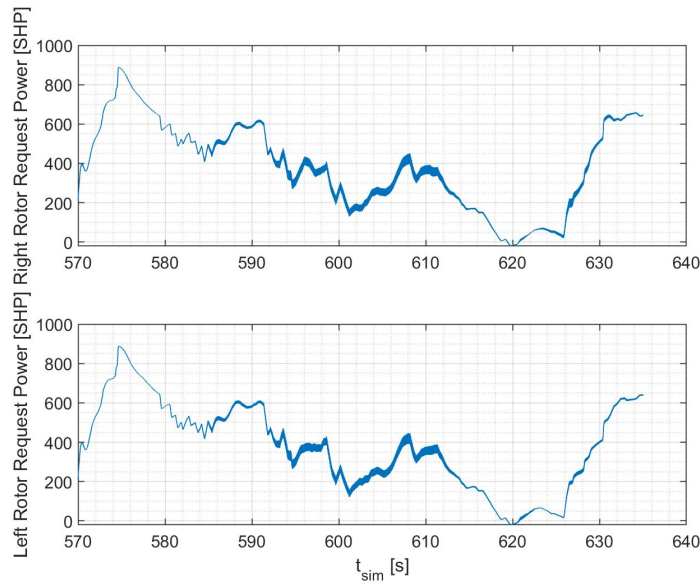


Figure 5.30: Power in A \rightarrow H Conversion

- **Aerodynamic Forces and Moments** Drag and lift decrease with the air-speed and, therefore, during the conversion. Due to the pitch change, this behaviour is not shown in Figure 5.31.
- **Flaps** During the conversion, just one step of flaps was lifted: the result was a decreasing in mach number, Figure 5.33. Before starting the conversion, a flap step was triggered to decrease speed and power.

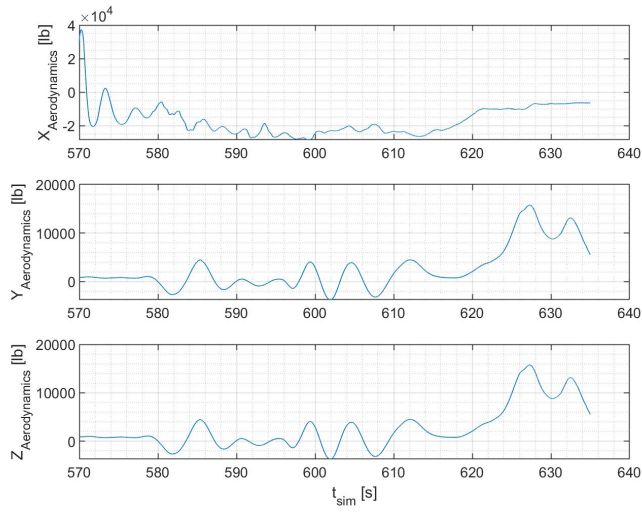


Figure 5.31: Aerodynamic Forces in **A**→**H** Conversion

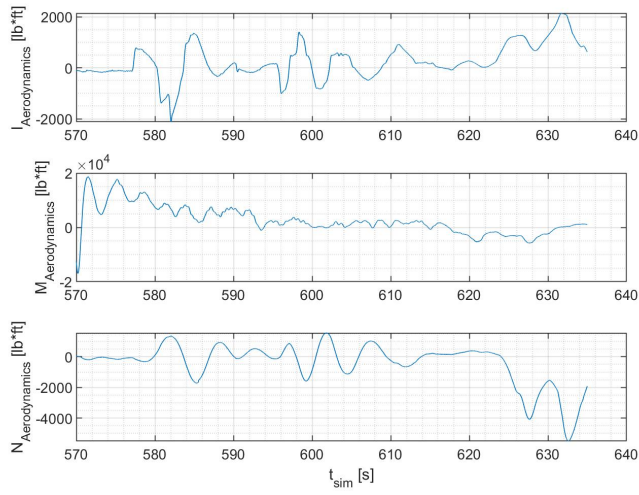


Figure 5.32: Aerodynamic Moments in **A**→**H** Conversion

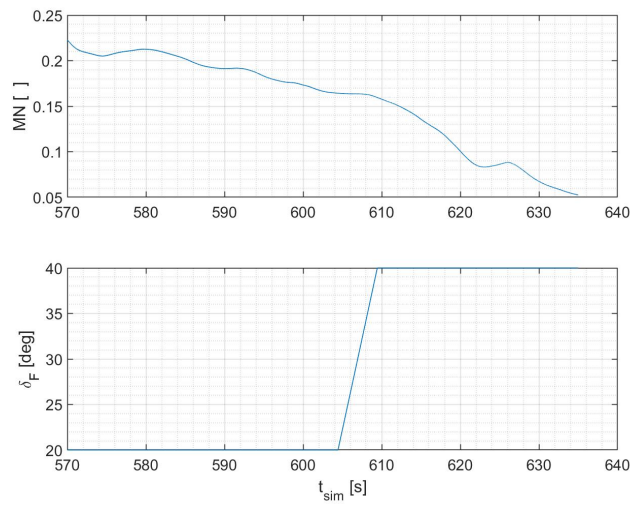


Figure 5.33: Flaps and Mach in **A**→**H** Conversion

Let's analyze a failed conversion from airplane to helicopter mode to understand which may have been the problems. Results are shown from Figure 5.34 to Figure 5.38 and may explain the reason for the failing conversion:

- Figure 5.34 shows the conversion corridor: sometimes, the pilot did not follow it, and therefore, it is a possible explanation for the increasing power or rotor X force;

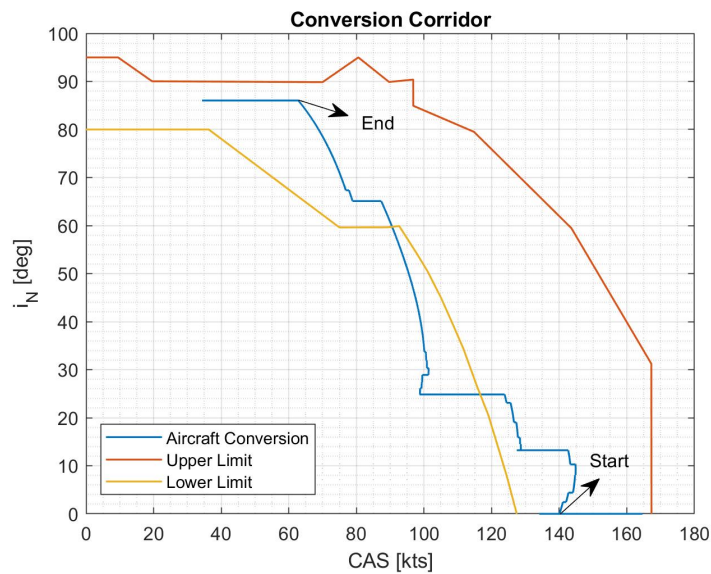


Figure 5.34: Conversion Corridor of a Failed Tilt **A** \rightarrow **H**

- Figure 5.36 shows that flaps were closed during the conversion and that before the interruption of the test, the mach number suddenly decreased. In relation with this, as shown in Figure 5.35, both angle of attack and sideslip suddenly changed, but it is impossible to establish cause and effect;

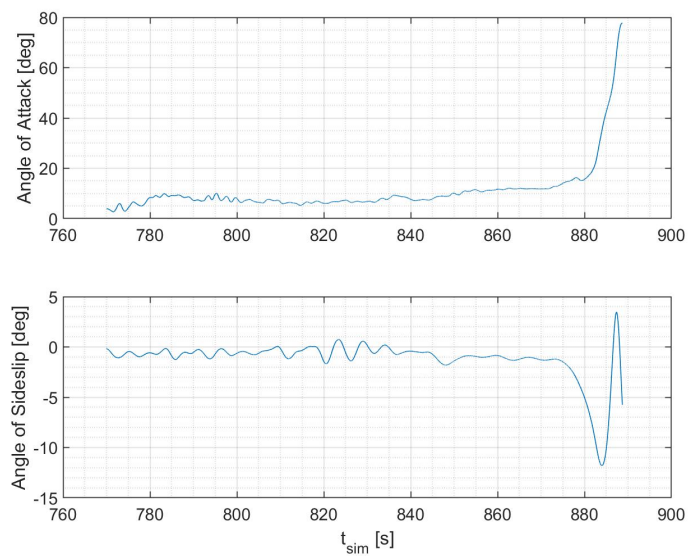


Figure 5.35: Angle of Attack and Sideslip of a Failed Conversion **A** \rightarrow **H**

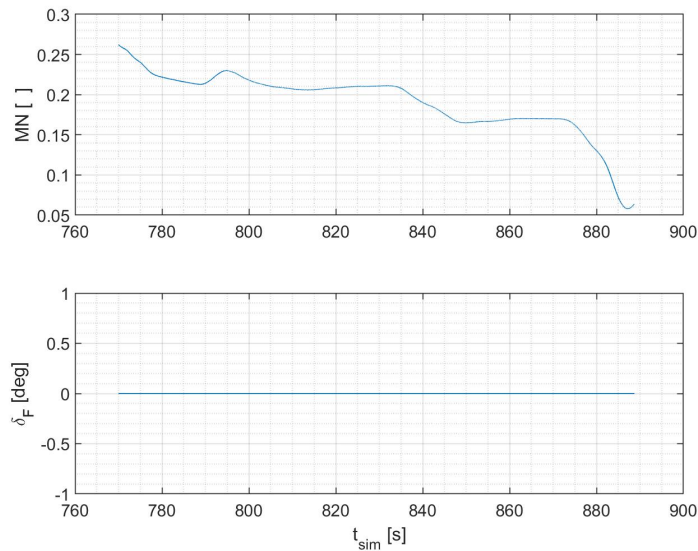


Figure 5.36: Flap Angle and Mach Number of a Failed Conversion **A** \rightarrow **H**

- Figure 5.37 shows that the rotor thrust grows, which seems in contradiction with the decrease in drag with speed and with Figure 5.28. Moreover, in Figure 5.38, the power increases, unlike Figure 5.30. The pilot noticed this last point, and he explained that it was impossible to reduce the power, although the altitude was growing.

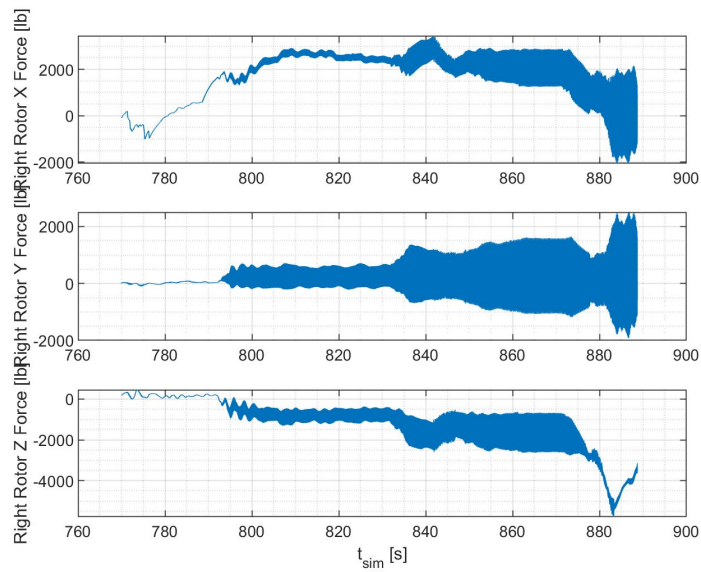


Figure 5.37: Rotor Forces of a Failed Conversion **A** \rightarrow **H**

At the end of all tests, the pilot evaluated **6/7** following the Cooper-Harper rating scale. Indeed, it was the most difficult task for him, but the evaluation is affected by a correct procedure's unawareness. However, he told that the aircraft is maneuverable and responds well to commands. The most critical issue for him is the ascent ratio, which is too high in some situations.

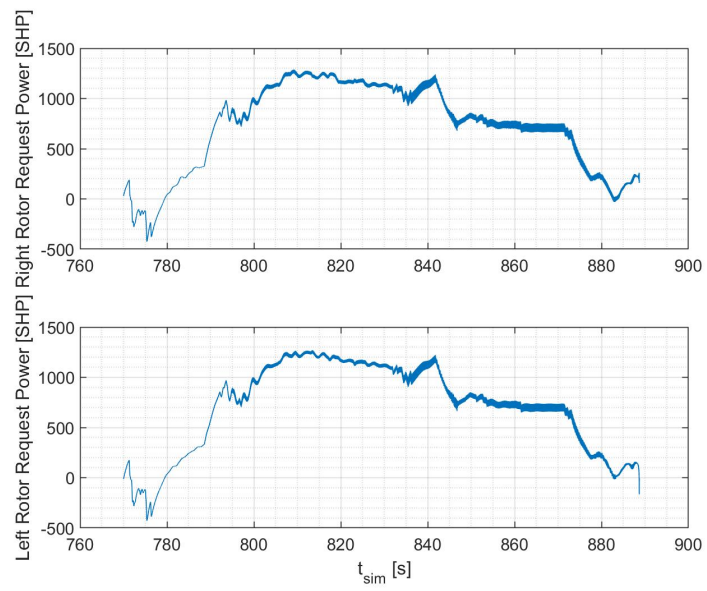


Figure 5.38: Power of a Failed Conversion **A** \rightarrow **H**

6 | CONCLUSIONS

6.1 ACHIEVEMENTS

The author's main result was a significant improvement of the XV-15 tilt-rotor simulation model implemented in ZHAW, which is now more reliable and realistic. This is testified by:

- the comparison of trim points with the GTRS model in Section 3.1: in all the tested conditions presented in Table 3.1, it appears to be an improvement in results compared to those of the initial model, therefore without the modifications explained in Chapter 2, when compared to the GTRS data from Ref. [23];
- the comparison of trim points with several flight test data, both in helicopter and airplane mode, in Section 3.2: ZHAW-Polito model reliably predict the behaviour of the XV-15 Tilt-Rotor, as shown by the comparison with available flight test results, from Ref. [23]. In addition, the longitudinal stick was compared with both flight test data and GTRS results in helicopter, conversion and airplane mode. Data was provided from Ref. [22], while results are shown in Section 3.3 and prove the reliability of the ZHAW-Polito simulation model;
- several piloted simulations in Chapter 5: it is shown that the aircraft is well controllable and maneuverable in helicopter mode, as testified with tasks from Ref. [35], and in airplane mode, as confirmed by pilot feedback. Moreover, the pilot converted the aircraft from helicopter to airplane mode and from airplane to helicopter mode several times, despite not knowing the correct procedure. The handling-qualities were evaluated by the pilot in all tested conditions with a grade from one to ten by referring to the Cooper-Harper rating scale, Figure 5.1. All the tasks were evaluated with a grade which falls in **Level 1** (levels range from one to three), which is the highest level in the Cooper-Harper rating scale, apart from the conversions which were evaluated with a grade in **Level 2**, even due to the lack of a reference procedure. Furthermore, the pilot found the model greatly improved, particularly in hover and yaw, as he often repeated during the tests.

These results have been obtained with a complete review of the existing aerodynamic model, which is now better comprehended, and with an improvement of it through the definition of reference systems more appropriate to the model,

both for the loads and the geometric characteristics of the tilt-rotor, the correction of the wing-pylon induced aerodynamics with Ref. [13] and of the wake at the vertical stabilizer, which now takes into account the flight during a maneuver or asymmetrical conditions. Beyond these, other changes or corrections were implemented in the existing aerodynamic model and are presented in Chapter 2.

Further validation was possible with the trimmed model's eigenvalues in Section 3.4, both with flight test data and other mathematical models, from Ref. [19] and [20].

Besides the corrections and improvements mentioned above, the author implemented some contributes which were not present in the existing model:

- **Ground Effect:** the correction proposed by Ref. [6] was not adaptable to the existing inflow model (from Pitt and Peters formulation) of ZHAW-Polito. Therefore, Bennet's ground effect equation, Ref. [27], was used. The main differences between the tilt-rotor and the helicopter were considered, and modifications were made to Bennet's Equation, where necessary. The ground effect prediction is the one expected in different flight conditions, and the aircraft was maneuverable during the piloted simulations;
- **Jet Thrust:** this contribute was added with the model presented in Ref. [6], but it was necessary to adapt it to the ZHAW-Polito rotor model. Unlike the GTRS, the contribution of the lateral mast tilt (ϕ_M) was added for a further generalization;
- **Landing Gear Drag:** the landing gear model was homemade in ZHAW, but it only considered the compression and extension during take-off and landing. Hence, the drag contribute was added with the equations provided by Ref. [6].

Despite these achievements, some problems still have to be solved in the model. When trim points are compared with the GTRS model, there are still offsets for various quantities and, even if some hypothesis were presented in Section 3.1, the reason is not clear yet. The side-by-side effect that can be implemented from Ref. [6] and which modelling has already been done by the author has to be integrated into the model later. Finally, the conversion during piloted simulations has to be fully understood in order to have a more reliable evaluation of the handling-qualities during this task. Moreover, the problem on the climb rate is not yet solved.

6.2 FUTURE DEVELOPMENTS

The various activities carried out with the thesis's aim highlighted the necessity to improve some aspects of the model in future work since they exceed this scope. These points can represent a good starting for planning the next steps:

- due to the shortage of data available in literature, aerodynamic data could not be fully validated: to aim this, it is possible to prepare some CFD analysis for a full-scale XV-15 or the main aerodynamic components, hence wing,

horizontal and vertical stabilizer. In addition, it is possible to validate the same data with homemade wind-tunnel experiments, both for the entire aircraft or the main aerodynamic bodies;

- the generalization of some aerodynamic contributes (spinner drag, pylon lateral drag), in order to divide loads of the two rotors for further precision during a maneuver and lateral flight;
- the implementation of the left contributes: side-by-side effect, side-ward flight rotor correction and the rolling moment in ground effect;
- a full evaluation of the handling-qualities of an XV-15 tilt-rotor with piloted simulations with the existing model. In particular, airplane mode and conversion mode have to be still evaluated with standardized tasks, like the ones provided in Ref. [35] in helicopter mode;
- the evaluation of the aircraft dynamics with the extrapolation of the eigenvalues in different flight conditions.

A | AERODYNAMIC MODEL EQUATIONS

A.1 FUSELAGE

Fuselage Dynamic Pressure

$$q_F = \frac{1}{2} \rho V_T^2 \quad (\text{A.1})$$

Fuselage Forces in Wind Axes

$$L_F = q_F \left(L_{\alpha|\beta_F=0} \cos^2 \beta_F + L_\beta + L_{BF0} + L_{LANG} \right) \quad (\text{A.2})$$

$$D_F = q_F \left(D_{\alpha|\beta_F=0} \cos^2 \beta_F + D_\beta + D_{BF0} + D_{LANG} \right) \quad (\text{A.3})$$

$$Y'_F = q_F Y_\beta \quad (\text{A.4})$$

Fuselage Moments in Wind Axes

$$l'_F = q_F l_\beta \quad (\text{A.5})$$

$$M_F = q_F \left(M_{\alpha|\beta_F=0} \cos^2 \beta_F + M_\beta + M_{BF0} \right) \quad (\text{A.6})$$

$$N'_F = q_F N_\beta \quad (\text{A.7})$$

Fuselage Forces in Body Axes

$$\begin{Bmatrix} X_F \\ Y_F \\ Z_F \end{Bmatrix} = \begin{bmatrix} -\cos \alpha_F \cos \beta_F & -\cos \alpha_F \sin \beta_F & \sin \alpha_F \\ -\sin \beta_F & \cos \beta_F & 0 \\ -\sin \alpha_F \cos \beta_F & -\sin \alpha_F \sin \beta_F & -\cos \alpha_F \end{bmatrix} \begin{Bmatrix} D_F \\ Y'_F \\ L_F \end{Bmatrix} \quad (\text{A.8})$$

Fuselage Moments in Body Axes

$$\begin{Bmatrix} l_F \\ M_F \\ N_F \end{Bmatrix} = \begin{bmatrix} \cos \alpha_F \cos \beta_F & -\cos \alpha_F \sin \beta_F & -\sin \alpha_F \\ \sin \beta_F & \cos \beta_F & 0 \\ \sin \alpha_F \cos \beta_F & -\sin \alpha_F \sin \beta_F & \cos \alpha_F \end{bmatrix} \begin{Bmatrix} l'_F \\ M'_F \\ N'_F \end{Bmatrix} \quad (\text{A.9})$$

Summation of Fuselage Moments in Body Axes

$$l_F = -Y_F (WL_{CG} - WL_F) + Z_F (BL_F - BL_{CG}) + l_F \quad (\text{A.10})$$

$$M_F = X_F (WL_{CG} - WL_F) - Z_F (SL_{CG} - SL_F) + M_F \quad (\text{A.11})$$

$$N_F = -X_F (BL_F - BL_{CG}) + Y_F (SL_{CG} - SL_F) + N_F \quad (\text{A.12})$$

A.2 HORIZONTAL STABILIZER

Geometric Distances between the c.g. and the Horizontal Stabilizer c.p.

$$l_{XH} = SL_{CG} - SL_H \quad (\text{A.13})$$

$$l_{YH} = BL_H - BL_{CG} \quad (\text{A.14})$$

$$l_{ZH} = WL_{CG} - WL_H \quad (\text{A.15})$$

$$(\text{A.16})$$

Velocities at the Horizontal Stabilizer

$$U_H = U + U_{i_{R|H}} + q \cdot l_{ZH} \quad (\text{A.17})$$

$$V_H = V + r \cdot l_{XH} - p \cdot l_{ZH} \quad (\text{A.18})$$

$$W_H = W + W_{i_{R|H}} - q \cdot l_{XH} \quad (\text{A.19})$$

Total Velocity at the Horizontal Stabilizer

$$V_{HT} = \sqrt{U_H^2 + W_H^2} \quad (\text{A.20})$$

Where:

$$\text{if } U_H < 0.01 \implies U_H = 0.01$$

in order to avoid division by zero.

Aerodynamic Angles at the Horizontal Stabilizer

$$\alpha_{HD} = -i_H + \arctan\left(\frac{W_H}{U_H}\right) + \varepsilon_{W/H} + (1 - K_e)\tau_e\delta_e \quad (\text{A.21})$$

$$\alpha_{HL} = -i_H + \arctan\left(\frac{W_H}{U_H}\right) + \varepsilon_{W/H}, \text{ if } M_N < 0.2 \quad (\text{A.22})$$

$$\alpha_{HL} = -i_H + \arctan\left(\frac{W_H}{U_H}\right) + \varepsilon_{W/H} + (1 - K_e)\tau_e\delta_e, \text{ if } M_N \geq 0.2 \quad (\text{A.23})$$

$$\beta_H = \arctan\left(\frac{V_H}{\sqrt{U_H^2 + W_H^2}}\right) \quad (\text{A.24})$$

Where:

Algorithm A.1: K_e Calculation

```

1 if  $|\delta_e| < 15$  then
2    $K_e = XK_e$ ;
3 else
4    $K_e = XK_e - DK_e \left(\frac{|\delta_e| - 15}{15}\right)$ ;

```

and where:

$$\begin{aligned}\varepsilon_{W/H} &= f(\alpha_W, \beta_M, \delta_F, M_N) \\ XK_e &= f(M_N)\end{aligned}$$

Dynamic Pressure

$$q_H = \frac{1}{2} \rho K_{HNU} \left[(U\sqrt{\eta_{HS}} + q \cdot l_{ZH})^2 + (W\sqrt{\eta_{HS}} - q \cdot l_{XH})^2 \right] \quad (\text{A.25})$$

Where:

Algorithm A.2: η_{HS} Calculation

```

1 if ( $U \geq 0 \vee |\beta_H| < 90$ ) then
2    $\eta_{HS} = 1 - (1 - \eta_H) K_{\beta HS}$ ;
3   else
4      $\eta_{HS} = 1$ ;

```

and where:

$$\begin{aligned}K_{\beta HS} &= f(\beta_F) \\ \eta_H &= f(V_T, \alpha_F, \beta_M)\end{aligned}$$

Angle of Attack at the Horizontal Stabilizer

$$\alpha_H = \arctan\left(\frac{W_H}{U_H}\right) + \varepsilon_{W/H} \quad (\text{A.26})$$

Horizontal Stabilizer Forces and Moments in Wind Axes

$$L_H = q_H S_H [C_{LH} + C_{LH\beta} \cdot \min(15, |\beta_H|) \cos \beta_M] \quad (\text{A.27})$$

$$D_H = q_H S_H C_{DH} \quad (\text{A.28})$$

$$M'_H = q_H S_H c_H (C_{MH0} + C_{MHA} \alpha_{HL}) \quad (\text{A.29})$$

Where:

$$C_{LH} = f(\alpha_{HL}, \delta_e, M_N)$$

$$C_{DH} = f(\alpha_{HD}, M_N)$$

Horizontal Stabilizer Forces in Body Axes

$$\begin{Bmatrix} X_H \\ Y_H \\ Z_H \end{Bmatrix} = \begin{bmatrix} -\cos \alpha_H \cos \beta_H & -\cos \alpha_H \sin \beta_H & \sin \alpha_H \\ -\sin \beta_H & \cos \beta_H & 0 \\ -\sin \alpha_H \cos \beta_H & -\sin \alpha_H \sin \beta_H & -\cos \alpha_H \end{bmatrix} \begin{Bmatrix} D_H \\ 0 \\ L_H \end{Bmatrix} \quad (\text{A.30})$$

Horizontal Stabilizer Moments in Body Axes

$$\begin{Bmatrix} l_H \\ M_H \\ N_H \end{Bmatrix} = \begin{bmatrix} \cos \alpha_H \cos \beta_H & -\cos \alpha_H \sin \beta_H & -\sin \alpha_H \\ \sin \beta_H & \cos \beta_H & 0 \\ \sin \alpha_H \cos \beta_H & -\sin \alpha_H \sin \beta_H & \cos \alpha_H \end{bmatrix} \begin{Bmatrix} 0 \\ M'_H \\ 0 \end{Bmatrix} \quad (\text{A.31})$$

Summation of Horizontal Stabilizer Moments in Body Axes

$$l_H = -Y_H (WL_{CG} - WL_H) + Z_H (BL_H - BL_{CG}) + l_H \quad (\text{A.32})$$

$$M_H = X_H (WL_{CG} - WL_H) - Z_H (SL_{CG} - SL_H) + M_H \quad (\text{A.33})$$

$$N_H = -X_H (BL_H - BL_{CG}) + Y_H (SL_{CG} - SL_H) + N_H \quad (\text{A.34})$$

A.3 VERTICAL STABILIZER

Geometric Distances between the c.g. and the Vertical Stabilizer c.p.

$$l_{XV}(j) = SL_{CG} - SL_V(j), \quad j = 1, 2 \quad (\text{A.35})$$

$$l_{XV}(j) = BL_V(j) - BL_{CG}, \quad j = 1, 2 \quad (\text{A.36})$$

$$l_{ZV}(j) = WL_{CG} - WL_V(j), \quad j = 1, 2 \quad (\text{A.37})$$

Matrix of the Butt Line Coordinates of the Rotor Tips

$$[T] = \begin{bmatrix} BL_{RTIP_e} & BL_{RTIP_i} & BL_{LTIP_i} & BL_{LTIP_e} \\ BL_{RTIP_e} & BL_{RTIP_i} & BL_{LTIP_i} & BL_{LTIP_e} \end{bmatrix} \quad (\text{A.38})$$

Matrix of the Butt Line Coordinates of the Vertical Fins

$$[B] = \begin{bmatrix} BL_{V1} & BL_{V1} & BL_{V1} & BL_{V1} \\ BL_{V2} & BL_{V2} & BL_{V2} & BL_{V2} \end{bmatrix} \quad (\text{A.39})$$

Matrix of the Distances between the Fins and the Shaft-Pivot

$$[S] = \begin{bmatrix} l_{X|RV1} & l_{X|RV1} & l_{X|RV1} & l_{X|RV1} \\ l_{X|RV2} & l_{X|RV2} & l_{X|RV2} & l_{X|RV2} \end{bmatrix} \quad (\text{A.40})$$

Matrix of the Angles between the Station Line and the Line which Connects Rotor Tips and Vertical Fins

$$[\gamma_{RV}] = \arctan \left(\frac{[T] - [B]}{[S]} \right) \quad (\text{A.41})$$

Calculation of Induced Velocities at Each Fin

Algorithm A.3: Rotor Wake at the Vertical Stabilizer Calculation

```

1   $[\gamma_{RV}] = [\gamma_{RV}]'$ ;
2  for  $j = 1 : 2$  do
3      if  $\beta_F > \gamma_{RV}(1, j)$  then
4           $U_{iB|RV_{wake}}(j) = 0$ ;
5           $W_{iB|RV_{wake}}(j) = 0$ ;
6      else
7          if  $(\gamma_{RV}(3, j) < \beta_F \leq \gamma_{RV}(2, j))$  then
8               $U_{iB|RV_{wake}}(j) = 0$ ;
9               $W_{iB|RV_{wake}}(j) = 0$ ;
10         else
11             if  $\beta_F < \gamma_{RV}(4, j)$  then
12                  $U_{iB|RV_{wake}}(j) = 0$ ;
13                  $W_{iB|RV_{wake}}(j) = 0$ ;
14             else
15                  $U_{iB|RV_{wake}}(j) = U_{iR|V}$ ;
16                  $W_{iB|RV_{wake}}(j) = W_{iR|V}$ ;

```

Velocities at the Vertical Stabilizer

$$U_V(j) = U + U_{iB|RV_{wake}}(j) + q \cdot l_{ZV}(j) - r \cdot l_{YV}(j), \quad j = 1, 2 \quad (\text{A.42})$$

$$V_V(j) = V - p \cdot l_{ZV}(j) + r \cdot l_{XV}(j), \quad j = 1, 2 \quad (\text{A.43})$$

$$W_V(j) = W + W_{B|RV_{wake}}(j) + p \cdot l_{YV}(j) - q \cdot l_{XV}(j), \quad j = 1, 2 \quad (\text{A.44})$$

Total Velocity at the Vertical Stabilizer

$$V_{VT}(j) = \sqrt{U_V^2 + V_V^2 + W_V^2}, \quad j = 1, 2 \quad (\text{A.45})$$

Aerodynamic Angles at the Vertical Stabilizer

$$\text{if } U_V(j) < 35 \implies U_V(j) = 35 \text{sign}(U_V)$$

$$\beta_V(j) = i_V(j) + \arctan \left(\frac{V_V(j)}{\sqrt{U_V(j)^2 + W_V(j)^2}} \right) + \quad (\text{A.46})$$

$$- \frac{1}{2} \frac{b_W}{U_V(j)} \left(\frac{\partial \sigma}{\partial p} p + \frac{\partial \sigma}{\partial r} r \right) - \frac{l_{XV}(j)}{U_V(j)} \frac{\partial \sigma}{\partial \beta_F} \dot{\beta}, \quad j = 1, 2$$

$$\beta_{VD}(j) = \beta_V(j) + K_r \tau_r \delta_r, \quad j = 1, 2 \quad (\text{A.47})$$

Where:

Algorithm A.4: K_r Calculation

```

1 if  $|\delta_r| < 15$  then
2    $K_r = XK_r$ ;
3   else
4      $K_r = XK_r - DK_r \left( \frac{|\delta_r| - 15}{15} \right)$ ;

```

and where:

$$\begin{aligned}
 XK_r &= f(M_N) \\
 \frac{\partial \sigma}{\partial \beta_F} &= 1 - \left(1 - \frac{\partial \sigma}{\partial \beta_F} \right) \\
 \left(1 - \frac{\partial \sigma}{\partial \beta_F} \right) &= f(\alpha_F, \beta_F, \beta_M, \delta_F)
 \end{aligned}$$

Dynamic Pressure

$$\begin{aligned}
 q_V(j) = \frac{1}{2} \rho K_{VNU} \left\{ \right. & \left[U \sqrt{\eta_{VS}(j)} + q \cdot l_{ZV}(j) - r \cdot l_{YV}(j) \right]^2 + \\
 & + \left[V \sqrt{\eta_{VS}(j)} - p \cdot l_{ZV}(j) + r \cdot l_{XV}(j) \right]^2 + \\
 & \left. + \left[W \sqrt{\eta_{VS}(j)} + p \cdot l_{YV}(j) - q \cdot l_{XV}(j) \right]^2 \right\} \quad (\text{A.48})
 \end{aligned}$$

Where:

Algorithm A.5: η_{HS} Calculation

```

1 if  $(U \geq 0 \vee |\beta_V < 90|)$  then
2    $\eta_{VS} = 1 - (1 - \eta_V) K_{\beta VS}$ ;
3   else
4      $\eta_{VS} = 1$ ;

```

and where:

$$\begin{aligned}
 K_{\beta VS} &= f(\beta_F) \\
 \eta_V &= f(V_T, \alpha_F, \beta_M)
 \end{aligned}$$

Vertical Stabilizer Aerodynamic Coefficients

$$\begin{aligned}
 C_{YV}(j) = C_{YV|\delta_r=0}(j) & \left[K_{\beta r} \left(1 - \frac{\partial \sigma}{\partial \beta_F} \right) \right] + \\
 & + \left[C_{YV|\delta_r}(j) - C_{YV|\delta_r=0}(j) \right], \quad M_N \leq 0.2, j = 1, 2 \quad (\text{A.49})
 \end{aligned}$$

$$C_{YV}(j) = C_{YV|\delta_r=0}(j) \left[K_{\beta r} \left(1 - \frac{\partial \sigma}{\partial \beta_F} \right) \right] + a_V(j) K_r \tau_r \delta_r, \quad M_N > 0.2, \quad j = 1, 2 \quad (\text{A.50})$$

$$C_{DV}(j) = C_{DV|\delta_r}(j) \left[K_{\beta r} \left(1 - \frac{\partial \sigma}{\partial \beta_F} \right) \right], \quad j = 1, 2 \quad (\text{A.51})$$

Where:

$$\begin{aligned} C_{YV|\delta_r=0}(j) &= f(\beta_V(j), \delta_r = 0, M_N), \quad j = 1, 2 \\ C_{YV|\delta_r}(j) &= f(\beta_V(j), \delta_r, M_N), \quad j = 1, 2 \\ C_{DV|\delta_r}(j) &= f(\beta_{VD}(j), M_N), \quad j = 1, 2 \\ K_{\beta R} &= f(\beta_F, V_T) \end{aligned}$$

Vertical Stabilizer Forces and Moments in Wind Axes

$$Y'_V(j) = -C_{YV}(j) q_V(j) S_V(j), \quad j = 1, 2 \quad (\text{A.52})$$

$$D_V(j) = C_{DV}(j) q_V(j) S_V(j), \quad j = 1, 2 \quad (\text{A.53})$$

Vertical Stabilizer Forces in Body Axes

$$\begin{Bmatrix} X_V(j) \\ Y_V(j) \\ Z_V(j) \end{Bmatrix} = \begin{bmatrix} -\cos \alpha_H \cos \beta_V(j) & -\cos \alpha_H \sin \beta_V(j) & \sin \alpha_H \\ -\sin \beta_V(j) & \cos \beta_V(j) & 0 \\ -0 \cdot \cos \beta_V(j) & -0 \cdot \sin \beta_V(j) & -1 \end{bmatrix} \begin{Bmatrix} D_V(j) \\ Y'_V(j) \\ 0 \end{Bmatrix} \quad (\text{A.54})$$

Summation of Vertical Stabilizer Moments in Body Axes

$$l_V = -\sum_j [Y_V(j) l_{ZV}(j)] \quad (\text{A.55})$$

$$M_V = \sum_j [X_V(j) l_{ZV}(j)] \quad (\text{A.56})$$

$$N_V = \sum_j [Y_V(j) l_{XV}(j) - X_V(j) l_{YV}(j)] \quad (\text{A.57})$$

A.4 WING-PYLON

A.4.1 Induced Aerodynamics

Initialization of Values for the Calculation of the Portion of the Wing Being Affected by the Rotor Induced Velocity

$$G = \arctan \left(\frac{\cos \phi_M \sin \beta_M}{\cos \beta_M} \right), \quad [rad] \quad (\text{A.58})$$

$$SG = \sin G, \quad [ND] \quad (\text{A.59})$$

$$CG = \cos G, \quad [ND] \quad (\text{A.60})$$

$$ZL = l_m \cos \phi_M CG, \quad [ft] \quad (\text{A.61})$$

Velocities at the Wing

$$U_{WK} = -U - W_{i|RWK}SG, [ft/s] \quad (A.62)$$

$$W_{WK} = -W + W_{i|RWK} \cos \phi_M CG, [ft/s] \quad (A.63)$$

$$V_{WR} = V + W_{i|RWR} \sin \phi_M SG, [ft/s] \quad (A.64)$$

$$V_{WL} = V + W_{i|RWL} \sin \phi_M SG, [ft/s] \quad (A.65)$$

Wing Geometry Information

$$\bar{e} = SL_{WTE} - SL_{SP}, [ft] \quad (A.66)$$

$$X_{TEK} = -\bar{e} - l_m SG - \frac{U_{WK}}{W_{WK}} ZL K_{RW}, [ft] \quad (A.67)$$

$$X_{LEK} = c_W + X_{TEK}, [ft] \quad (A.68)$$

$$Y_{TIPK} = ZL \left[\tan \phi_M - \frac{V_{WK}}{\sqrt{U_{WK}^2 + W_{WK}^2}} \text{sign}(W_{WK}) \right], [ft] \quad (A.69)$$

$$R_{WXK} = R_{WK} \sqrt{\left(\frac{U_{WK}}{W_{WK}} \sin \phi_M \right)^2 + \left(CG - \frac{U_{WK}}{W_{WK}} SG \cos \phi_M \right)^2}, [ft] \quad (A.70)$$

$$R_{WYK} = R_{WK} \left\{ \left(\frac{V_{WK}}{W_{WK}} SG \cos \phi_M - SG \sin \phi_M \right)^2 + \left[\cos \phi_M + \frac{V_{WK} \sin \phi_M}{\sqrt{U_{WK}^2 + W_{WK}^2}} \text{sign}(W_{WK}) \right]^2 \right\}^{\frac{1}{2}}, [ft] \quad (A.71)$$

$$\delta_K = \arctan \left(\frac{\frac{U_{WK}}{W_{WK}} \sin \phi_M}{CG - \frac{U_{WK}}{W_{WK}} \cos \phi_M SG} \right) + \arctan \left[\frac{V_{WK} \sin \phi_M}{\text{sign}(W_{WK}) \sqrt{U_{WK}^2 + W_{WK}^2}} \right], [rad] \quad (A.72)$$

$$F_{RWK} = \frac{R_{WYK}}{R_{WXK}}, [ND] \quad (A.73)$$

$$S_{DELK} = \sin \delta_K, [ND] \quad (A.74)$$

$$C_{DELK} = |\cos \delta_K|, [ND] \quad (A.75)$$

Procedure

- if $\beta_M > 30^\circ$ the procedure is bypassed and the following variables are set to zero: X_K , Y_K and S_{iWK} ;
- if $\beta_M \leq 30^\circ$ the procedure starts. It is shown from Figure A.1 to Figure A.6.

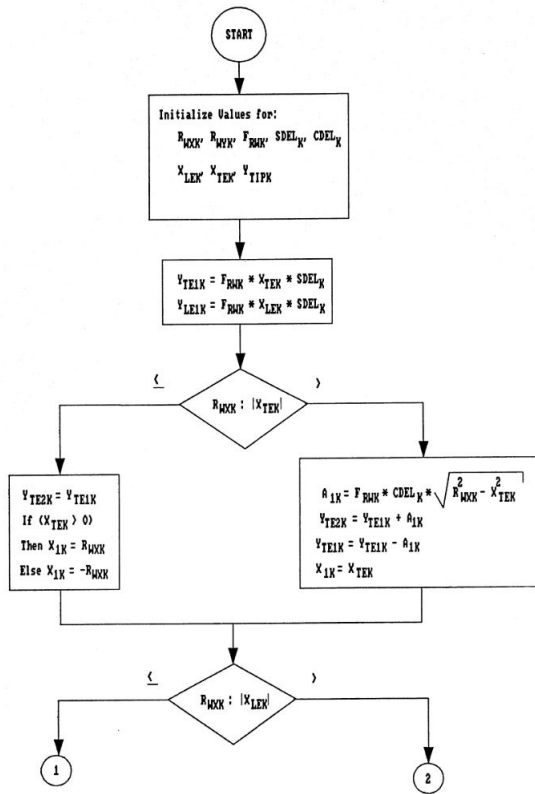


Figure A.1: Procedure Part 1

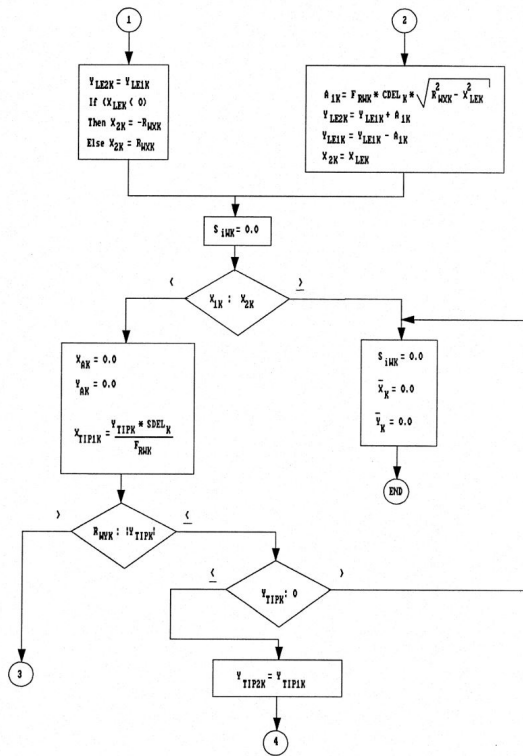


Figure A.2: Procedure Part 2

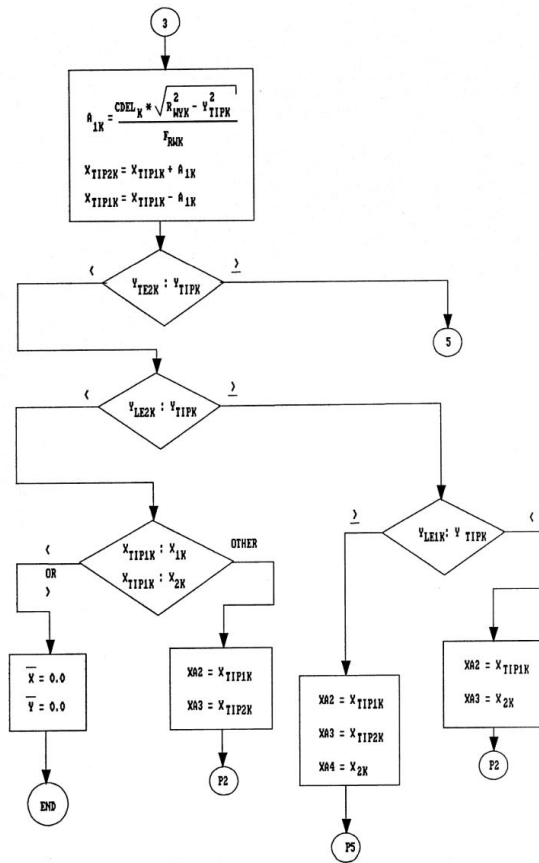


Figure A.3: Procedure Part 3

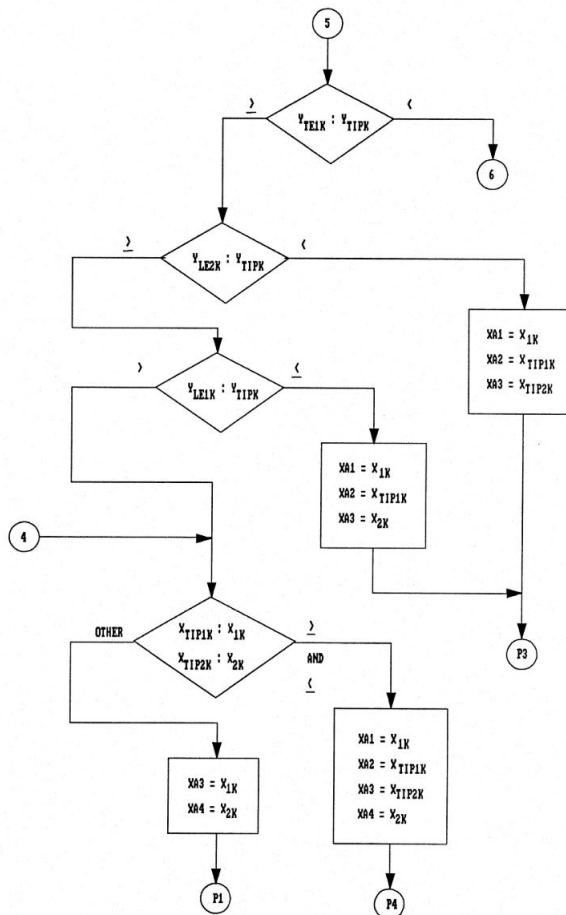


Figure A.4: Procedure Part 4

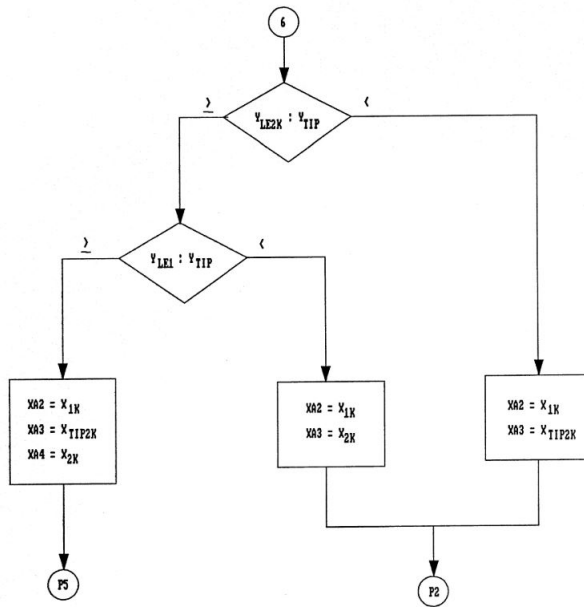


Figure A.5: Procedure Part 5

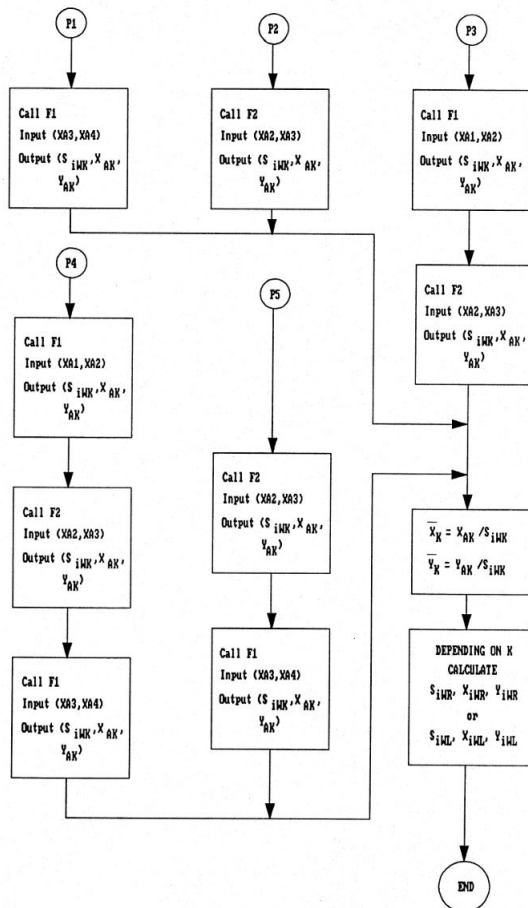


Figure A.6: Procedure Part 6

When $F1$ is Called:

$$F1 = F1(C_{1K}, C_{2K})$$

$$S_{iWK} = S_{iWK} + A_{1K} \quad (\text{A.76})$$

$$X_{AK} = X_{AK} + XA_{1K} \quad (\text{A.77})$$

$$Y_{AK} = Y_{AK} + XA_{1K}S_{DELK}F_{RWK} \quad (\text{A.78})$$

When $F2$ is Called:

$$F2 = F2(C_{1K}, C_{2K})$$

$$S_{iWK} = S_{iWK} + \frac{1}{2} \left[A_{1K} + F_{RWK}S_{DELK} (C_{2K}^2 - C_{1K}^2) \right] - Y_{TIPK} (C_{2K} - C_{1K}) \quad (\text{A.79})$$

$$X_{AK} = X_{AK} + \frac{1}{2}XA_{1K} + \frac{1}{3}F_{RWK}S_{DELK} (C_{2K}^3 - C_{1K}^3) - Y_{TIPK} (C_{2K}^2 - C_{1K}^2) \quad (\text{A.80})$$

$$Y_{AK} = Y_{AK} + F_{RWK} \left[\frac{1}{2}XA_{1K}S_{DELK} + \frac{1}{6}F_{RWK} (S_{DELK}^2 - C_{DELK}^2) (C_{2K}^3 - C_{1K}^3) + \frac{1}{2} (R_{WYK}R_{WXK}C_{DELK}^2 - Y_{TIPK}^2) (C_{2K} - C_{1K}) \right] \quad (\text{A.81})$$

Where:

$$\theta_{C_{1K}} = \arcsin \left(\frac{C_{1K}}{R_{WXK}} \right) \quad (\text{A.82})$$

$$\theta_{C_{2K}} = \arcsin \left(\frac{C_{2K}}{R_{WXK}} \right) \quad (\text{A.83})$$

$$A_{1K} = R_{WXK}R_{WYK}C_{DELK} (\sin \theta_{C_{2K}} \cos \theta_{C_{2K}} - \sin \theta_{C_{1K}} \cos \theta_{C_{1K}} + \theta_{C_{2K}} - \theta_{C_{1K}}) \quad (\text{A.84})$$

$$XA_{1K} = -\frac{2}{3}F_{RWK}C_{DELK} \left[(R_{WYK}^2 - C_{2K}^2)^{\frac{3}{2}} - (R_{WYK}^2 - C_{1K}^2)^{\frac{3}{2}} \right] \quad (\text{A.85})$$

Affected Area and Arm of the Induced Forces for the Right Semi-Wing

if $K = R$:

$$S_{iWR} = S_{iWK} \quad (\text{A.86})$$

$$X_{iWR} = X_R + SL_{CG} - SL_{WTE} - X_{TER} \quad (\text{A.87})$$

$$Y_{iWR} = -Y_R - BL_{CG} + BL_{SP} + Y_{TIPR} \quad (\text{A.88})$$

Affected Area and Arm of the Induced Forces for the Left Semi-Wing

if $K = L$:

$$S_{iWL} = S_{iWK} \quad (\text{A.89})$$

$$X_{iWL} = X_L + SL_{CG} - SL_{WTE} - X_{TEL} \quad (\text{A.90})$$

$$Y_{iWL} = Y_L - BL_{CG} - BL_{SP} - Y_{TIP_L} \quad (\text{A.91})$$

Where:

$$X_K = \frac{X_{AK}}{S_{iWK}} \quad (\text{A.92})$$

$$Y_K = \frac{Y_{AK}}{S_{iWK}} \quad (\text{A.93})$$

Total Velocity, Angle of Attack, Sideslip Angle and Dynamic Pressure

$$V_{TiWK} = \sqrt{(U + U_{iB|RWK})^2 + (W + W_{iB|RWK})^2} \quad (\text{A.94})$$

$$\alpha_{iWK} = \arctan\left(\frac{W + W_{iB|RWK}}{U + U_{iB|RWK}}\right) \quad (\text{A.95})$$

$$\beta_{iWK} = \arctan\left[\frac{V}{\sqrt{(U + U_{iB|RWK})^2 + (W + W_{iB|RWK})^2}}\right] \quad (\text{A.96})$$

$$q_{iWK} = \frac{1}{2}\rho V_{TiWK}^2 \quad (\text{A.97})$$

Lift and Drag in Wind Axes System

$$L_{iWPK} = q_{iWK} S_{iWK} C_{LWPK} K_{FW} \quad (\text{A.98})$$

$$D_{iWPK} = q_{iWK} S_{iWK} C_{DWPK} K_{FW} \quad (\text{A.99})$$

Where:

$$K_{FW} = K_{FW0} + K_{FWDF} \delta_F \quad (\text{A.100})$$

$$C_{LWPK} = f(\alpha_{iWK}, \beta_M, \delta_F, M_N)$$

$$C_{DWPK} = f(\alpha_{iWK}, \beta_M, \delta_F, M_N)$$

Induced Forces in Body Axes

$$\begin{Bmatrix} X_{iWPK} \\ Y_{iWPK} \\ Z_{iWPK} \end{Bmatrix} = \begin{bmatrix} -\cos \alpha_{iWK} \cos \beta_{iWK} & -\cos \alpha_{iWK} \sin \beta_{iWK} & \sin \alpha_{iWK} \\ -\sin \beta_{iWK} & \cos \beta_{iWK} & 0 \\ -\sin \alpha_{iWK} \cos \beta_{iWK} & -\sin \alpha_{iWK} \sin \beta_{iWK} & -\cos \alpha_{iWK} \end{bmatrix} \begin{Bmatrix} D_{iWPK} \\ Y'_{iWPK} \\ L_{iWPK} \end{Bmatrix} \quad (\text{A.101})$$

Moments due to Induced Forces in Body Axes

Notation for forces and arms are similar: when "WP" appears, they are forces, when just "W" appears, they are arms.

$$l_{iWPK} = -(Y_{iWPL} + Y_{iWPL})(WL_{CG} - WL_{WP}) + Z_{iWPR}Y_{iWR} + Z_{iWPL}Y_{iWL} \quad (\text{A.102})$$

$$M_{iWPK} = (X_{iWPL} + X_{iWPL})(WL_{CG} - WL_{WP}) - Z_{iWPR}X_{iWR} - Z_{iWPL}X_{iWL} \quad (\text{A.103})$$

$$N_{iWPK} = Y_{iWPR}X_{iWR} + Y_{iWPL}X_{iWL} - X_{iWPR}Y_{iWR} - X_{iWPL}Y_{iWL} \quad (\text{A.104})$$

A.4.2 Freestream Aerodynamics

Wing Area for Freestream

$$S_{WFS} = S_W - (S_{iWL} + S_{iWR}) \quad (\text{A.105})$$

Dynamic Pressure

$$q_{WFS} = \frac{1}{2}\rho(U^2 + W^2) \quad (\text{A.106})$$

Angle of Attack

$$\alpha_{WFS} = \alpha_F - K_{X_{RW}}X_{RW} \left\{ \frac{C_{RFR} + C_{RFL}}{\left[\max\left(0.15, \frac{\mu_R + \mu_L}{2}\right)\right]^2} \right\} \quad (\text{A.107})$$

Where:

$$X_{RW} = X_{RW0} + \beta_M(X_{RW1} + \beta_M X_{RW2}) \quad (\text{A.108})$$

Longitudinal Loads in Wind Axes

$$L_{WP} = q_{WFS}S_{WFS}C_{LWP_{FS}} - q_{WFS}S_W C_{L\delta_a}|\delta_a| \quad (\text{A.109})$$

$$D_{WP} = q_{WFS}S_{WFS}C_{DWP_{FS}} \quad (\text{A.110})$$

$$M'_{WP} = q_{WFS}S_W c_W C_{m_{WP}} \quad (\text{A.111})$$

Where:

$$C_{LWP_{FS}} = f(\alpha_{WFS}, \beta_M, \delta_F, M_N)$$

$$C_{DWP_{FS}} = f(\alpha_{WFS}, \beta_M, \delta_F, M_N)$$

$$C_{L\delta_a} = f(\delta_F)$$

$$C_{m_{WP}} = f(\beta_M, \delta_F)$$

Lateral-Directional Loads in Wind Axes

$$Y'_{WP} = q_{WFS} S_W \left[C_{Y\beta} \beta_F + \frac{b_W}{2U} (C_{Yp} p_w + C_{Yr} r_w) \right] \quad (\text{A.112})$$

$$l'_{WP} = q_{WFS} S_W b_W \left[C_{l\beta} \beta_F + \frac{b_W}{2U} (C_{lp} p_w + C_{lr} r_w) \right] + S_W b_W \left[\left(\frac{q_{iWR} + q_{iWL}}{2} \right) (C_{l\delta_a} \delta_a) \right] \quad (\text{A.113})$$

$$N'_{WP} = q_{WFS} S_W b_W \left[C_{n\beta} \beta_F + \frac{b_W}{2U} (C_{np} p_w + C_{nr} r_w) \right] + S_W b_W \left[\left(\frac{q_{iWR} + q_{iWL}}{2} \right) (C_{n\delta_a} \delta_a) \right] \quad (\text{A.114})$$

Where:

- $C_{Y\beta} = C_\beta C_{Y\beta|_{M_N=0}}$
- $C_{Yp} = C_\beta C_{LWP_{FS}} \left(\frac{C_{Yp}}{C_{LWP}} \Big|_{M_N=0} \right) \frac{AR_W B_c + \cos \Lambda_W}{AR_W + \cos \Lambda_W}$
- $C_{Yr} = C_\beta C_{Yr|_{M_N=0}}$
- $C_{l\beta} = C_\beta C_{l\beta|_{C_{LWP}=M_N=0}} + C_{LWP_{FS}} \left(\frac{C_{l\beta}}{C_{LWP}} \Big|_{M_N=0} \right)$,
where:

$$C_{l\beta|_{C_{LWP}=M_N=0}} = f(\delta_F, \beta_F, \beta_M)$$

$$\frac{C_{l\beta}}{C_{LWP}} \Big|_{M_N=0} = f(\delta_F, \beta_F, \beta_M)$$

and (outputs must be in radiant since $C_{l\beta}$ is in $[rad^{-1}]$. Hence equations are multiplied for $\pi/180$)

Algorithm A.6: $C_{l\beta} \beta_F$ Calculation

```

1 if  $0 < |\beta_F| \leq 15^\circ$  then
2    $C_{l\beta} \beta_F = C_{l\beta} \beta_F \frac{\pi}{180}$ ;
3 else
4   if  $15^\circ < |\beta_F| < 165^\circ$  then
5      $C_{l\beta} \beta_F = 15 C_{l\beta} \text{sign}(\beta_F) \frac{\pi}{180}$ ;
6   else
7     if  $165^\circ \leq |\beta_F| < 180^\circ$  then
8        $C_{l\beta} \beta_F = [15 C_{l\beta} - C_{l\beta} (\beta_F - 165^\circ)] \text{sign}(\beta_F) \frac{\pi}{180}$ ;

```

- $C_{lp} = C_\beta C_{lp|_{C_{LWP}=M_N=0}} \left[\frac{\frac{\partial C_{LWP_{FS}}}{\partial \alpha_{WFS}}}{\left(\frac{\partial C_{LWP_{FS}}}{\partial \alpha_{WFS}} \right) \Big|_{C_{LWP}=0}} \right] - \frac{1}{8} \left(C_{DWP_{FS}} - \frac{C_{LWP_{FS}}^2}{\pi AR_W} \right)$, where
 $\left(\frac{\partial C_{LWP_{FS}}}{\partial \alpha_{WFS}} \right) \Big|_{C_{LWP}=0} = f(M_N, \beta_F, \beta_M)$

- $C_{lr} = C_{LWPFS} \left(\frac{C_{lr}}{C_{LWP}} \Big|_{M_N=0} \right) \frac{1+AR_W(1-B_C)^2}{2B_C(AR_W B_C+2)} + \frac{\Delta C_{lr}}{\frac{\partial \alpha_{WFS}}{\partial \delta_F} \delta_F} \frac{\partial \alpha_{WFS}}{\partial \delta_F} \delta_F$
- $C_{l\delta_a} = K_{l\delta_a} C_{l\delta_a} \Big|_{\alpha_{WFS} < 8^\circ}^{\delta_F=0^\circ}$, where $K_{l\delta_a} = f(\delta_F, \beta_M, \alpha_{WFS})$
- $C_{n\beta} = C_\beta C_{n\beta} \Big|_{C_{LWP}=M_N=0} + C_{LWPFS}^2 \left(\frac{C_{n\beta}}{C_{LWPFS}^2} \Big|_{M_N=0} \right)$
- $C_{np} = C_{lp} \alpha_{WFS} (K_{np} - 1) + K_{np} C_\beta B_C C_{LWPFS} \frac{C_{np}}{C_{LWP}} \Big|_{M_N=0}$
- $C_{nr} = \frac{C_{nr}}{C_{LWP}^2} C_{LWPFS}^2 + \frac{C_{nr}}{C_{D0WP}} C_{D0WP} \Big|_{C_{LWP}=0}$,
where $C_{D0WP} \Big|_{C_{LWP}=0} = f(\delta_F, \beta_M, M_N)$
- $C_{n\delta_a} = K_{n0\delta_a} + K_{n\delta_a} C_{l\delta_a} C_{LWPFS}$, where $K_{n0\delta_a} = f(\delta_F, \beta_M)$ and $K_{n\delta_a} = f(\delta_F, \beta_M)$.

Some variables of the previous equations are used to take into account compressibility effects:

$$B_C = \sqrt{1 - M_N^2 \cos^2 \Lambda_W} \quad (\text{A.115})$$

$$AR_W = \frac{b_w^2}{S_W} \quad (\text{A.116})$$

$$C_\beta = \frac{AR_W + 4 \cos \Lambda_W}{AR_W B_C + 4 \cos \Lambda_W} \quad (\text{A.117})$$

Freestream Forces in Body Axes

$$\begin{Bmatrix} X_{WP} \\ Y_{WP} \\ Z_{WP} \end{Bmatrix} = \begin{bmatrix} -\cos \alpha_{WFS} \cos \beta_{WFS} & -\cos \alpha_{WFS} \sin \beta_{WFS} & \sin \alpha_{WFS} \\ -\sin \beta_{WFS} & \cos \beta_{WFS} & 0 \\ -\sin \alpha_{WFS} \cos \beta_{WFS} & -\sin \alpha_{WFS} \sin \beta_{WFS} & -\cos \alpha_{WFS} \end{bmatrix} \begin{Bmatrix} D_{WP} \\ Y'_{WP} \\ L_{WP} \end{Bmatrix} \quad (\text{A.118})$$

Freestream Moments in Body Axes

$$\begin{Bmatrix} l_{WP} \\ M_{WP} \\ N_{WP} \end{Bmatrix} = \begin{bmatrix} \cos \alpha_{WFS} \cos \beta_{WFS} & -\cos \alpha_{WFS} \sin \beta_{WFS} & -\sin \alpha_{WFS} \\ \sin \beta_{WFS} & \cos \beta_{WFS} & 0 \\ \sin \alpha_{WFS} \cos \beta_{WFS} & -\sin \alpha_{WFS} \sin \beta_{WFS} & \cos \alpha_{WFS} \end{bmatrix} \begin{Bmatrix} l'_{WP} \\ M'_{WP} \\ N'_{WP} \end{Bmatrix} \quad (\text{A.119})$$

Total Freestream moments in Body Axes

$$l_{WP} = -Y_{WP} (WL_{CG} - WL_{WP}) + Z_{WP} (BL_{SP} - BL_{CG}) + l_{WP} \quad (\text{A.120})$$

$$M_{WP} = X_{WP} (WL_{CG} - WL_{WP}) - Z_{WP} (SL_{CG} - SL_{WP}) + M_{WP} \quad (\text{A.121})$$

$$N_{WP} = Y_{WP} (SL_{CG} - SL_{WP}) - X_{WP} (BL_{SP} - BL_{CG}) + N_{WP} \quad (\text{A.122})$$

A.4.3 Wing Wake Deflection at the Horizontal Tail

$$\varepsilon_{W/H} = \varepsilon_{W/HOGE} \left(\frac{1}{\sqrt{1 - M_N^2}} \right) \quad (\text{A.123})$$

Where:

$$\varepsilon_{W/HOGE} = f(\alpha_{WFS}, \beta_M, \delta_F)$$

A.4.4 Wing-Pylon Interference Drag

Wing-Pylon Interference Drag in Wind Axes

$$D_{PYLN} = D_{PYINT} \left(\frac{q_{iWL} + q_{iWR}}{2} \right) \quad (\text{A.124})$$

Where:

$$D_{PYINT} = f(\beta_M)$$

Wing-Pylon Interference Drag in Body Axes

$$\begin{Bmatrix} X_{iPYL} \\ Y_{iPYL} \\ Z_{iPYL} \end{Bmatrix} = \begin{bmatrix} -\cos \alpha_{iWAV} \cos \beta_{iWAV} & -\cos \alpha_{iWAV} \sin \beta_{iWAV} & \sin \alpha_{iWAV} \\ -\sin \beta_{iWAV} & \cos \beta_{iWAV} & 0 \\ -\sin \alpha_{iWAV} \cos \beta_{iWAV} & -\sin \alpha_{iWAV} \sin \beta_{iWAV} & -\cos \alpha_{iWAV} \end{bmatrix} \begin{Bmatrix} D_{PYINT} \\ 0 \\ 0 \end{Bmatrix} \quad (\text{A.125})$$

Where:

$$\alpha_{iWAV} = \frac{\alpha_{iWR} + \alpha_{iWL}}{2} \quad (\text{A.126})$$

$$\beta_{iWAV} = \frac{\beta_{iWR} + \beta_{iWL}}{2} \quad (\text{A.127})$$

Moments due to Wing-Pylon Interference Drag

$$l_{iPYL} = -Y_{iPYL} (WL_{CG} - WL_{SP}) + Z_{iPYL} (BL_{SP} - BL_{CG}) \quad (\text{A.128})$$

$$M_{iPYL} = X_{iPYL} (WL_{CG} - WL_{SP}) - Z_{iPYL} (SL_{CG} - SL_{SP}) \quad (\text{A.129})$$

$$N_{iPYL} = -X_{iPYL} (BL_{SP} - BL_{CG}) + Y_{iPYL} (SL_{CG} - SL_{SP}) \quad (\text{A.130})$$

A.4.5 Spinner Drag

Average Induced Velocity in Body Axes

$$U_{iSP} = \left(\frac{W_{iL} + W_{iR}}{2} \right) \sin \beta_M \quad (\text{A.131})$$

$$W_{iSP} = - \left(\frac{W_{iL} + W_{iR}}{2} \right) \cos \beta_M \quad (\text{A.132})$$

Total Velocity and Dynamic Pressure in Mast Axes System

$$U_{MSP} = U \cos \beta_M + W \sin \beta_M \quad (\text{A.133})$$

$$W_{MSP} = - \left(\frac{W_{iL} + W_{iR}}{2} \right) - U \sin \beta_M + W \cos \beta_M \quad (\text{A.134})$$

$$V_{TSP} = \sqrt{U_{MSP}^2 + V^2 + W_{MSP}^2} \quad (\text{A.135})$$

$$q_{SP} = \frac{1}{2} \rho V_{TSP}^2 \quad (\text{A.136})$$

Spinner/Pylon Angle of Attack in Mast Axes

$$\alpha_{SPN} = \arctan \left(\frac{\sqrt{U_{MSP}^2 + V^2}}{|W_{MSP}|} \right) \quad (\text{A.137})$$

Spinner Drag in Wind Axes

$$SD = 2q_{sp} \left[(SD/q)_{\beta_M=90^\circ} + (SD/q) \sin^3 \alpha_{SPN} \right] \quad (\text{A.138})$$

Angles of Attack and Sideslip for Transformation into Body Axes

$$\alpha_{SP} = \arctan \left(\frac{W + W_{iSP}}{U + U_{iSP}} \right), \quad [\text{rad}] \quad (\text{A.139})$$

$$\beta_{SP} = \arctan \left(\frac{V}{\sqrt{(U + U_{iSP})^2 + (W + W_{iSP})^2}} \right), \quad [\text{rad}] \quad (\text{A.140})$$

Where:

$$U + U_{iSP} = \min(0.15, U + U_{iSP})$$

Spinner Drag in Body Axes

$$\begin{Bmatrix} X_{SD} \\ Y_{SD} \\ Z_{SD} \end{Bmatrix} = \begin{bmatrix} -\cos \alpha_{SP} \cos \beta_{SP} & -\cos \alpha_{SP} \sin \beta_{SP} & \sin \alpha_{SP} \\ -\sin \beta_{SP} & \cos \beta_{SP} & 0 \\ -\sin \alpha_{SP} \cos \beta_{SP} & -\sin \alpha_{SP} \sin \beta_{SP} & -\cos \alpha_{SP} \end{bmatrix} \begin{Bmatrix} SD \\ 0 \\ 0 \end{Bmatrix} \quad (\text{A.141})$$

Moments due to Spinner Drag

$$l_{SD} = -Y_{SD} (WL_{CG} - WL_{SP} - l_m \cos \beta_M) \quad (\text{A.142})$$

$$M_{SD} = X_{SD} (WL_{CG} - WL_{SP} - l_m \cos \beta_M) + Z_{SD} (SL_{CG} - SL_{SP} + l_m \sin \beta_M) \quad (\text{A.143})$$

$$N_{SD} = Y_{SD} (SL_{CG} - SL_{SP} + l_m \sin \beta_M) \quad (\text{A.144})$$

A.4.6 Pylon Drag

Pylon Drag in Wind Axes

$$D_{PLAT} = 2q_{PLAT}S_{PLAT}K_{PLAT} \quad (A.145)$$

Where:

$$S_{PLAT} = S_{PYL} \left| \frac{V}{\sqrt{U_{MSP}^2 + V^2}} \right| \quad (A.146)$$

$$K_{PLAT} = f(\alpha_{PYL})$$

$$\alpha_{PYL} = \alpha_{SPN}$$

$$q_{PLAT} = q_{SP}$$

Angles of Attack and Sideslip For Transformation into Body Axes

$$\alpha_{PLAT} = \alpha_{SP} \quad (A.147)$$

$$\beta_{PLAT} = \beta_{SP} \quad (A.148)$$

Pylon Drag in Body Axes

$$\begin{Bmatrix} X_{PLAT} \\ Y_{PLAT} \\ Z_{PLAT} \end{Bmatrix} = \begin{bmatrix} -\cos \alpha_{PLAT} \cos \beta_{PLAT} & -\cos \alpha_{PLAT} \sin \beta_{PLAT} & \sin \alpha_{PLAT} \\ -\sin \beta_{PLAT} & \cos \beta_{PLAT} & 0 \\ -\sin \alpha_{PLAT} \cos \beta_{PLAT} & -\sin \alpha_{PLAT} \sin \beta_{PLAT} & -\cos \alpha_{PLAT} \end{bmatrix} \begin{Bmatrix} D_{PLAT} \\ 0 \\ 0 \end{Bmatrix} \quad (A.149)$$

Moments due to Pylon Drag

$$l_{PLAT} = -Y_{PLAT} (WL_{CG} - WL_{SP}) \quad (A.150)$$

$$M_{PLAT} = X_{PLAT} (WL_{CG} - WL_{SP}) - Z_{PLAT} (SL_{CG} - SL_{SP}) \quad (A.151)$$

$$N_{PLAT} = Y_{PLAT} (SL_{CG} - SL_{SP}) \quad (A.152)$$

A.5 LANDING GEAR

Dynamic Pressure

$$q_{LG} = \frac{1}{2} \rho V_T^2 \quad (A.153)$$

Angles for Transformation between Wind and Body Axes

$$\alpha_{MG} = \alpha_{NG} = \alpha_F \quad (A.154)$$

$$\beta_{MG} = \beta_{NG} = \beta_F \quad (A.155)$$

Landing Gear Drag in Wind Axes

$$D_{MG} = q_{LG} (D_{0MG} + D_{POD}) \quad (\text{A.156})$$

$$D_{NG} = q_{LG} D_{0NG} \quad (\text{A.157})$$

Landing Gear Drag in Body Axes Due to the Main

$$\begin{Bmatrix} X_{MG} \\ Y_{MG} \\ Z_{MG} \end{Bmatrix} = \begin{bmatrix} -\cos \alpha_F \cos \beta_F & -\cos \alpha_F \sin \beta_F & \sin \alpha_F \\ -\sin \beta_F & \cos \beta_F & 0 \\ -\sin \alpha_F \cos \beta_F & -\sin \alpha_F \sin \beta_F & -\cos \alpha_F \end{bmatrix} \begin{Bmatrix} D_{MG} \\ 0 \\ 0 \end{Bmatrix} \quad (\text{A.158})$$

Landing Gear Drag in Body Axes Due to the Nose

$$\begin{Bmatrix} X_{NG} \\ Y_{NG} \\ Z_{NG} \end{Bmatrix} = \begin{bmatrix} -\cos \alpha_F \cos \beta_F & -\cos \alpha_F \sin \beta_F & \sin \alpha_F \\ -\sin \beta_F & \cos \beta_F & 0 \\ -\sin \alpha_F \cos \beta_F & -\sin \alpha_F \sin \beta_F & -\cos \alpha_F \end{bmatrix} \begin{Bmatrix} D_{NG} \\ 0 \\ 0 \end{Bmatrix} \quad (\text{A.159})$$

Landing Gear Moments Due to the Main

$$l_{MG} = -Y_{MG} (WL_{CG} - WL_{MG}) \quad (\text{A.160})$$

$$M_{MG} = X_{MG} (WL_{CG} - WL_{MG}) - Z_{MG} (SL_{CG} - SL_{MG}) \quad (\text{A.161})$$

$$N_{MG} = Y_{MG} (SL_{CG} - SL_{MG}) \quad (\text{A.162})$$

Landing Gear Moments Due to the Nose

$$l_{NG} = -Y_{NG} (WL_{CG} - WL_{NG}) \quad (\text{A.163})$$

$$M_{NG} = X_{NG} (WL_{CG} - WL_{NG}) - Z_{NG} (SL_{CG} - SL_{NG}) \quad (\text{A.164})$$

$$N_{NG} = Y_{NG} (SL_{CG} - SL_{NG}) \quad (\text{A.165})$$

A.6 JET THRUST**Jet Thrust in Wind Axes**

$$JT_K = K_{JT1} + K_{JT2} HP_{ENG} X_{EK} \quad (\text{A.166})$$

Jet Thrust in Body Axes

$$X_{JTR} = JT_R \sin \beta_M \quad (\text{A.167})$$

$$Y_{JTR} = JT_R \sin \phi_M \quad (\text{A.168})$$

$$Z_{JTR} = -JT_R \cos \beta_M \cos \phi_M \quad (\text{A.169})$$

$$X_{JTL} = JT_L \sin \beta_M \quad (\text{A.170})$$

$$Y_{JTL} = -JT_L \sin \phi_M \quad (\text{A.171})$$

$$Z_{JTL} = -JT_L \cos \beta_M \cos \phi_M \quad (\text{A.172})$$

Moments Due to Jet Thrust

$$l_{JT} = Z_{JTR} (BL_{SP} - BL_{CG}) + Z_{JTL} (-BL_{SP} - BL_{CG}) + \quad (A.173)$$

$$- (Y_{JTR} + Y_{JTL}) (WL_{CG} - WL_{SP})$$

$$M_{JT} = (X_{JTR} + X_{JTL}) (WL_{CG} - WL_{SP}) + \quad (A.174)$$

$$- (Z_{JTR} + Z_{JTL}) (SL_{CG} - SL_{SP})$$

$$N_{JT} = -X_{JTR} (BL_{SP} - BL_{CG}) - X_{JTL} (-BL_{SP} - BL_{CG}) + \quad (A.175)$$

$$+ (Y_{JTR} + Y_{JTL}) (SL_{CG} - SL_{SP})$$

B | AERODYNAMIC TABLES

B.1 FUSELAGE

[-7.23	-3.61	0.01	3.63	7.25	10.87
	15.00	17.00	18.00	19.00	20.00	20.00
	18.00	14.00	6.00	0.00	-6.00	-14.00
	-18.00	-20.00	-20.00	-19.00	-18.00	-17.00
	-15.00	-10.87	-7.25	-3.63	-0.01	3.61
	7.23	10.85	14.47	18.09	21.71	25.33
	28.00	32.00	36.00	40.00	43.00	45.00
	40.00	35.00	25.00	0.00	-25.00	-35.00
	-40.00	-45.00	-43.00	-40.00	-36.00	-32.00
	-28.00	-25.33	-21.71	-18.09	-14.47	-10.85
	-7.23;	%Lalpha				
	-180	-176	-172	-168	-164	-160
	-156	-152	-148	-144	-140	-130
	-120	-110	-100	-90	-80	-70
	-60	-50	-40	-36	-32	-28
	-24	-20	-16	-12	-8	-4
	0	4	8	12	16	20
	24	28	32	36	40	50
	60	70	80	90	100	110
	120	130	140	144	148	152
	156	160	164	168	172	176
	180];	%alphaF				

Figure B.1: Fuselage $L_\alpha: L_\alpha \rightarrow [ft^2], \alpha_F \rightarrow [deg]$

```

[ 1.56 1.80 3.00 6.17 10.78 15.39
 20.00 25.00 35.00 45.00 55.00 80.00
100.00 108.00 111.50 114.00 115.50 116.00
115.50 114.00 111.50 108.00 100.00 80.00
 55.00 45.00 35.00 25.00 20.00 15.39
 10.78 6.17 3.00 1.80 1.56 1.80
 2.30 3.67 5.78 7.89 10.00 15.00
20.00 25.00 30.00 50.00 70.00 80.00
90.00 93.75 95.00 93.75 90.00 80.00
70.00 50.00 30.00 25.00 20.00 15.00
10.00 7.89 5.78 3.67 2.30 1.80
1.56; %Dalpha
-180 -176 -172 -168 -164 -160
-156 -152 -148 -144 -140 -130
-120 -110 -105 -100 -95 -90
 -85 -80 -75 -70 -60 -50
 -40 -36 -32 -28 -24 -20
 -16 -12 -8 -4 0 4
 8 12 16 20 24 28
 32 36 40 50 60 70
 80 85 90 95 100 110
120 130 140 144 148 152
156 160 164 168 172 176
180]; %alphaF

```

Figure B.2: Fuselage D_α : $D_\alpha \rightarrow [ft^2]$, $\alpha_F \rightarrow [deg]$

```

[ -66.50 -142.50 -219.00 -295.00 -370.00 -380.00
-430.00 -440.00 -440.00 -410.00 -360.00 -160.00
 70.00 270.00 445.00 570.00 645.00 670.00
645.00 570.00 445.00 270.00 70.00 -160.00
-360.00 -410.00 -440.00 -440.00 -430.00 -380.00
-370.00 -295.00 -219.00 -142.50 -66.50 9.50
 85.50 123.50 142.50 133.00 95.00 95.00
133.00 114.00 95.00 20.00 -50.00 -130.00
-210.00 -277.50 -300.00 -277.50 -210.00 -130.00
-50.00 20.00 95.00 114.00 133.00 95.00
 95.00 133.00 142.50 123.50 85.50 9.50
-66.50; %Malpha
-180 -176 -172 -168 -164 -160
-156 -152 -148 -144 -140 -130
-120 -110 -105 -100 -95 -90
 -85 -80 -75 -70 -60 -50
 -40 -36 -32 -28 -24 -20
 -16 -12 -8 -4 0 4
 8 12 16 20 24 28
 32 36 40 50 60 70
 80 85 90 95 100 110
120 130 140 144 148 152
156 160 164 168 172 176
180]; %alphaF

```

Figure B.3: Fuselage M_α : $M_\alpha \rightarrow [ft^3]$, $\alpha_F \rightarrow [deg]$

```

[ 7.23    5.00    0.00  -15.00  -40.00  -90.00
-120.00 -121.93 -123.73 -125.40 -126.93 -128.33
-129.60 -130.73 -131.73 -132.60 -133.33 -133.93
-134.40 -134.73 -134.93 -135.00 -134.93 -134.73
-134.40 -133.93 -133.33 -132.60 -131.73 -130.73
-129.60 -128.33 -126.93 -125.40 -123.73 -121.93
-120.00  -90.00  -40.00  -15.00    0.00    5.00
 5.2174  5.4237  5.6188  5.8028  5.9756  6.1373
 6.2878  6.4272  6.5554  6.6725  6.7784  6.8732
 6.9568  7.0293  7.0906  7.1408  7.1798  7.2077
 7.2244  7.2300  7.2244  7.2077  7.1798  7.1408
 7.0906  7.0293  6.9568  6.8732  6.7784  6.6725
 6.5554  6.4272  6.2878  6.1373  5.9756  5.8028
 5.6188  5.4237  5.2174    5.00    0.00  -15.00
 -40.00  -90.00 -120.00 -121.93 -123.73 -125.40
-126.93 -128.33 -129.60 -130.73 -131.73 -132.60
-133.33 -133.93 -134.40 -134.73 -134.93 -135.00
-134.93 -134.73 -134.40 -133.93 -133.33 -132.60
-131.73 -130.73 -129.60 -128.33 -126.93 -125.40
-123.73 -121.93 -120.00  -90.00  -40.00  -15.00
  0.00    5.00    7.23 ; %Lbeta
 -180   -170   -160   -150   -140   -130
 -120   -118   -116   -114   -112   -110
 -108   -106   -104   -102   -100   -98
  -96    -94    -92    -90    -88    -86
  -84    -82    -80    -78    -76    -74
  -72    -70    -68    -66    -64    -62
  -60    -50    -40    -30    -20    -10
 -9.50  -9.00  -8.50  -8.00  -7.50  -7.00
 -6.50  -6.00  -5.50  -5.00  -4.50  -4.00
 -3.50  -3.00  -2.50  -2.00  -1.50  -1.00
 -0.50    0    0.50  1.00  1.50  2.00
  2.50  3.00  3.50  4.00  4.50  5.00
  5.50  6.00  6.50  7.00  7.50  8.00
  8.50  9.00  9.50   10   20   30
   40   50   60   62   64   66
   68   70   72   74   76   78
   80   82   84   86   88   90
   92   94   96   98  100  102
  104  106  108  110  112  114
  116  118  120  130  140  150
  160  170  180]; %betaF

```

Figure B.4: Fuselage L_β : $L_\beta \rightarrow [ft^2]$, $\beta_F \rightarrow [deg]$

```

[ 1.56    5.00   10.00   20.00   40.00   60.00
 80.00  100.00  120.00  124.20  125.00  124.2
120.00  100.00   80.00   60.00   40.00   20.00
 10.00    5.00  4.6646  4.3464  4.0454  3.7616
 3.4950  3.2456  3.0134  2.7984  2.6006  2.4200
 2.2566  2.1104  1.9814  1.8696  1.7750  1.6976
 1.6374  1.5944  1.5686  1.5600  1.5686  1.5944
 1.6374  1.6976  1.7750  1.8696  1.9814  2.1104
 2.2566  2.4200  2.6006  2.7984  3.0134  3.2456
 3.4950  3.7616  4.0454  4.3464  4.6646    5.00
 10.00   20.00   40.00   60.00   80.00  100.00
120.00  124.20  125.00  124.20  120.00  100.00
 80.00   60.00   40.00   20.00   10.00    5.00
 1.56; %DBeta
-180   -170   -160   -150   -140   -130
-120   -110   -100   -94    -90    -86
 -80    -70    -60    -50    -40    -30
 -20    -10    -9.50  -9.00  -8.50  -8.00
-7.50  -7.00  -6.50  -6.00  -5.50  -5.00
-4.50  -4.00  -3.50  -3.00  -2.50  -2.00
-1.50  -1.00  -0.50   0     0.50   1.00
 1.50   2.00   2.50   3.00   3.50   4.00
 4.50   5.00   5.50   6.00   6.50   7.00
 7.50   8.00   8.50   9.00   9.50   10
 20     30     40     50     60     70
 80     86     90     94     100    110
 120    130    140    150    160    170
180]; %betaF

```

Figure B.5: Fuselage D_β : $D_\beta \rightarrow [ft^2]$, $\beta_F \rightarrow [deg]$

```

[ -66.50  -66.50  -54.80  -34.00  -14.00   0.00
 70.00   140.00  210.00  210.00  140.00  70.00
 0.00   -14.00  -34.00  -54.80  -66.50  -66.50
-66.50  -54.80  -34.00  -14.00   0.00  70.00
140.00  210.00  210.00  140.00  70.00   0.00
-14.00  -34.00  -54.80  -66.50  -66.50  -66.50
-54.80  -34.00  -14.00   0.00  70.00  140.00
210.00  210.00  140.00   70.00   0.00  -14.00
-34.00  -54.80  -66.50  -66.50  -66.50  -54.80
-34.00  -14.00   0.00   70.00  140.00  210.00
210.00  140.00   70.00   0.00  -14.00  -34.00
-54.80  -66.50  -66.50; %MBeta
-180   -178   -176   -174   -172   -170
-160   -150   -140   -130   -120   -110
-100   -98    -96    -94    -92    -90
 -88    -86    -84    -82    -80    -70
 -60    -50    -40    -30    -20    -10
  -8     -6     -4     -2     0     2
   4     6     8     10    20    30
  40    50    60    70    80    82
  84    86    88    90    92    94
  96    98   100   110   120   130
 140   150   160   170   172   174
 176   178   180]; %betaF

```

Figure B.6: Fuselage M_β : $M_\beta \rightarrow [ft^3]$, $\beta_F \rightarrow [deg]$

```
[ 0.00 -75.00 -150.00 -225.00 -275.00 -275.00
-225.00 -150.00 -75.00 0.00 75.00 150.00
225.00 275.00 275.00 225.00 150.00 75.00
0.00 -75.00 -150.00 -225.00 -275.00 -275.00
-225.00 -150.00 -75.00 0.00 75.00 150.00
225.00 275.00 275.00 225.00 150.00 75.00
0.00; %lbeta
-180 -170 -160 -150 -140 -130
-120 -110 -100 -90 -80 -70
-60 -50 -40 -30 -20 -10
0 10 20 30 40 50
60 70 80 90 100 110
120 130 140 150 160 170
180]; %betaF
```

Figure B.7: Fuselage l_β : $l_\beta \rightarrow [ft^3]$, $\beta_F \rightarrow [deg]$

```
[ 0.00 -202.00 -404.00 -600.00 -700.00 -700.00
-600.00 -404.00 -202.00 0.00 202.00 404.00
600.00 700.00 700.00 600.00 404.00 202.00
0.00 -202.00 -404.00 -600.00 -700.00 -700.00
-600.00 -404.00 -202.00 0.00 202.00 404.00
600.00 700.00 700.00 600.00 404.00 202.00
0.00; %NBeta
-180 -170 -160 -150 -140 -130
-120 -110 -100 -90 -80 -70
-60 -50 -40 -30 -20 -10
0 10 20 30 40 50
60 70 80 90 100 110
120 130 140 150 160 170
180]; %betaF
```

Figure B.8: Fuselage N_β : $N_\beta \rightarrow [ft^3]$, $\beta_F \rightarrow [deg]$

```
[ 0.00 -14.50 -29.00 -43.50 -50.00 -50.00
-43.50 -29.00 -14.50 0.00 14.50 29.00
43.50 50.00 50.00 43.50 29.00 14.50
0.00 -14.50 -29.00 -43.50 -50.00 -50.00
-43.50 -29.00 -14.50 0.00 14.50 29.00
43.50 50.00 50.00 43.50 29.00 14.50
0.00; %Ybeta
-180 -170 -160 -150 -140 -130
-120 -110 -100 -90 -80 -70
-60 -50 -40 -30 -20 -10
0 10 20 30 40 50
60 70 80 90 100 110
120 130 140 150 160 170
180]; %lbeta
```

Figure B.9: Fuselage Y_β : $Y_\beta \rightarrow [ft^2]$, $\beta_F \rightarrow [deg]$

B.2 HORIZONTAL STABILIZER

$$\begin{aligned} MN &= [0.0 \ 0.2 \ 0.4 \ 0.5 \ 0.6 \ 0.7] \\ XK_e &= [1.0 \ 1.0 \ 0.965 \ 0.95 \ 0.93 \ 0.90] \end{aligned}$$

Figure B.10: $XK_e=f(M_N): XK_e \rightarrow [ND], M_N \rightarrow [ND]$

$$\begin{aligned} \text{betaF} &= [-60 \quad -45 \quad -30 \quad -20 \quad -15 \quad -10 \quad -5 \quad 0 \\ &\quad \quad \quad 5 \quad 10 \quad 15 \quad 20 \quad 30 \quad 45 \quad 60 \quad]; \\ \text{KbetaHS} &= [\quad 0.5 \quad 0.707 \quad 0.866 \quad 0.94 \quad 0.966 \quad 0.985 \quad 0.996 \quad 1.0 \\ &\quad \quad 0.996 \quad 0.985 \quad 0.966 \quad 0.94 \quad 0.866 \quad 0.707 \quad 0.5 \quad]; \end{aligned}$$

Figure B.11: $K_{\beta HS}=f(\beta_F): K_{\beta HS} \rightarrow [ND], \beta_F \rightarrow [deg]$

[-180 -40 -30 -28 -24 -20 -16 -12 -8 -4 | 0 4 8 12 16 20 30 180]

(a) α_F for η_H

[1	1	1	1	1	1	1	1	1	1	1	1	1	1	1	1	1	1]	
[1	1	1.17	1.20	1.40	1.70	1.90	2.08	2.20	2.20	2.07	1.90	1.70	1.55	1.37	1.20	1.00	1]	
[1	1	1.08	1.12	1.21	1.43	1.67	1.80	1.88	1.80	1.70	1.60	1.46	1.30	1.05	0.93	1.00	1]	
[1	1	1.00	1.00	1.00	1.05	1.18	1.37	1.54	1.52	1.35	1.10	1.00	0.90	0.82	0.80	1.00	1]	
[1	1	0.92	0.92	0.92	0.93	0.96	1.00	1.25	1.23	1.05	1.00	0.93	0.86	0.80	0.80	1.00	1]	
[1	1	0.935	0.935	0.935	0.935	0.935	0.935	0.935	0.935	0.935	0.935	0.935	0.935	0.860	0.80	0.72	1.00	1]

(b) η_H for $\beta_M = 0$ deg

[1	1	1.000	1.00	1.000	1.00	1.000	1.00	1.00	1.00	1.00	1.00	1.00	1.00	1.00	1.00	1.00	1]
[1	1	1.240	1.37	1.540	1.80	2.000	2.20	2.38	2.44	2.42	2.36	2.23	2.00	1.80	1.60	1.00	1]
[1	1	1.100	1.14	1.240	1.35	1.520	1.63	2.04	2.24	2.25	2.00	1.80	1.60	1.40	1.20	1.00	1]
[1	1	0.970	0.98	0.990	1.00	1.030	1.08	1.15	1.25	1.30	1.23	1.15	1.06	1.00	0.92	1.00	1]
[1	1	0.920	0.90	0.880	0.87	0.870	0.92	0.97	1.00	1.05	1.06	1.05	1.03	0.97	0.90	1.00	1]
[1	1	0.935	0.935	0.935	0.935	0.935	0.935	0.935	0.935	0.935	0.935	0.935	0.935	0.935	0.80	1.00	1]

(c) η_H for $\beta_M = 15$ deg

[1	1	1	1	1	1	1	1	1	1	1	1	1	1	1	1	0.8	1.00	1]
----	---	---	---	---	---	---	---	---	---	---	---	---	---	---	---	-----	------	----

(d) η_H for $\beta_M = 30$ deg

[1	1	1	1	1	1	1	1.05	1.05	1.05	1.05	1.05	1.05	1.05	1.05	1.05	0.80	1.00	1]
----	---	---	---	---	---	---	------	------	------	------	------	------	------	------	------	------	------	----

(e) η_H for $\beta_M = 60$ deg

[1	1	1	1	1	1	1	1	1	1	1	1	1	1	1	1	0.8	1.00	1]
----	---	---	---	---	---	---	---	---	---	---	---	---	---	---	---	-----	------	----

(f) η_H for $\beta_M = 90$ deg

Figure B.12: $\eta_H = f(\alpha_F, V_T, \beta_M): \eta_H \rightarrow [ND], V_T \rightarrow [kts], \beta_M \rightarrow [deg]$. Each column is referred to a certain α_F . Rows depend on V_T : from the first to the last row of each sub-table $V_T = 0, 20, 40, 60, 80, > 100$ kts. For $\beta_M > 30$ deg, η_H for $V_T < 100$ kts is not defined, since they are flight conditions out of the conversion corridor, therefore the single row is referred for $V_T > 100$ kts.

-180	-170	-160	-150	-140	-130
-120	-110	-100	-90	-80	-70
-60	-50	-40	-36	-32	-28
-24	-20	-18.4	-18.0	-17.5	-16.8
-16.0	-15.6	-14.2	-14.0	-12.5	-12
-10	-8	-6	-4	-2	0
2	4	6	8	10	12
12.2	13.0	14.0	15.0	16.0	16.8
18.0	20.0	24	28	32	36
40	50	60	70	80	90
100	110	120	130	140	150
160	170	180];			

(a) α_{HL} for C_{LH} , elements along rows

$$\text{deltaF} = [-20 \quad -15 \quad -10 \quad 0 \quad 10 \quad 15 \quad 20]$$

(b) δ_e for C_{LH} , elements along columns

-1.10		
-1.09		
-1.04		
-1.00		
-0.90		
-0.93		
-0.962		
-0.97		
-0.9825	-0.80	-0.79
-1.00	-0.84	-0.798
-1.02	-0.85	-0.80
-1.0120	-0.865	-0.8175
-0.9840	-0.886	-0.842
-0.98	-0.91	-0.87
-0.9425	-0.916	-0.876
-0.93	-0.937	-0.897
-0.775	-0.94	-0.90
-0.620	-0.895	-0.87
-0.465	-0.88	-0.86
-0.310	-0.78	-0.75
-0.155	-0.656	-0.63
0.000	-0.492	-0.528
0.155	-0.328	-0.352
0.310	-0.164	-0.176
0.465	0.000	0.000
0.620	0.164	0.176
0.775	0.328	0.352
0.93	0.492	0.528
0.935	0.656	0.63
0.955	0.780	0.75
0.98	0.880	0.86
1.0	0.886	0.864
1.02	0.91	0.88
1.00	0.94	0.90
0.97	0.925	0.885
0.93	0.91	0.87
0.9	0.886	0.842
1	0.85	0.8
1.04	0.80	0.79
1.09		
1.1		

(c) C_{LH} for $M_N = 0.4$,
 $-40 < \alpha_{HL} < 40$ deg,
 $\delta_e = 0$ deg

(d) C_{LH} for $M_N = 0.5$,
 $-20 < \alpha_{HL} < 20$ deg,
 $\delta_e = 0$ deg

(e) C_{LH} for $M_N = 0.6$,
 $-20 < \alpha_{HL} < 20$ deg,
 $\delta_e = 0$ deg

-0.8	-0.6	-0.4	0	0.4	0.6	0.8;
-0.1	0.1	0.3	0.7	1.1	1.3	1.5;
-0.1	0.08	0.28	0.6	0.95	1.13	1.3;
-0.04	0.16	0.39	0.84	1.2	1.35	1.45;
0	0.2	0.48	0.98	1.38	1.49	1.6;
0.03	0.22	0.5	0.99	1.36	1.43	1.54;
0.04	0.2	0.46	0.86	1.15	1.23	1.3;
0.04	0.16	0.38	0.66	0.9	0.96	1;
0.04	0.1	0.24	0.4	0.5	0.56	0.6;
0	0	0	0	0	0	0;
-0.6	-0.58	-0.56	-0.425	-0.36	-0.285	-0.22;
-0.92	-0.89	-0.865	-0.72	-0.6	-0.49	-0.38;
-1.12	-1.09	-1.06	-0.9	-0.77	-0.64	-0.51;
-1.24	-1.205	-1.175	-1.002	-0.89	-0.745	-0.6;
-1.3	-1.26	-1.24	-1.05	-0.96	-0.8	-0.64;
-1.3	-1.26	-1.24	-1.04	-0.92	-0.775	-0.63;
-1.29	-1.255	-1.23	-1.03	-0.89	-0.735	-0.6;
-1.28	-1.24	-1.21	-1.01	-0.84	-0.68	-0.56;
-1.26	-1.22	-1.185	-0.98	-0.78	-0.615	-0.5;
-1.235	-1.198	-1.16	-0.93	-0.69	-0.5	-0.42;
-1.24	-1.21	-1.2	-0.92	-0.66	-0.54	-0.48;
-1.2444	-1.2278	-1.2267	-0.9244	-0.6822	-0.5511	-0.4667;
-1.25	-1.25	-1.26	-0.93	-0.71	-0.565	-0.45;
-1.31	-1.29	-1.31	-0.99	-0.74	-0.55	-0.42;
-1.33	-1.33	-1.4	-1.12	-0.71	-0.51	-0.38;
-1.35	-1.38	-1.44	-1.10	-0.70	-0.48	-0.35;
-1.45	-1.55	-1.4	-1.0082	-0.61	-0.4	-0.27;
-1.4676	-1.5429	-1.3894	-0.9940	-0.5947	-0.3859	-0.2559;
-1.60	-1.49	-1.31	-0.8875	-0.48	-0.28	-0.15;
-1.60318	-1.464375	-1.26025	-0.852	-0.44375	-0.239625	-0.10082;
-1.4612	-1.3224	-1.1182	-0.710	-0.3017	-0.0976	0.0412;
-1.3192	-1.1804	-0.9762	-0.568	-0.1597	0.0444	0.1832;
-1.1772	-1.0384	-0.8342	-0.426	-0.0177	0.1864	0.3252;
-1.0352	-0.8964	-0.6923	-0.284	0.1243	0.3284	0.4672;
-0.8932	-0.7544	-0.5503	-0.142	0.2663	0.4704	0.6092;
-0.7512	-0.6124	-0.4083	0.000	0.4083	0.6124	0.7512;
-0.6092	-0.4704	-0.2662	0.142	0.5503	0.7544	0.8932;
-0.4672	-0.3284	-0.1243	0.284	0.6923	0.8964	1.0352;
-0.3252	-0.1864	0.0177	0.426	0.8343	1.0384	1.1772;
-0.18318	-0.044375	0.15975	0.568	0.97625	1.180375	1.31918;
-0.0412	0.0976	0.3017	0.710	1.1131	1.3002	1.4096;
0.10082	0.239625	0.44375	0.852	1.25	1.42	1.5;
0.11502	0.253825	0.45795	0.8662	1.27	1.43	1.48;
0.17182	0.310625	0.51475	0.923	1.30	1.37	1.45;
0.2309	0.3803	0.5824	0.9615	1.25	1.32	1.405;
0.29	0.45	0.65	1.0	1.20	1.27	1.36;
0.32	0.475	0.69	0.98	1.16	1.24	1.32;
0.34	0.49	0.70	0.94	1.15	1.20	1.32;
0.37	0.5	0.68	0.89	1.13	1.22	1.34;
0.38	0.465	0.6	0.88	1.18	1.28	1.38;
0.33	0.455	0.66	0.935	1.3	1.38	1.44;
0.38	0.5	0.73	1	1.37	1.44	1.5;
0.4	0.54	0.78	1.05	1.43	1.49	1.54;
0.41	0.56	0.82	1.08	1.47	1.535	1.57;
0.41	0.57	0.84	1.1	1.51	1.56	1.59;
0.36	0.56	0.83	1.09	1.5	1.56	1.59;
0.29	0.45	0.63	0.88	1.15	1.22	1.26;
0.2	0.3	0.42	0.62	0.78	0.8	0.83;
0.1	0.16	0.21	0.34	0.4	0.41	0.42;
0	0	0	0	0	0	0;
-0.6	-0.56	-0.5	-0.4	-0.24	-0.1	-0.04;
-1	-0.96	-0.9	-0.66	-0.38	-0.16	-0.04;
-1.3	-1.23	-1.15	-0.86	-0.46	-0.2	-0.04;
-1.45	-1.43	-1.36	-0.99	-0.5	-0.22	-0.03;
-1.6	-1.49	-1.38	-0.98	-0.48	-0.2	0;
-1.45	-1.35	-1.2	-0.84	-0.39	-0.16	0.04;
-1.3	-1.13	-0.95	-0.6	-0.28	-0.08	0.1;
-1.5	-1.3	-1.1	-0.7	-0.3	-0.1	0.1;
-0.8	-0.6	-0.4	0	0.4	0.6	0.8;

(a) C_{LH} for $M_N = 0 - 0.2$

Figure B.14: $C_{LH} = f(\alpha_{HL}, \delta_e, M_N): C_{LH} \rightarrow [ND], \alpha_{HL} \rightarrow [deg], \delta_e \rightarrow [deg], M_N \rightarrow [ND]$

-180	-170	-160	-150	-140	-130	-120	-110	-100	-90
-80	-70	-60	-50	-40	-36	-32	-28	-24	-20
-16	-12	-8	-4	0	4	8	12	16	20
24	28	32	36	40	50	60	70	80	90
100	110	120	130	140	150	160	170	180]	

(a) α_{HD} for C_{DH}

[0.01	0.02	0.20	0.40	0.55	0.67	0.78	0.85	0.89
0.92	0.91	0.87	0.81	0.72	0.60	0.54	0.47	0.39
0.30	0.20	0.115	0.068	0.035	0.015	0.00875	0.015	0.035
0.068	0.115	0.20	0.34	0.48	0.61	0.72	0.80	0.93
1.05	1.14	1.18	1.20]					

(b) C_{DH} for $M_N = 0 - 0.2$

[0.135	0.068	0.035	0.015	0.00875	0.015	0.035	0.075	0.145]
--------	-------	-------	-------	---------	-------	-------	-------	--------

(c) C_{DH} for $M_N = 0.4, -16 \text{ deg} < \alpha_{HD} < 16 \text{ deg}$

[0.088	0.035	0.015	0.00875	0.015	0.045	0.105	0.115]
--------	-------	-------	---------	-------	-------	-------	--------

(d) C_{DH} for $M_N = 0.5, -12 \text{ deg} < \alpha_{HD} < 12 \text{ deg}$

[0.045	0.015	0.00875	0.015	0.065	0.068]
--------	-------	---------	-------	-------	--------

(e) C_{DH} for $M_N = 0.6, -8 \text{ deg} < \alpha_{HD} < 8 \text{ deg}$ **Figure B.15:** $C_{DH} = f(\alpha_{HD}, M_N)$: $C_{DH} \rightarrow [ND]$, $\alpha_{HD} \rightarrow [deg]$, $M_N \rightarrow [ND]$

B.3 VERTICAL STABILIZER

XK_V and η_V are shared with the Horizontal Stabilizer, where they are called XK_e and η_H .

[-10 3 0 7 13 28]
(a) α_F for sidewash, along rows
[0 4 8 12 16 20 50 51]
(b) β_F for sidewash, along columns
[1.0000 1.0000 1.0000 1.0000 1.0000 1.0000 1.0000 1.0000;
1.1000 1.1000 1.0500 1.0150 0.9850 1.0100 1.0100 1.0000;
1.0380 1.0380 1.0440 0.9650 0.9330 1.0000 1.0000 1.0000;
0.8630 0.8630 0.8100 0.7720 0.7870 0.9580 0.9580 1.0000;
0.5240 0.5240 0.5170 0.4740 0.4910 0.6730 0.6730 1.0000;
1.0000 1.0000 1.0000 1.0000 1.0000 1.0000 1.0000 1.0000]
(c) Sidewash factor for $\beta_M = 0$ deg
[1.0000 1.0000 1.0000 1.0000 1.0000 1.0000 1.0000 1.0000;
1.1300 1.1300 1.0720 0.9700 1.0250 1.0000 1.0000 1.0000;
1.2480 1.2480 1.0930 0.9770 1.0150 1.0560 1.0560 1.0000;
0.9950 0.9950 0.9610 0.8650 0.8450 0.9530 0.9530 1.0000;
0.6770 0.6770 0.5950 0.5230 0.5260 0.6810 0.6810 1.0000;
1.0000 1.0000 1.0000 1.0000 1.0000 1.0000 1.0000 1.0000]
(d) Sidewash factor for $\beta_M = 30$ deg
[1.0000 1.0000 1.0000 1.0000 1.0000 1.0000 1.0000 1.0000;
1.1500 1.1500 1.0500 1.0000 1.0600 1.1000 1.1000 1.0000;
1.2100 1.2100 1.0800 0.9750 1.0200 1.0250 1.0250 1.0000;
0.9450 0.9450 0.9750 0.9000 0.8800 0.9200 0.9200 1.0000;
0.6900 0.6900 0.6450 0.5850 0.5900 0.7000 0.7000 1.0000;
1.0000 1.0000 1.0000 1.0000 1.0000 1.0000 1.0000 1.0000]
(e) Sidewash factor for $\beta_M = 60$ deg
[1.0000 1.0000 1.0000 1.0000 1.0000 1.0000 1.0000 1.0000;
1.0900 1.0900 1.1000 1.1800 1.1500 1.0400 1.0400 1.0000;
1.0000 1.0000 1.0000 1.0000 1.0000 1.0000 1.0000 1.0000;
0.8340 0.8340 0.8650 0.8660 0.8420 0.9240 0.9240 1.0000;
0.6590 0.6590 0.6760 0.6220 0.6420 0.6800 0.6800 1.0000;
1.0000 1.0000 1.0000 1.0000 1.0000 1.0000 1.0000 1.0000]
(f) Sidewash factor for $\beta_M = 90$ deg

Figure B.16: Sidewash Factor for $X_{FL} = 0/0$. $\left(1 - \frac{\partial \sigma}{\partial \beta_F}\right) = f(\alpha_F, |\beta_F|, \beta_M, X_{FL})$:
 $\left(1 - \frac{\partial \sigma}{\partial \beta_F}\right) \rightarrow [ND], \alpha_F \rightarrow [deg], \beta_F \rightarrow [deg], \beta_M \rightarrow [deg]$

			[-10	3	0	7	13	28]	
			(a) α_F for sidewash, along rows						
			[0	4	8	12	16	20	50 51]
			(b) β_F for sidewash, along columns						
			[1.0000	1.0000	1.0000	1.0000	1.0000	1.0000	1.0000; 1.0000;
			1.3150	1.3150	1.2600	1.1850	1.1000	1.0590	1.0590 1.0000;
			1.2280	1.2280	1.2080	1.1200	1.0450	1.0000	1.0000 1.0000;
			0.8900	0.8900	0.9100	0.8600	0.8090	0.8600	0.8600 1.0000;
			0.5350	0.5350	0.5900	0.3960	0.4430	0.6780	0.6780 1.0000;
			1.0000	1.0000	1.0000	1.0000	1.0000	1.0000	1.0000 1.0000]
			(c) Sidewash factor for $\beta_M = 0$ deg						
			[1.0000	1.0000	1.0000	1.0000	1.0000	1.0000	1.0000; 1.0000;
			1.0650	1.0650	1.0270	1.0550	1.1400	1.0550	1.0550 1.0000;
			1.1000	1.1000	1.1150	1.0580	1.1200	1.0650	1.0650 1.0000;
			1.0250	1.0250	0.9350	0.9720	0.8820	0.8600	0.8600 1.0000;
			0.8840	0.8840	0.8200	0.6290	0.4560	0.6890	0.6890 1.0000;
			1.0000	1.0000	1.0000	1.0000	1.0000	1.0000	1.0000 1.0000]
			(d) Sidewash factor for $\beta_M = 30$ deg						
			[1.0000	1.0000	1.0000	1.0000	1.0000	1.0000	1.0000; 1.0000;
			1.0200	1.0200	1.0300	1.0800	1.1170	1.0400	1.0400 1.0000;
			0.9450	0.9450	1.0700	0.9980	1.0500	1.0900	1.0900 1.0000;
			1.0300	1.0300	0.9850	1.0150	0.9500	0.9080	0.9080 1.0000;
			0.9150	0.9150	0.9000	0.8000	0.6100	0.7450	0.7450 1.0000;
			1.0000	1.0000	1.0000	1.0000	1.0000	1.0000	1.0000 1.0000]
			(e) Sidewash factor for $\beta_M = 60$ deg						
			[1.0000	1.0000	1.0000	1.0000	1.0000	1.0000	1.0000; 1.0000;
			1.0700	1.0700	1.1210	1.1600	1.0720	1.0400	1.0400 1.0000;
			0.9840	0.9840	1.1500	1.0900	1.0500	1.0640	1.0640 1.0000;
			0.9820	0.9820	1.0350	1.0300	0.9930	1.0150	1.0150 1.0000;
			0.8420	0.8420	0.7400	0.7700	0.6950	0.7250	0.7250 1.0000;
			1.0000	1.0000	1.0000	1.0000	1.0000	1.0000	1.0000 1.0000]
			(f) Sidewash factor for $\beta_M = 90$ deg						

Figure B.18: Sidewash Factor for $X_{FL} = 40/25$. $\left(1 - \frac{\partial \sigma}{\partial \beta_F}\right) = f(\alpha_F, |\beta_F|, \beta_M, X_{FL})$:
 $\left(1 - \frac{\partial \sigma}{\partial \beta_F}\right) \rightarrow [ND], \alpha_F \rightarrow [deg], \beta_F \rightarrow [deg], \beta_M \rightarrow [deg]$

[-10 3 0 7 13 28]							
(a) α_F for sidewash, along rows							
[0 4 8 12 16 20 50 51]							
(b) β_F for sidewash, along columns							
[1.0000	1.0000	1.0000	1.0000	1.0000	1.0000	1.0000	1.0000;
1.1800	1.1800	1.2200	1.1550	1.1050	1.0480	1.0480	1.0000;
1.1280	1.1280	1.1850	1.1250	1.0450	1.0100	1.0100	1.0000;
0.8460	0.8460	0.9900	0.9480	0.9200	0.8620	0.8620	1.0000;
0.5350	0.5350	0.6500	0.4400	0.5100	0.6500	0.6500	1.0000;
1.0000	1.0000	1.0000	1.0000	1.0000	1.0000	1.0000	1.0000]
(c) Sidewash factor for $\beta_M = 0$ deg							
[1.0000	1.0000	1.0000	1.0000	1.0000	1.0000	1.0000	1.0000;
1.0500	1.0500	1.0720	1.1400	1.1350	1.0800	1.0800	1.0000;
0.9790	0.9790	1.0100	1.1050	1.1000	1.0350	1.0350	1.0000;
0.8200	0.8200	0.8620	0.9980	0.9860	0.9320	0.9320	1.0000;
0.6500	0.6500	0.7200	0.7000	0.5200	0.7800	0.7800	1.0000;
1.0000	1.0000	1.0000	1.0000	1.0000	1.0000	1.0000	1.0000]
(d) Sidewash factor for $\beta_M = 30$ deg							
[1.0000	1.0000	1.0000	1.0000	1.0000	1.0000	1.0000	1.0000;
1.0250	1.0250	1.0850	1.1500	1.1150	1.0750	1.0750	1.0000;
0.9150	0.9150	1.0050	1.1000	1.1000	1.0400	1.0400	1.0000;
0.8550	0.8550	0.9000	1.0150	0.9550	0.9950	0.9950	1.0000;
0.7300	0.7300	0.8000	0.8000	0.6100	0.8200	0.8200	1.0000;
1.0000	1.0000	1.0000	1.0000	1.0000	1.0000	1.0000	1.0000]
(e) Sidewash factor for $\beta_M = 60$ deg							
[1.0000	1.0000	1.0000	1.0000	1.0000	1.0000	1.0000	1.0000;
1.0580	1.0580	1.1500	1.1450	1.0750	1.0400	1.0400	1.0000;
1.0000	1.0000	1.1200	1.1200	1.0500	1.0880	1.0880	1.0000;
0.9050	0.9050	1.0050	1.0300	0.9900	1.0280	1.0280	1.0000;
0.7820	0.7820	0.7600	0.7200	0.6600	0.7100	0.7100	1.0000;
1.0000	1.0000	1.0000	1.0000	1.0000	1.0000	1.0000	1.0000]
(f) Sidewash factor for $\beta_M = 90$ deg							

Figure B.19: Sidewash Factor for $X_{FL} = 75/47$. $\left(1 - \frac{\partial \sigma}{\partial \beta_F}\right) = f(\alpha_F, |\beta_F|, \beta_M, X_{FL})$:
 $\left(1 - \frac{\partial \sigma}{\partial \beta_F}\right) \rightarrow [ND], \alpha_F \rightarrow [deg], \beta_F \rightarrow [deg], \beta_M \rightarrow [deg]$

[0 20 40 60 80 100 120 350]							
(a) V_T for $K_{\beta R}$, along rows							
[0 5 10 15 20 25 30]							
(b) β_F for $K_{\beta R}$, along columns							
[1.0000	1.0000	1.0000	1.0000	1.0000	1.0000	1.0000	1.0000;
1.0000	1.0000	1.0000	1.0000	1.0000	1.0000	1.0000	1.0000;
0.5000	0.2500	0.8000	1.2500	1.5000	1.0000	1.0000	1.0000;
0.2000	0.4000	0.8000	1.1000	1.4000	1.0000	1.0000	1.0000;
0.5000	0.6000	0.8000	1.0000	1.2000	1.0000	1.0000	1.0000;
0.7500	0.8000	0.8000	1.0000	1.0000	1.0000	1.0000	1.0000;
1.0000	1.0000	1.0000	1.0000	1.0000	1.0000	1.0000	1.0000;
1.0000	1.0000	1.0000	1.0000	1.0000	1.0000	1.0000	1.0000]
(c) $K_{\beta R}$							

Figure B.20: $K_{\beta R} = f(\beta_F, V_T)$: $K_{\beta R} \rightarrow [ND], \beta_F \rightarrow [deg], V_T \rightarrow [kts]$

[-180 -170 -160 -150 -140 -130 -120 -110 -100 -90 -80 -70 -60 -50 -40 -32 -28 -26 -24 -22 -20 -18 -16 -14 -12 -10 -8 8 10 12 14 16 18 20 22 24 26 28 32 40 50 60 70 80 90 100 110 120 130 140 150 160 170 180]
(a) β_V for C_{YV}
[-0.33 0.20 0.40 0.52 0.60 0.60 0.49 0.37 0.20 0 -0.42 -0.70 -0.91 -1.07 -1.11 -1.08 -1.10 -1.12 -1.16 -1.22 -1.30 -1.3584 -1.2584 -1.1459 -1.0334 -0.9284 -0.8234 0.0266 0.1316 0.2366 0.3491 0.4616 0.5616 0.67 0.71 0.72 0.71 0.68 0.74 0.92 0.88 0.72 0.52 0.28 0 -0.31 -0.60 -0.81 -0.97 -0.98 -0.92 -0.80 -0.86 -0.33];
(b) C_{YV} for $\delta_r = -20$ deg and $M_N = 0 - 0.2$
[-0.20 0.33 0.50 0.62 0.70 0.69 0.57 0.44 0.23 0 -0.41 -0.67 -0.90 -1.05 -1.07 -1.06 -1.08 -1.10 -1.12 -1.17 -1.25 -1.265 -1.165 -1.0525 -0.94 -0.845 -0.73 0.12 0.225 0.33 0.4425 0.555 0.655 0.73 0.77 0.77 0.76 0.77 0.86 0.96 0.92 0.77 0.57 0.33 0 -0.30 -0.55 -0.73 -0.86 -0.89 -0.82 -0.70 -0.73 -0.20];
(c) C_{YV} for $\delta_r = -15$ deg and $M_N = 0 - 0.2$
[0 0.53 0.60 0.72 0.79 0.77 0.64 0.47 0.24 0 -0.40 -0.64 -0.84 -0.99 -1.0 -0.93 -0.94 -0.98 -1.03 -1.05 -1.05 -0.96 -0.86 -0.7475 -0.635 -0.53 -0.425 0.425 0.53 0.635 0.7475 0.86 0.96 1.05 1.05 1.03 0.98 0.94 0.93 1.0 0.99 0.84 0.64 0.40 0 -0.24 -0.47 -0.64 -0.77 -0.79 -0.72 -0.60 -0.53 0];
(d) C_{YV} for $\delta_r = 0$ deg and $M_N = 0 - 0.2$
[0.20 0.73 0.70 0.82 0.89 0.86 0.73 0.55 0.30 0 -0.33 -0.57 -0.77 -0.92 -0.96 -0.86 -0.77 -0.76 -0.77 -0.77 -0.73 -0.655 -0.555 -0.4425 -0.33 -0.225 -0.12 0.73 0.835 0.94 1.0525 1.165 1.265 1.25 1.17 1.12 1.10 1.08 1.06 1.07 1.05 0.90 0.67 0.41 0 -0.23 -0.44 -0.57 -0.69 -0.70 -0.62 -0.50 -0.33 0.20];
(e) C_{YV} for $\delta_r = 15$ deg and $M_N = 0 - 0.2$
[0.33 0.86 0.80 0.92 0.98 0.97 0.81 0.60 0.31 0 -0.28 -0.52 -0.72 -0.88 -0.92 -0.74 -0.68 -0.71 -0.72 -0.71 -0.67 -0.5616 -0.4616 -0.3491 -0.2366 -0.1316 -0.0266 0.8234 0.9284 1.0334 1.1459 1.2584 1.3584 1.30 1.22 1.16 1.12 1.10 1.08 1.11 1.07 0.91 0.70 0.42 0 -0.20 -0.37 -0.49 -0.60 -0.60 -0.52 -0.40 -0.20 0.33];
(f) C_{YV} for $\delta_r = 20$ deg and $M_N = 0 - 0.2$
[-1.0 -0.97 -0.90 -0.865 -0.83 -0.835 -0.84 -0.85 -0.83 -0.775 -0.696 -0.58 -0.464 0.464 0.58 0.696 0.775 0.83 0.85 0.84 0.835 0.83 0.865 0.90 0.97 1.0]
(g) C_{YV} for $\delta_r = 0$ deg, $M_N = 0.4$, -40 deg $< \beta_V < 40$ deg
[-0.70 -0.73 -0.75 -0.73 -0.70 -0.61 -0.488 0.488 0.61 0.70 0.73 0.75 0.73 0.70]
(h) C_{YV} for $\delta_r = 0$ deg, $M_N = 0.5$, -20 deg $< \beta_V < 20$ deg
[-0.35 -0.375 -0.40 -0.425 -0.45 -0.47 -0.45 0.45 0.47 0.45 0.425 0.40 0.375 0.35]
(i) C_{YV} for $\delta_r = 0$ deg, $M_N = 0.6$, -20 deg $< \beta_V < 20$ deg

Figure B.21: $C_{YV} = f(\beta_V, \delta_r, M_N)$: $C_{YV} \rightarrow [ND]$, $\beta_V \rightarrow [deg]$, $\delta_r \rightarrow [deg]$, $M_N \rightarrow [ND]$

-180.00	-170.00	-160.00	-150.00	-140.00	-130.00	-120.00	-110.00
-100.00	-90.00	-80.00	-70.00	-60.00	-50.00	-40.00	-32.00
-28.00	-24.00	-20.00	-16.00	-12.00	-8.00	-4.00	0
4.00	8.00	12.00	16.00	20.00	24.00	28.00	32.00
40.00	50.00	60.00	70.00	80.00	90.00	100.00	110.00
120.00	130.00	140.00	150.00	160.00	170.00	180.00	

(a) β_{VD} for C_{DV}

0.0071	0.03	0.60	0.88	1.13	1.30	1.43	1.51	1.58	1.60
1.58	1.52	1.45	1.34	1.20	1.10	0.87	0.58	0.324	0.16
0.08	0.024	0.014	0.0071	0.014	0.024	0.08	0.16	0.324	0.58
0.87	1.10	1.20	1.34	1.45	1.52	1.58	1.60	1.58	1.51
1.43	1.30	1.13	0.88	0.60	0.03	0.0071			

(b) C_{DV} for $M_N = 0 - 0.2$

0.33	0.15	0.044	0.014	0.0071	0.014	0.044	0.15	0.33
------	------	-------	-------	--------	-------	-------	------	------

(c) C_{DV} for $M_N = 0.4, -16 \text{ deg} < \beta_V < 16 \text{ deg}$

0.20	0.07	0.015	0.0071	0.015	0.07	0.20
------	------	-------	--------	-------	------	------

(d) C_{YV} for $M_N = 0.5, -12 \text{ deg} < \beta_V < 12 \text{ deg}$

0.32	0.12	0.02	0.0071	0.02	0.12	0.32
------	------	------	--------	------	------	------

(e) C_{YV} for $M_N = 0.6, -12 \text{ deg} < \beta_V < 12 \text{ deg}$ Figure B.22: $C_{DV} = f(\beta_{VD}, M_N)$: $C_{YV} \rightarrow [ND]$, $\beta_{VD} \rightarrow [deg]$, $M_N \rightarrow [ND]$

[-0.84 -0.86 -0.94 -0.772 -0.37 -0.025 0.38 0.75 1.12 1.46 1.32]

(a) C_{LWP} for $M_N = 0.4$, $-20 \text{ deg} < \alpha < 20 \text{ deg}$

[-0.675 -0.80 -0.40 -0.01 0.39 0.77 1.16 1.27]

(b) C_{LWP} for $M_N = 0.5$, $-16 \text{ deg} < \alpha < 16 \text{ deg}$

[-0.49 -0.50 -0.41 -0.01 0.41 0.83 1.09 1.12]

(c) C_{LWP} for $M_N = 0.6$, $-16 \text{ deg} < \alpha < 16 \text{ deg}$

Figure B.24: C_{LWP} for $M_N \neq 0$. For these coefficients, flaps are set to zero since at high speeds opening the flaps generates drag. Data for $\beta_M = 0 \text{ deg}$ is not provided in this case since, in helicopter mode, the tilt-rotor cannot reach $M_N = 0.4$.

[0.312 0.175 0.089 0.042 0.025 0.0170 0.0204 0.0418 0.072
0.128 0.194 0.3050 0.500]

(a) C_{DWP} for $M_N = 0.4$, $-24 \text{ deg} < \alpha < 24 \text{ deg}$

[0.275 0.135 0.050 0.025 0.0170 0.0204 0.0418 0.082 0.168
0.289]

(b) C_{DWP} for $M_N = 0.5$, $-20 \text{ deg} < \alpha < 20 \text{ deg}$

[0.24 0.11 0.052 0.040 0.042 0.062 0.127 0.268]

(c) C_{DWP} for $M_N = 0.6$, $-16 \text{ deg} < \alpha < 16 \text{ deg}$

Figure B.25: C_{DWP} for $M_N \neq 0$. For these coefficients, flaps are set to zero since at high speeds opening the flaps generates drag. Data for $\beta_M = 0 \text{ deg}$ is not provided in this case since, in helicopter mode, the tilt-rotor cannot reach $M_N = 0.4$.

[0 15 30 60 90]
(a) β_M for C_{mWP}
[0 20 45 75]
(b) Flaps for C_{mWP}
[0.025 0.070 0.080 0.050 -0.025;
-0.05 -0.01 0.000 -0.05 -0.11;
-0.110 -0.09 -0.060 -0.11 -0.170;
-0.115 -0.110 -0.080 -0.130 -0.190]
(c) C_{mWP}

Figure B.27: $C_{mWP} = f(\beta_M, \delta_F): C_{mWP} \rightarrow [ND], \beta_M \rightarrow [deg]$

[-90 -16 -12 -8 -4 0 4 8 12 16 20 24 28 90]
(a) α for $\varepsilon_{W/H}$
[0 20 45 75]
(b) Flaps for $\varepsilon_{W/H}$
[0 0 0 0.09 1.62 3.15 4.68 6.21 7.10 7.50 7.00 4.80 0 0]
[0 0 0.80 1.60 3.10 4.70 6.20 7.80 8.50 8.60 7.50 4.90 0 0]
[0 0 1.47 3.03 4.59 6.15 7.71 9.27 9.80 9.70 8.00 5.00 0 0]
[0 0 1.47 3.03 4.59 6.15 7.71 9.27 9.80 9.70 8.00 5.00 0 0]
(c) Downwash factor for $\beta_M = 0$ deg
[0 0 0 0 1.26 2.80 4.34 5.88 7.10 7.30 6.70 4.10 0 0]
[0 0 0.40 1.20 2.70 4.30 6.00 7.10 8.70 8.90 8.20 5.30 0 0]
[0 0 0.70 2.40 4.10 5.80 7.50 9.20 10.40 10.80 9.80 6.40 0 0]
[0 0 0.70 2.40 4.10 5.80 7.50 9.20 10.40 10.80 9.80 6.40 0 0]
(d) Downwash factor for $\beta_M = 15$ deg
[0 0 0 0 1.18 2.70 4.22 5.74 7.00 7.30 6.70 4.10 0 0]
[0 0 0 0.70 2.10 3.60 5.20 6.70 7.90 8.20 7.40 4.80 0 0]
[0 0 0 1.30 2.90 4.50 6.10 7.70 8.90 9.10 8.10 5.50 0 0]
[0 0 0 1.30 2.90 4.50 6.10 7.70 8.90 9.10 8.10 5.50 0 0]
(e) Downwash factor for $\beta_M = 30$ deg
[0 0 0 0 1.20 2.60 4.00 5.20 6.40 6.80 6.30 4.10 0 0]
[0 0 0 0.90 2.25 3.80 5.30 6.80 7.80 8.20 7.40 4.80 0 0]
[0 0 0 1.78 3.38 4.98 6.58 8.18 9.20 9.50 8.40 5.50 0 0]
[0 0 0 1.78 3.38 4.98 6.58 8.18 9.20 9.50 8.40 5.50 0 0]
(f) Downwash factor for $\beta_M = 60$ deg
[0 0 0 0.06 1.32 2.58 3.84 5.10 5.90 6.30 6.00 4.00 0 0]
[0 0 0.45 1.25 2.60 4.08 5.35 6.6 7.40 7.55 6.70 4.40 0 0]
[0 0 0.95 2.54 3.92 5.40 6.88 8.26 8.90 8.80 7.30 4.80 0 0]
[0 0 0.95 2.54 3.92 5.40 6.88 8.26 8.90 8.80 7.30 4.80 0 0]
(g) Downwash factor for $\beta_M = 90$ deg

Figure B.28: $\varepsilon_{W/H} = f(\beta_M, \delta_F, \alpha): \varepsilon_{W/H} \rightarrow [deg], \beta_M \rightarrow [deg], \alpha \rightarrow [deg]$

[0 20 45 75]
(a) Flaps for $C_{L\delta a}$
[0.00316 0.00396 0.00476 0.0]
(b) $C_{L\delta a}$

Figure B.29: $C_{L\delta a} = f(\delta_F): C_{L\delta a} \rightarrow [deg^{-1}]$

$$\begin{array}{c}
[0 \quad 20 \quad 45 \quad 75] \\
\text{(a) Flaps for } \frac{\partial C_{LWPFES}}{\partial \alpha_{WFS}} \Big|_{C_{LWP}=0} \\
[0.2 \quad 0.4 \quad 0.5 \quad 0.6] \\
\text{(b) } M_N \text{ for } \frac{\partial C_{LWPFES}}{\partial \alpha_{WFS}} \Big|_{C_{LWP}=0} \\
[0 \quad 90] \\
\text{(c) } \beta_M \text{ for } \frac{\partial C_{LWPFES}}{\partial \alpha_{WFS}} \Big|_{C_{LWP}=0} \\
[0.057 \quad 0.0575 \quad 0.057 \quad 0.0563] \\
[0.0799 \quad 0.08 \quad 0.08 \quad 0.08] \\
\text{(d) } \frac{\partial C_{LWPFES}}{\partial \alpha_{WFS}} \Big|_{C_{LWP}=0} \text{ for } M_N = 0, \text{ Flaps} \\
\text{along columns, } \beta_M \text{ along rows} \\
[0.0799 \quad 0.0837 \quad 0.0915 \quad 0.0988] \\
\text{(e) } \frac{\partial C_{LWPFES}}{\partial \alpha_{WFS}} \Big|_{C_{LWP}=0} \text{ for } \beta_M = 90 \text{ deg,} \\
\delta_F = 0 \text{ deg, } M_N \text{ along columns}
\end{array}$$

Figure B.30: $\frac{\partial C_{LWPFES}}{\partial \alpha_{WFS}} \Big|_{C_{LWP}=0} = f(\beta_M, \delta_F, M_N): \frac{\partial C_{LWPFES}}{\partial \alpha_{WFS}} \Big|_{C_{LWP}=0} \rightarrow [ND], \beta_M \rightarrow [deg],$
 $\delta_F \rightarrow [deg], M_N \rightarrow [ND]$

$$\begin{array}{c}
[0 \quad 20 \quad 45 \quad 75] \\
\text{(a) Flaps for } \frac{C_{I\beta}}{C_{LWP}} \Big|_{M_N=0} \\
[0 \quad 30 \quad 60 \quad 90] \\
\text{(b) } \beta_M \text{ for } \frac{C_{I\beta}}{C_{LWP}} \Big|_{M_N=0} \\
[0.09 \quad 0 \quad -0.02 \quad -0.05] \\
[0.09 \quad -0.01 \quad 0 \quad 0]
\end{array}$$

(c) $\frac{C_{I\beta}}{C_{LWP}} \Big|_{M_N=0}$: β_M along columns, while the first row is referred to $\delta_F = 0$ deg and the second row to $\delta_F \neq 0$ deg

Figure B.31: $\frac{C_{I\beta}}{C_{LWP}} \Big|_{M_N=0} = f(\beta_M, \delta_F): \frac{C_{I\beta}}{C_{LWP}} \Big|_{M_N=0} \rightarrow [rad^{-1}], \beta_M \rightarrow [deg], \delta_F \rightarrow [deg]$

$$\begin{array}{c}
[0 \quad 20 \quad 45 \quad 75] \\
\text{(a) Flaps for } C_{I\beta} \Big|_{C_{LWP}=M_N=0} \\
[0 \quad 30 \quad 60 \quad 90] \\
\text{(b) } \beta_M \text{ for } C_{I\beta} \Big|_{C_{LWP}=M_N=0} \\
[-0.012 \quad 0.089 \quad 0.078 \quad 0.039] \\
[-0.136 \quad 0.064 \quad 0.034 \quad -0.051]
\end{array}$$

(c) $C_{I\beta} \Big|_{C_{LWP}=M_N=0}$: β_M along columns, while the first row is referred to $\delta_F = 0$ deg and the second row to $\delta_F \neq 0$ deg

Figure B.32: $C_{I\beta} \Big|_{C_{LWP}=M_N=0} = f(\beta_M, \delta_F): C_{I\beta} \Big|_{C_{LWP}=M_N=0} \rightarrow [rad^{-1}], \beta_M \rightarrow [deg],$
 $\delta_F \rightarrow [deg]$

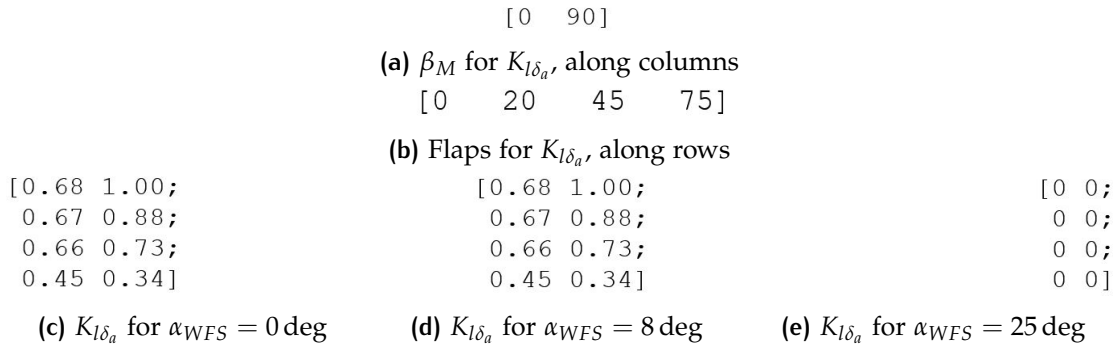


Figure B.33: $K_{l\delta_a} = f(\beta_M, \alpha_{WFS}, \delta_F)$: $K_{l\delta_a} \rightarrow [ND]$, $\beta_M \rightarrow [deg]$, $\alpha_{WFS} \rightarrow [deg]$, $\delta_F \rightarrow [deg]$

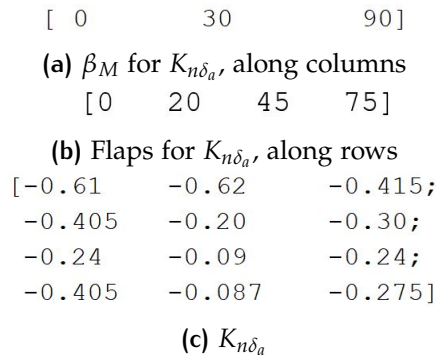


Figure B.34: $K_{n\delta_a} = f(\beta_M, \delta_F)$: $K_{n\delta_a} \rightarrow [ND]$, $\beta_M \rightarrow [deg]$, $\delta_F \rightarrow [deg]$

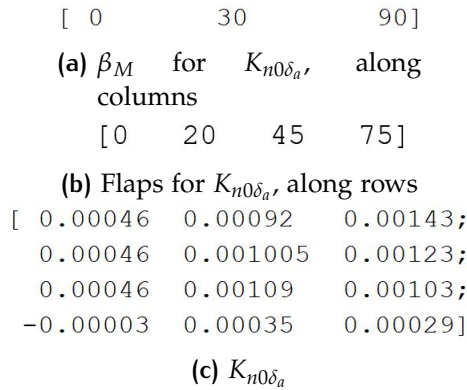


Figure B.35: $K_{n0\delta_a} = f(\beta_M, \delta_F)$: $K_{n0\delta_a} \rightarrow [deg^{-1}]$, $\beta_M \rightarrow [deg]$, $\delta_F \rightarrow [deg]$

$$\begin{aligned}
& [0 \quad 20 \quad 45 \quad 75] \\
\text{(a) Flaps for } C_{D_{0WP}}|_{C_{L_{WP}}=0} & \\
& [0.2 \quad 0.4 \quad 0.5 \quad 0.6] \\
\text{(b) } M_N \text{ for } C_{D_{0WP}}|_{C_{L_{WP}}=0} & \\
& [0 \quad 90] \\
\text{(c) } \beta_M \text{ for } C_{D_{0WP}}|_{C_{L_{WP}}=0} & \\
& [0.2126 \quad 0.2512 \quad 0.256 \quad 0.442] \\
& [0.0177 \quad 0.0419 \quad 0.058 \quad 0.243] \\
\text{(d) } C_{D_{0WP}}|_{C_{L_{WP}}=0} \text{ for } M_N = 0, \text{ Flaps along columns, } \beta_M \text{ along rows} & \\
& [0.0177 \quad 0. \quad 0.0178 \quad 0. \quad 0.0179 \quad 0.0405] \\
\text{(e) } C_{D_{0WP}}|_{C_{L_{WP}}=0} \text{ for } \beta_M = 90 \text{ deg, } \delta_F = 0 \text{ deg, } M_N \text{ along} & \\
& \text{columns}
\end{aligned}$$

Figure B.36: $C_{D_{0WP}}|_{C_{L_{WP}}=0} = f(\beta_M, \delta_F, M_N)$: $C_{D_{0WP}}|_{C_{L_{WP}}=0} \rightarrow [ND]$, $\beta_M \rightarrow [deg]$, $\delta_F \rightarrow [deg]$, $M_N \rightarrow [ND]$

$$\begin{aligned}
& [-5 \quad 0 \quad 15 \quad 30 \quad 45 \quad 50 \quad 55 \\
& 60 \quad 65 \quad 70 \quad 75 \quad 80 \quad 85 \quad 90] \\
\text{(a) } \beta_M \text{ for } D_{PYNT} & \\
& [13.5 \quad 13.50 \quad 13.50 \quad 13.50 \quad 13.50 \quad 13.40 \quad 13.25 \\
& 13.00 \quad 12.00 \quad 10.50 \quad 8.00 \quad 5.70 \quad 3.40 \quad 1.00] \\
\text{(b) } D_{PYNT} &
\end{aligned}$$

Figure B.37: $D_{PYNT} = f(\beta_M)$: $D_{PYNT} \rightarrow [ft^2]$, $\beta_M \rightarrow [deg]$

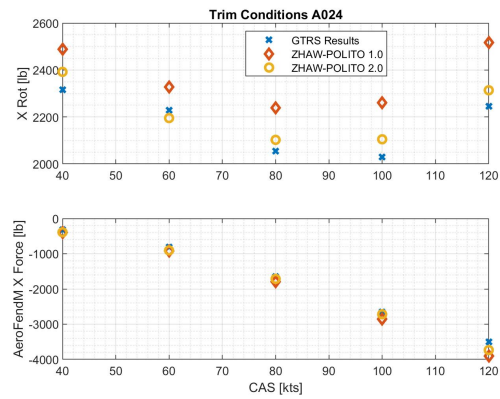
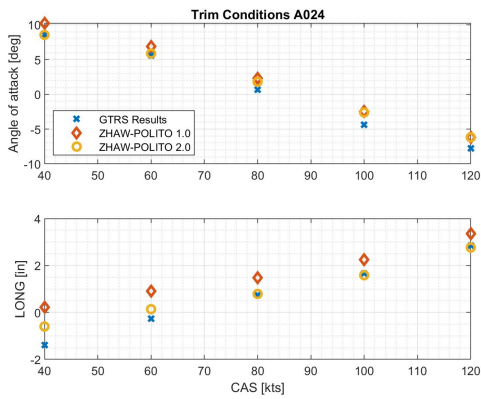
$$\begin{aligned}
& [0.0 \quad 10.0 \quad 20.0 \quad 30.0 \quad 40.0 \quad 45.0 \quad 90.0] \\
\text{(a) } \alpha_{PYL} \text{ for } K_{PLAT} & \\
& [0.0 \quad 0.04 \quad 0.1 \quad 0.5 \quad 0.95 \quad 1.0 \quad 1.0] \\
\text{(b) } K_{PLAT} &
\end{aligned}$$

Figure B.38: $K_{PLAT} = f(\alpha_{PYL})$: $K_{PLAT} \rightarrow [ND]$, $\alpha_{PYL} \rightarrow [deg]$

C | TRIM RESULTS

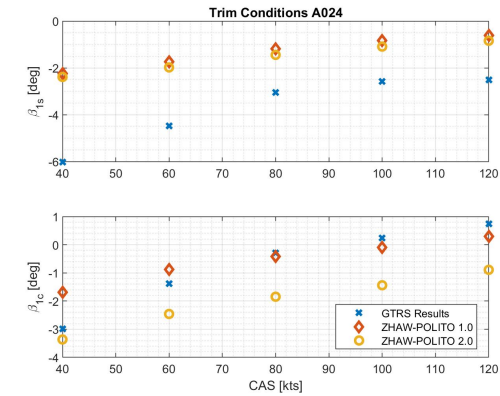
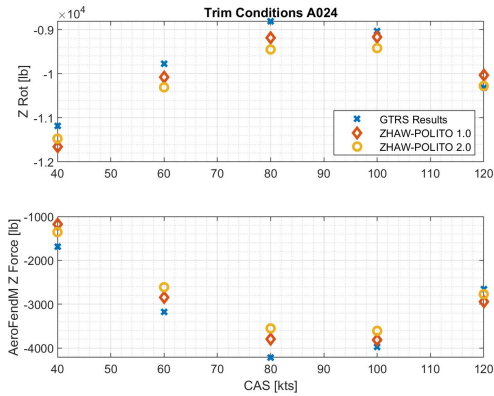
C.1 GTRS DATA

C.1.1 Conversion Mode



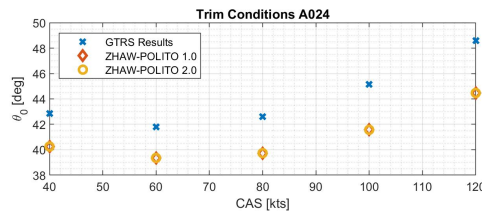
(a) Angle of Attack and Longitudinal Stick

(b) Rotor and Aerodynamic X Force



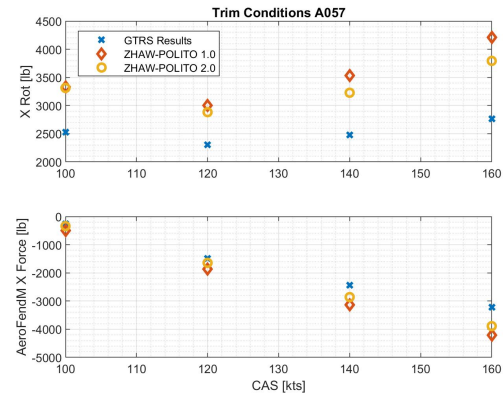
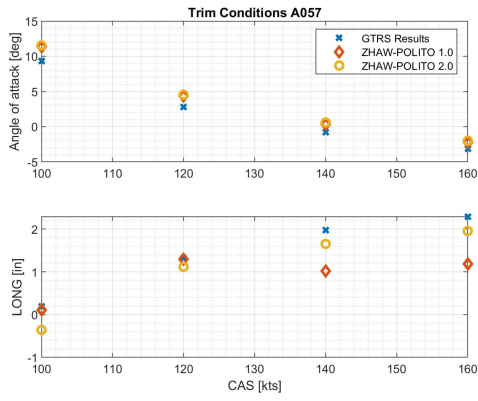
(c) Rotor and Aerodynamic Z Force

(d) Rotor Disk Flapping Angles



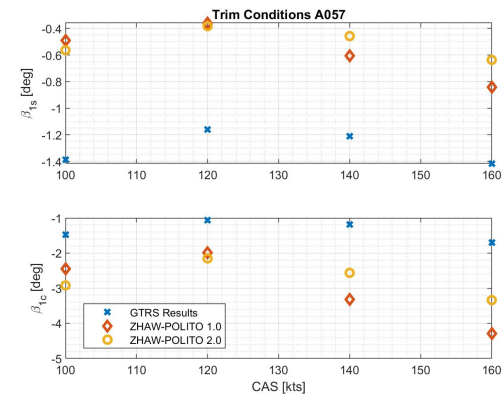
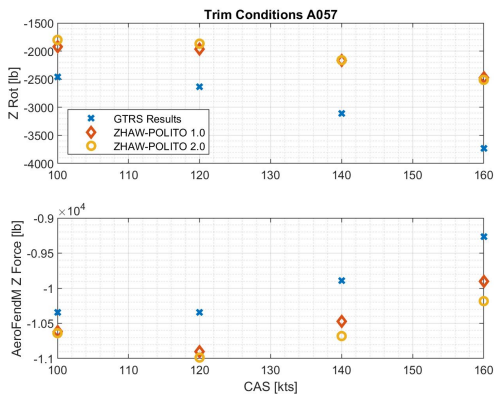
(e) Root Collective Pitch

Figure C.1: Test A024



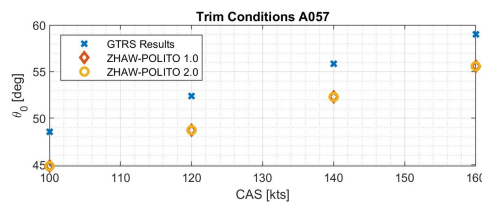
(a) Angle of Attack and Longitudinal Stick

(b) Rotor and Aerodynamic X Force



(c) Rotor and Aerodynamic Z Force

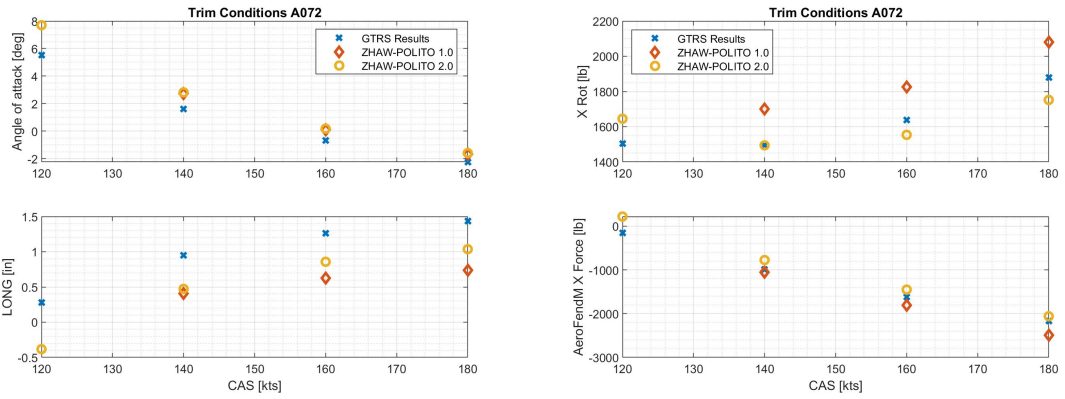
(d) Rotor Disk Flapping Angles



(e) Root Collective Pitch

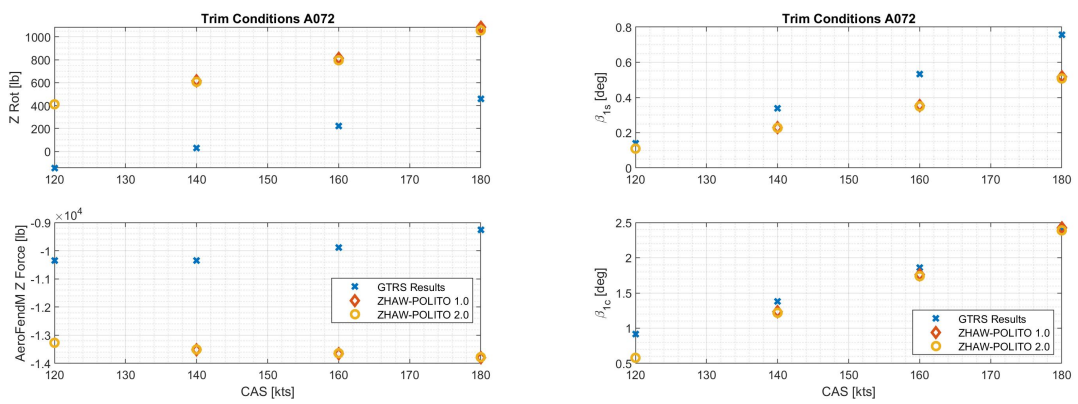
Figure C.2: Test A057

c.1.2 Airplane Mode



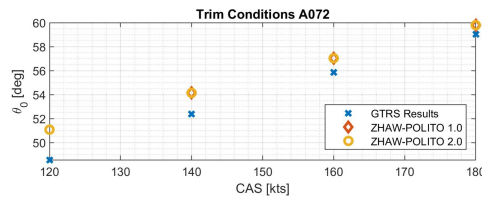
(a) Angle of Attack and Longitudinal Stick

(b) Rotor and Aerodynamic X Force



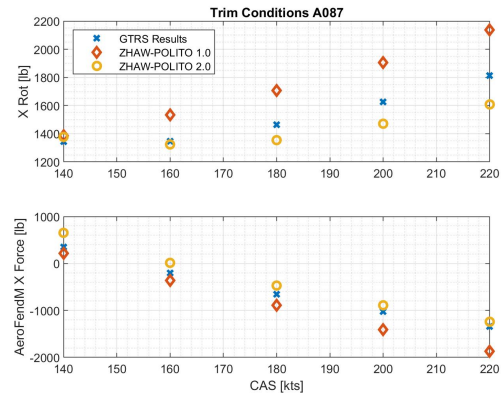
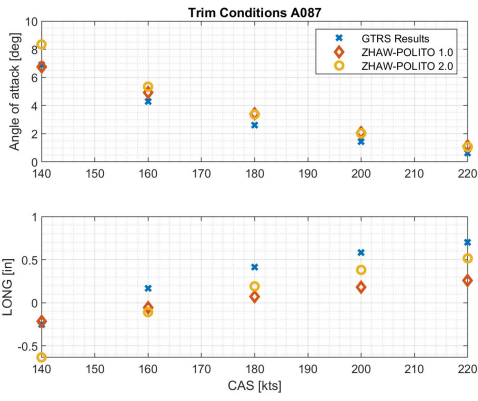
(c) Rotor and Aerodynamic Z Force

(d) Rotor Disk Flapping Angles



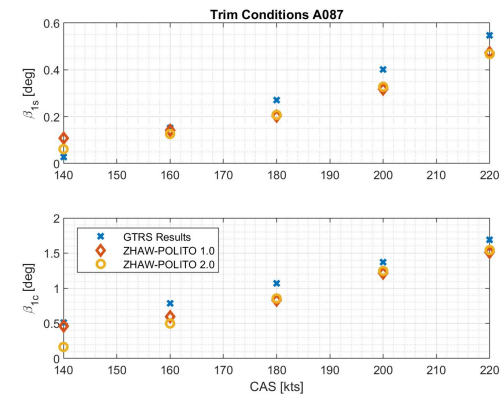
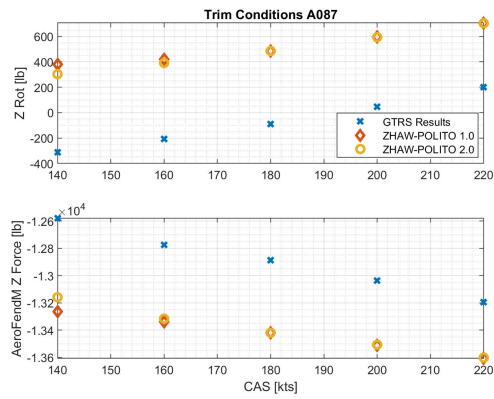
(e) Root Collective Pitch

Figure C.3: Test A072



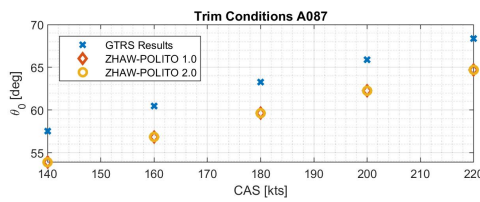
(a) Angle of Attack and Longitudinal Stick

(b) Rotor and Aerodynamic X Force



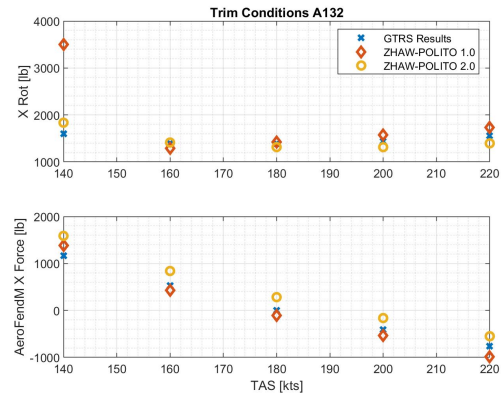
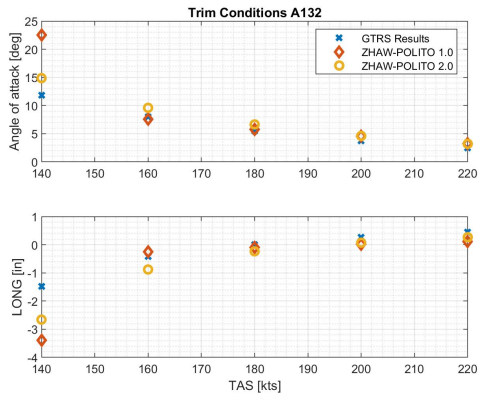
(c) Rotor and Aerodynamic Z Force

(d) Rotor Disk Flapping Angles



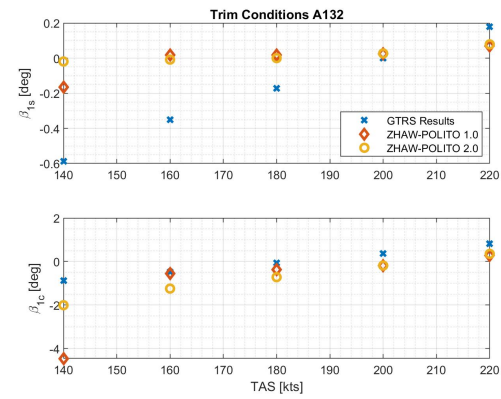
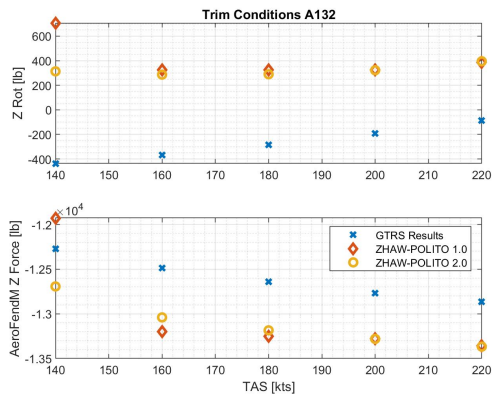
(e) Root Collective Pitch

Figure C.4: Test A087



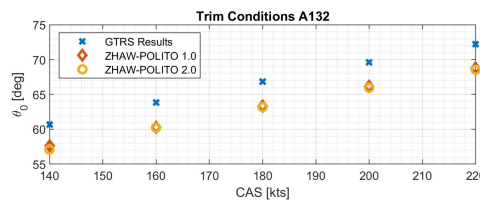
(a) Angle of Attack and Longitudinal Stick

(b) Rotor and Aerodynamic X Force



(c) Rotor and Aerodynamic Z Force

(d) Rotor Disk Flapping Angles



(e) Root Collective Pitch

Figure C.5: Test A132

C.2 FLIGHT TEST

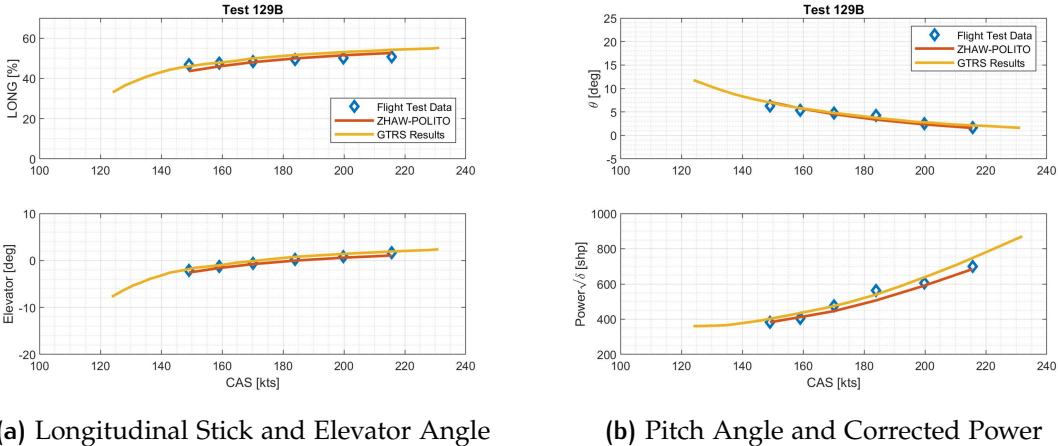


Figure C.6: Test 129B

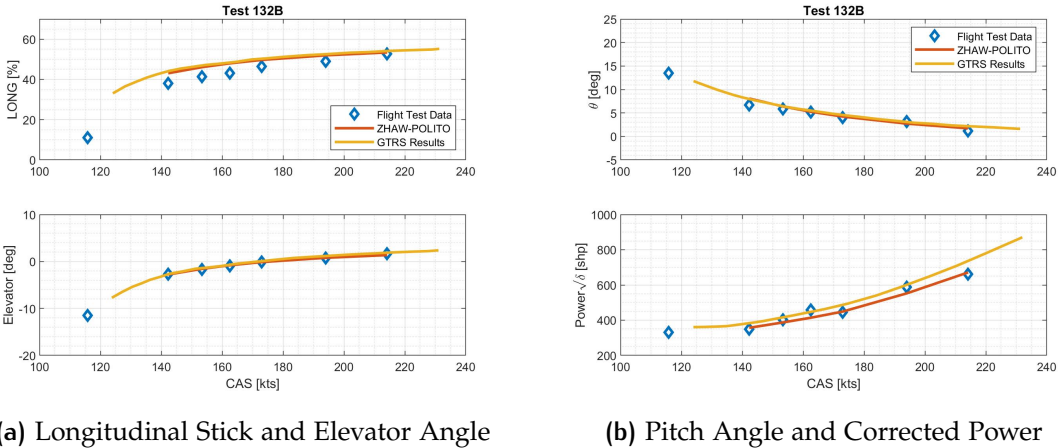


Figure C.7: Test 132B

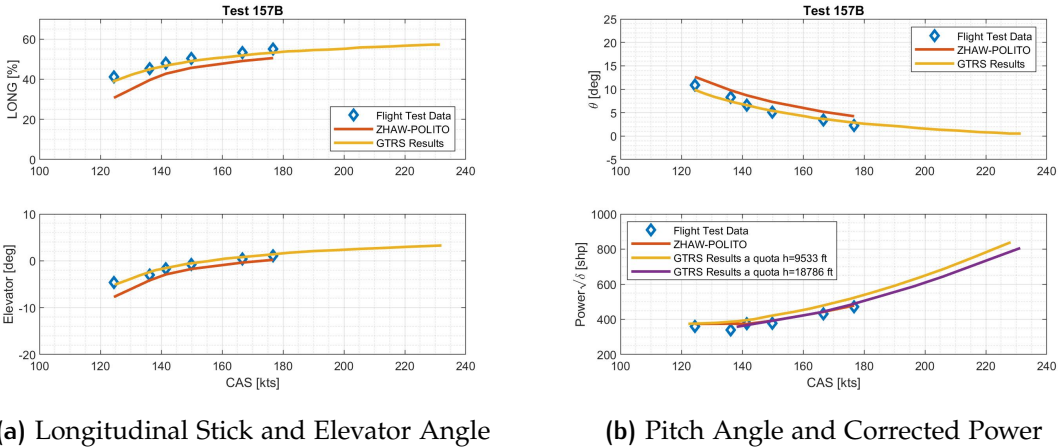
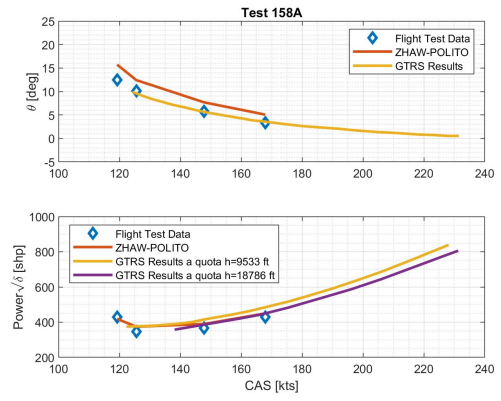
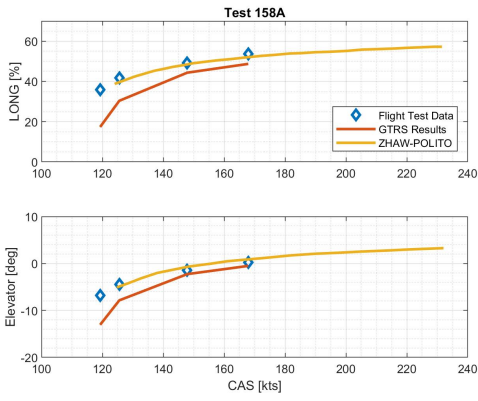


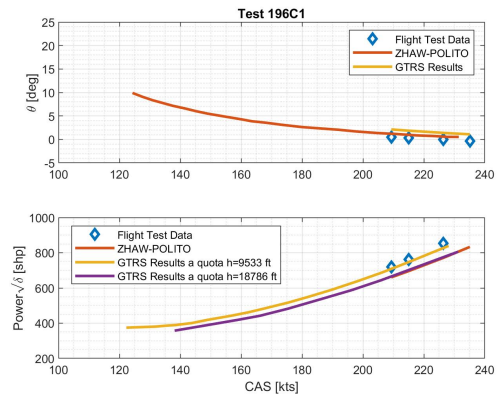
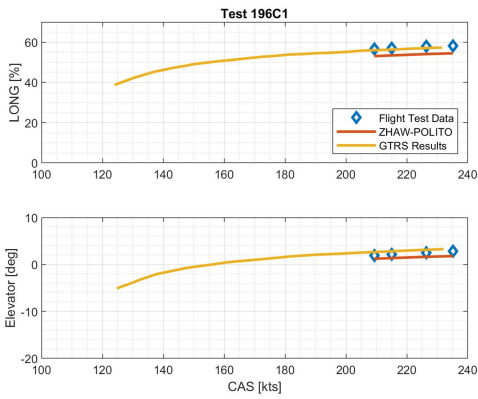
Figure C.8: Test 157B



(a) Longitudinal Stick and Elevator Angle

(b) Pitch Angle and Corrected Power

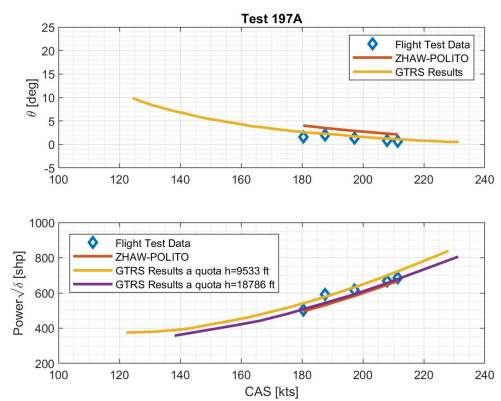
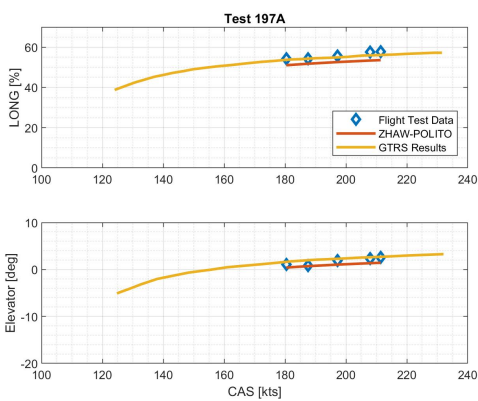
Figure C.9: Test 158A



(a) Longitudinal Stick and Elevator Angle

(b) Pitch Angle and Corrected Power

Figure C.10: Test 196C1



(a) Longitudinal Stick and Elevator Angle

(b) Pitch Angle and Corrected Power

Figure C.11: Test 197A

D | FLIGHT TEST CARDS

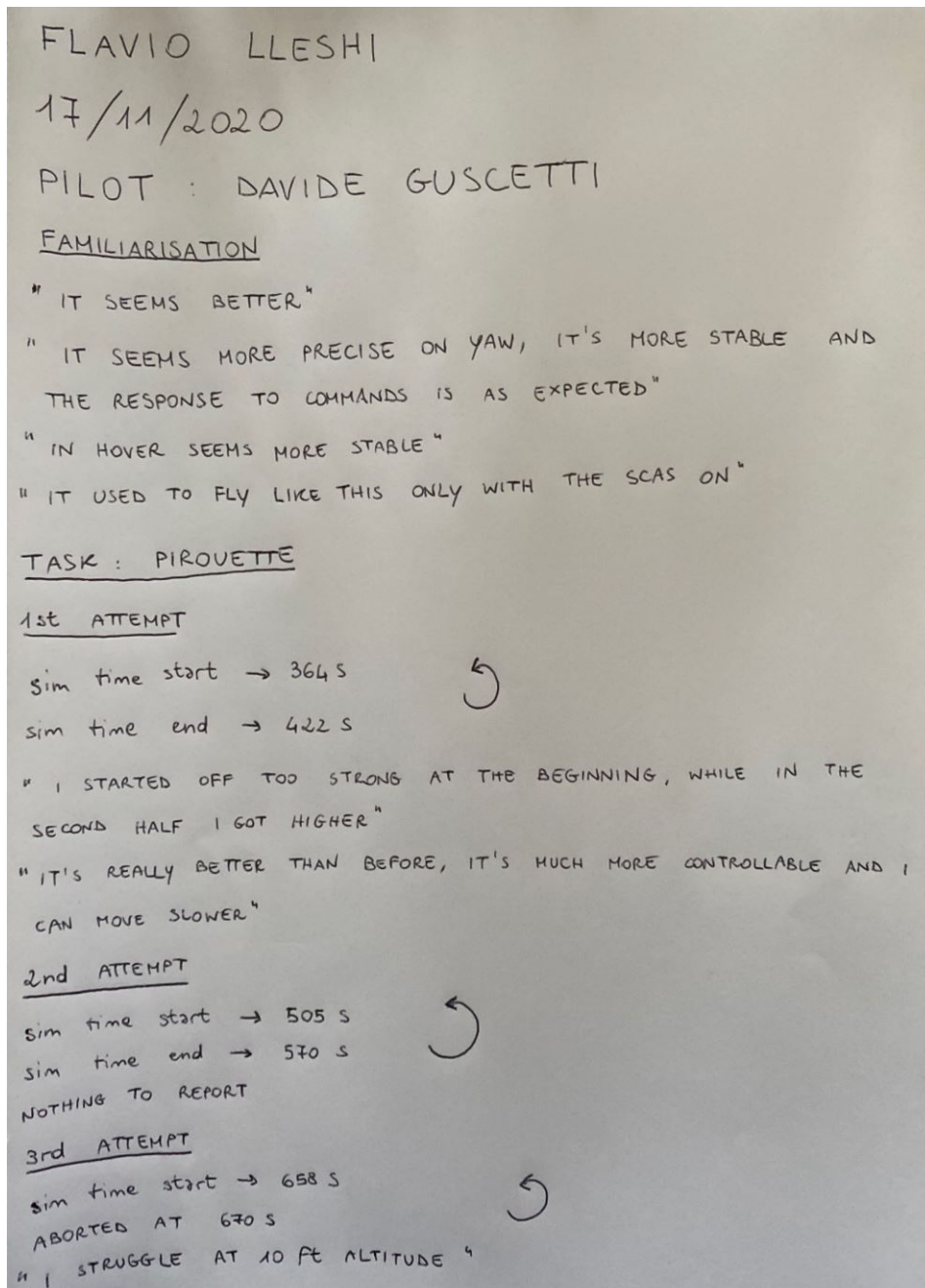


Figure D.1: Flight Test Card 1

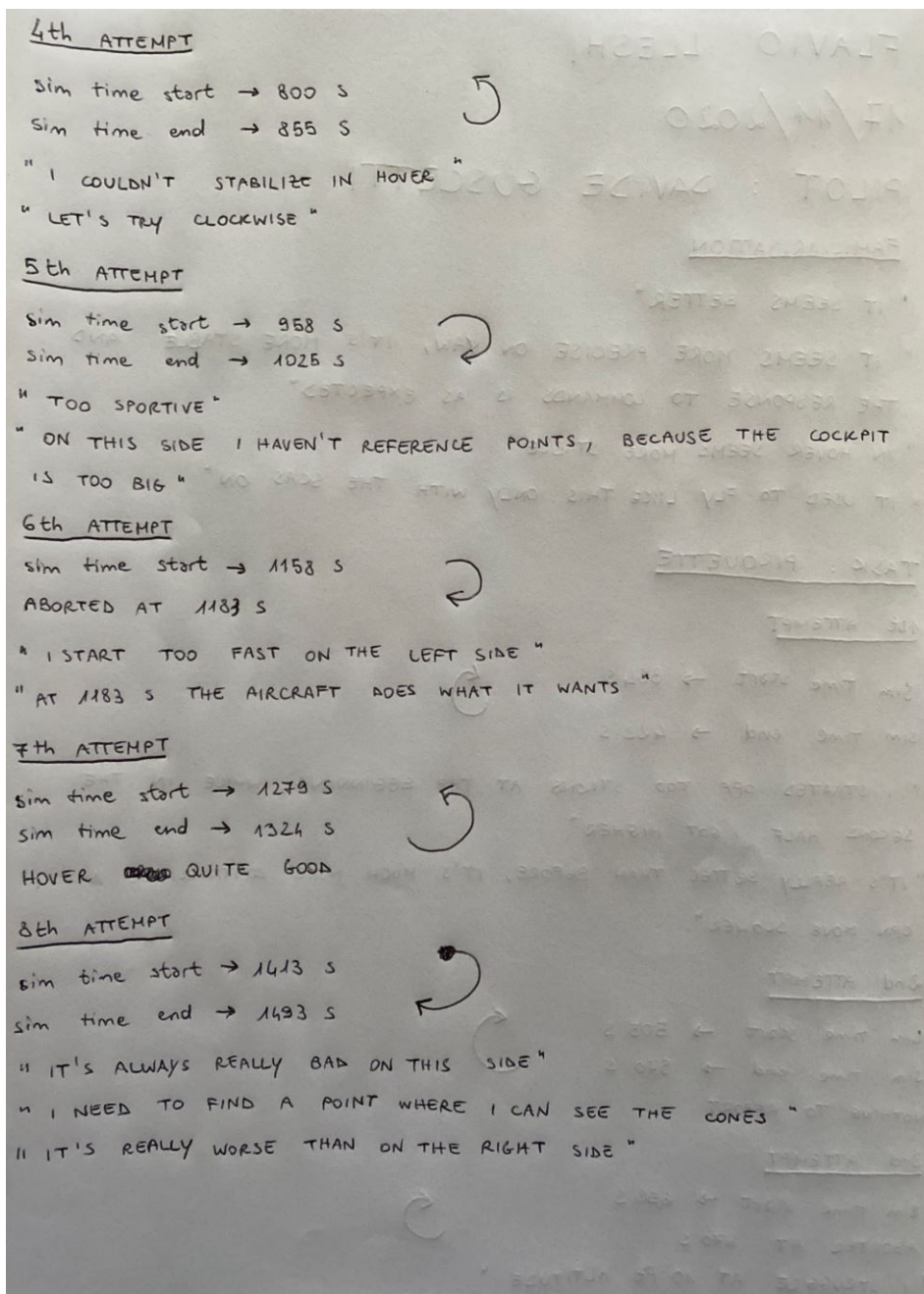


Figure D.2: Flight Test Card 2

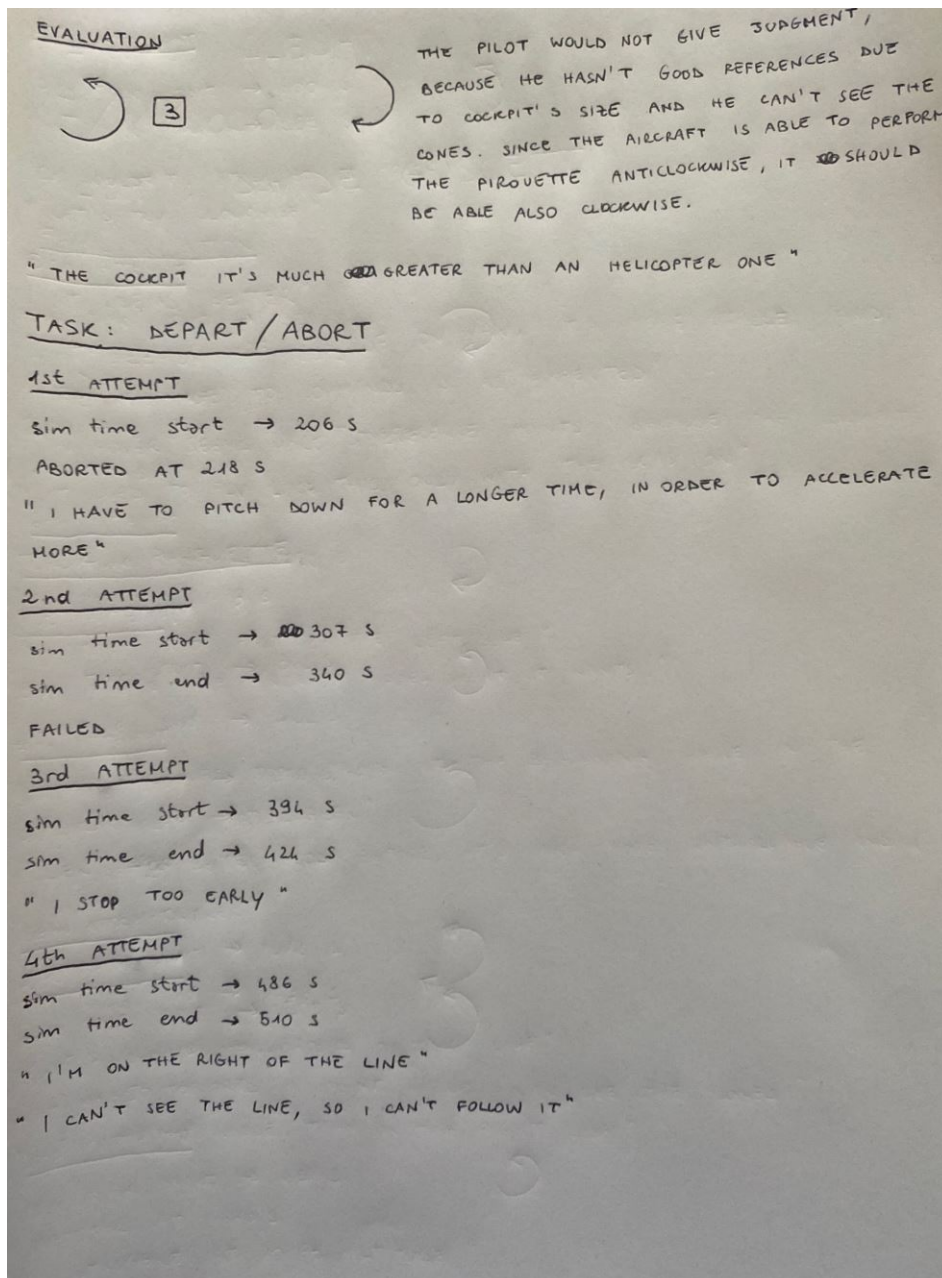


Figure D.3: Flight Test Card 3

5th ATTEMPT

" THE VISUAL DOESN'T HELP TO STAY STRAIGHT WITH ~~THE~~ THE NOSE "

sim time start → 566 s

sim time end → 593 s

" WE ARE IMPROVING "

" I SUCCEEDED BETTER THAN THE OTHER TIMES "

6th ATTEMPT

sim time start → 667 s

sim time end → 695 s

" I STARTED GOOD, BUT THE FINISH WAS REALLY BAD SINCE I LOST SIGHT OF THE LINE "

7th ATTEMPT

sim time start → 800 s

sim time end → 823 s

" I WENT TOO HIGH "

" THE STOP WAS OK "

" DURING THE SIMULATION IS DIFFICULT TOO ESTIMATE THE HEIGHT, HENCE I HAVE TO LOOK AT THE RADAR, BUT I MISS THE VISUAL IN THIS WAY "

8th ATTEMPT

sim time start → 923 s

sim time end → 947 s

" I WENT DOWN 20 FT "

EVALUATION

2 " THIS MANOEUVRE CAN BE DONE REALLY WELL "

" IT FLIGHTS REALLY WELL, CONGRATS! "

Figure D.4: Flight Test Card 4

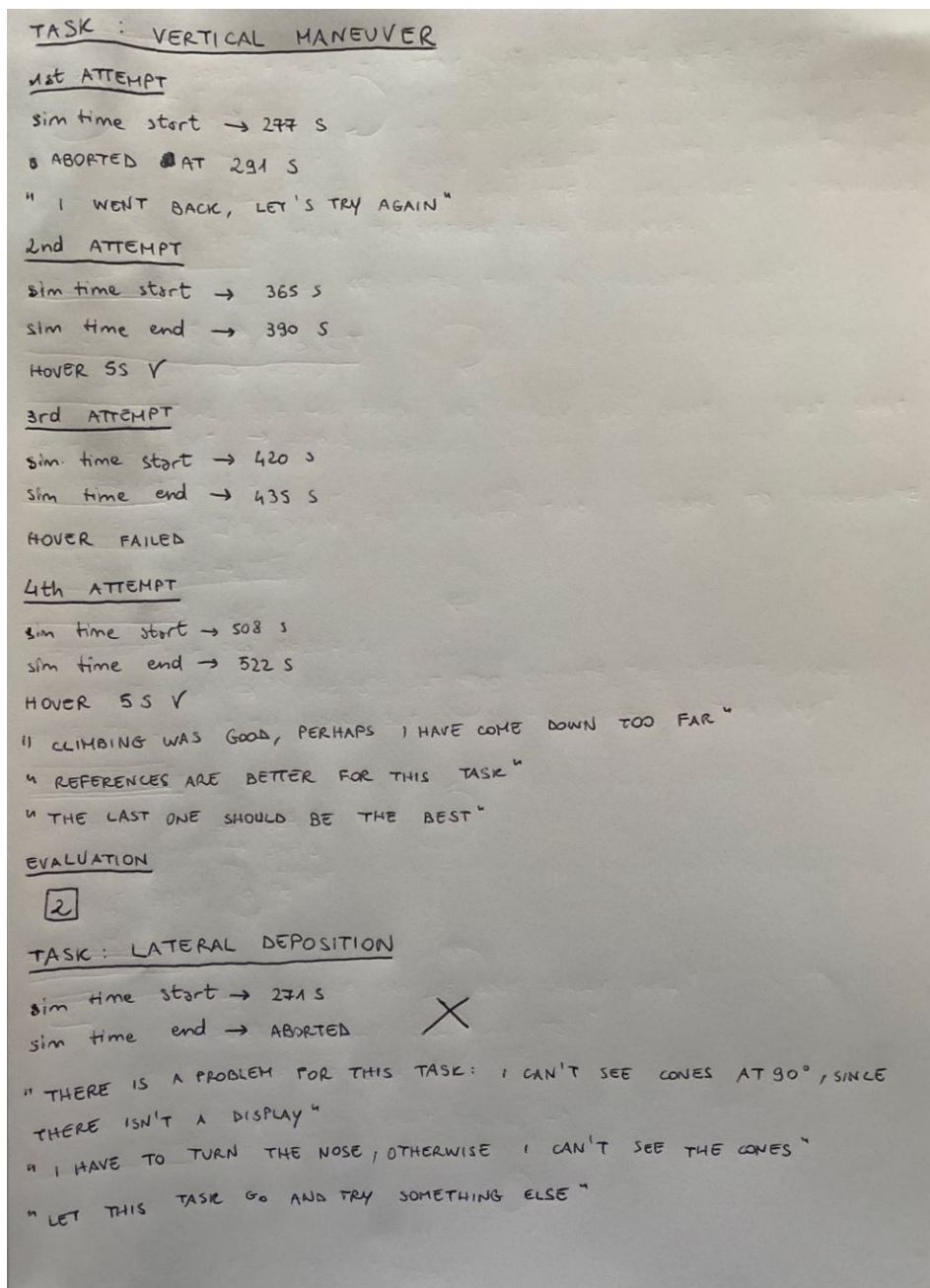


Figure D.5: Flight Test Card 5

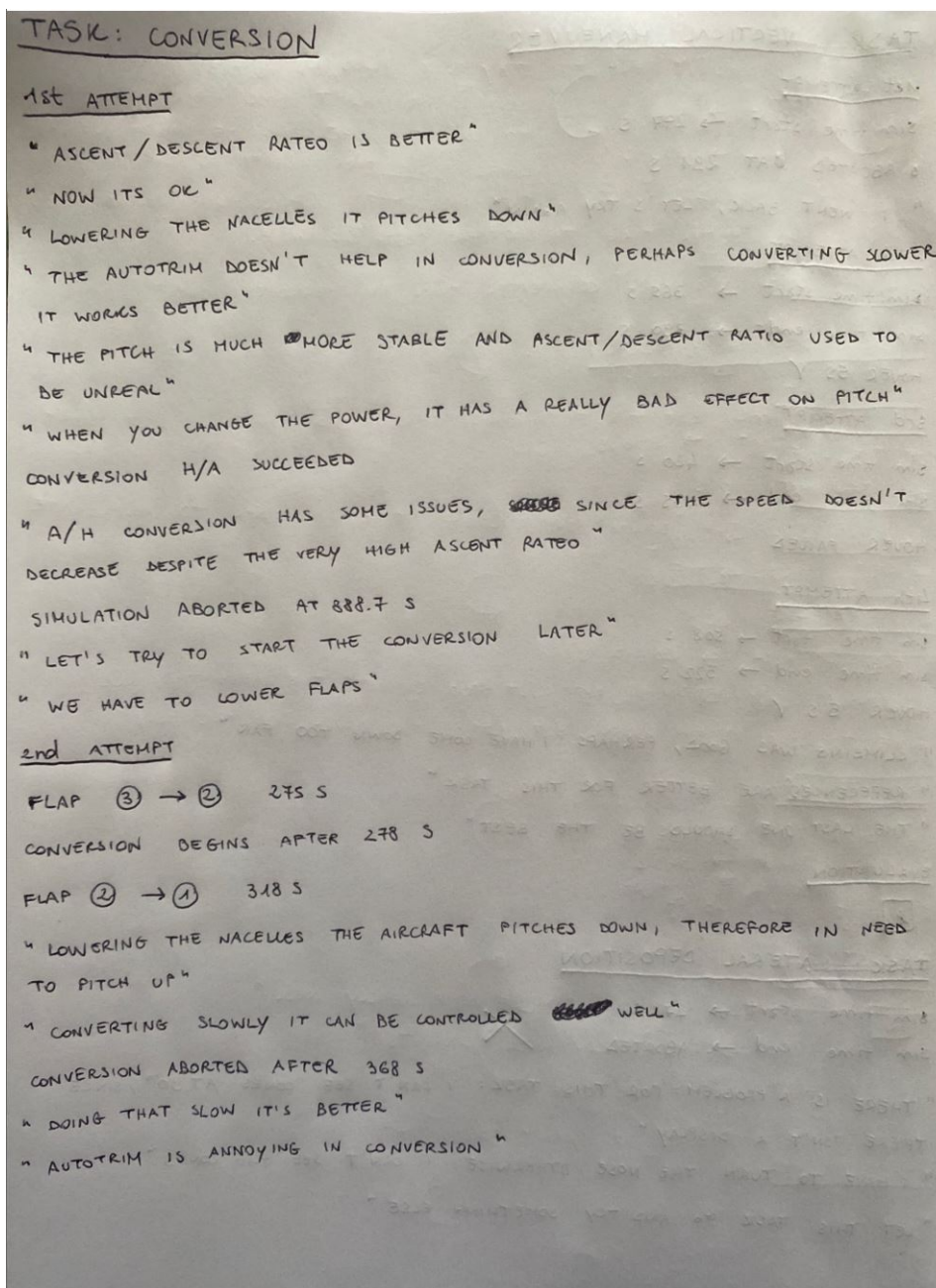


Figure D.6: Flight Test Card 6

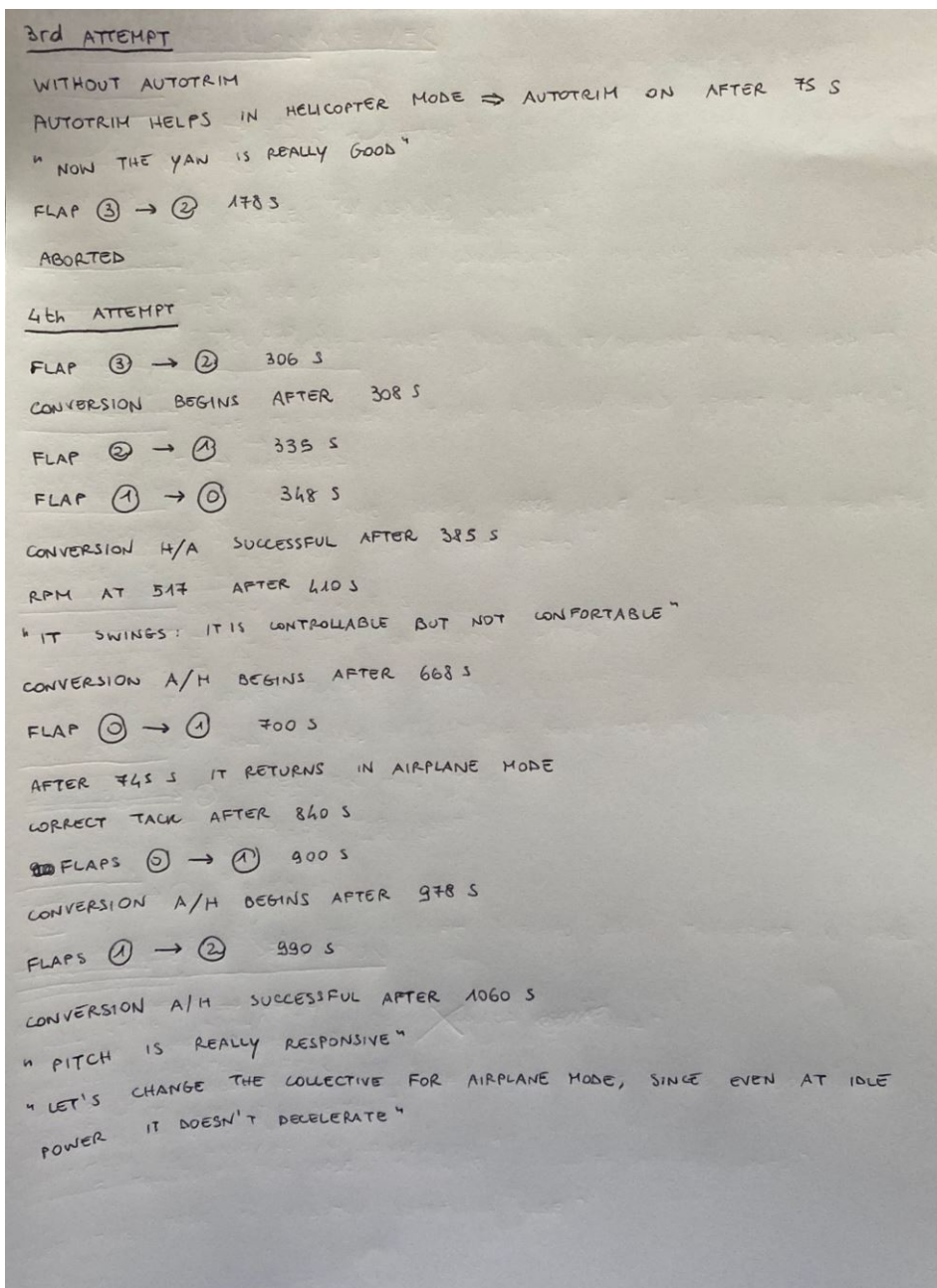


Figure D.7: Flight Test Card 7

5th ATTEMPT

FLAP ③ → ② 345 s

CONVERSION H/A BEGINS AFTER 347 s

FLAP ② → ① 360 s

FLAP ① → ① 368 s

CONVERSION H/A SUCCESSFUL AFTER 408 s

RPM AT 517 AFTER 475 s

" CHANGIN THE POWER EXCITES THE PITCH "

CONVERSION A/H BEGINS AFTER 588 s

FLAP ① → ① 547 s

RPM AT 589 AFTER 565 s

FLAP ① → ② 604 s

CONVERSION A/H SUCCESSFUL AFTER 620 s

" WE SUCCEEDED BETTER "

" TO DECREASE THE SPEED WE HAVE TO LIFT THE NACELLES "

EVALUATION

H/A : 4/5 A/H : 6/7

" WE DON'T KNOW THE CORRECT PROCEDURE FOR THE CONVERSION, THEREFORE MY JUDGEMENT IS WORTH WHAT IT IS WORTH "

" THE PROBLEM OF THE AUTOTRIM IS IN HELICOPTER MODE, SINCE WHEN I START THE CONVERSION THE AIRCRAFT IS PITCHED DOWN, BUT I WOULD PREFER A PITCH UP BEFORE LOWERING THE NACELLES. THIS IS A CRITICAL ISSUE. "

" THE REST WORKS WELL, A PART FROM THE PITCH THAT OSCILLATES "

" WE WOULD NEED TO KNOW THE CORRECT PROCEDURE AS IT IS THOUGHT, MOREOVER WHEN I REMOVE POWER THE AIRCRAFT DOESN'T ~~DE~~ DECELERATE AND IT CLIMBS WITH A RATIO OF 600 f/s, THEREFORE SOMETHING IS STILL WRONG "

" THE JUDGMENT IS AFFECTED FROM THE ~~PRO~~ UNWARENESS OF THE PROCEDURE "

" IT IS SURE THAT IS CONTROLLABLE "

Figure D.8: Flight Test Card 8

LIST OF FIGURES

Figure 1.1	V-22 Osprey in Helicopter, Conversion and Airplane Mode	2
Figure 1.2	Range Comparison between Bell 525 and Bell-Boeing V-22	3
Figure 1.3	Disk Load Comparison between Different Rotor-Aircraft	4
Figure 1.4	XV-15 in Different Flight's Configurations	5
Figure 1.5	General Layout and Major Components of the XV-15	6
Figure 1.6	ZHAW RedSim	7
Figure 1.7	Bell V-22	8
Figure 1.8	Comparison between Helicopters and V-22 During a Mission	9
Figure 1.9	AW 609	10
Figure 1.10	Flight Altitude Comparison between AW 609 and a Generic Helicopter	10
Figure 1.11	Bell V-280 in Flight	11
Figure 1.12	Range Comparison between V-280 and UH-60 Black Hawk	11
Figure 1.13	Airbus A ³ Vahana	12
Figure 1.14	Electric Tilt-Wing Aircraft Currently Developed by Dufour Aerospace	13
Figure 1.15	Bell Eagle Eye Tilt-Rotor UAV	13
Figure 2.1	Rotor Axes System	15
Figure 2.2	Station Line, Water Line and Butt Line	15
Figure 2.3	Body Axis System	16
Figure 2.4	Forces Rotation from Wind into Body Axes	17
Figure 2.5	Moments Rotation from Wind into Body Axes	18
Figure 2.6	Rotations for Transformation from Body into Wind Axes	19
Figure 2.7	Arm Calculation's Example	20
Figure 2.8	Wing and Fuselage Vector Diagram	20
Figure 2.9	Angles of Attack and Sideslip Conventions	22
Figure 2.10	Horizontal Stabilizer Vector Diagram	23
Figure 2.11	Discontinuity Due to the Horizontal Stabilizer's Lift Angle of Attack	25
Figure 2.12	Results with the New Horizontal Stabilizer's Lift Angle of Attack	25
Figure 2.13	C_{LH} Table for $M_N = 0 - 0.2$	27
Figure 2.14	C_{DH} Table	28
Figure 2.15	Vertical Stabilizer Diagram	29
Figure 2.16	Rotor Wake's Angles at the Vertical Stabilizer	31
Figure 2.17	C_{YV} Table	35
Figure 2.18	Vertical Stabilizer's Loads at Different Airspeed	36
Figure 2.19	C_{DV} Table	37
Figure 2.20	Wing Vector Diagram	38
Figure 2.21	Induced Aerodynamics' Scheme	40
Figure 2.22	Induced Forces' Discontinuity	41

Figure 2.23	Continuity for the Induced Forces' Arm	41
Figure 2.24	Induced Forces' Application Point and Affected Area . . .	42
Figure 2.25	Affected Area and Induced Forces' Arm with Airspeed . .	43
Figure 2.26	Induced Forces' Application Point and Affected Area Layout	43
Figure 2.27	Freestream Aerodynamics Vectors	49
Figure 2.28	Vectors for Average Velocities in Mast Axes	53
Figure 2.29	Moments' Arms Due to Spinner Drag	54
Figure 3.1	Trim Data Example	57
Figure 3.2	Angle of Attack and Longitudinal Stick, Test A003	59
Figure 3.3	Rotor and Aerodynamic X Force, Test A003	59
Figure 3.4	Rotor and Aerodynamic Z Force, Test A003	60
Figure 3.5	Root Collective Pitch, Test A003	60
Figure 3.6	Rotor Disk Flapping Angles, Test A003	61
Figure 3.7	Angle of Attack and Longitudinal Stick, Test A042	61
Figure 3.8	Rotor and Aerodynamic X Force, Test A042	62
Figure 3.9	Rotor and Aerodynamic Z Force, Test A042	62
Figure 3.10	Root Collective Pitch, Test A042	63
Figure 3.11	Rotor Disk Flapping Angles, Test A042	63
Figure 3.12	Angle of Attack and Longitudinal Stick, Test A105	64
Figure 3.13	Rotor and Aerodynamic X Force, Test A105	64
Figure 3.14	Rotor and Aerodynamic Z Force, Test A105	65
Figure 3.15	Rotor Disk Flapping Angles, Test A105	65
Figure 3.16	Root Collective Pitch, Test A105	65
Figure 3.17	Flight Test Data Example	66
Figure 3.18	Longitudinal Stick and Elevator Angle, Test 132A	67
Figure 3.19	Pitch Angle and Corrected Power, Test 132A	68
Figure 3.20	Longitudinal Stick and Elevator Angle, Test 157A	68
Figure 3.21	Pitch Angle and Corrected Power, Test 157A	69
Figure 3.22	Longitudinal Stick and Elevator Angle, Test 196C2	69
Figure 3.23	Pitch Angle and Corrected Power, Test 196C2	70
Figure 3.24	Longitudinal Stick of Test 132A with the Correction Pro- vided by Ref. [23]	71
Figure 3.25	Longitudinal Stick and Elevator Angle, Test 159C	72
Figure 3.26	Pitch Angle and Corrected Power, Test 159C	73
Figure 3.27	Longitudinal Stick Map	74
Figure 4.1	Behaviour of a Hovering Rotor's Wake	78
Figure 4.2	Comparison between Flight Test Data and Bennet's Equation	79
Figure 4.3	Flow's Behaviour for a Rotor in Forward Flight Near the Ground	79
Figure 4.4	Ground Effect with Blade Loading in Different Flight Con- ditions	81
Figure 4.5	Ground Effect at Different Disk Load for a Quad tilt-rotor	81
Figure 4.6	Partial Ground Effect Due to the Wing	82
Figure 4.7	Ground Effect for a Wing-Rotor Combination	82
Figure 4.8	Ground Effect with Nacelle Angle	83
Figure 4.9	Ground Effect Model in Simulink	84

Figure 4.10	Rotor Thrust IGE and OGE	85
Figure 4.11	Jet Thrust Transformation from Wind into Body Axes	90
Figure 5.1	Cooper-Harper Rating Scale	92
Figure 5.2	Conversion Corridor for XV-15 Tilt-Rotor	93
Figure 5.3	Pirouette Task Preparation	94
Figure 5.4	Height and Position During Pirouette	95
Figure 5.5	Heading and Lateral Velocity During Pirouette	95
Figure 5.6	3D Position During Pirouette	96
Figure 5.7	Vertical Maneuver Task Preparation	97
Figure 5.8	Aircraft Position During Vertical Maneuver	98
Figure 5.9	Aircraft Height and Heading During Vertical Maneuver	98
Figure 5.10	Depart/Abort Task Preparation	99
Figure 5.11	Aircraft Position During Depart/Abort	100
Figure 5.12	Aircraft Heading and Height During Depart/Abort	101
Figure 5.13	Pitch and Power with CAS	102
Figure 5.14	Mast Angle and Centre of Gravity in $H \rightarrow A$ Conversion	103
Figure 5.15	Conversion Corridor from Helicopter to Airplane	103
Figure 5.16	Commands in $H \rightarrow A$ Conversion	104
Figure 5.17	Euler's Angles in $H \rightarrow A$ Conversion	104
Figure 5.18	Right Rotor Forces in $H \rightarrow A$ Conversion	105
Figure 5.19	Right Rotor Moments in $H \rightarrow A$ Conversion	105
Figure 5.20	Power in $H \rightarrow A$ Conversion	106
Figure 5.21	Aerodynamic Forces in $H \rightarrow A$ Conversion	106
Figure 5.22	Aerodynamic Moments in $H \rightarrow A$ Conversion	107
Figure 5.23	Flaps and Mach in $H \rightarrow A$ Conversion	107
Figure 5.24	Mast Angle and Centre of Gravity in $A \rightarrow H$ Conversion	108
Figure 5.25	Conversion Corridor from Airplane to Helicopter	109
Figure 5.26	Commands in $A \rightarrow H$ Conversion	109
Figure 5.27	Euler's Angles in $A \rightarrow H$ Conversion	110
Figure 5.28	Right Rotor Forces in $A \rightarrow H$ Conversion	110
Figure 5.29	Right Rotor Moments in $A \rightarrow H$ Conversion	111
Figure 5.30	Power in $A \rightarrow H$ Conversion	111
Figure 5.31	Aerodynamic Forces in $A \rightarrow H$ Conversion	112
Figure 5.32	Aerodynamic Moments in $A \rightarrow H$ Conversion	112
Figure 5.33	Flaps and Mach in $A \rightarrow H$ Conversion	112
Figure 5.34	Conversion Corridor of a Failed Tilt $A \rightarrow H$	113
Figure 5.35	Angle of Attack and Sideslip of a Failed Conversion $A \rightarrow H$	113
Figure 5.36	Flap Angle and Mach Number of a Failed Conversion $A \rightarrow H$	114
Figure 5.37	Rotor Forces of a Failed Conversion $A \rightarrow H$	114
Figure 5.38	Power of a Failed Conversion $A \rightarrow H$	115
Figure A.1	Procedure Part 1	127
Figure A.2	Procedure Part 2	127
Figure A.3	Procedure Part 3	128
Figure A.4	Procedure Part 4	128
Figure A.5	Procedure Part 5	129

Figure A.6	Procedure Part 6	129
Figure B.1	Fuselage L_α	140
Figure B.2	Fuselage D_α	141
Figure B.3	Fuselage M_α	141
Figure B.4	Fuselage L_β	142
Figure B.5	Fuselage D_β	143
Figure B.6	Fuselage M_β	143
Figure B.7	Fuselage l_β	144
Figure B.8	Fuselage N_β	144
Figure B.9	Fuselage Y_β	144
Figure B.10	XK_e Table	145
Figure B.11	$K_{\beta HS}$ Table	145
Figure B.12	η_H Table	145
Figure B.14	C_{LH} Table	147
Figure B.15	C_{DH} Table	148
Figure B.16	Sidewash Factor for $X_{FL} = 0/0 \text{ deg}$	149
Figure B.17	Sidewash Factor for $X_{FL} = 20/12.5 \text{ deg}$	150
Figure B.18	Sidewash Factor for $X_{FL} = 40/25 \text{ deg}$	151
Figure B.19	Sidewash Factor for $X_{FL} = 75/47 \text{ deg}$	152
Figure B.20	$K_{\beta R}$ Table	152
Figure B.21	C_{YV} Table	153
Figure B.22	C_{DV} Table	154
Figure B.23	C_{LWP} for $M_N = 0$	155
Figure B.24	C_{LWP} for $M_N \neq 0$	156
Figure B.25	C_{DWP} for $M_N \neq 0$	156
Figure B.26	C_{DWP} for $M_N = 0$	157
Figure B.27	C_{mWP} Table	158
Figure B.28	$\varepsilon_{W/H}$ Table	158
Figure B.29	$C_{L\delta_a}$ Table	158
Figure B.30	$\frac{\partial C_{LWPFES}}{\partial \alpha_{WFS}} _{C_{LWP}=0}$ Table	159
Figure B.31	$\frac{C_{l\beta}}{C_{LWP}} _{M_N=0}$ Table	159
Figure B.32	$C_{l\beta} _{C_{LWP}=M_N=0}$ Table	159
Figure B.33	$K_{l\delta_a}$ Table	160
Figure B.34	$K_{n\delta_a}$ Table	160
Figure B.35	$K_{n0\delta_a}$ Table	160
Figure B.36	$C_{D0WP} _{C_{LWP}=0}$ Table	161
Figure B.37	D_{PYNT} Table	161
Figure B.38	K_{PLAT} Table	161
Figure C.1	Test A024	162
Figure C.2	Test A057	163
Figure C.3	Test A072	164
Figure C.4	Test A087	165
Figure C.5	Test A132	166
Figure C.6	Test 129B	167
Figure C.7	Test 132B	167

Figure C.8	Test 157B	167
Figure C.9	Test 158A	168
Figure C.10	Test 196C1	168
Figure C.11	Test 197A	168
Figure D.1	Flight Test Card 1	169
Figure D.2	Flight Test Card 2	170
Figure D.3	Flight Test Card 3	171
Figure D.4	Flight Test Card 4	172
Figure D.5	Flight Test Card 5	173
Figure D.6	Flight Test Card 6	174
Figure D.7	Flight Test Card 7	175
Figure D.8	Flight Test Card 8	176

LIST OF TABLES

Table 2.1	$k_{\beta r}$ Table Provided by GTRS Model	36
Table 2.2	Modified $k_{\beta r}$ Table	37
Table 3.1	Trim Conditions for GTRS Model	57
Table 3.2	Trim Conditions for Flight Test Data in Airplane Mode . .	67
Table 3.3	Trim Conditions from Flight Test Data in Helicopter Mode	72
Table 3.4	Trim Conditions Set for the Map	73
Table 3.5	Conditions for Eigenvalues Comparison	75
Table 3.6	Eigenvalues Comparison in Hover	75
Table 4.1	Eigenvalues Comparison in Hover and IGE	85
Table 4.2	Landing Gear Drag Coefficient	87
Table 4.3	Jet Thrust Coefficients	88
Table 4.4	Jet Thrust Horse Power	89
Table 5.1	DVE Performance Standards for the Pirouette	94
Table 5.2	DVE Performance Standards for the Vertical Maneuver . .	97
Table 5.3	DVE Performance Standards for the Depart/Abort	100

ACRONYMS

DVE Degraded Visual Condition	93
GTRS Generic Tilt-Rotor Simulation	8
GVE Good Visual Condition	93
IGE In Ground Effect	77
OGE Out of Ground Effect	78
S/N Ship Number	67
V/STOL Vertical and Short Take-Off Landing	2
VTOL Vertical Take-Off Landing	2

LIST OF ABBREVIATIONS

c.g.	Centre of Gravity
c.p.	Centre of Pressure
Ref.	Reference

NOMENCLATURE

$\left(1 - \frac{\partial \sigma}{\partial \beta_F}\right)$	Vertical Stabilizer Sidewash Factor	[ND]
AR_W	Aspect Ratio	[ND]
a_V	Lift Curve Slope of the Vertical Tail	[rad ⁻¹]
B	Blade Tip Loss Factor	[ND]
B_C	Prandtl-Glauert Compressibility Factor	[ND]
BL_{CG}	Butt Line of c.g.	[in]
BL_F	Butt Line of the Fuselage c.p.	[in]
BL_H	Butt Line of the Horizontal Stabilizer c.p.	[in]
BL_{LTIP_e}	Butt Line of the External Tip of the Left Rotor	[in]
BL_{LTIP_i}	Butt Line of the Internal Tip of the Left Rotor	[in]
BL_{RTIP_e}	Butt Line of the External Tip of the Right Rotor	[in]
BL_{RTIP_i}	Butt Line of the Internal Tip of the Right Rotor	[in]
BL_{SP}	Butt Line of the Shaft-Pivot	[in]
BL_V	Butt Line of the Vertical Stabilizer c.p.	[in]
BL_{WP}	Butt Line of the Wing-Pylon c.p.	[in]
b_W	Wing Span	[ft]
CAS	Calibrated Air Speed	[kts]
$C_{D0WP} _{C_{LWP}=0}$	Aerodynamic Coefficient in the Wing Yawing Moment Equation	[rad ⁻¹]
C_{DH}	Horizontal Stabilizer Drag Coefficient	[ND]
C_{DV}	Vertical Stabilizer Drag Coefficient	[ND]
$C_{DV} _{\delta_r}$	Vertical Stabilizer Drag Coefficient in Output from the Table	[ND]
C_{DWP}	Wing-Pylon Drag Coefficient	[ND]
c_H	Horizontal Stabilizer Chord	[ft]
C_{LH}	Horizontal Stabilizer Lift Coefficient	[ND]
$C_{LH\beta}$	Horizontal Stabilizer Lift Coefficient as a Function of Sideslip Angle	[deg ⁻¹]

- C_{lp} Aerodynamic Angular Coefficient in the Wing Rolling Moment Equation
Due to Pitching $[rad^{-1}]$
- $C_{lp|C_{LWP}=M_N=0}$ Aerodynamic Coefficient in the Wing Rolling Moment Equation $[rad^{-1}]$
- C_{lr} Aerodynamic Angular Coefficient in the Wing Rolling Moment Equation
Due to Rolling $[rad^{-1}]$
- $C_{lr|C_{LWP}=M_N=0}$ Aerodynamic Coefficient in the Wing Rolling Moment Equation $[rad^{-1}]$
- C_{LWP} Wing-Pylon Lift Coefficient $[ND]$
- $C_{l\beta}$ Aerodynamic Angular Coefficient in the Wing Rolling Moment Equation
Due to Sideslip $[rad^{-1}]$
- $C_{l\beta|C_{LWP}=M_N=0}$ Aerodynamic Coefficient in the Wing Rolling Moment Equation $[rad^{-1}]$
- $\left(\frac{C_{l\beta}}{C_{LWP}}\right)_{M_N=0}$ Aerodynamic Coefficient in the Wing Rolling Moment Equation $[rad^{-1}]$
- $C_{L\delta_a}$ Aerodynamic Coefficient for the Wing Lift Coefficient Reduction Due to
Aileron Deflection $[deg^{-1}]$
- $C_{l\delta_a}$ Aerodynamic Angular Coefficient in the Wing Rolling Moment Equation
Due to Aileron Deflection $[deg^{-1}]$
- $C_{l\delta_a}^{\delta_F=0^\circ}_{\alpha_{WFS}<8^\circ}$ Aerodynamic Coefficient in the Wing Rolling Moment Equation $[deg^{-1}]$
- C_{MH0} Horizontal Stabilizer Pitching Moment Coefficient at Zero Angle of Attack $[ND]$
- C_{MHA} Horizontal Stabilizer Pitching Moment Coefficient Variation with Angle
of Attack $[deg^{-1}]$
- C_{mWP} Wing-Pylon Pitching Moment Coefficient $[ND]$
- C_{np} Aerodynamic Angular Coefficient in the Wing Yawing Moment Equation
Due to Pitching $[rad^{-1}]$
- $\left(\frac{C_{np}}{C_{LWP}}\right)_{M_N=0}$ Aerodynamic Coefficient in the Wing Yawing Moment Equation $[rad^{-1}]$
- C_{nr} Aerodynamic Angular Coefficient in the Wing Yawing Moment Equation
Due to Rolling $[rad^{-1}]$
- $\left(\frac{C_{nr}}{C_{DOWP}}\right)$ Aerodynamic Coefficient in the Wing Yawing Moment Equation $[rad^{-1}]$
- $\left(\frac{C_{nr}}{C_{LWP}^2}\right)$ Aerodynamic Coefficient in the Wing Yawing Moment Equation $[rad^{-1}]$
- $C_{n\beta}$ Aerodynamic Angular Coefficient in the Wing Yawing Moment Equation
Due to Sideslip $[rad^{-1}]$
- $C_{n\beta|C_{LWP}=M_N=0}$ Aerodynamic Coefficient in the Wing Yawing Moment Equation $[rad^{-1}]$

$\left(\frac{C_{n\beta}}{C_{LWPFs}^2} \Big _{M_N=0} \right)$	Aerodynamic Coefficient in the Wing Yawing Moment Equation	$[rad^{-1}]$
$C_{n\delta_a}$	Aerodynamic Angular Coefficient in the Wing Yawing Moment Equation Due to Aileron Deflection	$[rad^{-1}]$
C_{RFL}	Left Rotor Force Coefficient	$[ND]$
C_{RFR}	Right Rotor Force Coefficient	$[ND]$
C_T	Thrust Coefficient	$[ND]$
C_{TIGE}	Thrust Coefficient In Ground Effect	$[ND]$
C_{TOGE}	Thrust Coefficient Out of Ground Effect	$[ND]$
c_W	Wing Chord	$[ft]$
C_{Yp}	Aerodynamic Angular Coefficient in the Wing Side Force Equation Due to Rolling	$[rad^{-1}]$
$\left(\frac{C_{Yp}}{C_{LWP}} \Big _{M_N=0} \right)$	Aerodynamic Coefficient in the Wing Side Force Equation	$[rad^{-1}]$
C_{Yr}	Aerodynamic Angular Coefficient in the Wing Side Force Equation Due to Yawing	$[rad^{-1}]$
$C_{Yr M_N=0}$	Aerodynamic Coefficient in the Wing Side Force Equation	$[rad^{-1}]$
C_{YV}	Vertical Stabilizer Side Force Coefficient	$[ND]$
$C_{YV \delta_r}$	Vertical Stabilizer Side Force Coefficient in Output from the Table at any δ_r	$[ND]$
$C_{YV \delta_r=0}$	Vertical Stabilizer Side Force Coefficient in Output from the Table at $\delta_r = 0$	$[ND]$
$C_{Y\beta}$	Aerodynamic Angular Coefficient in the Wing Side Force Equation Due to Sideslip	$[rad^{-1}]$
$C_{Y\beta M_N=0}$	Aerodynamic Coefficient in the Wing Side Force Equation	$[rad^{-1}]$
C_β	Prandtl-Glauert Compressibility Factor	$[ND]$
D_{BF0}	Fuselage Drag at $\alpha = 0^\circ$ and $\beta = 0^\circ$	$[ft^2]$
D_F	Aerodynamic Drag on Fuselage (Wind Axis)	$[lb]$
D_H	Aerodynamic Drag on Horizontal Stabilizer (Wind Axis)	$[lb]$
D_{iWK}	Aerodynamic Drag of the Wing Portion Immersed in the Rotor Wake in Wind Axis, K=R \rightarrow Right, K=L \rightarrow Left	$[lb]$
D_{Ke}	Elevator Effectiveness Reduction Factor for Large Elevator Angles	$[ND]$

D_{Kr}	Rudder Effectiveness Reduction Factor for Large Elevator Angles	[ND]
D_{LANG}	Extra Fuselage Drag	[ft ²]
D_{M0G}	Drag Coefficient of the Main Landing Gear	[ft ²]
D_{MG}	Aerodynamic Drag on Main Landing Gear	[lb]
D_{N0G}	Drag Coefficient of the Nose Landing Gear	[ft ²]
D_{NG}	Aerodynamic Drag on Nose Landing Gear	[lb]
D_{P0D}	Fuselage Landing Gear Pod Drag	[ft ²]
D_{PLAT}	Pylon Drag Due to Sideslip	[lb]
D_{PYINT}	Pylon Interference Drag Coefficient	[ft ²]
D_{PYLN}	Pylon Interference Drag	[lb]
D_V	Aerodynamic Drag on Vertical Stabilizer (Wind Axis)	[lb]
D_{WP}	Aerodynamic Drag of the Wing Portion Outside the Rotor Wake in Wind Axis (Freestream)	[lb]
D_α	Fuselage Drag Variation with Angle of Attack	[ft ²]
D_β	Fuselage Drag Variation with Sideslip Angle	[ft ²]
h_m	Altitude of the Aircraft c.g.	[ft]
h_{mGND}	Altitude of the Ground	[ft]
i_H	Horizontal Stabilizer Incidence	[deg]
i_V	Vertical Stabilizer Incidence	[deg]
JT_K	Jet Thrust in Wind Axes, K=R→Right, K=L→Left	[lb]
K_e, XK_e	Elevator Effectiveness Factor	[ND]
K_{FW}	Rotor Downwash/Wing Equation for Flap Effects	[ND]
K_{FW0}	Constant in the Rotor Downwash/Wing Equation for Flap Effects	[ND]
K_{FWDF}	Slope in the Rotor Downwash/Wing Equation for Flap Effects	[deg ⁻¹]
K_{GE}	Ground Effect Coefficient	[ND]
K_{HNU}	Horizontal Stabilizer Dynamic Pressure Loss Multiplier	[ND]
K_{JT1}	Jet Thrust Coefficient	[lb]
K_{JT2}	Jet Thrust Coefficient	[lb/SHP]
$K_{l\delta_a}$	Aileron Effectiveness Correction Factor	[ND]

$K_{n0\delta_a}$	Yawing Moment (Aileron) Coefficient	$[deg^{-1}]$
$K_{n\delta_a}$	Yawing Moment (Aileron) Coefficient	$[ND]$
K_{PLAT}	Pylon Lateral Drag Coefficient	$[ND]$
K_r, XK_r	Rudder Effectiveness Factor	$[ND]$
K_{RW}	Rotor Skew Angle Velocity Distribution Factor	$[ND]$
K_{VNU}	Vertical Stabilizer Dynamic Pressure Loss Multiplier	$[ND]$
K_{XRW}	Constant in the Rotor Downwash/Wing Equation	$[ND]$
$K_{\beta HS}$	Sideslip Factor on Dynamic Pressure Ratio at the Horizontal Stabilizer	$[ND]$
$K_{\beta r}$	Rotor Sidewash Factor on Dynamic Pressure	$[ND]$
$K_{\beta VS}$	Sideslip Factor on Dynamic Pressure Ratio at the Vertical Stabilizer	$[ND]$
L_{BF0}	Fuselage Lift at $\alpha = 0^\circ$ and $\beta = 0^\circ$	$[ft^2]$
L_F	Aerodynamic Lift on Fuselage (Wind Axis)	$[lb]$
l_F	Aerodynamic Rolling Moment on Fuselage (Body Axis)	$[lb \cdot ft]$
l'_F	Aerodynamic Rolling Moment on Fuselage (Wind Axis)	$[lb \cdot ft]$
L_H	Aerodynamic Lift on Horizontal Stabilizer (Wind Axis)	$[lb]$
l_H	Aerodynamic Rolling Moment on Horizontal Stabilizer (Body Axis)	$[lb \cdot ft]$
l_{iPYL}	Aerodynamic Rolling Moment Due to Pylon Interference Drag (Body Axis)	$[lb \cdot ft]$
L_{iWK}	Aerodynamic Lift of the Wing Portion Immersed in the Rotor Wake in Wind Axis, K=R \rightarrow Right, K=L \rightarrow Left	$[lb]$
l_{iWK}	Aerodynamic Rolling Moment in Body Axis Due to Induced Forces, K=R \rightarrow Right, K=L \rightarrow Left	$[lb \cdot ft]$
l_{JT}	Rolling Moment Due to Jet Thrust (Body Axis)	$[lb \cdot ft]$
L_{LANG}	Extra Fuselage Lift	$[ft^2]$
l_{MG}	Rolling Moment Due to Main Landing Gear Drag (Body Axis)	$[lb \cdot ft]$
l_{NG}	Rolling Moment Due to Nose Landing Gear Drag (Body Axis)	$[lb \cdot ft]$
l_{PLAT}	Aerodynamic Rolling Moment Due to Pylon Drag During Sideslip (Body Axis)	$[lb \cdot ft]$
l_{SD}	Aerodynamic Rolling Moment Due to Spinner Drag (Body Axis)	$[lb \cdot ft]$
l_V	Aerodynamic Rolling Moment on Vertical Stabilizer (Body Axis)	$[lb \cdot ft]$

L_{WP}	Aerodynamic Lift of the Wing Portion Outside the Rotor Wake (Freestream) in Wind Axis	[lb]
l_{WP}	Aerodynamic Rolling Moment on Wing-Pylon (Body Axis)	[lb · ft]
l'_{WP}	Aerodynamic Rolling Moment on Wing-Pylon (Wind Axis)	[lb · ft]
l_{XF}	Fuselage Arm along X Respect to c.g.	[ft]
l_{XH}	Horizontal Stabilizer Arm along X Respect to c.g.	[ft]
$l_{X RV}$	X Arm between the Vertical Stabilizer and the Shaft-Pivot	[ft]
l_{XV}	Vertical Stabilizer Arm along X Respect to c.g.	[ft]
l_{YF}	Fuselage Arm along Y Respect to c.g.	[ft]
l_{YH}	Horizontal Stabilizer Arm along Y Respect to c.g.	[ft]
l_{YV}	Vertical Stabilizer Arm along Y Respect to c.g.	[ft]
l_{ZF}	Fuselage Arm along Z Respect to c.g.	[ft]
l_{ZH}	Horizontal Stabilizer Arm along Z Respect to c.g.	[ft]
l_{ZV}	Vertical Stabilizer Arm along Z Respect to c.g.	[ft]
L_{α}	Fuselage Lift Variation with Angle of Attack	[ft ²]
L_{β}	Fuselage Lift Variation with Sideslip Angle	[ft ²]
l_{β}	Fuselage Rolling Moment Variation with Sideslip Angle	[ft ³]
M_F	Aerodynamic Pitching Moment on Fuselage (Body Axis)	[lb · ft]
M'_F	Aerodynamic Pitching Moment on Fuselage (Wind Axis)	[lb · ft]
M'_H	Aerodynamic Pitching Moment on Horizontal Stabilizer (Wind Axis)	[lb · ft]
M_H	Aerodynamic Pitching Moment on Horizontal Stabilizer (Body Axis)	[lb · ft]
M_{iPYL}	Aerodynamic Pitching Moment Due to Pylon Interference Drag (Body Axis)	[lb · ft]
M_{iWK}	Aerodynamic Pitching Moment in Body Axis Due to Induced Forces, K=R → Right, K=L → Left	[lb · ft]
M_{JT}	Pitching Moment Due to Jet Thrust (Body Axis)	[lb · ft]
M_{MG}	Pitching Moment Due to Main Landing Gear Drag (Body Axis)	[lb · ft]
M_N	Mach Number	[ND]

M_{NG}	Pitching Moment Due to Nose Landing Gear Drag (Body Axis)	$[lb \cdot ft]$
M_{PLAT}	Aerodynamic Pitching Moment Due to Pylon Drag During Sideslip (Body Axis)	$[lb \cdot ft]$
M_{SD}	Aerodynamic Pitching Moment Due to Spinner Drag (Body Axis)	$[lb \cdot ft]$
M_V	Aerodynamic Pitching Moment on Vertical Stabilizer (Body Axis)	$[lb \cdot ft]$
M_{WP}	Aerodynamic Pitching Moment on Wing-Pylon (Body Axis)	$[lb \cdot ft]$
M'_{WP}	Aerodynamic Pitching Moment on Wing-Pylon (Wind Axis)	$[lb \cdot ft]$
M_α	Fuselage Pitching Moment Variation with Angle of Attack	$[ft^3]$
M_β	Fuselage Pitching Moment Variation with Sideslip Angle	$[ft^3]$
N_F	Aerodynamic Yawing Moment on Fuselage (Body Axis)	$[lb \cdot ft]$
N'_F	Aerodynamic Yawing Moment on Fuselage (Wind Axis)	$[lb \cdot ft]$
N_H	Aerodynamic Yawing Moment on Horizontal Stabilizer (Body Axis)	$[lb \cdot ft]$
N_{iPYL}	Aerodynamic Yawing Moment Due to Pylon Interference Drag (Body Axis)	$[lb \cdot ft]$
N_{iWK}	Aerodynamic Yawing Moment in Body Axis Due to Induced Forces, K=R \rightarrow Right, K=L \rightarrow Left	$[lb \cdot ft]$
N_{JT}	Yawing Moment Due to Jet Thrust (Body Axis)	$[lb \cdot ft]$
N_{MG}	Yawing Moment Due to Main Landing Gear Drag (Body Axis)	$[lb \cdot ft]$
N_{NG}	Yawing Moment Due to Nose Landing Gear Drag (Body Axis)	$[lb \cdot ft]$
N_{PLAT}	Aerodynamic Yawing Moment Due to Pylon Drag During Sideslip (Body Axis)	$[lb \cdot ft]$
N_{SD}	Aerodynamic Yawing Moment Due to Spinner Drag (Body Axis)	$[lb \cdot ft]$
N_V	Aerodynamic Yawing Moment on Vertical Stabilizer (Body Axis)	$[lb \cdot ft]$
N_{WP}	Aerodynamic Yawing Moment on Wing-Pylon (Body Axis)	$[lb \cdot ft]$
N'_{WP}	Aerodynamic Yawing Moment on Wing-Pylon (Wind Axis)	$[lb \cdot ft]$
N_β	Fuselage Yawing Moment Variation with Sideslip Angle	$[ft^3]$
p	Body Axis Rolling Rate	$[rad/s]$
p_w	Wind Axis Rolling Rate	$[rad/s]$
q	Body Axis Pitching Rate	$[rad/s]$

q_F	Fuselage Dynamic Pressure	$[lb/ft^2]$
q_H	Horizontal Stabilizer Dynamic Pressure	$[lb/ft^2]$
q_{iWK}	Dynamic Pressure of the Wing Portion Immersed in the Rotor Wake	$[lb/ft^2]$
q_{LG}	Landing Gear Dynamic Pressure	$[lb/ft^2]$
q_{PLAT}	Dynamic Pressure for Pylon Drag Due to Sideslip	$[lb/ft^2]$
q_{SP}	Dynamic Pressure in Mast Axis System	$[lb/ft^2]$
q_V	Vertical Stabilizer Dynamic Pressure	$[lb/ft^2]$
q_w	Wind Axis Pitching Rate	$[rad/s]$
q_{WFS}	Dynamic Pressure of the Wing Portion Outside the Rotor Wake (Freestream)	$[lb/ft^2]$
R	Rotor Radius	$[ft]$
r	Body Axis Yawing Rate	$[rad/s]$
R_{SHP}	Commanded (Throttle) Referred Optimum SHP on One Engine	$[SHP]$
r_w	Wind Axis Yawing Rate	$[rad/s]$
R_{WK}	Rotor Wake Contraction Ratio, K=R→Right, K=L→Left	$[ft]$
SD	Spinner Drag	$[lb]$
SD/q	Constant in the variable Drag Portion of the Spinner Drag Equation	$[ft^2]$
$SD/q_{\beta_M=90^\circ}$	Constant for Drag of the spinner at 90 degrees of Mast conversion Angle	$[ft^2]$
S_H	Horizontal Stabilizer Area	$[ft^2]$
S_{iWK}	Wing surface Immersed in the Rotor wake, K=R→Right, K=L→Left	$[ft^2]$
SL_{CG}	Station Line of the c.g.	$[in]$
SL_F	Station Line of Fuselage c.p.	$[in]$
SL_H	Station Line of the Horizontal Stabilizer c.p.	$[in]$
SL_{MG}	Station Line of Main Landing Gear	$[in]$
SL_{NG}	Station Line of Nose Landing Gear	$[in]$
SL_{SP}	Station Line of the Shaft-Pivot	$[in]$
SL_V	Station Line of the Vertical Stabilizer c.p.	$[in]$
SL_{WP}	Station Line of the Wing-Pylon c.p.	$[in]$
SL_{WTE}	Station Line of the Wing Trailing Edge	$[in]$

S_{PLAT}	Surface for Pylon Drag Due to Sideslip	[ft^2]
S_{PYL}	Projected Lateral Pylon Area	[ft^2]
S_V	Vertical Stabilizer Fin Area	[ft^2]
S_W	Wing Area	[ft^2]
S_{WFS}	Wing surface Outside the Rotor Wake (Freestream)	[ft^2]
TAS	True Air Speed	[kts]
T_{IGE}	Thrust In Ground Effect	[lb]
T_{OGE}	Thrust Out of Ground Effect	[lb]
U	X-Velocity of the Aircraft c.g. in Body Axis with Respect to the Air	[ft/s]
U_H	Overall X-Velocity at the Horizontal Stabilizer in Body Axis	[ft/s]
$U_{i_{BR WK}}$	Induced X-Velocity at the Wing, in Body Axis, Due to the Rotor, K=R → Right, K=L → Left	[ft/s]
$U_{i_{RH}}$	Induced X-Velocity at Horizontal Stabilizer, in Body Axis, Due to the Rotor	[ft/s]
$U_{i_{RV}}$	Induced X-Velocity at Vertical Stabilizer, in Body Axis, Due to the Rotor	[ft/s]
$U_{i_{SP}}$	Average Induced X-Velocity in Body Axis	[ft/s]
U_{MSP}	X-Velocity in Mast Axis System	[ft/s]
U_V	Overall X-Velocity at the Vertical Stabilizer in Body Axis	[ft/s]
U_{WK}	Overall X-Velocity at the Wing in Body Axis, K=R → Right, K=L → Left	[ft/s]
V	Y-Velocity of the Aircraft c.g. in Body Axis with Respect to the Air	[ft/s]
V_H	Overall Y-Velocity at the Horizontal Stabilizer in Body Axis	[ft/s]
V_{HT}	Total Velocity at the Horizontal Stabilizer in Body Axis	[ft/s]
V_T	Total Linear Velocity of the Rotorcraft c.g. with Respect to the Air	[ft/s]
$V_{Ti_{WK}}$	Total Velocity at the Wing in Body Axis for the Induced Aerodynamics	[ft/s]
V_{TSP}	Total Velocity in Mast Axis System	[ft/s]
V_V	Overall Y-Velocity at the Vertical Stabilizer in Body Axis	[ft/s]
V_{VT}	Total Velocity at the Vertical Stabilizer in Body Axis	[ft/s]
V_{WK}	Overall Y-Velocity at the Wing in Body Axis, K=R → Right, K=L → Left	[ft/s]
W	Z-Velocity of the Aircraft c.g. in Body Axis with Respect to the Air	[ft/s]

W_H	Overall Z-Velocity at the Horizontal Stabilizer in Body Axis	[ft/s]
$W_{i_{BR WK}}$	Induced Z-Velocity at the Wing, in Body Axis, Due to the Rotor, K=R→Right, K=L→Left	[ft/s]
W_{iK}	Mast Axis uniform component of Induced Velocity at: K=R→Right Rotor, K=L→Left Rotor	[ft/s]
$W_{i_{RH}}$	Induced Z-Velocity at Horizontal Stabilizer, in Body Axis, Due to the Rotor	[ft/s]
$W_{i_{RV}}$	Induced Z-Velocity at Vertical Stabilizer, in Body Axis, Due to the Rotor	[ft/s]
$W_{i_{RWK}}$	Induced Velocity at the Wing in Mast Axis Due to the Rotor, K=R→Right, K=L→Left	[ft/s]
W_{iSP}	Average Induced Z-Velocity in Body Axis	[ft/s]
WL_{CG}	Water Line of c.g.	[in]
WL_F	Water Line of the Fuselage c.p.	[in]
WL_H	Water Line of the Horizontal Stabilizer c.p.	[in]
WL_{MG}	Water Line of Main Landing Gear	[in]
WL_{NG}	Water Line of Nose Landing Gear	[in]
WL_V	Water Line of the Vertical Stabilizer c.p.	[in]
WL_{WP}	Water Line of the Wing-Pylon c.p.	[in]
W_{MSP}	Z-Velocity in Mast Axis System	[ft/s]
W_V	Overall Z-Velocity at the Vertical Stabilizer in Body Axis	[ft/s]
W_{WK}	Overall Z-Velocity at the Wing in Body Axis, K=R→Right, K=L→Left	[ft/s]
X_{EK}	Engine Operating Flag, K=R→Right, K=L→Left	[ND]
X_F	Aerodynamic X-Force on Fuselage (Body Axis)	[lb]
X_H	Aerodynamic X-Force on Horizontal Stabilizer (Body Axis)	[lb]
X_{iPYL}	Aerodynamic X-Force Due to Pylon Interference Drag (Body Axis)	[lb]
X_{iWK}	Arm between the X-Coordinate of the Application Point of Induced Forces on the Wing and the c.g., K=R→Right, K=L→Left	[ft]
X_{iWPK}	Aerodynamic X-Force on the Wing Portion Immersed in the Rotor Wake in Body Axis, K=R→Right, K=L→Left	[lb]
X_{JTK}	Jet Thrust along X-Body, K=R→Right, K=L→Left	[lb]

X_K	Mobile Coordinate for the Definition of the Induced Aerodynamics' Application Point along X, K=R→Right, K=L→Left	[ft]
X_{MG}	Main Landing Gear Force in X-Body	[lb]
X_{NG}	Nose Landing Gear Force in X-Body	[lb]
X_{PLAT}	Aerodynamic X-Force Due to Pylon Drag During Sideslip (Body Axis)	[lb]
X_{RW}	Rotor Downwash/Wing Function	[ND]
X_{RW0}	Constant in the Rotor Downwash/Wing Equation	[ND]
X_{RW1}	Constant in the Rotor Downwash/Wing Equation	[deg ⁻¹]
X_{RW2}	Constant in the Rotor Downwash/Wing Equation	[deg ⁻²]
X_{THK}	Engine Throttle Position at the Fuel Control, K=R→Right, K=L→Left	[deg]
X_{SD}	Aerodynamic X-Force Due to Spinner Drag (Body Axis)	[lb]
X_{SS}	Mutual Induction Coefficient	[ND]
X_V	Aerodynamic X-Force on Vertical Stabilizer (Body Axis)	[lb]
X_{WP}	Aerodynamic X-Force on the Wing Portion Outside the Rotor Wake (Freestream) in Body Axis	[lb]
Y_F	Aerodynamic Y-Force on Fuselage (Body Axis)	[lb]
Y'_F	Aerodynamic Y-Force on Fuselage (Wind Axis)	[lb]
Y_H	Aerodynamic Y-Force on Horizontal Stabilizer (Body Axis)	[lb]
Y_{iPYL}	Aerodynamic Y-Force Due to Pylon Interference Drag (Body Axis)	[lb]
Y_{iWK}	Arm between the Y-Coordinate of the Application Point of Induced Forces on the Wing and the c.g., K=R→Right, K=L→Left	[ft]
Y_{iWPK}	Aerodynamic Y-Force on the Wing Portion Immersed in the Rotor Wake in Body Axis, K=R→Right, K=L→Left	[lb]
Y_{JTK}	Jet Thrust along Y-Body, K=R→Right, K=L→Left	[lb]
Y_K	Mobile Coordinate for the Definition of the Induced Aerodynamics' Application Point along Y, K=R→Right, K=L→Left	[ft]
Y_{MG}	Main Landing Gear Force in Y-Body	[lb]
Y_{NG}	Nose Landing Gear Force in Y-Body	[lb]
Y_{PLAT}	Aerodynamic Y-Force Due to Pylon Drag During Sideslip (Body Axis)	[lb]
Y_{SD}	Aerodynamic Y-Force Due to Spinner Drag (Body Axis)	[lb]

Y_V	Aerodynamic Y-Force on Vertical Stabilizer (Body Axis)	[lb]
Y'_V	Aerodynamic Y-Force on Vertical Stabilizer (Wind Axis)	[lb]
Y_{WP}	Aerodynamic Y-Force on Wing-Pylon (Body Axis)	[lb]
Y'_{WP}	Aerodynamic Y-Force on Wing-Pylon (Wind Axis)	[lb]
Y_β	Fuselage Side Force Variation with Sideslip Angle	[ft ²]
z	Distance between the Rotor and the Ground	[ft]
Z_F	Aerodynamic Z-Force on Fuselage (Body Axis)	[lb]
Z_H	Aerodynamic Z-Force on Horizontal Stabilizer (Body Axis)	[lb]
Z_{iPYL}	Aerodynamic Z-Force Due to Pylon Interference Drag (Body Axis)	[lb]
Z_{iWPK}	Aerodynamic Z-Force on the Wing Portion Immersed in the Rotor Wake in Body Axis, K=R→Right, K=L→Left	[lb]
Z_{JTK}	Jet Thrust along Z-Body, K=R→Right, K=L→Left	[lb]
Z_{MG}	Main Landing Gear Force in Z-Body	[lb]
Z_{NG}	Nose Landing Gear Force in Z-Body	[lb]
Z_{PLAT}	Aerodynamic Z-Force Due to Pylon Drag During Sideslip (Body Axis)	[lb]
Z_{SD}	Aerodynamic Z-Force Due to Spinner Drag (Body Axis)	[lb]
Z_V	Aerodynamic Z-Force on Vertical Stabilizer (Body Axis)	[lb]
Z_{WP}	Aerodynamic Z-Force on the Wing Portion Outside the Rotor Wake (Freestream) in Body Axis	[lb]
α	Angle of Attack	[deg]
α_F	Fuselage Angle of Attack	[deg]
α_H	Horizontal Stabilizer Angle of Attack	[deg]
α_{HD}	Horizontal Stabilizer Angle of Attack for Drag Equation	[deg]
α_{HL}	Horizontal Stabilizer Angle of Attack for Lift Equation	[deg]
α_{iWK}	Angle of Attack of the Wing Portion Immersed in the Rotor Wake	[deg]
α_{PLAT}	Pylon Angle of Attack Used for Transformation from Wind to Body Axis	[deg]
α_{PYL}	Pylon Angle of Attack in Mast Axis	[deg]
α_{SP}	Spinner Angle of Attack Used for Transformation from Wind to Body Axis	[deg]
α_{SPN}	Spinner Angle of Attack in Mast Axis	[deg]

α_{WFS}	Angle of Attack of the Wing Portion Outside the Rotor Wake (Freestream)	[deg]
β	Angle of Sideslip	[deg]
β_{DV}	Vertical Stabilizer Angle of Sideslip for Drag	[deg]
β_F	Fuselage Angle of Sideslip	[deg]
β_H	Horizontal Stabilizer Angle of Sideslip	[deg]
β_{iWK}	Angle of Sideslip of the Wing Portion Immersed in the Rotor Wake	[deg]
β_M	Mast Angle	[deg]
β_{PLAT}	Pylon Angle of Sideslip Used for Transformation from Wind to Body Axis	[deg]
β_{SP}	Spinner Angle of Attack Used for Transformation from Wind to Body Axis	[deg]
β_V	Vertical Stabilizer Angle of Sideslip	[deg]
$[\gamma_{RV}]$	Matrix of Angles between the Line which Connects Rotor Tips and Vertical Fins and the Station Line	[deg]
δ	Ratio between Air Density and Air Density at Sea Level	[ND]
δ_a	Aileron Mean Deflection Angle (+ Right Aileron Up)	[deg]
$\frac{\Delta C_{lr}}{\frac{\partial \alpha_{WFS}}{\partial \delta_F} \delta_F}$	Aerodynamic Coefficient in the Wing Rolling Moment Equation	[rad ⁻¹]
$\frac{\partial C_{LWPFS}}{\partial \alpha_{WFS}}$	Aerodynamic Coefficient in the Wing Rolling Moment Equation	[rad ⁻¹]
$\left(\frac{\partial C_{LWPFS}}{\partial \alpha_{WFS}} \right) _{C_{LWP}=0}$	Aerodynamic Coefficient in the Wing Rolling Moment Equation	[rad ⁻¹]
δ_e	Elevator Angle	[deg]
δ_F	Flap Angle (Sometimes Flap Position Indicator, in this Case [ND])	[deg]
δ_r	Rudder Angle	[deg]
ΔV_{iSS}	Induced Velocity Due to Side-by-Side Effect	[ft/s]
$\frac{\partial \alpha_{WFS}}{\partial \delta_F}$	Partial of Wing Angle of Attack with Respect to Partial of Flap Deflection	[rad ⁻¹]
$\frac{\partial \sigma}{\partial \beta}$	Rolling Rate Correction Coefficient to Fin Sideslip Angle	[ND]
$\frac{\partial \sigma}{\partial \beta}$	Yawing Rate Correction Coefficient to Fin Sideslip Angle	[ND]
$\epsilon_{W/H}$	Wing Wake Deflection at the Horizontal Stabilizer (Downwash Factor)	[deg]
$\epsilon_{W/HOGE}$	Wing Wake Deflection at the Horizontal Stabilizer (Downwash Factor) without Compressibility Effects	[deg]

η_H	Dynamic Pressure Loss Function at the Horizontal Stabilizer	[<i>ND</i>]
η_{HS}	Dynamic Pressure Ratio at the Horizontal Stabilizer	[<i>ND</i>]
η_V	Dynamic Pressure Loss Function at the Vertical Stabilizer	[<i>ND</i>]
η_{VS}	Dynamic Pressure Ratio at the Vertical Stabilizer	[<i>ND</i>]
θ	Pitching Attitude of the Aircraft	[<i>deg</i>]
θ_0	Root Collective Pitch	[<i>deg</i>]
μ	Advance Ratio	[<i>ND</i>]
μ_L	Left Rotor Tip Advance Ratio	[<i>ND</i>]
μ_R	Right Rotor Tip Advance Ratio	[<i>ND</i>]
ρ	Air Density	[<i>slug/ft³</i>]
τ_e	Elevator Effectiveness	[<i>ND</i>]
τ_r	Rudder Effectiveness	[<i>ND</i>]
ϕ_M	Lateral Mast tilt	[<i>deg</i>]
Λ_i	Rotor Inflow	[<i>ND</i>]
Λ_{IGE}	Rotor Inflow In Ground Effect	[<i>ND</i>]
Λ_{OGE}	Rotor Inflow Out of Ground Effect	[<i>ND</i>]
Λ_W	Wing Quarter Chord Sweep Angle	[<i>deg</i>]
Ω	Instantaneous Rotor Speed	[<i>rad/s</i>]

BIBLIOGRAPHY

- [1] Harris Franklin D. *Introduction to Autogyros, Helicopters, and Other V/STOL Aircraft*. Moffet Field, California: National Aeronautics and Space Administration, 2015 (cit. on p. 2).
- [2] URL: <https://www.bellflight.com/> (cit. on pp. 3, 8, 9, 11).
- [3] Maisel Martin D., Giulianetti Demo J., and Dugan Daniel C. *The History of the XV-15 Tilt Rotor Research Aircraft: From Concept to Flight*. Washington, D.C.: National Aeronautics, Space Administration Office of Policy, and Plans NASA History Division, 2000 (cit. on pp. 4, 6).
- [4] URL: <https://www.nasa.gov/centers/dryden/multimedia/imagegallery/XV-15/ECN-13850.html> (cit. on p. 5).
- [5] URL: <https://www.zhaw.ch/en/engineering/institutes-centres/zav/aircraft-technologies/flight-mechanics-and-flight-control-systems/redsim-laboratory/> (cit. on p. 7).
- [6] Ferguson S. W. *A mathematical model for real time flight simulation of a generic tilt-rotor aircraft*. Mountain View, California: NASA, Ames Research Center, 1988 (cit. on pp. 7, 8, 14, 15, 20, 23, 26, 27, 29, 34, 35, 38–40, 45–47, 49, 52, 54, 77, 80, 84, 86, 88, 103, 117).
- [7] Barra Federico. “Development of a Tilt-Rotor Model for Real-Time Flight Simulation”. MA thesis. Torino: Politecnico di Torino, 2018 (cit. on p. 8).
- [8] Abà Anna. “Implementation of a Comprehensive Real-Time Simulation Model of a Tilt-Rotor Aircraft”. MA thesis. Torino: Politecnico di Torino, 2020 (cit. on p. 8).
- [9] Abà Anna, Barra Federico, Capone Pierluigi, and Guglieri Giorgio. “Mathematical Modelling of Gimbaled Tilt-Rotors for Real-Time Flight Simulation”. In: *MDPI* 1 (2020) (cit. on pp. 8, 15, 77).
- [10] URL: <https://www.leonardocompany.com/en/products/aw609> (cit. on pp. 9, 10).
- [11] URL: <https://www.airbus.com/newsroom/press-releases/en/2018/02/vahana--the-self-piloted--evtol-aircraft-from-a--by-airbus--succ.html> (cit. on p. 12).
- [12] URL: <https://dufour.aero/vision/> (cit. on pp. 12, 13).
- [13] Harendra P. B., Joglekar M. J., Gaffey T. M., and Marr R.L. *A mathematical model for real time flight simulation of the Bell Model 301 Tilt Rotor Research Aircraft*. Fort Worth, Texas: Bell Helicopter Company, 1973 (cit. on pp. 14, 25, 27, 34, 39, 40, 117).
- [14] URL: <https://aviation.stackexchange.com/questions/3863/what-is-the-coordinate-system-used-in-an-aircraft> (cit. on p. 15).

- [15] *Load Alleviation for a Tilt-Rotor Aircraft in Airplane Mode*. 2006. URL: https://www.researchgate.net/publication/245430649_Load_Alleviation_for_a_Tilt-Rotor_Aircraft_in_Airplane_Mode/figures?lo=1 (cit. on p. 16).
- [16] Napolitano Marcello. *Aircraft Dynamics From Modeling to Simulation*. West Virginia University: John Wiley & Sons, 2012 (cit. on p. 17).
- [17] Knight, Montgomery, and Wenzinger. *Wind Tunnel Tests on a Series of Wing Models Through a Large Angle of Attack Range. Part I-Force Tests*. NACA Report N° 317 (cit. on pp. 27, 48, 51).
- [18] Wernicke K. and Magee J. "XV-15 Flight Test Results Compared with Design Goals". In: *NASA, Ames Research Center* (1979) (cit. on pp. 30, 43).
- [19] Padfield Gareth D. *Helicopter Flight Dynamic*. Blackwell Publishing, 1996 (cit. on pp. 36, 75, 117).
- [20] Kleinhesselink K.M and Celi Roberto. "Stability and Control Modeling of tilt-rotor aircraft". MA thesis. College Park: University of Maryland, 2007 (cit. on pp. 36, 75, 117).
- [21] Anon. *USAF Stability and Control Datcom*. Wright-Patterson Air Force Base, Ohio: Air Force Flight Dynamics Laboratory, 1970 (cit. on p. 51).
- [22] Churchill G. B. and Dugan D. C. "Simulation of the XV-15 Tilt Rotor Research Aircraft". In: *NASA 1* (1982) (cit. on pp. 51, 73, 116).
- [23] Ferguson S. W. *Development and Validation of a Simulation for a generic tilt-rotor aircraft*. Moffett Field, California: NASA, Ames Research Center, 1989 (cit. on pp. 52, 56, 57, 63, 66, 67, 70–72, 102, 116).
- [24] Peters D. A. and Barwey D. "A General Theory of Rotorcraft Trim". In: *Hindawi 2* (1995) (cit. on p. 56).
- [25] Pitt D. M. and Peters D. A. "Theoretical prediction of dynamic-inflow derivatives". In: *Sixth European rotorcraft and powered lift aircraft forum* (1980) (cit. on p. 77).
- [26] Takahashi M. D. *A Flight-Dynamic Helicopter Mathematical Model with a Single Flap-Lag-Torsion Main Rotor*. TM-102267, 1990 (cit. on p. 77).
- [27] Leishman J. G. *Principles of Helicopter Aerodynamics*. Cambridge University, Cambridge: Cambridge, 2006 (cit. on pp. 77–79, 117).
- [28] Chen Robert T. N. *A Survey of Nonuniform Inflow Models for Rotorcraft Flight Dynamics and Control Applications*. Moffett Field, California: NASA Ames Research Center, 1989 (cit. on p. 80).
- [29] Van Hoydonck W. R. M., Haverdings H., and Pavel M. D. "A Review of Rotorcraft Wake Modeling Methods for Flight Dynamics Applications". In: *35th European Rotorcraft Forum* (2009) (cit. on p. 80).
- [30] Cheeseman I.C. and Bennet W. E. "The Effect of the Ground on a Helicopter Rotor in Forward Flight". In: *Aeronautical Research Council Reports and Memoranda* (1957) (cit. on pp. 80–82).

- [31] Mylapore Anand Radhakrishnan and Schmitz Fredric H. "An Experimental Investigation of Ground Effect on a Quad Tilt Rotor in Hover". In: *Journal of The American Helicopter Society* (2015) (cit. on p. 81).
- [32] Rosenstein Hal. *Tilt-Rotor Aerodynamics*. Washington D.C., 1992 (cit. on p. 82).
- [33] Young Larry A. and Derby Michael R. *Rotor/Wing Interactions in Hover*. Moffett Field, California: NASA, Ames Research Center, 2002 (cit. on p. 86).
- [34] Cooper George E. and Harper Jr. Robert P. *The Use of Pilot Rating in the Evaluation of Aircraft Handling Qualities*. West Virginia University: NASA, Ames Research Center, 1969 (cit. on p. 91).
- [35] *Aeronautical Design Standard Performance Specification Handling Qualities Requirements for Military Rotorcraft*. 1996 (cit. on pp. 91–94, 97, 99, 100, 116, 118).
- [36] Tischler Mark B. *Frequency-Response Identification of XV-15 Tilt-Rotor Aircraft Dynamics*. Moffett Field. California: Nasa, Ames Research Centre, 1987 (cit. on p. 93).